PROCEEDING

The 10th AUN/SEED-Net Regional Conference on Mechanical and Manufacturing Engineering

AUN/SEED-Net

The 10th RC MEManuE 2019
7-8 November 2019,
Phnom Penh, Cambodia

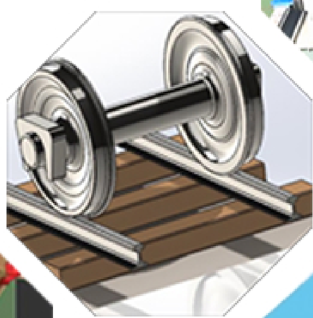

PROCEEDINGS

THE 10TH AUN/SEED-NET REGIONAL CONFERENCE ON MECHANICAL AND MANUFACTURING ENGINEERING

"Mechanical and Manufacturing Mobilization for Industrial 4.0"

November 7-8, 2019, Sokha Hotel, Phnom Penh, Cambodia

THE 10TH AUN/SEED-NET REGIONAL CONFERENCE ON MECHANICAL AND MANUFACTURING ENGINEERING

November 7-8, 2019, Sokha Hotel, Phnom Penh, Cambodia

Conference Chair	:Dr. Kinnaleth VONGCHANH
Co-Chair	:Dr. Sarin CHAN
	:Dr. Kollika NGOUN
	:Dr. Seingheng HUL
Coordinator	:Mr. Vanyi CHAO (ITC), Cambodia
Technical Committees	:Prof. Andi Isra Mahyuddin (ITB), Indonesia
	:Prof. Iman K. Reksowardojo (ITB), Indonesia
	:Dr. Eng. Agung Wibowo (ITB), Indonesia
	:Dr. Sri Raharno (ITB), Indonesia
	:Dr. Bambang Pramujati (ITS), Indonesia
	:Dr. To Dara (ITC), Cambodia
	:Dr. Chan Sarin (ITC), Cambodia
	:Dr. Yos Phanny (ITC), Cambodia
	:Dr. Chhith Saosometh (ITC), Cambodia
	:Dr. Sry Vannie (ITC), Cambodia
	:Dr. Liv Yi (ITC), Cambodia
	:Dr. Kinnaleth Vongchanh (ITC), Cambodia
	:Dr. Alvin Chua (DLSU), Philippines
	:Dr. Arie Wibowo (ITB), Indonesia
Editor	:Mr. Seab Piseth
	:Mr. Van Daro
	:Mr. Chhoun Bora

TABLE OF CONTENT

Geopolymers Derived from Philippine Coal Ash as Sustainable Alternative Low Heat Transmission and Fire Resistant Material for Buildings

Martin Ernesto L. Kalaw[1,*], Joshua Martin L. Kalaw[2],
Michael Angelo B. Promentilla[2]

[1)] Mechanical Engineering Dept., De La Salle University, 2401 Taft Ave., Malate, 1004 Manila, Philippines
[2)] Chemical Engineering Dept., De La Salle University, 2401 Taft Ave., Malate 1004 Manila, Philippines

[*]Corresponding e-mail: martin.kalaw@dlsu.edu.ph

ABSTRACT – Geopolymers are formed from alumina and silica rich materials by alkali dissolution and subsequent polycondensation into a polymeric network. As part of this study reported in Kalaw et al, 2016 [1], different mix proportions of coal ash and rice hull ash, as the alumino-silicate materials, were synthesized using NaOH-Na_2SiO_3 solutions, as the alkaline activator. The specimens formed were evaluated for heat transmission, heat and fire resistance, and strength. In the results obtained, the compressive strength ranged from 17 to 20 MPa, density of 1620 to 1800 kg/m^3, and thermal conductivity of 0.45 to 0.55 W/m-K. In the extension of this study, geopolymer samples were evaluated for fire resistance using ASTM E119 [2]. Also, using the optimum mix proportion obtained (85-10-5 fly ash-bottom ash- rice hull ash wt/wt ratio), two types of foaming agents, hydrogen peroxide and sodium perborate were used to determine their effects on strength, density, and thermal conductivity. Results gave compressive strength values ranging from 0.37 to 0.71 MPa and densities of 1430-1560 kg/m^3 at 0.3% to 0.4% peroxide (wt/wt) added. Values of thermal conductivity are within 0.033-0.037 W/m-K for all samples tested. Without foaming agents, the geopolymer properties were comparable to OPC-concrete for lightweight, moderate load-bearing structural applications with similar or better heat transmission characteristics. The fire resistance tests show that the geopolymer samples perform better than OPC concrete. However, the foamed geopolymers with their low strength are suitable for non-load bearing, insulation applications.

Keywords: geopolymers, waste utilization, foaming agents, fire resistance, sustainability.

1. INTRODUCTION

In this study, three sustainability issues are relevant: (i) the reduction in the use of natural resources via industrial waste utilization in the production of geopolymers; (ii) the reduction in greenhouse gas emissions via geopolymer production vis-à-vis OPC production; and (iii) the reduction of energy consumption in space cooling with the use of low heat transmission building materials.

Considering the first and second issues, it is known that the building sector has been dominated by ordinary Portland cement (OPC) for more than a century that OPC has become the second most consumed commodity in the world – second only to water [3]. But OPC production has high GHG emissions and energy consumption and causes the depletion of natural resources, such as limestone, sand, and clay, among others. Thus, while it is the OPC-based building sector that is presented with the environmental issues, geopolymers have been shown to be comparable if not better than OPC in terms of technical properties and its production has 80% less CO_2 emissions [4]. Moreover, sustainability is accessible since geopolymers can be formed from alumina- and silica- rich industrial wastes such as coal ash, mine tailings, furnace slag, etc. [5].

On the benefit of waste utilization, the major impact in the Philippines is in coal ash management. As of 2018, the Philippine Department of Energy (DOE) reported a total coal consumption of 30.8 MMT of which 84.6% was utilized by coal-fired power plants [6]. This is expected to rise as more coal-fired power plants are being built in the country [7].

On the third issue, the United Nations Environment Programme Sustainable Buildings and Climate Initiative (UNEP-SBCI) recognizes that the building sector utilizes “about 40% of global energy, 25% of global water, 40% of global resources, and emit approximately 1/3 of GHG emissions” and “yet, buildings also offer the greatest potential for achieving significant GHG emission reductions, at least cost, in developed and developing countries” and that “energy consumption in buildings can be reduced by 30 to 80% using proven and commercially available technologies” [8].

The Philippines is in the Tropics with hot and humid climates. As such the use of space cooling has become a necessity for the thermal comfort and productivity of occupants. As space cooling requirements increase with heat transmission across the building envelope, a better if not comparable alternative low heat transmission material should provide a positive impact towards decreasing the energy consumption associated with the space cooling in buildings [9].

The overall study aims to assess the characteristics of geopolymers formed using local waste materials particularly coal ash with the addition of rice hull ash and utilizing not just the fly ash but also significant amounts of bottom ash.

In the initial investigation [1], the optimum combination of coal fly ash (CFA), coal bottom ash (CBA), and rice hull ash (RHA) vis-à-vis strength and thermal properties were evaluated. Rice hull ash was considered as an additive since it contains a high percentage of silica [10] and its reaction with sodium hydroxide may increase the amount of sodium silicate which acts as the alkaline activator of the mixture [10, 11, 12].

In the extension of this study, geopolymer samples were evaluated for fire resistance using ASTM E119 [2]. Also, using the optimum mix proportion obtained in the initial study, two types of foaming agents, hydrogen peroxide and sodium perborate were used to determine their effects on strength, density, and thermal conductivity.

2. METHODOLOGY

In the initial study [1], different mix ratios of coal fly ash (CFA) with coal bottom ash (CBA) and rice hull ash (RHA) were used as dry raw materials. A mixture of 80-20 by mass ratio of 12M NaOH and Na_2SiO_3 (w/w: 2.5:1) solution is used as the activator. The composition of the raw materials, in percentage by mass, is listed in Table 1.

Table 1. Composition of raw materials using XRF

	CFA	CBA	RHA
Al_2O_3	21.75	18.40	
SiO_2	66.5	57.0	70.1
Cl		0.76	
K_2O	1.49		1.10
CaO	5.30	11.05	0.19
TiO_2	0.40	1.14	
Cr_2O_3		0.08	
Fe_2O_3	2.52	10.50	
LOI	2.18	1.07	28.64

In the extension study, the foamed geopolymers followed the same steps but small amounts (0.1 to 0.4 % by mass of the total mixture) of foaming agents hydrogen peroxide (H_2O_2) or sodium perborate, $Na_2B_2O_4(OH)_4$, were added.

The geopolymer samples were then cured for 28 days at a slightly elevated temperature of 80°C in a convection oven.

The raw materials and as-cured samples were analyzed using thermogravimetric analysis (TGA) to determine the range of thermal stability.

Fourier transform infra-red spectroscopy (FTIR) was used on the geopolymer samples to determine the extent of geopolymerization. X-ray diffraction (XRD) and scanning electron microscopy with energy dispersive x-ray analysis (SEM-EDX) were used to evaluate the composition and micro-structure of the raw materials and geopolymer samples.

Compressive strength was tested using an automatic uniframe compression tester and the thermal conductivity was measured using a thermal conductivity meter.

The fire resistance tests were conducted following ASTM E119, Standard Test Methods for Fire Tests of Building Construction and Materials [2]. Based on this standard, specimen failure is considered if the temperature of the unexposed surface of the sample rises an average of 140°C above its initial temperature. Visual cracking is also considered an indication of material failure due to fire exposure.

3. RESULTS AND DISCUSSION

In the initial characterization of the ternary mixture of CFA, CBA and RHA, the TGA analyses of samples, Figure 1, showed that more water is retained as more RHA is added. The high mass reduction up until about 110°C represents moisture loss due to evaporation. This high-water retention may be attributed to the high porosity and high unburned carbon content of the RHA as evidenced by its loss of ignition (LOI) of 28.64%. There is also an exothermic process from 350°C - 450°C which can be attributed to the combustion of the unburned carbon in the RHA. It is also noted that the compressive strength greatly decreases as RHA content is increased [1]. According to Davidovits [13], this effect is a result of the inhibition of the geopolymerization process due to unburned carbon content. For samples with very small amount of RHA, these events are very minor and the geopolymer samples can be considered thermally stable within the temperature range used for the test (ambient up to 800°C). Thermographs of geopolymer samples exposed to 1000°C for two hours show both chemical and thermal stability for the given temperature range. A sample of these thermographs is shown in Figure 2.

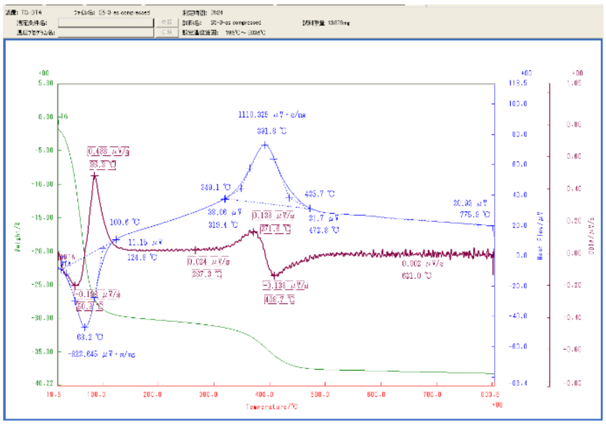

Figure 1. Sample TGA thermograph of an unfoamed geopolymer containing RHA

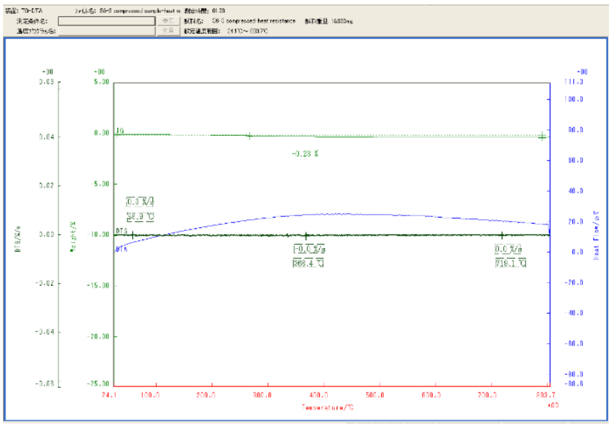

Figure 2. Sample thermograph of geopolymer after exposure to 1000°C for 2 hours

XRD diffractograms with varying amounts of RHA is shown in Figure 3. Increasing the RHA content results in higher amount of unreacted silica in the geopolymer as seen from the peaks in the diffractograms.

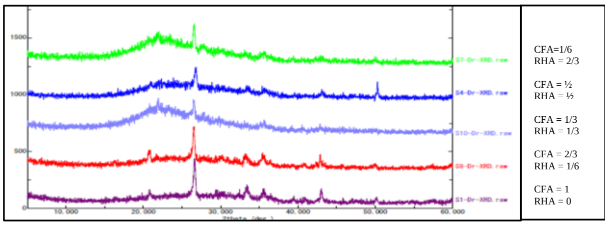

Figure 3. XRD diffractograms of geopolymer samples with varying amounts of RHA

In the FTIR spectrographs of unfoamed geopolymers, a sample of which is shown inFigure 4, the H-O-H bond stretching and bending were observed at wavenumber of 3450 cm^{-1}. The Si-O-Si, Si-O- bondings were observed at 1080 cm^{-1}. Si-O, Si-O-Al bondings were seen at 794 cm^{-1}. Si-O-Fe were seen at 467 cm^{-1}. The presence of Si-O-Al is an indication of geopolymer formation [14]. For samples containing high amount of RHA, very little shifting of the peaks towards Si-O-Al wavenumbers indicates that the geopolymerization process can still be improved because high amounts of silica remain unreacted. However, for samples that contain less RHA and those without RHA, the geopolymers have shown a higher shifting of peaks in the spectrographs indicating better geopolymerization. This correlates to higher compressive strengths as tested.

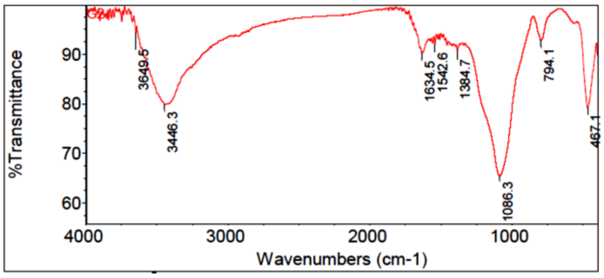

Figure 3. Sample FTIR spectrograph of geopolymer samples

Figure 4 shows SEM micrographs of the mixtures that gave the best strength and thermal conductivity combination. The SEM micrographs gave visual representations of the microstructure of the geopolymer samples and comparison with the micrographs of the materials prior to geopolymerization gave a qualitative indication of the degree of geopolymerizarion. In comparison with the base (raw) materials, the decreased sizes of particles indicate the extent of dissolution and subsequent polycondensation. However, the unchanged appearance of globules, particularly in Fig.4 (b), was indicative of poor reaction in comparison to Fig. 4 (a) and Fig. 4 (b). Fig. 4 (c) and Fig. 4 (d) compares the micro-structures of the unfoamed and foamed geopolymers using the 85-10-5 CFA-CBA-RHA mix. It is seen from the micrograph in Fig. 4 (c) that the structure is more compact compared to the micrograph in Fig. 4 (d) where the structure is have bigger pores.

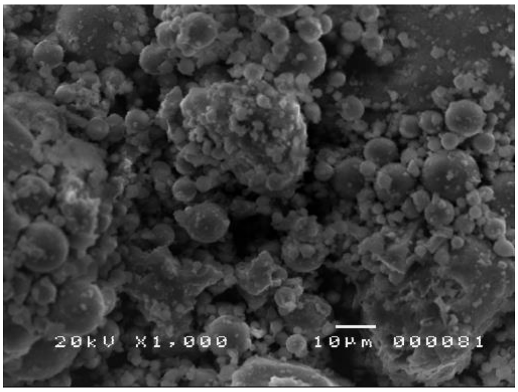

(a) 85-15 CFA-CBA

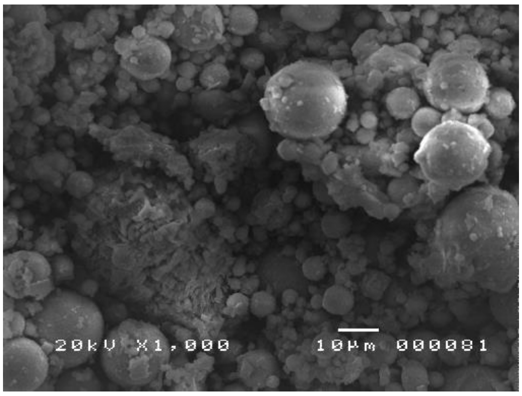

(b) 95-5 CFA-RHA

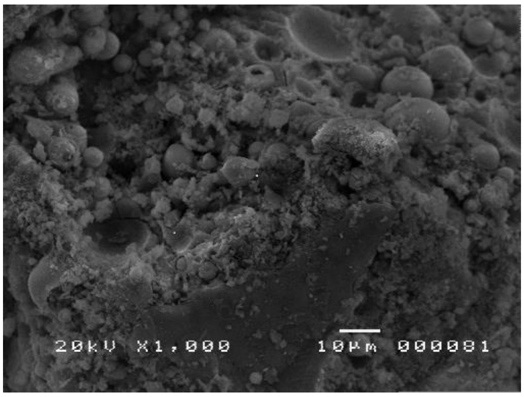

(c) 85-10-5 mix (unfoamed)

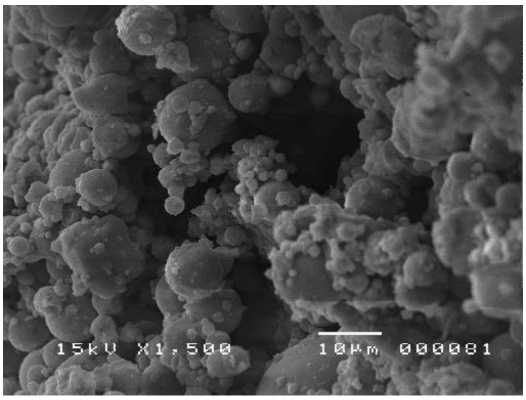

(d) 85-10-5 mix (foamed, 0.3% perborate)

Figure 4. Sample SEM micrographs unfoamed geopolymers (a) 85-15 CFA-CBA, (b) 95-5 CFA-RHA, (c) 85-10-5 CFA-CBA-RHA; and foamed geopolymer (d) 85-10-5 mix (foamed, 0.3% perborate)

The properties of the mixtures that gave the best strength and thermal conductivity combination are summarized in Table 2.

Table 2. Properties of unfoamed geopolymers mixtures with best combination of properties

Mix	CFA %	CBA %	RHA %	density kg/m^3	Ther cond W/m-K	comp str MPa
1	0.95	0.00	0.05	1617	0.452	16.6
2	0.85	0.15	0.00	1792	0.553	19.3
3	0.85	0.10	0.05	1743	0.480	18.1

ASTM C90-14, Standard Specification for Loadbearing Concrete Masonry Units [15] specifies a compressive strength greater than 11.7 MPa and a volumetric weight less than 1680 kg/m^3 for lightweight, moderate load bearing concrete. The American Concrete Institute [16] estimates the thermal conductivity of concrete to be around 0.54 W/mK at a volumetric weight of 1620 kg/m^3 and 0.67 W/mK at a volumetric weight of 1792 kg/m^3. Thus, for this range of applications, the strength matches that of concrete and the geopolymers have better thermal conductivity than concrete of similar volumetric weight.

With foaming agents, strength values are very low but the geopolymer samples are more lightweight and with have very low thermal conductivity. Results, as summarized in Table 3, gave compressive strength values ranging from 0.37 to 0.71 MPa and densities of 1430-1560 kg/m^3 at 0.3% to 0.4% foaming agent (wt/wt) added. Values of thermal conductivity are within 0.033-0.037 W/m-K for all samples tested.

Table 3. Summary of results for foamed geopolymers

Foaming Agent	% by dry mass	Therm Cond (W/m-K)	Comp strength (MPa)	Density (kg/m^3)
Peroxide	0.1	0.037	0.49	1810
	0.2	0.033	0.43	1860
	0.3	0.034	0.71	1440
	0.4	0.037	0.45	1540
Perborate	0.1	0.033	0.50	1820
	0.2	0.034	0.37	1850
	0.3	0.033	0.42	1430
	0.4	0.037	0.40	1560

Fire resistance tests were conducted on 50 mm thickness of different CFA-CBA-CFA mixtures of unfoamed geopolymer specimens including pure CFA and pure CBA geopolymers. The reference values are the tests done on pure OPC mortar and 1:2:3 ratio of OPC concrete. The results of these tests are tabulated in Table 4. From these results, the geopolymer samples obtained higher fire resistance ratings (FRR) than similar OPC samples. Figure 5 also shows that the geopolymer samples are essentially intact after exposure to fire.

Table 4. Fire resistance rating (FRR) of unfoamed samples.

Sample (50mm)	Mixture (CFA-CBA-RHA	FRR minutes
geopolymer	95-0-5	64
geopolymer	50-50-0	67
geopolymer	100-0-0	77
geopolymer	0-100-0	58
geopolymer	85-15-0	71
geopolymer	85-10-5	65
cement	mortar (pure)	35
concrete	1:2:3	31

Figure 5. Geopolymer samples after fire resistance test.

4. CONCLUSIONS

Based on the results of this study, the following conclusions are made:

1. Lightweight, low thermal conductivity, with moderate strength and having good fire resistance geopolymers can be developed from coal fly ash with coal bottom ash and rice hull ash as additives and with sodium hydroxide-sodium silicate ($NaOH$- Na_2SiO_3) solution as alkali activator.
2. However, based on the raw materials composition and loss on ignition values, increasing the RHA content does not improve the strength characteristics of geopolymers due to low reactivity.
3. Using foaming agents significantly reduces the thermal conductivity and volumetric weight of the geopolymers formed however the strength is markedly reduced.
4. For the samples without foaming agents, the geopolymer properties obtained are comparable to OPC concrete for lightweight, moderate load bearing structural applications with similar or better heat transmission characteristics. The foamed geopolymers formed, being very lightweight and having very low thermal conductivity may find applications as non-load bearing, insulation materials.
5. The geopolymers formed performed better in terms of fire resistance compared to similar samples of cement mortar and concrete.

Thus, the coal fly ash-based geopolymers, with raw material proportions and characteristics used in this study, show that their properties are comparable to conventional materials such as concrete. As such, they can be practical and sustainable building materials. Further research to improve properties and to mass commercialization may lead to large scale utilization in the future and may ultimately result in helping to alleviate the environmental impact of coal ash generation in the Philippines.

ACKNOWLEDGEMENT

The authors acknowledge the Hinode Laboratory of the IDE Department of Tokyo Institute of Technology for the use of their facilities; JICA and AUN/SEEDNet for financial and technical support; and the DLSU undergraduate thesis group of Alfred Relucio, Melvin Lim, Paul Palaypayon and Timothy Ngo for conducting the fire resistance tests.

REFERENCES

[1] M.E. Kalaw, A. Culaba, H. Hinode, W. Kurniawan, S. Gallardo, M.A. Promentilla, “Optimizing and characterizing geopolymers from ternary blend of Philippine coal fly ash, coal bottom ash and rice hull ash”. Materials. Vol. 9, Issue 7, 2016.

[2] ASTM E119: Standard Test Methods for Fire Tests of Building Construction and Materials. American Society for Testing and Materials. Current edition approved July 10, 2000. Published October 2000.

[3] CEMENT 101. http://www.globalcement.com/magazine/articles/490-cement-101-an-introduction-to-the-worlds-most-important-building-material (accessed on June 26, 2019).

[4] J. Davidovits, “Properties of Geopolymer Cements”, First International Conference on Alkaline Cements and Concretes, Scientific Research Institute on Binders and Materials. Kiev State Technical University, Kiev, Ukraine, 1994, pp. 131-149.

[5] C. Shi, A.F. Jiménez, A. Palomo, “New cements for the 21st century: The pursuit of an alternative to Portland cement.” Cem. Concr. Res. Vol. 41, pp. 750–763, 2011.

[6] Department of Energy, 2018 Coal consumption. https://www.doe.gov.ph/energy-resources?q=energy-resources/coal-statistics (accessed on September 10, 2019).

[7] Business Mirror. 49 Power Projects Ready by 2019. https://businessmirror.com.ph/2015/07/05/49-power-projects-ready-by-2019/ (accessed on September 10, 2019)

[8] Energy Efficiency For Buildings. UNEP Info sheet - EE Buildings.pdf http://www.studiocollantin.eu/pdf/UNEP%20Info%20sheet%20-%20EE%20Buildings.pdf (accessed on June 26, 2019).

[9] R. Wimmer, “Adapting Zero Carbon Houses for Tropical Climates – Passive Cooling Design in the Philippines. Proceedings SB13 - Sustainable Buildings, Infrastructures and Communities in Emerging Economies, November 25 – 27, 2013 GrAT, Center for Appropriate Technology, Vienna, Austria.

[10] U. Kalapathya, A. Proctor, J. Shultz, J. “An improved method for production of silica from rice hull ash.” Bioresource Technology 85, pp. 285–289, 2002.

[11] H.K. Tchakouté, C.H. Rüscher, S. Kong, E. Kamseu, C. Leonelli, “Geopolymer binders from metakaolin using sodium waterglass from waste glass and rice husk ash as alternative activators: A comparative study”. Construction and Building Materials. Volume 114, Pages 276-289, 1 July 2016.

[12] H.K. Tchakouté, C.H. Rüscher, S. Kong, et al. “Comparison of metakaolin-based geopolymer cements from commercial sodium waterglass and sodium waterglass from rice husk ash”. J Sol-Gel Sci Technol 78: 492. 2016.

[13] J. Davidovits, *Geopolymer Chemistry and Applications*. 3rd ed. France, Institut Géopolymère; 2011.

[14] Ghasan Fahim Huseien, Jahangir Mirza, “Ch. 1: Theory of geopolymer synthesis”. *Theory and Applications of Geopolymer in Civil Engineering Construction*. Ed. by Mohammad Ismail, Mohd Azreen Mohd Ariffin. 1st edition, Penerbit UTM press, June 2016.

[15] ASTM C90-14, Standard Specification for Loadbearing Concrete Masonry Units, ASTM International, West Conshohocken, PA, 2014, www.astm.org.

[16] American Concrete Institute. Guide to thermal properties of concrete and masonry systems, ACI 122R-02, © 2002.

Design of a Residential Residual Waste Disposal and Energy Generation via Pyrolyzer and Steam Rankine Cycle

Ferdinand G. Manegdeg[1], Paolo Yves L. De Silos[2*], and Jonathan R. Medrano[1]

[1] Department of Mechanical Engineering. National Graduate School of Engineering, University of the Philippines Diliman, Quezon City, Philippines
[2] Energy Engineering Program, National Graduate School of Engineering, University of the Philippines Diliman, Quezon City, Philippines

[*]Corresponding e-mail: pldesilos1@up.edu.ph

ABSTRACT – The design study concerns the creation of a waste-to-energy conversion plant in the City of Muntinlupa to lessen the amount of non-recyclable municipal solid wastes that ends up in the landfill. Using the developed criteria, the cluster that can be used are the biodegradable and residual waste portions of the municipal solid wastes. From the amount of waste generated, the amount of energy that can be extracted is 324 to 380 TJ. In consideration of the processes for power generation, Rankine cycle was seen as the best alternative powerplant type to use the biogas and synthetic gas produced from the biodigester and pyrolyzer, respectively. It is estimated that 5.5 to 6.5 MW of electricity may be produced, translating to a 500 million pesos of savings to the government of Muntinlupa. The electricity generation project has a return of investment of 15% and a payback period of 4.5 years.

Keywords: Waste to Energy, Residential Residual Waste, Pyrolyzer, Waste Disposal

1. INTRODUCTION

The continuous growth and development in urbanization and industrialization, together with increasing population growth, results to an exponential increment in the quantity of municipal solid waste (MSW) in the territory concerned. The MSW includes metal, paper, organic waste, cardboard, leather, wood, rubber, plastics, and the like. In the southern part of Asia, about 70 million tons of wastes is generated per year. The value is expected to triple by the year 2025 [1]. Hence, there is a need to mitigate and control municipal solid wastes through proper management systems. However, countries having relatively lower Gross Domestic Product (GDP), such as Sri Lanka, Malaysia, Thailand, and the Philippines, are having trouble in coping up with this problem due to lack of resources and facilities in taking care of the solid wastes [2].

The Philippines' waste generation rate (WGR) for rural and urban sectors are 0.3 kg/capita/day and 0.5 kg/capita/day, respectively. This translates to 35,580,000 kg of wastes generated every day. Of this value, 74% is attributed to residential areas. In addition, Metro Manila has a waste generation rate of 0.7 kg/capita/day or a generation of about 8,636,000 kg of wastes per day [3].

Estimations show that a government unit spends at most $100/capita/year in a state wherein insufficient action is taken on proper municipal solid waste management. This is observably higher than the estimated $7/capita/year that a government spends when proper waste management mechanisms are applied [4].

The objective of the study is to (a) determine an appropriate Local Government Unit (LGU) in the Philippines for sampling, (b) identify the waste cluster for fuel source, (c) evaluate the suitable energy conversion technology in utilizing the waste, (d) determine the appropriate powerplant to be used for electricity generation, and (e) calculate the financial feasibility of the waste-to-energy study.

2. METHODOLOGY

2.1 Sampling Design

Stratified random sampling was applied on the process of selection of location, fuel type, energy conversion technologies, and powerplant type. For simplicity, Simple Multi-Attribute Rating Technique (SMART) was used in all of the sampling and selection processes. A screening criteria was applied as well to narrow the alternatives as data sensitivity treatment.

In the selection of location to be used among the 17 cities and municipality in Metro Manila for the study, several quantifying concept were used: GDP per capita, economic growth rate, population, proximity to Laguna Bay for water source, number of households, land area, and crime index. The screening criteria applied was that GDP per capita should not be less than 10,000 and LGU location should be near the Laguna Bay or those located in District 4. Afterwards, the cities of Makati, Muntinlupa, and Taguig were left wherein Muntinlupa got the highest value at normalized weight.

The City of Muntinlupa is a highly urbanized city in the southernmost portion of Metro Manila. As of 2018, it has a population of 531,932. It is bordered by Las Piñas in the west, Parañaque in the northwest, Taguig in the North, Bacoor and Dasmariñas in Southwest, and San Pedro and the Laguna de Bay in the east. The city is known for its medical tourism, the New Bilibid Prison, expensive residential communities, and large malls [5].

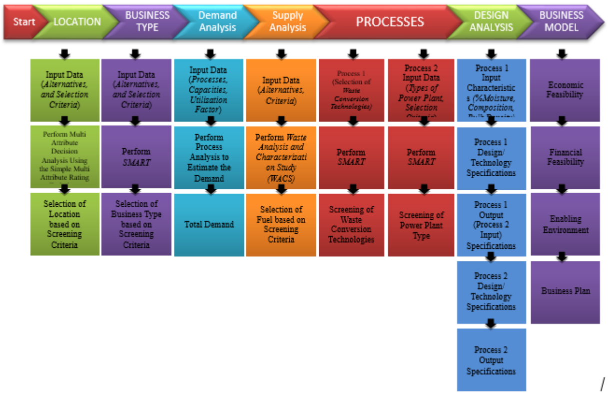

Figure 1 Methodology Flow

2.2 Waste Analysis and Characterization Study

To identify the waste conversion technology, a waste analysis and characterization study has to be available to see which waste type has the highest availability in percentage. The Waste Analysis and Characterization Study (WACS) was conducted by the City of Muntinlupa – Environmental Sanitation Center (ESC) in 2018. The waste-to-energy conversion technology to be used depends on the WACS of the municipal solid wastes. The average Waste Generation Rate (WGR) in Muntinlupa is 0.5417 kg/capita/day. Using the 2018 population of Muntinlupa, the city produces 288,147.56 kg of waste per day [6].

Table 1 shows the waste composition percentage and the corresponding computed heating value, as received from ESC.

Table 1 Summary of Muntinlupa MSW composition

Parameter	Percentage (%)	HHV (MJ/kg)
Biodegradable	43.39	4.36
Recyclable	29.17	-
Special Waste	0.15	-
Residual Waste for Possible Diversion	5.00	19.85
Residuals	22.29	

$$\text{Total CV of Feed} = \Sigma(CV_i)(x_i) \quad (1)$$

$$\text{Total CV of Feed} = (4.36\ MJ/kg)(0.4339) + (19.85\ MJ/kg)(0.05 + 0.2229)$$

$$\text{Total CV of Feed} = 1.8918 + 5.4171$$

$$\text{Total CV of Feed} = 7.3089\ MJ/kg$$

The MSW has a bulk moisture content of 39.5% as shown in Table 2.

Table 2 Moisture content of MSW according to generating sector

Sector	Moisture Content (%)
Low-income Residential	24.5
Mid-income Residential	47.6
High-income Residential	13.3
Commercial	56.6
Markets	80.6
Industrial	27.3
Institutional	16
All Sectors	39.5

2.3 Selection Processes

The SMART scheme was also used for the selection of the appropriate energy conversion technologies and powerplant type, the results of which are shown in Figures 2 and 3. The quantifying concepts used were technological maturity, reliability, energy potential, land area needed, water and air pollution, waste separation system, capital cost, operating and maintenance cost, and revenue. Incineration, biodigester, pyrolyzer, and gasifier were among the options for the energy conversation technologies. Biodigester was determined as most suitable for the converting biodegradable components of the MSW comprising 43.39% of the total wastes as shown in Table 1; on the other hand, pyrolyzer was the most applicable for residuals comprising 27.29% of the total wastes. For the powerplant type, the options were steam Rankine cycle, gas turbine, and internal combustion engine. The steam Rankine cycle was selected.

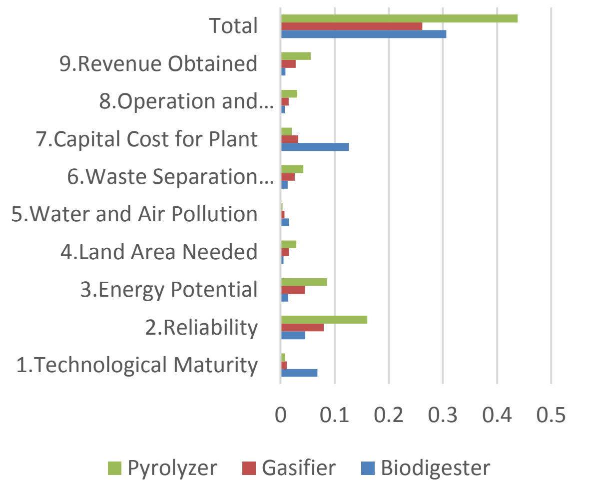

Figure 2 Normalized Screening of Energy Conversion Technology

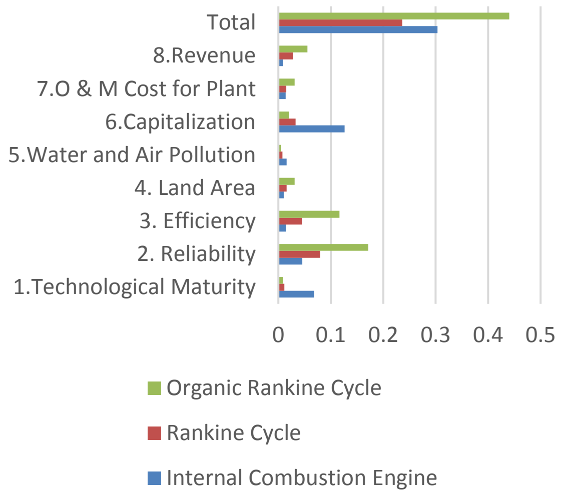

Figure 3 Selection of Power Plant Type

3. RESULTS AND DISCUSSION

The electricity demand in kilowatt-hour (kJ) was computed per capita. The information on the proposed powerplant supply or fuel, which is the waste generated, was provided by the Environmental Sanitation Center of Muntinlupa City.

3.1 Demand and Supply

In 2018, Muntinlupa City has an estimated energy demand of 110,272.46 kWh based on 746.30 kWh/capita [6] as a highly urbanized city (HUC).

$$\textit{Energy Demand (kWh)} = \textit{(Population)(746 kWh/capita)} \tag{2}$$

$$\textit{Energy Demand (kW)} = \textit{(Energy (kWh))/8766} \tag{3}$$

From equations (2) and (3), the city has an estimated energy demand of 50 MW by 2024 based on population growth and economic activity shown in Figure 3. Prior to 2018, waste generation was estimated to be 70,000 to 74,000 tons of waste consisting of biodegradables and residuals which comprises almost 95% of the total waste composition. Waste generation has a correlation with the population and economic activity of the city. It is projected that 117 million kg of waste per year will be generated by year 2024 from Figure 4 [7]

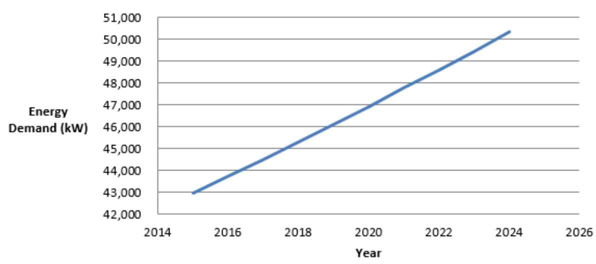

Figure 4 Energy Demand

3.2 Waste to Energy Conversion

The Pyrolyzer – Rankine Cycle Generator Power Plant System, which will convert MSW into energy, is divided into five major processes: pre-treatment, pyrolysis, synthetic gas clean-up, electricity generation, and post-treatment.

3.2.1 Pretreatment

The pre-treatment is done to remove the unwanted municipal solid waste. In the material recovery facility (MRF), the 30% recyclable MSW are separated from the non-recyclable residual wastes. Then, the MSW shall enter a hammer mill to reduce size. The size ranges of the milled MSW are differentiated with the use of a trommel screen. This is needed to ensure the removal of very small particles such as crushed glasses and soil. The non-ferrous metals shall be removed from the screened MSW using an eddy current separator. For the ferrous metals, a magnetic separator will be applied. After the removal of metals, size reduction will be employed again using a rotary shredder. The shredded MSW will be dried to an estimated moisture content of about 20%. After which, it will be sent to the rotary kilns.

3.2.2 Pyrolysis

Pyrolysis is defined as the thermal decomposition of biomass in a no-oxygen environment, or in this case, the pyrolyzer. The pyrolyzer will use an indirect-firing with rotary kiln at 500 °C. The pyrolysis char will be placed in the steam boiler as additional fuel. The synthetic gas (syngas) produced will undergo clean-up to remove impurities. The pyrolyzer has an estimated efficiency of 75%.

3.2.3 Gas Clean-up

To separate syngas and the pyrolysis tar, the gas clean-up system is needed. The system is composed of the cyclone separator, venture scrubber, clarifier, and a condenser. The syngas-tar will pass through the cyclone separator to remove the pure tar impurities. The pure tar will be placed in the boiler for additional fuel. The syngas will pass through the venture scrubber where the scrubbing water will be supplied by the clarifier. The water-syngas mixture will pass through the condenser. Likewise, the water-tar mixture will enter the clarifier. Using the condenser, the water will be liquefied and the syngas will be separated from the water. The water is recycled to the clarifier, while the purified syngas will go to the Rankine Cycle Generator.

3.2.4. Rankine Cycle Generator

To convert chemical energy into mechanical energy, the Rankine cycle powerplant is necessary. The unit is composed of a steam producer / boiler, a turbine-generator, a condenser, pumps, pipes and fittings. The steam boiler will fire the syngas to produce steam. The turbine-generator is necessary for the conversion of mechanical energy by the high-pressure steam received by the blades of the turbine, into electrical energy. The condenser will receive the outlet of the turbine to complete the Rankine cycle by condensing the steam then pumping it back to the steam boiler.

Equation (4) calculates the plant capacity in percentage form, where η_{Gen},$\eta_{Turbine}$,η_{Boiler},$\eta_{waste\ conv}$ are the estimated efficiencies of the Rankine cycle generator, turbine, boiler, and waste conversion (through pyrolysis), respectively.

$$\text{Plant Capacity, \%} = [(supply, kg/yr) \times \eta_{Gen} \times \eta_{Turbine} \times \eta_{Boiler} \times CV \times \eta_{waste\ conv})]/(3600 \times 24 \times 365) \quad (4)$$

Using equation (4), the plant capacity to be produced was computed to be 5.5 to 6.5 MW which is 10% to 15% of the total electricity demand of the city.

3.3 Financial Feasibility

The capital cost for the power plant is given by equation (5):

$$\text{Capital Cost} = \text{Direct Cost} + \text{Indirect Cost} + \text{Material Cost} + \text{Product Cost} \quad (5)$$

Direct costs includes the equipment costs, delivery charges, freight insurances, building and facilities, installation cost, land cost and administrative cost. Indirect costs includes engineering, supervision, design and construction, construction field expense and operational cost, contractor's fee and the building permit and licenses. Capital cost is estimated at 382 million pesos.

The proposed waste-to-energy is calculated to generate a 500 to 580 million peso annual savings to the City of Muntinlupa. Profitability analysis is seen at the return of investment at 15% and payback period of 4.5 years.

3.4 Economic Feasibility

Republic Act (RA) 9513 states that the power plant shall pay internal revenue tax after its seven year commercial operation. The Government will benefit from the Value-Added-Tax implementation on the seven year operation, plus the customs tax and duty tax, as well as the business related taxes.

The pyrolyzer-Rankine generator will generate revenue as a pioneer enterprise for waste collection, segregation, treatment and disposal at the Environmental Sanitation Center of Muntinlupa City. Since the peak demand for electricity rises during the semester break during the summer season, revenues can also be generated by selling the electricity to the grid.

Savings can also be generated for health and tourism for generating a good solid waste management per area or barangay. If 95% of generated waste convertible to energy are transformed, and the remaining 5% or recyclables are sold as scrap, there is an increase in the acceptability of the city for tourism, and health hazards are lowered by the absence of waste accumulation.

4. CONCLUSIONS

[1] The demand for electrical supply for the City of Muntinlupa is constant as well as the supply of residential residual waste or municipal solid waste is also consistent with respect to population growth, economic growth and general social habits.

[2] The residential residual waste disposal and energy generation via pyrolyzer-Rankine cycle generator has been found feasible promising a return on investment of 15% production and payback period of 4.5 years given all opportunities for revenues are achieved, which means all supply is sold.

[3] The City of Muntinlupa cannot depend totally on waste conversion for power generation based on the rate of waste generation; however, the city can properly dispose of 90 to 95% of its waste per capita by converting it to energy. It shall be able to empty most of its landfill in compliance will environmental and health laws.

[4] It is recommended that a detailed design be prepared.

ACKNOWLEDGEMENT

The authors would like to express their appreciation to the City of Muntinlupa - Environmental Sanitation Center for providing necessary data.

REFERENCES

[1] World Energy Council. (2016). World energy resources 2016. World Energy Council, London, UK.

[2] Castillo, A. L., & Otoma, S. (2013). Status of solid waste management in the Philippines. In Proceedings of the Annual Conference of Japan Society of Material Cycles and Waste Management The 24th Annual Conference of Japan Society of Material Cycles and Waste Management (p. 677). Japan Society of Material Cycles and Waste Management.

[3] Zhao, Y. (2017). Municipal solid waste management and waste to energy possibilities in the Philippines [Unpublished master's thesis]. Lappeenranta University of Technology, Lappeenranta, Finland.

[4] Soos, R. (2017). Financial aspects of solid waste management. Climate and Clean Air Coalition - Municipal Solid Waste Initiative, Dar es Salaam, Tanzania.

[5] City of Muntinlupa. (2019). About Muntinlupa. Retrieved July 5, 2019 from www.muntinlupacity.gov.ph/

[6] Muntinlupa Environmental Sanitation Center. (2018). Waste analysis and characterization study [Technical report], Muntinlupa, Philippines.

[7] Igoni, A. H., Ayotamuno, M. J., Eze, C. L., Ogaji, S. O. T., & Probert, S. D. (2008). Designs of anaerobic digesters for producing biogas from municipal solid-waste. Applied energy, 85(6), 430-438.

Fatigue Analysis of The Bogie in Automated People Mover

Satrio Wicaksono[1*], Khairunnas[1], Andi Isra Mahyuddin[1]

[1)] Faculty of Mechanical and Aerospace Engineering, Institut Teknologi Bandung, Jl. Ganesa 10, Bandung 40132, Indonesia

*Corresponding e-mail: satriowicaksono@ftmd.itb.ac.id

ABSTRACT – Recently, automated people mover (APM) becoming one of the popular transportation modes in the airport, tourism object and in the city, due to its lightweight, thus needed less expensive infrastructure in comparison to the mass rapid transportation (MRT) and normal train. In the design process of the APM, fatigue analysis needs to be performed to ensure the APM to reach its design life. As one of the main parts in the APM, fatigue analysis needs also to be performed on the bogie. In the current work, finite element analysis was performed on the bogie of an APM system. The stress results were then used to analyze the design life of the bogie. The simulation results show that the designed bogie was able to withstand the given load, which was shown from the value of equivalent stress that did not exceed the standards set by the Indonesian government. Additionally, the bogie also has infinite design life even if the APM operated under full load condition.

Keywords: Finite element analysis; fatigue analysis; bogie; monorail; automated people mover

1. INTRODUCTION

Automated people mover (APM) is popular nowadays, especially in the place where light infrastructure is preferable such as in the middle of the crowded city, tourism object and airport. One of the most popular APM is monorail. Monorail was first invented in the United Kingdom around 1820, almost at the same time as the widespread use of steam locomotive [1]. The first general usage of monorail happened in 1888 to carry passengers and goods in Ireland [1]. There are two types of monorail: straddle and suspended types, with the former being the more popular option [2]. One of the main components in the monorail is the bogie. The design of the bogie is varied depending on which train or monorail it is being installed. The service life of the bogie is greatly influenced by the ability to withstands irregular loads which will trigger the development of fatigue crack [3]. This ability is referred to as the fatigue strength. The testing which must be performed to the bogie frame in order to ensure its fatigue strength is governed in UIC 615-4 [4].

PT INKA, the only train manufacturers in Indonesia, recently designed a monorail system for automated people mover in one of the major airports. The bogie of the monorail system has 2 axles, with 2 wheels at each axle. Additionally, the bogie is also equipped with 4 guiding wheels and 2 balancing wheels. In order to check the fatigue strength as well as the service life of this monorail system's bogie, a set of test must be performed according to UIC 615-4 [4].

In the current work, finite element simulation will be performed on the bogie of a monorail system designed by PT INKA. The finite element simulation will be performed based on UIC 615-4 standard [4] which was combined with local Indonesian law PM 37 2014 [5] to ensure the safety of the bogie when it is in operation. Static and fatigue analysis then will be performed based on the value of the stress of each component in order to investigate the service life of the bogie.

2. METHODOLOGY

The bogie model was based on the actual design on the monorail which was planned to be used in one of the main airports in Indonesia as shown in Figure 1. Simplification of the model was performed especially on the interaction between all the wheels and bogie frame. In this case, the boundary and loading conditions were made such a way to represent the actual loading on the bogie. The bogie model was divided into two: the bogie frame model and the axle model. The final model of the bogie frame completes with boundary and loading conditions is shown in Figure 2. The given load was assumed based on the data from PT INKA, which includes: the empty weight of the train of 16093 kg, bogie weight of 3149 kg and passenger weight of 80 kg. Due to the bogie frame complex geometry, convergence test needs to be performed. The final bogie frame finite element model as shown in Figure 3, has 220000 elements with a relative error of 3%.

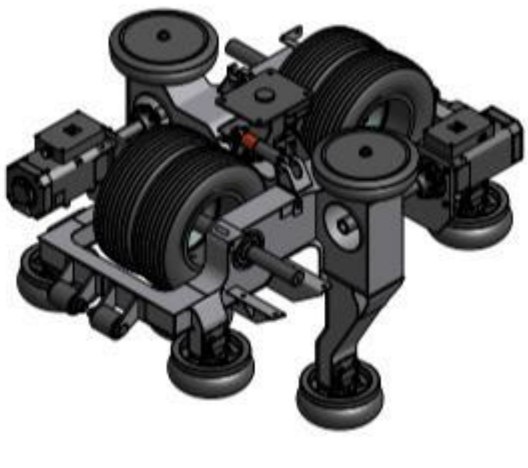

Figure 1 APM Bogie design

Two different loadings were implemented to the bogie frame based on UIC 615-4 [4]: exceptional load (static analysis) and full operation load (fatigue analysis). The exceptional load condition was performed in order to ensure no occurrence of plastic deformation in the bogie when in operation. In the case of exceptional load, the magnitude of the vertical load to the bogie is given as follows:

$$F_{z1\,max} = F_{z2\,max} = \frac{1.4g}{2n_b}(m_v + c_1 - n_b m^+) \quad (1)$$

where g is the gravitational acceleration, n_b is the number of bogie, m_v is the empty weight of the train, c_1 is the load due to passengers weight and $m^+$is the bogie weight. The other load in the case of exceptional load is the transversal load with magnitude as follows:

$$F_{y\,max} = 2\left(10^4 + \frac{(m_v+c_1)g}{3n_e n_b}\right) \quad (2)$$

where n_e is the number of wheelset at each bogie.

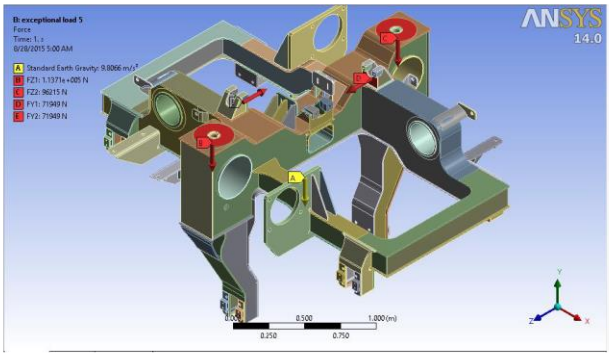

Figure 2 Finite element model loading condition

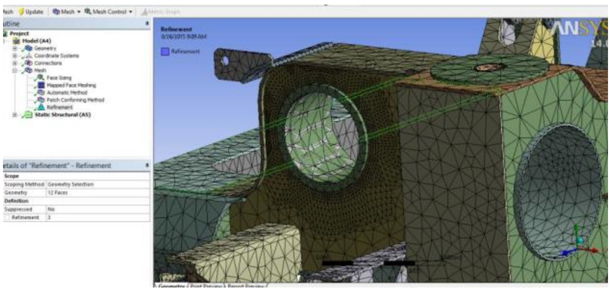

Figure 3 Refined mesh in the final finite element model

The fatigue analysis in full operating load, on the other hand, must be performed to ensure the design life of the bogie. The magnitude of the full operating load is given as follows:

$$F_z = \frac{g}{2n_b}(m_v + 1.2c_2 - n_b m^+) \quad (3)$$

$$F_y = 0.5(F_z + 0.5\, m^+ g) \quad (4)$$

where c_2 is the load due to passenger weight for main in-service load test. Based on UIC 615-4, for both loading cases, combined loading is given with loading variation due to vertical bounce and rolling movement of the train. The magnitude of rolling variation (α) is 0.1 and the magnitude of the bouncing variation (β) is 0.2. The complete combined loading for both loading cases is shown in Table 1.

The resulting stress from the finite element analysis was then used to evaluate the fatigue life of the bogie structure. The evaluation was performed by first calculating the mean and alternating stress from the resulting stress field. Then followed by checking whether the stress states were still below the endurance limit based on Soderberg, modified Goodman, Gerber, ASME-elliptic and Langer first-cycle-yielding criteria as stated in Equations (5) to (9) respectively.

$$\frac{S_a}{S_e} + \frac{S_m}{S_y} = 1 \quad (5)$$

$$\frac{S_a}{S_e} + \frac{S_m}{S_{ut}} = 1 \quad (6)$$

$$\frac{S_a}{S_e} + \left(\frac{S_m}{S_{ut}}\right)^2 = 1 \quad (7)$$

$$\left(\frac{S_a}{S_e}\right)^2 + \left(\frac{S_m}{S_y}\right)^2 = 1 \quad (8)$$

$$S_a + S_m = S_y \quad (9)$$

where S_a, S_e, S_m, S_y and S_{ut} are the alternating, endurance, mean, yield and ultimate strengths respectively.

Table 1 Combined loading cases

Load Case	**Vertical Load**		**Longitudinal Load**
	Fz1	**Fz2**	
1	Fz	Fz	0
2	(1 + α – β) Fz	(1 – α – β) Fz	0
3	(1 + α – β) Fz	(1 – α – β) Fz	+Fy
4	(1 + α + β)Fz	(1 – α + β) Fz	0
5	(1 + α + β)Fz	(1 – α + β) Fz	+Fy
6	(1 – α – β) Fz	(1 + α – β) Fz	0
7	(1 – α – β) Fz	(1 + α – β) Fz	-Fy
8	(1 – α + β) Fz	(1 + α + β)Fz	0
9	(1 – α + β) Fz	(1 + α + β)Fz	-Fy

In the case of bogie axle, the loading was given based on the exceptional load condition mentioned previously. Simple calculation was then performed to evaluate the actual load which happened on the axle. The loads were applied to 4 locations as shown in Figure 4: area 1 and 2 which are the wheelset locations, area 3 where the contact with the bearing of the bogie took place and area 4 where the gear would be directly connected to the motor. The final boundary and loading conditions of the bogie axle is shown in Figure 5. Additionally, Figure 6 shows the final finite element model of the bogie axle.

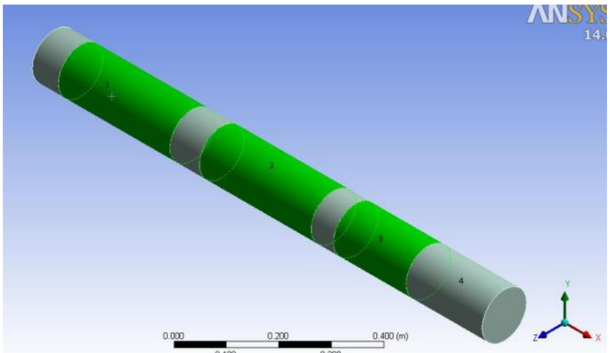

Figure 4 Basic geometry of the bogie axle

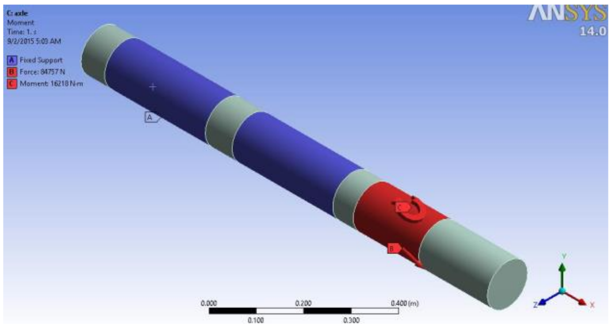

Figure 5 Boundary and loading conditions at bogie axle

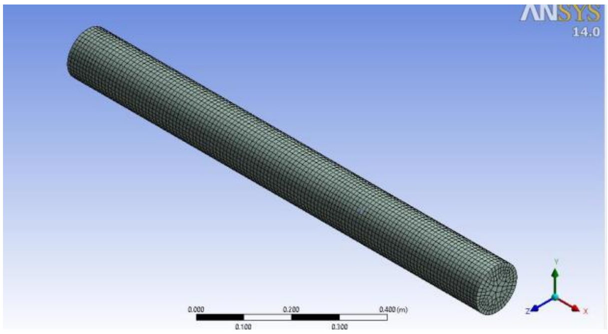

Figure 6 Final finite element model of the bogie axle

3. RESULTS AND DISCUSSION

The stress distribution of the most critical exceptional static load case (load case number 5) is shown in Figure 7. It is shown that the maximum Von Mises stress of 138.99 MPa happened at the location with the red tag. The result is still well below the bogie frame yield strength of 245 MPa (SM400A material).

The fatigue analysis in full operating load was also performed by first calculating the alternating and mean stresses at several different critical locations. The calculation results were then checked using the endurance limit based on Soderberg, modified Goodman, Gerber, ASME-elliptic and Langer first-cycle-yielding criteria as stated previously. It is shown in Figure 8 that the combination of alternating and mean stresses at all critical locations in the bogie were still below the endurance limit. Thus, it can be stated that the bogie frame has infinite design life.

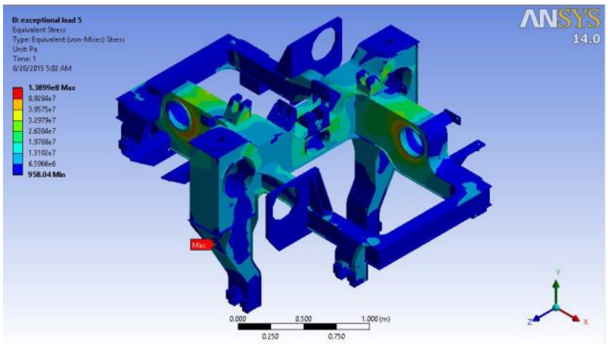

Figure 7 Stress distribution result in bogie mainframe for load case number 5.

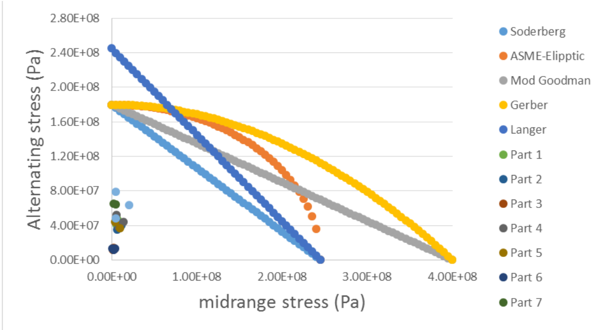

Figure 8 Fatigue failure condition according to Soderberg, modified Goodman, Gerber, ASME-elliptic and Langer first-cycle-yielding criteria

The static analysis of the axle for exceptional loading case, gave maximum Von Misses stress of 64.24 MPa as shown in Figure 9. With a safety factor of 2.5, the allowable stress of SM400A steel would be 98 MPa, which is still higher than the maximum Von Misses stress. Further analysis of the bogie axle also showed that the deflection was small enough, with the maximum deflection of 8.67x10^{-2} mm as shown in Figure 10. Both results confirmed the safety of the bogie axle.

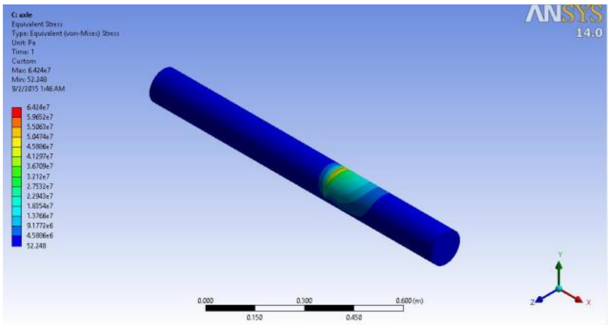

Figure 9 Stress distribution on the axle

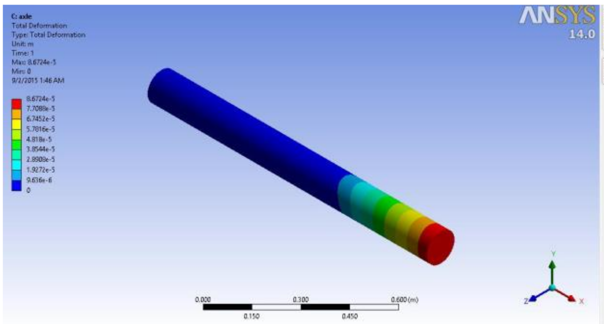

Figure 10 Deformation distribution on the axle

4. CONCLUSIONS

The finite element model of the bogie frame and bogie axle have successfully been created. The stress from the finite element results were then used the analyze the static condition and fatigue life of the bogie structure. Static analysis results of the bogie frame and bogie axle at exceptional loading conditions show that the bogie frame and bogie axle were safe. Additionally, the fatigue analysis of the bogie frame also shows that the stress states at all loading cases were still below the endurance limit of the material based on Soderberg, modified Goodman, Gerber, ASME-elliptic and Langer first-cycle-yielding criteria. Which prove that the bogie frame has infinite design life.

ACKNOWLEDGMENT

We gratefully acknowledge Research, Community Service and Innovation Program (P3MI) Institut Teknologi Bandung as well as Universities Outstanding Fundamental Research Program (PDUPT), RISTEKDIKTI for supplying the financial support.

REFERENCES

[1] Gilchrist, A.O., A History of Engineering Research on British Railways, Institute of Railways Studies and Transport History, University of York, Heslington, UK, 2009.

[2] Su Minghui, Application and Development of Chongqing Straddle Application and Development of Chongqing Straddle-type Monorail System, Kasetsart University, Bangkok, Thailand, 16 May 2013.

[3] Jishan Li, The Experiment Study for Fatigue Strength of Bogie Frame of Beijing Subway Vehicle Under Overload Situation, The Open Mechanical Engineering Journal, 2015 (9) pp 260-265.

[4] UIC CODE 615-4, Motive Power Units – Bogies and Running Gear – Bogie Frame Structure Strength Test, 2nd Edition, 2003.

[5] Pemerintah Republik Indonesia, Peraturan Menteri Perhubungan Republik Indonesia nomor 37 Tahun 2014 tentang Standar Spesifikasi Teknis Sarana Kereta Api Monorel, Jakarta, 2014.

Temperature Variation of Rubber under Uniaxial Cyclic Tension

Tam Hoai Le[1]*, Takumi Yoshikawa[2], Yu Kurokawa[1], Hirotsugu Inoue[1]

[1)] Department of Mechanical Engineering, Tokyo Institute of Technology,
O-okayama, Meguro, Tokyo 152-8552, Japan
[2)] Formerly Department of Mechanical Engineering, Tokyo Institute of Technology

*Corresponding e-mail: le.h.ac@m.titech.ac.jp

ABSTRACT – Thermal response of rubber materials under mechanical loading has special properties compared to other materials. However, most of existing researches remain qualitative discussions and its quantitative evaluations are not studied very well. The main objective of this study is to quantitatively clarify the relationship between cyclic deformation and temperature variation of carbon black filled styrene-butadiene rubber (SBR). The temperature variation under uniaxial cyclic tension is predicted by considering three factors: thermoelastic effect, Gough-Joule effect and viscous dissipation effect. Heat transfer between the specimen and the surrounding air is also taken into account. The result is compared to experimental data. It is found that the predicted temperature variation is in good agreement with the one measured by the infrared thermography.

Keywords: Rubber material, Temperature variation, Thermoelastic effect, Gough-Joule effect, Energy dissipation effect

1. INTRODUCTION

Studies on thermal response of rubber materials under mechanical loading focus on reversible and irreversible heat process. Gough (1805) observed that a rubber band warms under tension and cools during retraction [1]. This study was extended by Joule (1859) [2]. Since then, it is well known as Gough-Joule effect. Also in Joule's research, he found that under tension there is a slight decrease in temperature at small deformation. This is due to contribution of the thermoelastic effect. Afterward, there are very few researches dedicated to the thermal response. Hence, understanding on the reversible heat process of rubber materials under mechanical deformation is insufficient. Meanwhile, some excellent papers on the irreversible heat process have been published. Boukamel et al [3] proposed a thermo-mechanical constitutive model to describe self-heating of an elastomeric piece subjected to cyclic shearing. Rodas et al [4] simulated heat build-up in rubber materials under low-cycle fatigue by developing a finite strain thermo-viscoelastic constitutive model.

To the best of author's knowledge, there is no research that quantitatively evaluates temperature variation of rubber materials under cyclic tension by simultaneously considering three factors, namely, thermoelastic effect, Gough-Joule effect and energy dissipation effect. Accordingly, the main purpose of this paper is to give a quantitative discussion on the temperature variation caused by the three above-mentioned effects under uniaxial cyclic tension.

2. METHODOLOGY

The working flow of research methodology to consider temperature variation under steady state cyclic loading condition is organized in Figure 1.

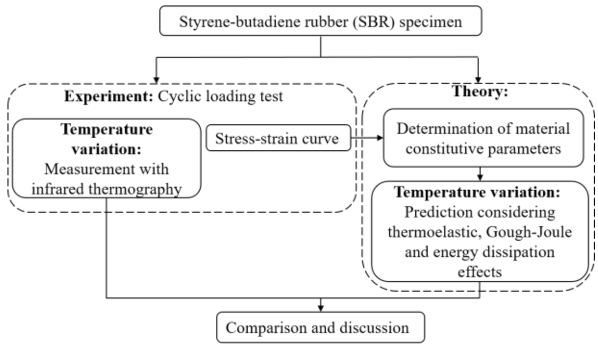

Figure 1 Flow of the present study

2.1 Experimental methodology

Carbon black filled styrene butadiene rubber (SBR) is selected for the test. The specimen with gauge dimensions of 5 mm width, 20 mm height, 2.4 mm thickness as shown in Figure 2 was cut according to Japanese Industrial Standard K 6251:2010 dumbbell type No.3 with the dimensions allowing to get a homogenous stress-strain and temperature fields.

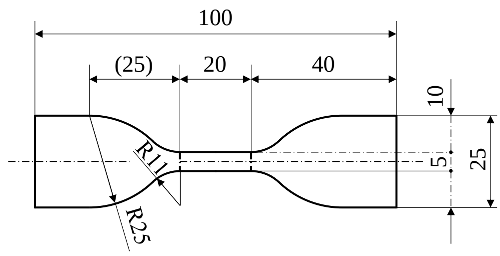

Figure 2 JIS K 6251:2010 Dumbbell No. 3 specimen

To investigate thermal response as well as to obtain mechanical data, the sinusoidal cyclic tensile loading test was conducted at strain amplitude of 0.1876 and mean strain of 0.4690 with hydraulic servo fatigue testing machine. The loading frequency was 1 Hz. Load and displacement signals were recorded by an oscilloscope to calculate nominal stress and strain. At the same time, temperature variation at the gauge zone surface was measured by infrared thermography.

2.2 Theoretical methodology

In this study, a three-element constitutive model with two rubber elastic elements and a linear viscous element was employed as shown in Figure 3.

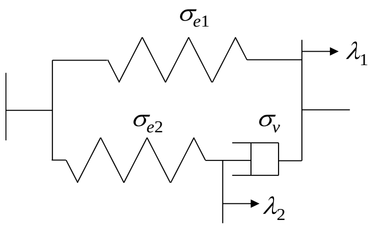

Figure 3 Constitutive model

Non-linear behavior of both springs is characterized by using three-chain network model [5] as follows:

$$\sigma_{ei} = C_{Ri}\left[L^{-1}\left(\frac{\lambda_i - a_i}{\sqrt{n_i}}\right) - \frac{L^{-1}\left(\frac{1}{\sqrt{(\lambda_i - a_i)n_i}}\right)}{(\lambda_i - a_i)^{\frac{3}{2}}} + b_i\right]. \quad (1)$$

The parameters a_i and b_i are additionally introduced to consider stress softening (Mullins effect) and residual strain. Constitutive equation for a linear dashpot is:

$$\sigma_v = \eta(\dot{\lambda_1} - \dot{\lambda_2}). \quad (2)$$

In the above equations, i=1,2 and C_{Ri}, n_i, a_i, b_i, η are material parameters which are determined so as to match the experimental data, λ is the stretch ratio and L^{-1} is the inverse Langevin function approximated as:

$$L^{-1}(x) = 3x + \frac{9}{5}x^3 + \frac{297}{175}x^5 + \frac{1539}{875}x^7 + \cdots. \quad (3)$$

The theoretical formulas for predicting temperature variation of rubber under cyclic loading due to thermoelastic, Gough-Joule and energy dissipation effects were derived. Firstly, temperature variation due to thermoelastic effect is expressed as follows:

$$\Delta T_1 = \int_0^t -\frac{T\alpha}{\rho c_p}(\dot{\sigma_{e1}} + \dot{\sigma_{e2}})\, dt. \quad (4)$$

Secondly, temperature variation due to Gough-Joule effect can be represented as:

$$\Delta T_2 = \int_0^t \frac{1}{\rho c_v}(\sigma_{e1}\dot{\lambda_1} + \sigma_{e2}\dot{\lambda_2})dt. \quad (5)$$

Finally, temperature variation due to energy dissipation effect can be obtained as:

$$\Delta T_3 = \int_0^t \frac{1}{\rho c_v}\eta(\dot{\lambda_1} - \dot{\lambda_2})^2 dt. \quad (6)$$

In the above equations, α is the coefficient of thermal expansion, T is the absolute temperature of the material, ρ is the density, c_p and c_v are the specific heat at constant pressure and volume, respectively, and over dot indicates differentiation with respect to time.

3. RESULTS AND DISCUSSION

Figure 4 shows the comparison between the theoretical and experimental stress-strain hysteresis loops under steady state. It can be seen that the model fits the experimental result very well. Hence, it is confident to use this model for prediction of the temperature variation.

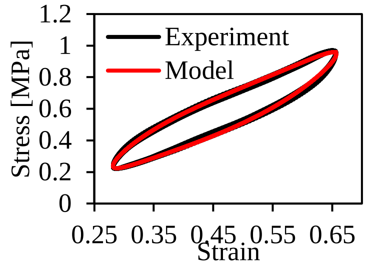

Figure 4 Stress-strain hysteresis loop

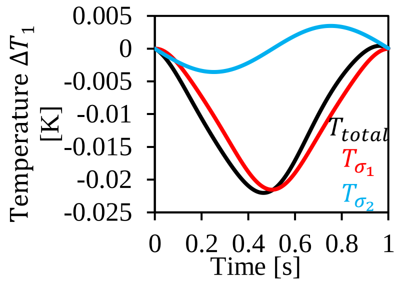

Figure 5 Temperature variation due to thermoelastic effect

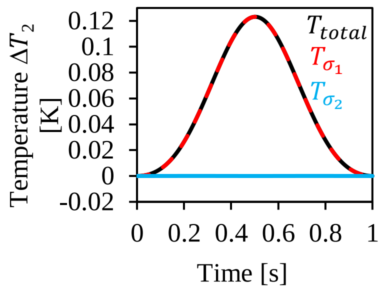

Figure 6 Temperature variation due to Gough-Joule effect

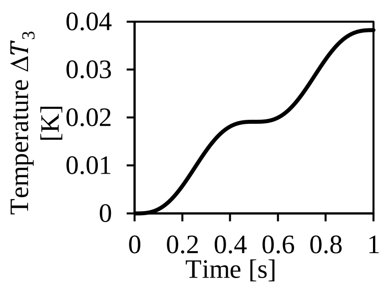

Figure 7 Temperature variation due to energy dissipation effect

Figures 5, 6 and 7 reveal the predicted temperature variation under cyclic tension due to thermoelastic, Gough-Joule and energy dissipation effects obtained by using equations (4), (5) and (6), respectively. Figures 5 and 6 indicate that temperature variation due to thermoelastic and Gough-Joule effects (black curve T_{total}) is the sum of temperature variation caused by elastic component (red curve T_{σ_1}) and viscoelastic component (blue curve T_{σ_2}). It is noted that the contribution of the viscoelastic component on Gough-Joule effect is insignificant. The temperature variation caused by these two effects returns to its initial value at the end of the loading cycle. On the other hand, the temperature variation caused by energy dissipation effect always increases and varies at a frequency twice of the loading frequency as shown in Figure 7. This is attributed to the effect of viscosity in both loading and unloading phases.

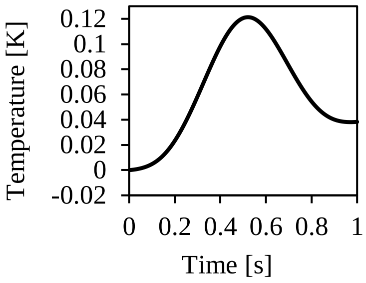

Figure 8 Temperature variation during a cycle under adiabatic condition

Combining these three, the temperature variation during one loading cycle is obtained as shown in Figure 8 in which the temperature variation is predicted under adiabatic condition. It can be seen that during loading phase the temperature increases mainly due to the Gough-Joule effect. During unloading phase, the temperature decreases and it does not return to its initial value. This is due to the contribution of energy dissipation effect.

In real steady state condition, however, there is some amount of heat exchange between the specimen and the surrounding air. Hence, in order to obtain a more realistic prediction, heat transfer should be taken into account. Figure 9 illustrates the method to consider the heat transfer in this study. At the beginning, real temperature $T_{r,0}$ is assumed to be equal to adiabatic temperature $T_{a,0}$ and equal to zero. Next, real temperature variation at the time step i is considered. If adiabatic condition is applied from point A, the temperature at the next time step will be point B. The increment of temperature from point A to point B is equal to the increment of adiabatic temperature $\Delta T_{a,i+1}$. In reality, because there is occurrence of heat transfer which can be assumed to be equal to $-b(T_{r,i} - T_{amb})$, where b is heat transfer coefficient which is determined by manual searching, $T_{r,i}$ is real temperature at time i and T_{amb} is ambient temperature. The negative sign in front of T_{amb} means that the heat flows away from the specimen if the ambient temperature is lower than the real temperature. On the other hand, the real temperature evolution is only equal to $\Delta T_{r,i+1} = T_{r,i+1} - T_{r,i}$. Based on these assumptions, the real temperature at the time step $i + 1$ will be calculated as:

$$T_{r,i+1} = (1 - b)T_{r,i} + \Delta T_{a,i+1} + bT_{amb}.$$

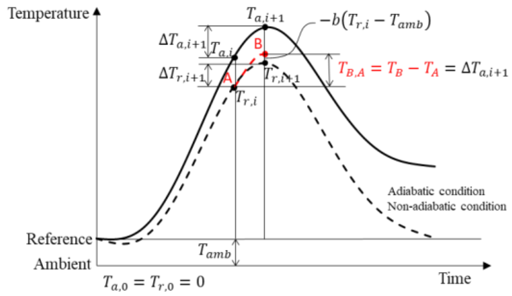

Figure 9 Modelling of the effect of heat transfer on temperature variation

The predicted temperature variation when heat transfer is considered is shown in Figure 10 (red curve) and is compared to experimental result (black curve). A good agreement is pointed out except for a slight decrease at the beginning of loading phase in the predicted one.

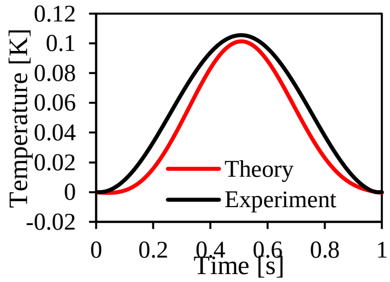

Figure 10 Comparison of the temperature variation between predicted and experimental results during a cycle

In Figure 11 comparison between the predicted and experimental temperature variation versus strain is presented. It can be seen that the temperature amplitude is predicted well. It is also noted that the temperature variations during loading and unloading phase are different each other, which is due to the energy dissipation in both prediction and experiment. Besides that, there are some discrepancies which are mainly related to a slight decrease in temperature at the beginning of the loading phase and the predicted temperature variation is lower than that of the experimental one. This can be attributed to the insufficient assumption on the heat transfer. Hence, further study is needed to consider the heat transfer between the specimen and the surrounding air.

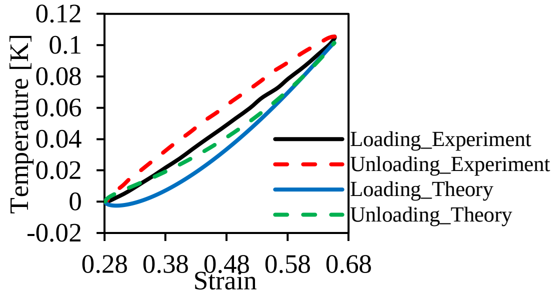

Figure 11 Comparison between the predicted and experimental temperature variation versus strain

4. CONCLUSIONS

A theoretical prediction of temperature variation of rubber material under cyclic tension was conducted. An experiment using infrared thermography was also conducted to confirm the theoretical result. It has been found that the predicted temperature variation is in good agreement with the ones obtain from infrared thermography. Further study is needed to consider the heat transfer between the specimen and the surrounding air.

ACKNOWLEDGEMENT

We gratefully acknowledge the ASEAN University Network Southeast Asian Engineering Education Development Network (AUN/SEED-Net) project of the Japan International Cooperation Agency (JICA) for financial support.

REFERENCES

[1] J. Gough, "A description of a property of caoutchouc, or Indian rubber; with some reflections on the cause of the elasticity of this substance," Memoirs of the Literary and Philosophical Society of Manchester, vol. 1, pp. 288-295, 1805.

[2] J. P. Joule, "On some thermo-dynamic properties of solids," Philosophical Transactions of the Royal Society of London, vol. 149, pp. 91-131, 1859.

[3] A. Boukamel, S. Meo, O. Debordes, M. Jaeger, "A thermo-viscoelastic model for elastomeric behaviour and its numerical application," Archive of Applied Mechanics, vol. 71, no. 12, pp. 785-801, 2001.

[4] C.O. Rodas, F.Zairi, M. Nait-Abdelaziz, "A finite strain thermo-viscoelastic constitutive model to describe the self-heating in elastomeric materials during low-cycle fatigue," Journal of the Mechanics and Physics Solids, vol. 64, pp. 396-410, 2014.

[5] M.C. Wang, E. Guth, "Statistical Theory of Networks of Non-Gaussian Flexible Chains," The Journal of Chemical Physics, vol. 20, no. 7, pp. 1144-1157, 1952.

High-Speed Displacement Measurements Based on a High Frequency Modulated Interferometer

Thanh Tung Vu[1], Hong Hai Hoang[1], Vu Hai Linh Nguyen[1], Toan Thang Vu[1*]

[1]School of Mechanical Engineering, Hanoi University of Science and Technology

No. 1, Dai Co Viet Road, Hanoi, Viet Nam

[*]Corresponding e-mail: thang.vutoan@hust.edu.vn

ABSTRACT

In this paper, a novel, compact and high-speed displacement measuring Michelson interferometer system is developed to meet the requirements of modern technology in industry such as lithography and semi-conductor production. Normally, heterodyne interferometers are a powerful system for small displacement measurements due to its property which is less sensitive to temperature and pressure variations. However, the maximum measurement speed of heterodyne interferometer is around 5 m/s because it is usually limited by the difference in frequency between the two components of the laser beam which is no larger than 3 MHz or 20 MHz corresponding laser source based on Zeeman effect and Acousto-optic modulator, respectively. The proposed measuring system is realized by modulating the frequency of the laser diode source and using lock-in amplifiers to extract intensity signal. The measurement speed is proportional to the modulation frequency. Thus, the higher the modulation frequency is, the higher the measuring speed attains. By this approach, the speed of such system is improved in comparison to heterodyne interferometers and it can be a capable solution for high-speed measurements in industry.

Keywords: Displacement measurement, Frequency modulation, Interferometry, Optical instruments.

1. INTRODUCTION

Laser interferometers are widely utilized for displacement measurements with nanometer-order uncertainty because of their inherent accuracy and their traceability to the metric standard through the frequency of the laser source. Various signal-processing techniques have been developed for displacement-measuring interferometers such as homodyne [1-4], heterodyne [5, 6] and frequency modulation techniques [7-9].

The homodyne interferometer technique is widely utilized in small displacement measurements with very high measurement resolution. In particular, measurement accuracy of 10 pm [3] and a resolution of sub-picometer [4] order have been reported. The interference signal of a homodyne interferometer is time-independent, and therefore it enables an ultrafast response because interference converts instantaneously phase variations into intensity variations. The upper bandwidth limit is determined by the response time of the photodetector and the bandwidth of the signal-processing electronics. Therefore, homodyne interferometers have the potential to be used for high-speed applications. However, homodyne interferometers require highly stable laser intensity during each measurement. This means that the misalignment of the optics, disturbance of the environment or shifting of a measured point will strongly affect the measurement uncertainty.

A heterodyne interferometer is less sensitive to temperature and pressure variations but it is slower because of the delay introduced by electronic signal processing for phase acquisition. The maximum measurable speed of a heterodyne interferometer is limited by the heterodyne frequency. A high cost, voluminous complicated system are also disadvantages of heterodyne interferometers.

Among these techniques, sinusoidal frequency modulated (SFM) techniques have many advantages. The signal of SFM interference, which is a continuous function of time, is a series of harmonics of the modulation frequency. The phase shift, which is induced by the displacement of the target mirror in the interferometer, can be accurately extracted from the interference signal using the synchronous detection method [10-11]. Moreover, the measurement speed of an SFM interferometer is only limited by the modulation frequency, for which a very high frequency can be obtained by modulating the injection on a normal laser diode (LD). In this paper, a sinusoidal injection current of 3 MHz frequency was used to modulate the frequency of an LD and then the modulated LD was used as a light sour of the Michelson interferometer. The displacement was detection from the interference signal using the synchronous detection method.

2. METHODOLOGY

The interference signal of an SFM interferometer can be written as [10]

$$I(L,t) = I_0\left[1 + V\cos\left(m\sin\omega_m t + \omega_0\frac{2Ln}{c}\right)\right] \quad (1)$$

Where $m = \frac{2\pi\Delta f L n}{c}$ (2)

is the modulation index; ω_m, Δf, I_0 and V are the angular modulation frequency, the frequency modulation amplitude, the average intensity and the contrast of a beat signal, respectively. Using the Bessel function, Eq. (1) is rewritten as

$$I(L,t) = I_0\left\{1 + V\left\{\cos\left(\omega_0 \frac{2Ln}{c}\right)[(J_0(m) + 2\textstyle\sum_{k=1}^{\infty} J_{2k}(m)\cos 2k\omega_m t)] - \sin\left(\omega_0 \frac{2Ln}{c}\right) 2\textstyle\sum_{k=1}^{\infty}[J_{2k-1}(m)\sin(2k-1)\omega_m t]\right\}\right\} \quad (3)$$

The initial path difference L can be expressed as

$$L = L_0 + \Delta L \quad (4)$$

Where L_0 is the initial unbalanced length between the two arms, ΔL is the displacement. Combining Eqs. (3) and (4) and using $\omega_0 = 2\pi\frac{c}{\lambda_0}$, we have

$$I(\Delta L,t) = I_0\left\{1 + V\left\{\cos\left(\frac{4\pi n}{\lambda_0}\Delta L\right)[J_0(m) + 2\textstyle\sum_{k=1}^{\infty}(J_{2k}(m)\cos 2k\omega_m t)] - \sin\left(\frac{4\pi n}{\lambda_0}\Delta L\right) 2\textstyle\sum_{k=1}^{\infty}(J_{2k-1}(m)\sin(2k-1)\omega_m t)\right\}\right\} \quad (5)$$

Using lock-in amplifiers (LIAs), we can extract any pair of consecutive harmonics, $(2k-1)\omega$ and $2k\omega$, where k is an integer ≥ 1, given by [11]

$$I_{(2k-1)\omega} = -I_0 V J_{2k-1}(m)\sin\left(\frac{4\pi n}{\lambda_0}\Delta L\right) \quad (6)$$

$$I_{2k\omega} = I_0 V J_{2k}(m)\cos\left(\frac{4\pi n}{\lambda_0}\Delta L\right) \quad (7)$$

In Eqs. (6) and (7), the gains of the two LIAs are assumed to be the same. Lissajous diagrams are obtained using these two consecutive quadrant-phase harmonics, and they are used to track the phase shift and the direction of the target. The displacement ΔL calculated from the phase shift is given by

$$\Delta L = \frac{\lambda_0}{4\pi n}\left\{\arctan\left(-\frac{J_{2k}(m) I_{(2k-1)\omega}}{J_{2k-1}(m) I_{2k\omega}}\right)\right\} \quad (8)$$

Evidently, the phase shift induced by the displacement can be determined from any pair of consecutive harmonics using the LIAs, and noise with frequency difference from the reference frequency of the LIAs is removed.

In the frequency modulated interferometer, two successive harmonics are detected by using LIAs. When the target moves, the Doppler frequency shortens the gap between these harmonics. The maximum measurement speed is limited when the bandwidth of two successive harmonics are overlapped. The maximum velocity of the target can be expressed as the following

$$V_{max} \leq \frac{\lambda_0}{4} f_m \quad (9)$$

Where V_{max}, f_m are the maximum velocity and modulation frequency, respectively.

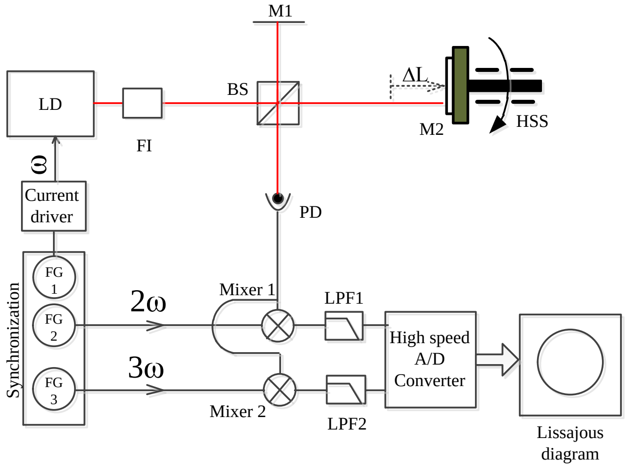

Figure 1 Frequency modulated interferometer; FI: Faraday isolator; BS: beam splitter; PD: photo detector; LPF: low pass filter; M: mirror; HSS: high speed spindle.

3. RESULTS AND DISCUSSION

The experimental conditions used in the displacement measurement are shown in Table 1. The moving mirror was driven by a high-speed spindle of 5000 rpm (ARS-4036-GM, Chuo Precision Industrial, Ltd.). Two simple LIA circuits were built to detect the intensity of harmonics by combining mixers (MX130-0S, R&K Co., Ltd.) and low-pass filters (LP1CH3 -0S, R&K Co., Ltd.). The modulation frequency of 3 MHz was used for a normal laser diode (HL6312G, Thorlabs Inc.). The experiment results are shown in Fig. 2. In Fig. 2a, the Lissajous diagram from 2nd and 3rd was obtained. From the diagram, the displacement was calculated (Fig. 2b). The Lissajous diagram was deformed because of vibration and the refractive index change.

Table 1 Example of table

Modulation frequency for LD	3 MHz
Speed of spindle	500 rpm
Laser source	HL6312G
Linewidth	≈ 100 MHz
Sampling frequency	10 MHz
Cut off frequency of low pass filters	1 MHz
Sampling time	5 s

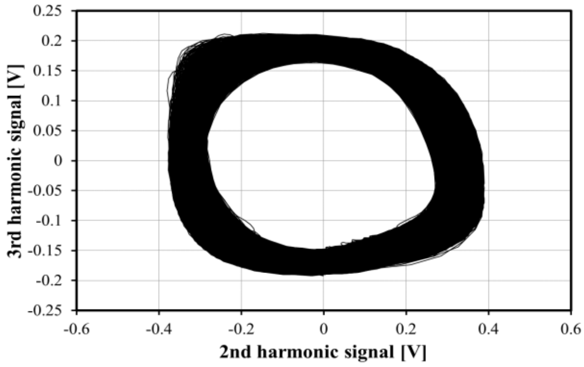

Figure 2 Lissajous diagram of 2nd ans 3rd harmonics

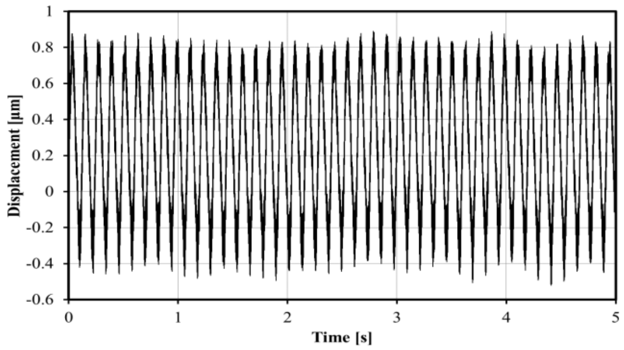

Figure 3 Displacement measurement result using the frequency modulated interferometer.

4. CONCLUSIONS

A frequency modulation displacement measuring interferometer was successfully developed. There was some deformation in the Lissajous diagram due to the effect of environment and vibration. However, the measurement resolution with the order of 20 nm can be achieved. The measuring system is compact, low-cost, and stable. It can be used for industrial applications. For future work, the proposed interferometer should be compared with heterodyne interferometer to clarify clearly the measurement accuracy and measurement.

ACKNOWLEDGEMENT

This work was funded by Vietnam Ministry of Education and Training under project number B2018-BKA-07-CTrVL

REFERENCES

[1] P. Gregorči et al., Quadrature phase-shift error analysis using a homodyne laser interferometer, Optics Express, vol. 17, pp. 16322-16331, 2009.

[2] F. Petrů and O. Číp, Problems regarding linearity of data of a laser interferometer with a single-frequency laser, Precision Engineering, vol. 23, pp. 39-50, 1999.

[3] T. Keem et al., Simple, real-time method for removing the cyclic error of a homodyne interferometer with a quadrature detector system, Applied Optics, vol. 44, pp. 3492-3498, 2005.

[4] J. Ahn et al., A passive method to compensate nonlinearity in a homodyne interferometer, Optics Express, vol. 17, pp. 23299-23308, 2009.

[5] C. C. Wu et al., Optical heterodyne laser encoder with sub-nanometer resolution, Measurement Science and Technology, vol. 19, 045305 (5pp), 2008.

[6] F. C. Demarest, High-resolution, high-speed, low data age uncertainty, heterodyne displacement measuring interferometer electronics, Measurement Science and Technology, vol. 9, pp. 1024-1031, 1998.

[7 O. Sasaki and H. Okazaki, Sinusoidal phase modulating interferometry for surface profile measurement, Applied Optics, vol. 25, pp. 3137-3140, 1986.

[8] T. Suzuki et al., Real time displacement measurement in sinusoidal phase modulating interferometry, Applied Optics, vol. 28, pp. 5270-5274, 1989.

[9] O. Sasaki et al., Double sinusoidal phase-modulating laser diode interferometer for distance measurement, Applied Optics, vol. 30, pp. 3617-3621, 1991.

[10] Vu, T. T., Higuchi, M., & Aketagawa, M. Accurate displacement-measuring interferometer with wide range using an I2 frequency-stabilized laser diode based on sinusoidal frequency modulation, Measurement Science and Technology, 27(10), 105201, 2016.

[11] Duong, Q. A., Vu, T. T., Higuchi, M., Wei, D., & Aketagawa, M. Iodine-frequency-stabilized laser diode and displacement-measuring interferometer based on sinusoidal phase modulation. *Measurement Science and Technology*, *29*(6), 065204, 2018.

Finite Element Analysis of Composite Plate Subject to Low Velocity Impact and Compression After Impact

MGSuada[1,*], H Syamsudin[1], HC Simanjorang[1]

1) Faculty of Mechanical and Aerospace Engineering, Bandung Institute of Technology, Jl Ganesa 10 Bandung-Indonesia

*Corresponding e-mail: mgsuada@gmail.com

ABSTRACT – Low Velocity Impact will form delamination in composite plate. The increasing size of delamination reduces the compression strength of composite plate. This study focuses on finite element analysis on delamination formations subject to low velocity impact and then sequentially followed by finite element analysis on compression after impact.
On the low velocity impact, the analysis focus on the effect of mesh size sensitivity on delamination profiles and threshold-peak force values. On the compression after impact the analysis focus on residual strength, local buckling prior to delamination propagation.
The finite element analysis results show that the low velocity impact and compression after impact simulations are in a good agreement to the experimental result. And the maximum residual strength obtained from the FE analysis is slightly conservative compared to the experimental results.
Keywords: Composite, low velocity impact, compression after impact, finite element

1. INTRODUCTION

Low velocity impact and compression after impact research on composite laminates structure have attracted attention from many researchers among other others are [1],[2], [4] and [6]. Mostly, the research done by numerical simulation using commercial finite element code or by their own subroutine codes. There are still many problems occur in the numerical simulation related to model capabilities to capture damage due to impact and compression load in the composite laminates structure i.e. delamination profile, damage propagations and mechanisms and also residual strength calculation. Besides that, another problems occur due to computational time needed to simulate impact and compression after impact. The efficiency in computational time calculation is important because it will help the industry to lower the cost of designing and testing the composite structures numerically instead of using direct experimental testing.

E.V Gonzalez et.al [5] conducted a study of the effects of ply clustering on polymer based laminated composite plates subjected to a drop weight impact loading. The research is to find the impact behavior and the damage threshold that result in significant reduction on the structure stiffness and strength due to delamination. They conducted the research by doing experimental test on Hexply AS4/8552 carbon epoxy unidirectional pre - preg with different stacking sequences i. e. [(45/0/-45/90)4]s, [(452/02/-452/902)2]s, [(454/04/-454/904)]s. They found that the most critical damage occur in drop weight impact is delamination.

In 2012, E.V Gonzalez et.al [4] conducted another research to develop their previous research in 2010. E.V Gonzalez et.al presented finite element simulations of two standardized and sequential tests performed in polymer matrix composite laminates reinforced by unidirectional fibers: the drop weight impact test and compression after impact test. These tests are performed on laboratory coupons, which are monolithic, flat, rectangular composite plates with conventional stacking sequences. They simulated the drop weight impact and compression after impact simulation and obtained the delamination profile, threshold force, and residual strength of the composite structure model. There are some problem with heavy computational time in simulating drop weight impact and compression after impact. This problem happened because of many contact interactions between plies interface in the composite structure model.

Bouvet et.al [6] conducted low velocity impact modelling in composite laminates that capture the permanent indentation. He developed the numerical model in order to simulate the different impact damages during low velocity/low energy impact. His model produced the novel approach to describe the physics behind the permanent indentation. Bouvet suggested to do mesh sensitivity analysis to determine the effect of element sizes to the results obtained from low velocity impact simulation.

Jikui Zhang [8] conducted a computationally efficient finite element model for predicting low velocity impact damage in laminated composites using a quasi-static load model with surface-based cohesive contact. He used surface-based cohesive contact instead of cohesive element in order to reduced computation time. He found two novel features for computation efficiency that by using the surfaced based cohesive contact model available in the Abaqus package can avoid using numerous and very small interface cohesive element and quasi static load can be used to simulate low velocity impact load. He also conduct sensitivity analysis on inter-laminar friction coefficient on CFRP and found the value between 0.6-0.8.

2. METHODOLOGY

In this research, the authors conduct mesh sensitivity analysis in low velocity impact simulation.

The objectives are to determine the effect of element sizes on the results of low velocity impact simulations i.e. threshold force, peak force, computational efficiency in term of time needed for low velocity impact simulation, and the damage profile. The finite element model for composite laminate is made using ABACUS. The laminate is divided into 2 main parts: the clusters and interfaces. For stacking sequences $[45_4/0_4/\text{-}45_4/90_4]_S$ there are 7 clusters with 2 clusters of 90_4 are merged in the middle and 6 interfaces. The clusters are 0.703 mm thick except the middle one with 1.431 mm thick and the interfaces are 0.025 mm thick. The interfaces and cluster elements are joined by node sharing. This is done to reduce the contact definition and reduce the computational time analysis.

The clusters are modeled as continuum shells meshed with single layer with SC8R reduced integration elements and the cohesive zone interface model is meshed with single layer COH3D8 cohesive element. The base plate is modeled as discrete rigid surface meshed with R3D4 elements. The pins are modeled as analytical rigid body cylinders. The fixture is placed in contact with the laminates with no compressive forces applied to the laminate. Both translation and rotation are constrained in all directions for the fixture. The impactor is modeled as an analytical rigid body sphere with 0.01 mm distance from the top of the laminate surface with an initial velocity of 2.779 m/s. The reference mass of 5 kg is placed in the middle of the sphere.

The translation is only permitted in the axis of transverse to the laminate surface. All other translations are constrained. The effect of gravitational acceleration is neglected to ease the energy analysis. Contact between fixtures – laminate, impactor – laminate, and cluster – cluster is defined by general contact option.

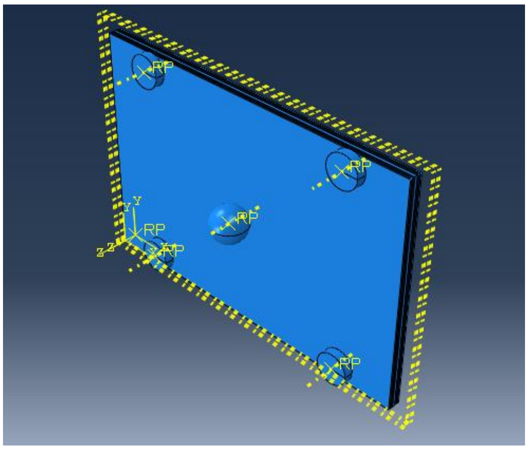

Figure 1 FEM model of composite plate

The cluster material model is modelled using the Hashim-Rothem model that available in Abaqus. The material for cluster is Hexply AS4/8552. The value of transverse shear stiffness (G23) is obtained from assuming that the transverse shear fiber cross section is isotropic and $\mu_{23} = \mu_{12}$ such that $G_{23}=E_{22}/2(1+\mu_{12})$. The fracture energies (Gc) are taken from Gonzales [4]. The friction coefficient μ is taken as 0.6. as suggested in [8]. The properties of Hexply AS4/8552 and cohesive zone interface as taken from [7] are as follow :

Properties	Values
Fiber direction stiffness, E_{11} (MPa)	131610
Transverse fiber direction stiffness, E_{22} (MPa)	9238.
In-plane shear stiffness, G_{12} (MPa)	4826.
Transverse shear stiffness, G_{13} (MPa)	3548
Longitudinal shear stiffness, G_{13} (MPa)	4826.
In-plane Poisson's ratio, μ_{12}	0.302
Density (tonne/mm^3)	1.59 x 10^{-9}
Fiber direction tension strength, X^T (MPa)	2063.
Fiber direction compression strength, X^C (MPa)	1484.
Transverse fiber direction tension strength, Y^T (MPa)	63.
Transverse fiber compression tension strength, Y^C (MPa)	267.
In-plane shear strength, τ_{12} (MPa)	91.
Transverse shear strength, τ_{23} (MPa)	133.
Gc fiber direction in tension (N/mm)	81.5
Gc fiber direction in compression (N/mm)	106.3
Gc transverse fiber direction in tension (N/mm)	0.28
Gc transverse fiber direction in compression (N/mm)	0.79

Table 1 Material properties for material cluster Hexply AS4/8552

Properties	Values
Normal stiffness, k_n (MPa/mm)	36955.92
Shear stiffness, k_t and k_s (MPa/mm)	19305.32
Maximum normal stress, σ_{max} (MPa)	26.26
Maximum shear stress, τ_{max} (MPa)	31.89
Normal fracture energy (N/mm)	0.28
Shear fracture energy (N/mm)	0.79
Density, ρ(tonne/mm^3)	1.59 x 10^{-9}
BK mix mode parameter, η	1.45

Table 2 cohesive zone interface properties

The simulation is done using Abaqus Explicit Solver [13]. The simulation time used is 6 microsecond to simulate the impact and rebound phenomena. Once the impact simulation is finished, the compression after impact is subsequently carried out by quasi static loading in Abaqus Explicit. The displacement is applied in compression after impact simulation. The finite element analysis is performed for every element size in two mesh configuration.

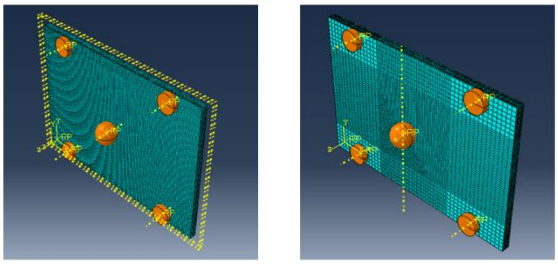

Figure 3 Two mesh configuration for finite element analysis.Type 1 on the left and type 2 on the right

At every finite element execution the force-time profile available will have a profile similar to the following figure.

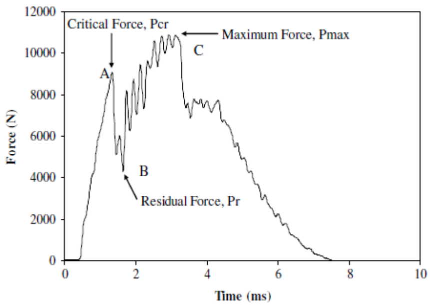

Figure 2 Force – time in low velocity impact [11]

The load at point A is defined as threshold force for onset of the delamination. This delamination process is accompanied by a rapid reduction of the force to a rest value point B due to reduction in the transverse stiffness of the laminate. Reloading phase into the maximum point C may occur if enough residual energy is stored in the impactor. Maximum force also related to the target plate stiffness after the initial impact damage at point A. The threshold force must be achieved for delamination damage to initiate

3. RESULTS AND DISCUSSION

The results of finite element analysis of low velocity impact for two type of mesh configurations are :

Element Sizes	Mesh Type 1 (kN)	% difference with [4]	Mesh Type 2 (kN)	% difference with [4]
0.75 mm	4.23	23.37 %	4.19	24.10 %
1.00 mm	4.28	22.46 %	4.29	22.28 %
1.25 mm	4.39	20.47 %	4.33	21.55 %
1.50 mm	4.27	22.64 %	3.91	29.16 %
1.75 mm	4.35	21.20 %	4.45	19.38 %

Table 3 Threshold force

From table above, it shows that element sizes affect the threshold force. The experimental [4] threshold force is 5.52 kN. As the element size increases, the threshold force is increasing, except in 1.50 mm and 1.75 mm. The threshold force is decrease when the element size 1.50 mm and then increase again in 1.75 mm. This is because the element become unstable where the viscous dissipation and artificial strain energy should be constantly small relative to total energy to ensure that only a small amount of energy in the system dissipated as energies that are not physically real.

Element Sizes	Mesh Type 1 (kN)	% difference with [4]	Mesh Type 2 (kN)	% difference with [4]
0.75 mm	7.53	3.21 %	7.44	4.37 %
1.00 mm	7.54	3.08 %	7.65	1.67 %
1.25 mm	7.88	1.29 %	7.95	2.19 %
1.50 mm	7.98	2.57 %	7.95	2.19 %
1.75 mm	7.86	1.03 %	8.14	4.63 %

Table 4 Peak Force

The results for peak forces are close to the experimental results 7.78 kN. As the element size increase, the peak force will also increase. As describe before that the peak force may occur if enough residual energy is stored in the impactor.

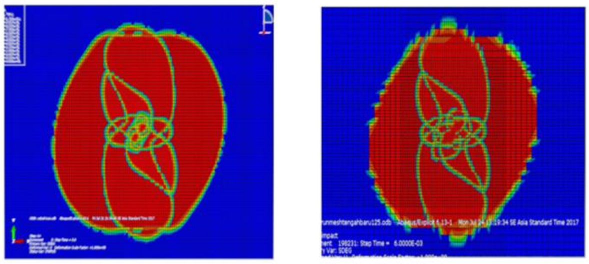

Figure 4 Delamination profile(left) mesh type 1 (right) mesh type 2

the delamination profile in general follow the “peanut” shape tendency for both mesh types. In both models, it can be seen that the cohesive zone models gives inaccurate results for the delamination profiles of the lower interface. The interface prior to the last 2 undergoes very large delamination. From the inspection this large delamination area encompasses the area that should have been delamination of the last 2 interfaces. This may be caused by damage energy is not properly dissipated by the last 2 interfaces and that makes the interface in the top of those interfaces dissipated the energy directly. During the numerical simulation using finite element no damage in the laminate is observed.

The result of finite element analysis for delamination area at each interface after low velocity impact is shown in figure 5. And final form of delamination after compression is shown in figure 6.

Interface no (top to bottom)	After impact before compression
1	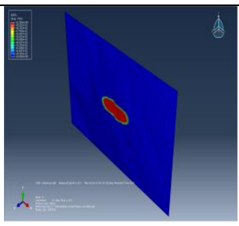
2	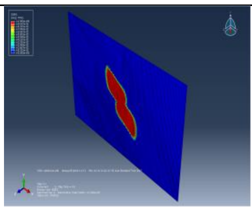
3	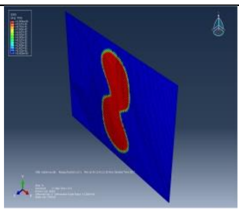
4	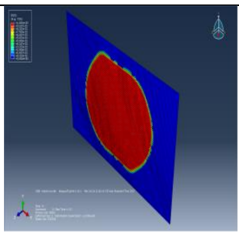
5	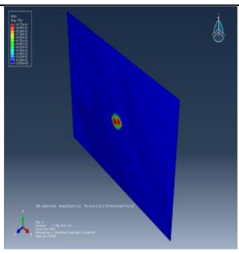
6	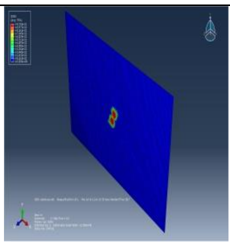

Figure 5 Delamination profile at every interface after low velocity impact before compressed

Interface no (top to bottom)	After compression far beyond maximum force
1	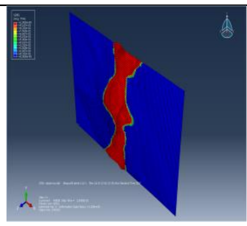
2	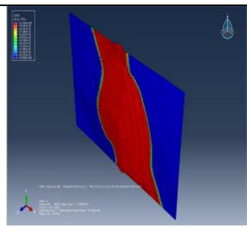
3	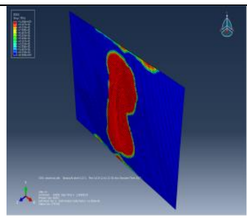
4	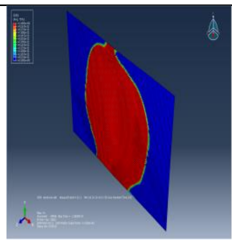
5	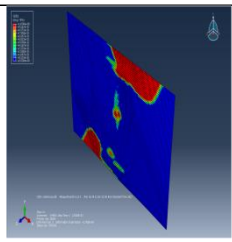
6	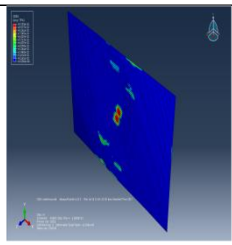

Figure 6 Delamination profile at every interface captured after compression

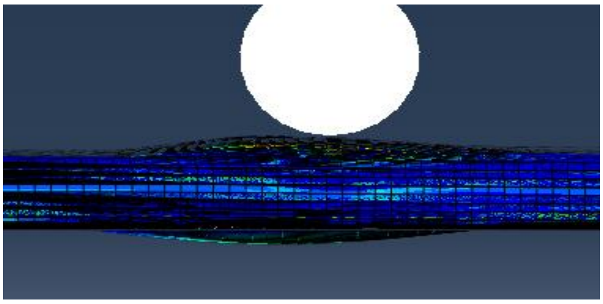

Figure 7 buckling around delaminated area after compression

As shown above, the local buckling trigger the delamination propagation in the composite laminates model. Under uniaxial compression loading, local buckling grows laterally (like a crack) from the impact site as the applied load is increased. These delaminated regions continued to propagate, first in short discrete increments and then rapidly at failure load. The damage pattern is very similar to that observed in laminated plates with open holes under compression loading. Post failure examination revealed that all specimens failed through the impact site in a direction transverse to the loading axis [17].

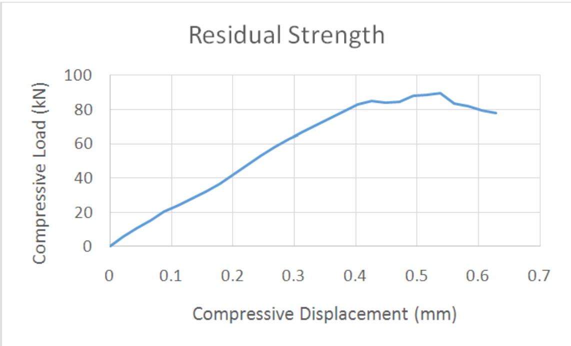

Figure 8 Residual strength compression after impact (Numerical simulation)

Note that the compression after impact finite element simulation was performed until the maximum residual strength and displacement are achieved. The maximum residual strength of the composite laminate model after compression after impact simulation is 90 kN with maximum displacement 0.54 mm. The experimental results for residual strength and maximum compressive displacement from reference [4] are 105 kN and 0.64 mm. These results already close enough and can be confirmed valid.

No	Parameters	Numerical	Experimental [4]	Difference
1	Max residual strength	90 kN	105 kN	14.28 %
2	Max displacement	0.54 mm	0.64 mm	15.60 %

Table 5 Numerical – experimental comparison in Compression after impact

4. CONCLUSIONS

The conclusions are as follow :

1. Both mesh type 1 and type 2 give close results with the experimental in terms of threshold force, peak force, and momentum change. However, the threshold forces obtained are lower than the experimental results. The delamination profile are nearly similar with both model mesh type 1 and type 2.
2. In compression after impact failure, local buckling occur first and then triggered the delamination propagation until all composite model fail. The delamination propagate in the direction transverse to the apply loading in all layers.
3. The maximum residual strength obtained from the simulation is slightly conservative compared to the experimental results. The result is lower (90kN) with 14.28 % difference with the experimental result (105kN). The maximum compressive displacement is also lower (0.54 mm) compared with the experimental results (0.64 mm) with 15.60 % difference
4. The cohesive element proves the ability to perform delamination modeling very well.

5 REFERENCES

[1] S. Sanchez. Compression after impact of thin laminates composite laminates. Composites Science and Technology; pp 1911-1919, 2005

[2] S. Rivallant. Failure analysis of CFRP laminates subjected to compression after impact: FE simulation using discrete interface elements. Composites: Part A.; pp 83-93,2013.

[3] S. Rivallant. Experimental analysis of CFRP laminates subjected to compression after impact: The role of impact-induced cracks in failure. Composite Structures; pp 147-157,2013.

[4] E. V. Gonzalez. Simulation of drop-weight impact and compression after impact tests on composite laminates. Composite Structures; pp 3364-3378, 2012.

[5] E. V. Gonzalez. Effects of ply clustering in laminated composites plates under low-velocity impact loading. Composites Science and Technology. pp 805-817, 2010.

[6] C. Bouvet. Low velocity impact modelling in composite laminates capturing permanent indentation. Composites Science and Technology. pp 1977-1988, 2012.

[7] Aldyandra. Comparison between cohesive zone and 3D brittle fracture models for simulating composite laminate delamination in low velocity impact. Master Thesis ITB. 2015

[8] Jikui Zhang. Simulating low – velocity impact induced delamination in composites by a quasi-static load model with surface – based cohesive contact. Composite Structures. pp 51-57,2015.

[9] M. O. W. Richardson. Review of low – velocity impact properties of composite materials. Composites Part A. pp 1123-1131, 1996.

[10] S. Abrate. Impact on composite structures. Cambridge University Press. 1998

[11] X. Zhang. Improvement of low – velocity impact and compression – after impact performance by z – fiber pinning. Composites Science and Technology, pp 2785-2794,2006.

[12] Y. Xiong. A prediction method for the compressive strength of impact damaged composite laminates. Composite Structure; pp 357-367, 1995.

[13] Abaqus 6.13 user's manual. Providence (RI, USA): Dassault Systemes Simulia Corp. 2011

[14] X. Zhang. Predicting low – velocity impact damage in composites by q quasi – static load model with cohesive interface elements. The Aeronautical Journal, pp 1367-1381,2012.

[15] G. A. Schoeppner. Delamination threshold loads for low velocity impact on composite laminates. Composites Part A,pp 903-915,2000

[16] E. Panettieri. Delaminations growth in compression after impact test simulations: Influence of cohesive elements parameters on numerical results. Composite Structure, pp 140-147,2016.

[17] C. Soutis. Prediction of the post-impact compressive strength of CFRP laminated composites. Composites Science and Technology. pp 677-684,1996.

Solidification and Microstructures Characteristic in Unidirectional Solidification of Al-7 wt.% Si Alloy

Seab Piseth[1*], Dedy Masnur[2], Suyitno[3]

[1)] Department of Industrial and Mechanical Engineering, Faculty of Electrical Engineering, Institute of Technology of Cambodia, Russian Federation Boulevard P.O. BOX 86 Phnom Penh, Cambodia
[2)] Mechanical Engineering Department, University of Riau, Kampus Bina Widya km 12.5 Simpang Baru, Pekanbaru 28293, Indonesia
[3)] Center for Innovation of Medical Equipment and Devices (CIMEDs), Universitas Gadjah Mada, Yogyakarta 55281, Indonesia

Email: [1*]pisethseab@gmail.com

ABSTRACT – This paper discusses about the characteristic of solidification parameters, cooling curve and microstructures in unidirectional solidification of Al-7 % wt. Si alloy. The experiment was conducted by using Bridgeman-type solidification furnace. The samples were formed in clay mold and moved downward with constant withdrawal rate 16.433 µm/s during solidification. Cooling data were plotted at 5, 15, 25, 35, 45, and 55 mm at solidification times. The solidification parameters such as temperature gradient, growth rate, cooling rate and local solidification time were defined at distance of 5 mm to 55 mm from the bottom of the sample. Whereas microstructures were observed on longitudinal and transverse cross section. The result show that both temperature gradient and growth rate decrease but they irregularly alter when undercooling occurs. Whereas the cooling rate decreases dramatically. The slope of curve is very steep at 5 mm and fall slightly at 55 mm. Even though the solidification parameters reduce irregularly but primary and secondary dendrites arm spacing increase certainly. The microstructure feature develops from fine to coarser and then to equiaxed.

Keywords: Aluminum alloys, Columnar dendrites, Growth rate, Unidirectional solidification

1. INTRODUCTION

Unidirectional solidification is a casting process that cast to guide microstructures to be columnar dendrites or single crystal. Turbine buckets, nozzles, and combustor components are the products of unidirectional solidification process [1]. Those applications are often casted by unidirectional casting techniques to have directionally solidified that are typically formed of nickel, cobalt or iron-base superalloys. Those materials can stand at high temperature. However, aluminum silicon alloys are the most important among cast alloy, especially in the aerospace and automotive industries. For examples, over-wing emergency door exit, avionic chase or wheel rim are product casting of aluminum alloy 6.5-7.5 wt.% of Si [2]. Moreover, other applications such as semiconductor, solar cell, heat and fluid flow equipment; the microstructure direction as cellular or dendritic affect its efficiency [3].

Unidirectional microstructures can be not archived if solidification parameters can be not controlled accurately. The unidirectional solidification is widely conducted by using Bridgman-type that align of crystal growth direction. By controlling the solidification process to obtain excellent structure, the material performance can be significantly improved. Under different solidification condition, the microstructure develops in the form of planar interface, cell or dendrites. Those formations changing are caused by long of freezing range during solidification [4]. During solidification of alloys, the dendrite morphologies affect the diffusion of solute growth. Those solute elements grow as dendric and they also affect the primary dendrite arm spacing (PDAS) and secondary dendrite arm spacing (SDAS). Furthermore, the PDAS appears linked to solidification parameter and SDAS is controlled by solidification time [5]. The fine of microstructure can be seen when solidification parameters increase. On the other hand, the hardness of the material or alloy depends on the grain size or lamellar spacing; in which, the smaller the lamellar spacing is higher of the hardness [6].

Many researchers are investigated of solidification process on aluminum alloy or other materials by using stainless steel, graphite crucible or alumina crucible. As can be seen some in [7], they used the stainless steel mold, glass [8], alumina crucible [3,8], graphite crucible [9–11]. Mold is the main equipment that influence on the solidification parameters and microstructure. It has own properties such as chemical composition and thermal conductivity. However, unidirectional process casted by using clay mold has not yet been reported.

By using the clay mold, this present work is investigated the characteristic of cooling curve and solidification parameters such as temperature gradient (˚C/mm), growth rate (mm/s), cooling rate (˚C/s) and local solidification time (s), Furthermore, it describes the microstructures in unidirectional solidification process of Al-7 wt.% Si alloy.

2. METHODOLOGY

2.1. Materials

High purity of Al-99.95 wt.% and master alloy of Al-15 wt.% Si alloy were weighted and melted in electric furnace to prepare new composition master alloy with 7 wt.% Si. To ensure their chemical composition, the raw materials and samples were analyzed by Thermo Scientific ARL OES Spectrometer. The chemical composition of the alloy is shown in Table 1.

Table 1 Chemical composition of sample

Element	Al	Si	Fe	Cu	Other
wt. %	92.545	7.008	0.329	0.007	±0.001

2.2. Directional Solidification Method

The directional solidification sample alloy was performed in Bridgman-type directional solidification furnace. The experimental apparatus schematic and details of Bridgman-type furnace are described in Ref. [13]. In Bridgman method, the molten alloy was formed in clay molds (60 mm in length, 6 mm inside diameter and 10 mm outside diameter). There are six holes along the mold which were inserted by K-type thermocouples to measure the temperature during melting and freezing. The location each of thermocouples was mounted at 5, 15, 25, 35, 45 and 55 mm from the bottom of the clay mold, as can be seen in Figure 1.

To create the samples, the aluminum silicon alloy was melted in electric furnace at temperature of 700 ˚C. The molten was poured in permanent mold (PM) to create cylindrical samples with dimension of 6 mm in diameter and 60 mm in length. Before pouring, the carbon steel mold was preheated at temperature 150˚C. The PM sample was in inserted in clay mold and re-melted in Bridgman-type solidification apparatus. To ensure temperature in furnace was uniform, it was kept 30 mins when the sample melted at temperature of 700 ˚C. In this process, the sample was pulled down by synchronous motor with constant of withdrawal rate (16.433 μm/s). The sample was form in clay mold and quenched by water under constant of flow rate during downward movement until outsize of the furnace.

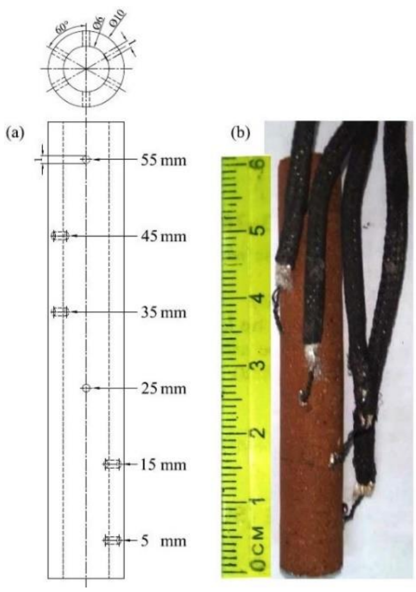

Figure 1. (a) Engineering drawing of mold and (b) the sample formed in mold and mounted with thermocouples

2.3. The Calculation of Solidification Parameters

- **Temperature gradient**

The temperature gradient was a ratio between the temperature difference between thermocouples at the same time with their distance. It could find this method in [11–13].

- **Growth rate**

The growth rate was a rate of liquid-solid interface that pass each of thermocouples. To calculate growth rate, it was described in [11–13].

- **Cooling rate**

The cooling rate was the rate of molten solidified. It is calculated from the slope of cooling curve before liquidus or nucleation temperature of Al dendrite. It can also be computed from dividing the total solidification temperature to the solidification time [17].

- **Local solidification time**

Local solidification time was the difference time between liquidus and solidus (t_L-t_S).

- **First derivative on cooling curve**

First derivative was calculated based on the difference each of temperatures (ΔT) dividing with their difference times during solidification (Δt). It can compute that $dT/dt= \Delta T/\Delta t$.

2.4. Microstructure Observation

The quenched sample was cut in longitudinal and transverse in cross section. Those sections were cold mounted with epoxy-resin and then were wet mechanically ground down with SiC paper to 5000 grit. After grinding, polishing and etching with NaOH solution for 2 s -3 s (95 ml H_2O and 10 g NaOH) for metallographic observation, the microstructures were examined by an OLYMPUS C-35AD-4 optical microscope from the bottom to the top of sample at the same of magnification. PDAS and SDAS in longitudinal cross section was measured by using ImageJ 1.52i software [18]. It was the same method as described in [13].

3. RESULTS AND DISCUSSION

3.1 Thermal Analysis

The cooling curves in various position are shown in Figure 2 and the cooling curve in position 55 mm with its first derivative are depicted in Figure 3. From this cooling curve, the slope of curve is very steep in position 5 mm. In contrast, the slope of curve falls slightly in position 55 mm. The inflection on curve can be seen clearly in position 55 mm. First inflection, it is crystal undercooling. It occurs when the α-Al dendrites start to nucleate. Second inflection, it is eutectic undercooling, see in Figure 2. It happens when the nucleation become to solid. The phase transformation during solidification can observe from the first derivative curve. The first derivative on cooling curve indicates the estimation of time at which various solidification events occur from the beginning to the end of transformations. As depicted in Figure 3, first peak indicates the formation of α-Al phase at the time 2-3 s (point 1). The second peak occurs before eutectic transformation at the time 105 s (point 2). Final peak is at the time 110 s (point 3). It relates to the formation of non-equilibrium eutectic transformation. The angle of the peak at the time of undercooling can estimate grain refinement [19].

The undercooling is necessary to give the driving force to nucleate the α-Al dendrites. In principle, the dip in the cooling curve might only correspond to the undercooling required to accelerate the growth of the nucleated solid. For nucleation may only correspond to a condition of delayed heat evolution because of slow growth [5]. It can see clearly of undercooling on curve when cooling rate is low at 1.18 ˚C/s. Furthermore, the depth of thermocouples using to measure temperature data affects cooling curve. Many factors influence on cooling curve and undercooling such as shape of the test cup or mold, pouring temperature, the quantity of metal poured, the degree of oxidation of metal in mold, mold material, cooling rate, composition of alloy and location of thermocouple [19]. From this experiment, the behavior of undercooling and eutectic temperature can be seen clearly when thermocouple is measured near the top. It is 5 mm from the surface of molten and the cooling rate is 1.18 ˚C/s.

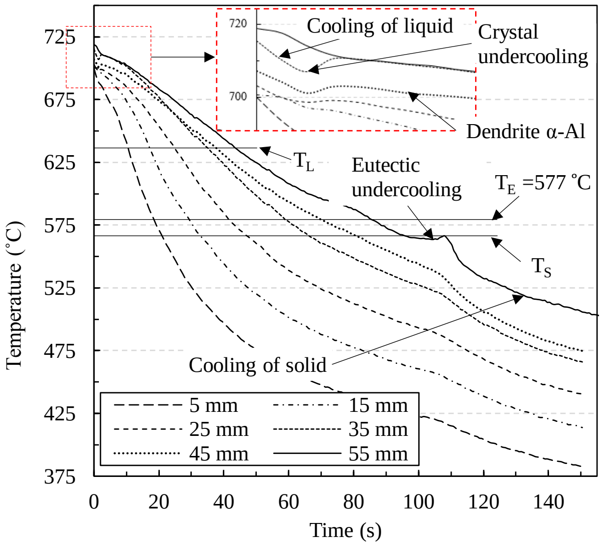

Figure 2. Cooling curves of directionally solidified in during solidification

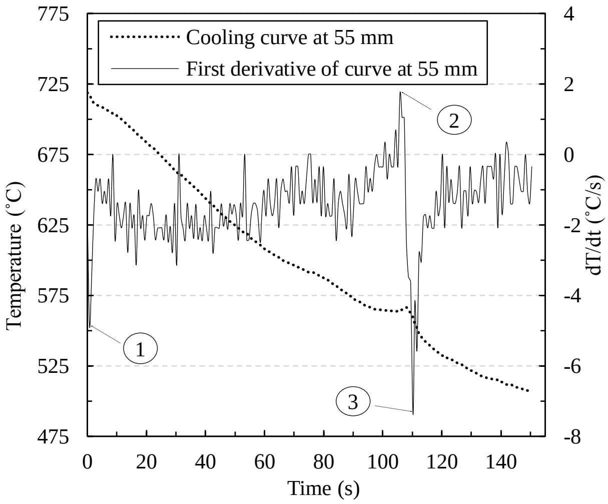

Figure 3. Cooling curve at 55 mm of directionally solidified and its first derivative during solidification

3.2. Solidification Parameters

Figure 4 shows about the temperature gradient, growth rate and cooling rate in various region from 5-15 mm to 45-55 mm. The local solidification time is shown in Figure 5. The highest temperature gradient is 3.68 ˚C/mm at the region 5-15 mm and the highest of growth rate is 3.46 mm/s at the region 35-45 mm. In contrast, the minimum temperature gradient is 0.50 ˚C/mm at the region 35-45 mm and the smallest growth rate is 0.99 mm/s at the region 25-35 mm. Temperature gradient significantly decreases when dendrites reach from 5 to 25 mm and the growth rate reduces from 1.55 to 0.99 mm/s at the region 5-35 mm. In the next, the growth rate increases rapidly until 3.46 ˚C/mm while temperature gradient presents at 1.62 ˚C/mm. And then, they seem to be balance at 45 to 55 mm. In other words, the maximum temperature gradient and cooling rate present at the place where cooled was applied. Whereas the cooling rate decreases dramatically from 2.98 ˚C/s in position 5 mm to 1.18 ˚C/s in position 55 mm even though both temperature gradient and growth rate irregularly alter. The local solidification time raises from 8 to 43 s that it coincides with the position from 5 to 55 mm.

The temperature gradient and growth rate change unstably because of eutectic undercooling occurs when cooling rate is 1.65 ˚C/s. Consequently, the molten cool bellow the temperature of melting point.

At the bottom of sample is nearby at the cooling zone but the top is at the heating zone that why the cooling rate at the bottom is higher than the cooling rate at the top. Because of that the cooling rate decreases, solid/liquid interface movement velocity also decreases. Moreover, when solid/liquid interface movement velocity is slow, less latent heat of molten releases [17]. From that the local solidification time also increase, as shown in Figure 5.

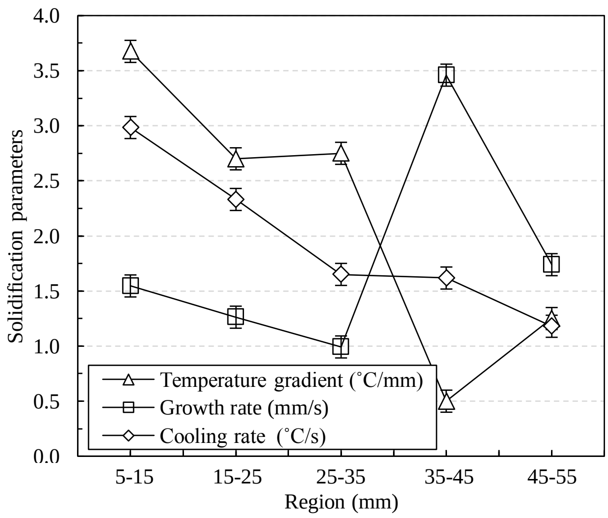

Figure 4. The value of temperature gradient, growth rate and cooing rate each of regions

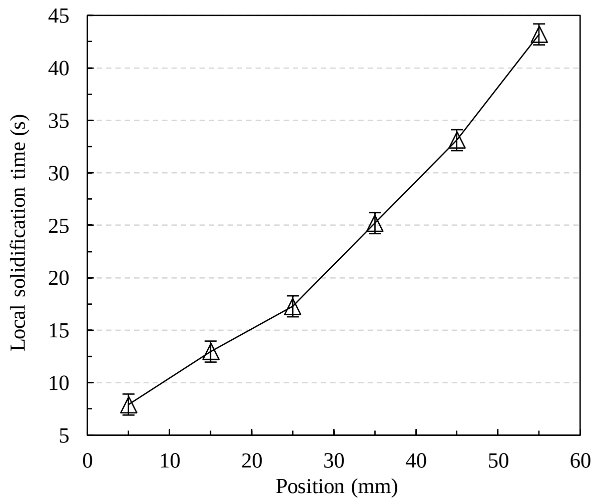

Figure 5. Local solidification time

3.3. Microstructures

Figure 6 depicts the variation of PDAS and SDAS in along of the sample. Transverse microstructures in cross sections are shown in Figure 7 and microstructures in longitudinal cross section at different location 0, 5, 10 until 55 mm are depicted in Figure 8. Both PDAS and SDAS increase from 118.37 to 245.15 µm (at 0 to 45 mm) and 15.66 to 42.72 µm (at 0 to 55 mm), respectively.

The microstructures of aluminum alloy of a sample are extremely different each of locations. At the bottom of sample, the microstructures are very fine. In contrast, at the top of sample, α-Al dendrites are coarser. On the other hand, primary and secondary dendrites alienate. As shown in Figure 7, the equiaxed of columnar growth become larger along of the sample. Because of the sample is cooled at bottom, the columnar dendrites grow from the bottom to the top. Moreover, the freezing time and mushy zone increase along of sample. High of cooling rate reduce the DAS and the surface of dendrite due to short of solidification time, as depicted in Figure 8 at location 1 to 6 (at 0 to 25 mm). In contrast, low of cooling rate is slow diffusion of solute which in turn becomes coarser of α-Al dendrites and tends to enlarge SDAS, as shown in Figure 8 at location 7 to 12 (at 30 to 55 mm). Secondary dendritic arms develop from the primary stems and the tertiary dendrites start to initiate from the secondary arms, as can be seen in Figure 8 at location 8 to 10 (at 35 to 45 mm).

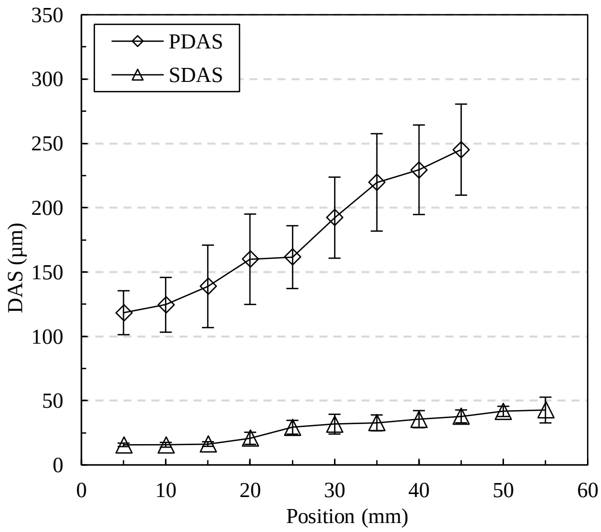

Figure 6. Variation of DAS and position in a sample

The behavior of dendrites and their columnar growth during solidification are depicted in Figure 9 and Figure 10. At the beginning, the molten nucleate that is called as heterogeneous nucleation. Next, it starts to grow as columnar and dendrites, as shown in Figure 9a. However, most of the time, microstructure is not in unidirectional at bottom of sample due to high of cooling rate. When cooling rate is low from 2.33 to 1.62 ˚C/s, the columnar of dendrites grow as parallel direction, see in Figure 9b.

The columnar dendrites are end and then the equiaxed occur due to slow growth of columnar dendrites, as shown in Figure 9c-d. This process is called as columnar-to equiaxed transition (CET) and it is good explanation which is reported by Dong et al. [19, 20]. To prevent CET, high temperature gradients in front of the solid/liquid interface and low solidification velocities are used to achieve a columnar dendritic structure. The equiaxed grains nucleate in undercooling region ahead of the columnar growth front. The alloy composition, temperature gradient ahead of the growth front, and tip growth rate affect CET [20]. However, some columnar of dendrites impinge on each other, see in Figure 10a. It may be the temperature of molten that is not uniform or the sample is not straight. Moreover, microstructures depend on chemical composition in sample. Some locations, microstructures of aluminum alloy enlarge the surface of α-Al dendrite due to rich of Al content on that place, see in Figure 10b. In situ, the molten of Al-Si is not good uniform chemical composition and well-dispersed.

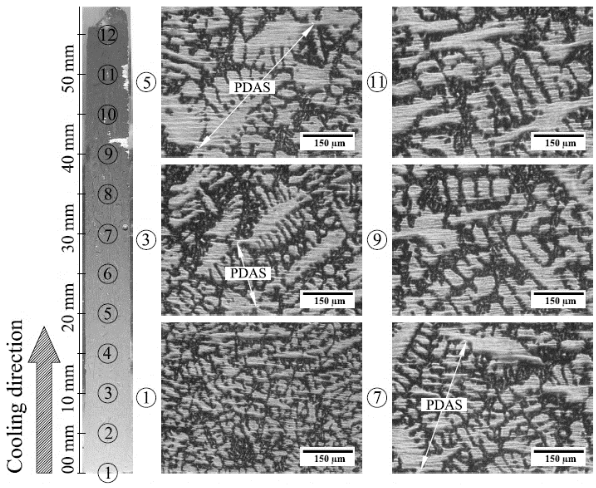

Figure 7. Transverse microstructure in cross section of directionally solidified

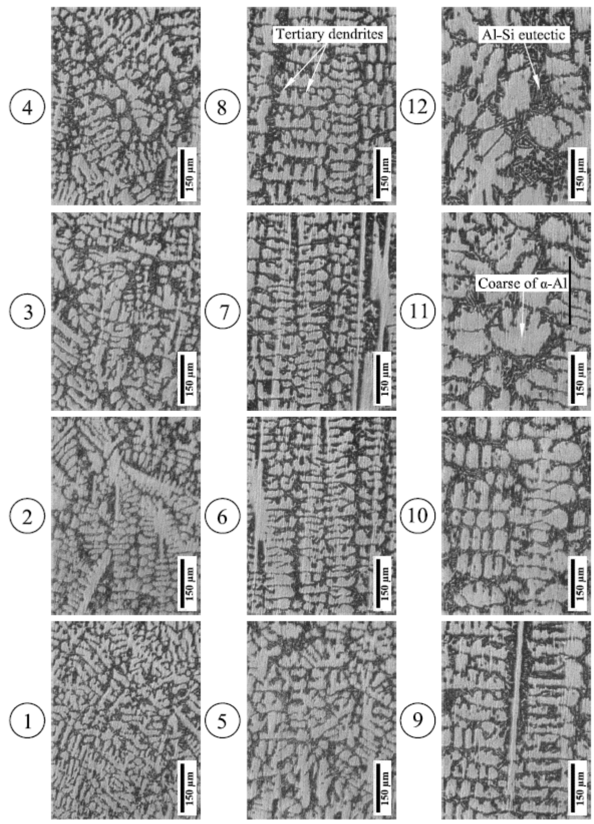

Figure 8. Longitudinal microstructure in cross section of directionally solidified

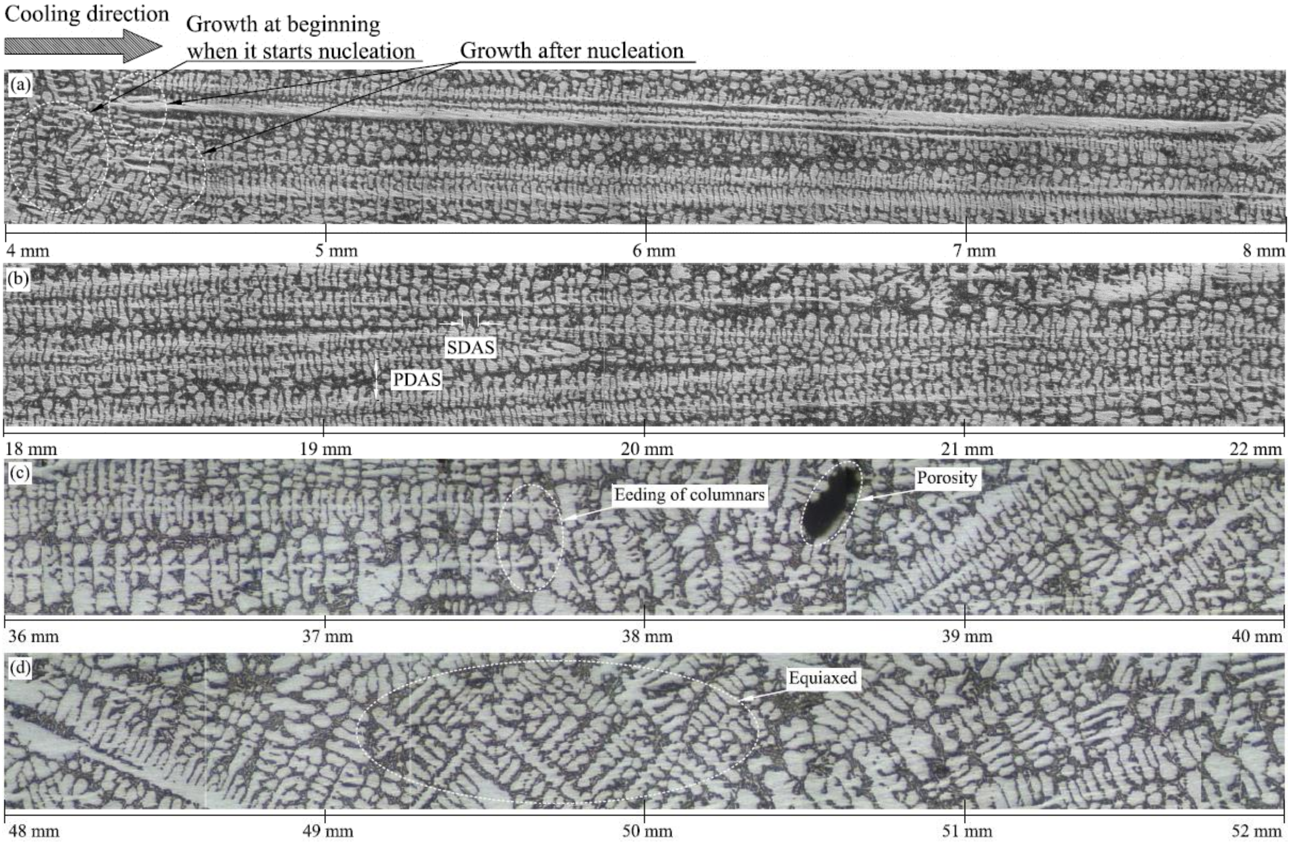

Figure 9. Behavior of dendrites and columnar dendrites growth during unidirectionally solidified in longitudinal cross section: (a) starting to grow after nucleation; (b) growing as parallel direction; (c) ending of columnar growth and starting to equiaxed and (d) the equiaxed region

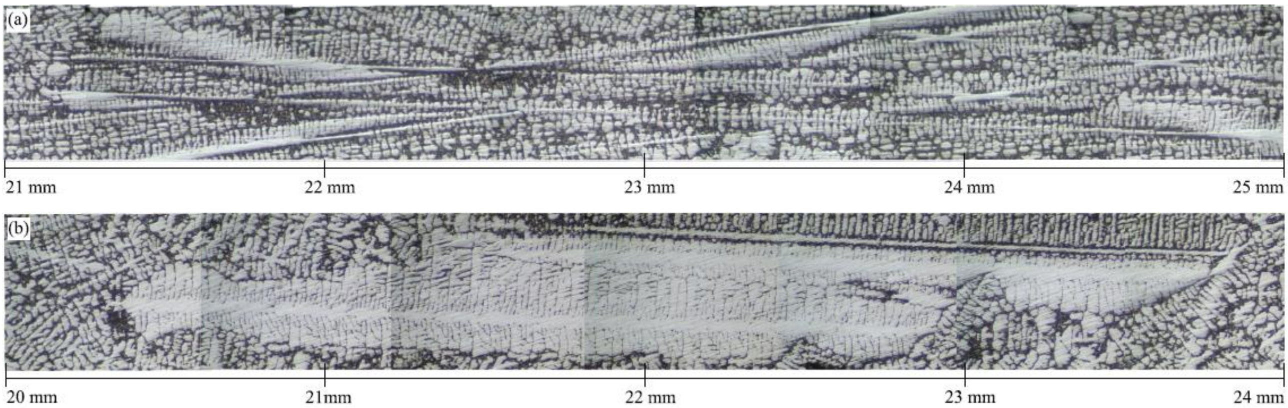

Figure 10. Other defects on columnar dendrites growth during unidirectionally solidified: (a) columnar dendrites impinge on each other and (b) columnar dendrites grow where rich of Al content

4. CONCLUSIONS

This study reveals of experimental in unidirectional solidification process of Al-7 % wt. Si alloy on cooling curve, solidification parameters and microstructures by using the clay mold. The following conclusions can be drawn from the experimental results.

a. Temperature gradient and growth rate irregularly alter due to eutectic undercooling occurs. Whereas the cooling rate decreases dramatically.
b. The slope of curve is very steep at bottom and fall slightly at top of sample. The eutectic undercooling can be seen clearly when thermocouple is measured in position 55 mm and cooling rate is 1.18 ˚C/s.
c. Decreasing of solidification parameters, microstructures become coarser and the PDAS and SDAS increase. Moreover, microstructures develop from columnar to columnar dendrites and become to equiaxed.

The solidification parameters and microstructures are extremely change in a sample of unidirectional solidification process. Thus, to achieve microstructure in unidirectional, solidification parameters and cooling condition should be controlled.

ACKNOWLEDGEMENT

The authors would like to thank Univeristas Gadjah Mada for providing of research facilities and acknowledge to KNB Dikti for financial support.

REFERENCES

[1] U. S. Patent, "Unidirectional Solidification Process and Apparatus Therefor," vol. 2, no. 12, pp. 1–8, 2012.

[2] F. C. Robles-Hernandez, J. M. H. Ramírez, and R. Mackay, *Al-Si Alloys*. Springer, 2017.

[3] H. Zhong *et al.*, "Effect of interdendritic thermoelectric magnetic convection on evolution of tertiary dendrite during directional solidification," *J. Cryst. Growth*, vol. 439, pp. 66–73, 2016.

[4] Y. Shen *et al.*, "Dendrite growth behavior in directionally solidified Fe–C–Mn–Al alloys," *J. Cryst. Growth*, vol. 511, no. October 2018, pp. 118–126, 2019.

[5] J. Campbell, *Complete Casting*, First edit. Elsevier, 2011.

[6] Y. Kaygısız and N. Maraşlı, "Directional solidification of Al–Cu–Si–Mg quaternary eutectic alloy," *J. Alloys Compd.*, vol. 721, pp. 764–771, 2017.

[7] M. Dias, C. Brito, F. Bertelli, and A. Garcia, "Cellular growth of single-phase Zn-Ag alloys unidirectionally solidified," *Mater. Chem. Phys.*, vol. 143, no. 3, pp. 895–899, 2014.

[8] N. Maraşli, K. Keşlioğlu, B. Arslan, H. Kaya, and E. Çadirli, "Effects of growth rate and temperature gradient on the microstructure parameters in the directionally solidified succinonitrile-7.5 wt.% carbon tetrabromide alloy," *J. Mater. Process. Technol.*, vol. 202, no. 1–3, pp. 145–155, 2008.

[9] Z. Chen, E. Wang, and X. Hao, "Microstructure and orientation evolution in unidirectional solidified Al-Zn alloys," *Mater. Sci. Eng. A*, vol. 667, pp. 1–8, 2016.

[10] M. Ghods, L. Johnson, M. Lauer, R. N. Grugel, S. N. Tewari, and D. R. Poirier, "Radial macrosegregation and dendrite clustering in directionally solidified Al – 7Si and Al – 19Cu alloys," vol. 441, pp. 107–116, 2016.

[11] U. Böyük, S. Engin, and N. Maraşli, "Microstructural characterization of unidirectional solidified eutectic Al-Si-Ni alloy," *Mater. Charact.*, vol. 62, no. 9, pp. 844–851, 2011.

[12] H. Kaya and A. Aker, "Effect of alloying elements and growth rates on microstruture and mechanical properties in the directionally solidified Al-Si-X alloys," *J. Alloys Compd.*, vol. 694, pp. 145–154, 2017.

[13] P. Seab and Suyitno, "The Effects of Stopping Duration of Withdrawal in Directional Solidification of Al-7 wt .% Si Alloy on Solidification Parameters , Microstructure and Microhardness," *J. Mater. Process. Charact.*, 2019. To be published.

[14] H. Kaya, E. Çadirli, and M. Gündüz, "Dendritic growth in an aluminum-silicon alloy," *J. Mater. Eng. Perform.*, vol. 16, no. 1, pp. 12–21, 2007.

[15] M. Şahin and E. Çadirli, "The effects of temperature gradient and growth rate on the microstructure of directionally solidified Sn-3.5Ag eutectic solder," *J. Mater. Sci. Mater. Electron.*, vol. 23, no. 2, pp. 484–492, 2012.

[16] H. Kaya, E. Çadirli, M. Gündüz, and A. Ülgen, "Effect of the temperature gradient, growth rate, and the interflake spacing on the microhardness in the directionally solidified Al-Si eutectic alloy," *J. Mater. Eng. Perform.*, vol. 12, no. 5, pp. 544–551, 2003.

[17] S. Farahany, A. Ourdjini, M. H. Idris, and S. G. Shabestari, "Computer-aided cooling curve thermal analysis of near eutectic Al-Si-Cu-Fe alloy: Effect of silicon modifier/refiner and solidification conditions on the nucleation and growth of dendrites," *J. Therm. Anal. Calorim.*, vol. 114, no. 2, pp. 705–717, 2013.

[18] W. Rasband, "Downloads - ImageJ," 2018. [Online]. Available: https://imagej.net/Downloads. [Accessed: 12-Apr-2019].

[19] D. M. Stefanescu, "Thermal analysis-theory and applications in metalcasting," *Int. J. Met.*, vol. 9, no. 1, pp. 7–22, 2015.

[20] H. B. Dong, X. L. Yang, P. D. Lee, and W. Wang, "Simulation of equiaxed growth ahead of an advancing columnar front in directionally solidified Ni-based superalloys," *J. Mater. Sci.*, vol. 39, no. 24, pp. 7207–7212, 2004.

[21] H. B. Dong and P. D. Lee, "Simulation of the columnar-to-equiaxed transition in directionally solidified Al-Cu alloys," *Acta Mater.*, vol. 53, no. 3, pp. 659–668, 2005.

The Crushing Characteristics of Environmentally Friendly Corrugated Core Structures

M.Y.M. Zuhri[1,2]*, A.A.F. Abdullah[2], S.M. Sapuan[1,2] and M.R. Ishak[3]

[1)] Advanced Engineering Materials and Composites Research Centre, Department of Mechanical and Manufacturing Engineering, Universiti Putra Malaysia, 43400 UPM Serdang, Selangor, Malaysia
[2)]Department of Mechanical and Manufacturing Engineering, Universiti Putra Malaysia, 43400 UPM Serdang, Selangor, Malaysia
[3)]Department of Aerospace Engineering, Universiti Putra Malaysia, 43400 UPM Serdang, Selangor, Malaysia[2]

*Corresponding e-mail: zuhri@upm.edu.my

ABSTRACT – This paper investigates the compression properties of corrugated core structures made of flax reinforced polylactide (hereinafter known as flax/PLA) composite. The corrugated cores were shaped using compression moulding method. Three layers of pre-preg woven flax/PLA material were arranged in a direction of 0°/90°. The flax/PLA material was pressed under a temperature of 190°C at about 15 minutes. After curing, the flax/polylactide composite corrugated core was removed and cut into required size. Here, the effect of the number of cells and their width lengths were investigated. Mechanical testing on the structures shown an increasing values of compression strength as the cell width increases. The corrugated flax/PLA cores failed as a result of local buckling, fibre fracture and debonding. Finally, by increasing the cell width and number of cells will resulted to a decrease in the energy-absorbing capacity of the core.
Keywords: Flax, Corrugated, Compression, Energy Absorption.

1. INTRODUCTION

Composite materials have been used in most of the engineering component in various industries. It can be divided into two category, namely synthetic and natural fibre. Natural fibre, a rising natural material which having many advantages and having comparable properties to those synthetic fibre. It can come from many natural resources such as agriculture, food and also animal. There are numbers of by-products has been investigated to produce composites such as kenaf, hemp, coconut, sisal, oil palm and banana [1]. It offers a fully biodegradable, non-toxic and environmentally friendly material. However, due to its hydrophilic in nature, it is facing a poor compatibility with the hydrophobic polymer matrix. To overcome this, many studies has been conducted to treat this natural fibre to improve the adhesion between fibre and matrix, such as alkali treatment and coupling agent [2-4].

It has been discovered that these natural fibre composites have better electrical protection, good mechanical properties, good thermal and acoustic protecting properties, and higher protection from break [5]. It also can produce a material that is less harmful to the environment. Meanwhile, the synthetic fibre contains some of the disadvantages such as strong contributor to carbon emissions and wastes during its manufacturing process. Therefore, natural fibre is a good choice that can produce a high quality and eco-friendly product.

Sandwich structure concept involves the combination of two thin and stiff faces attach to a thick and relatively light core, i.e. honeycomb, balsa or foam. The purpose of sandwich structure is to achieve a stiff and simultaneously light component. There are many advantages of sandwich structure such as high stiffness and strength of product can be achieved. Sandwich structures are used in a various of engineering applications such as automotive car, refrigerated transport containers, yachts and aircraft. This structure has commercialized by the industry as a structural concept that can solve the problem of product weight.

The use of natural fibre in sandwich structure has gained attention from many researchers and scientists, as it could be a potential replacement to a common material (e.g. glass and foam). It is believed that the use of natural fibre in sandwich structure could be an additional benefit to the structure which is environmentally friendly. A study on the development of paper honeycomb core has shown that it has potential to replace the PU foam core [6]. In addition, an initial experimental of an eco-friendly honeycomb cores made of flax fibre with polyethylene matrix have been investigated by Petrone et al. [7]. Stocchi et al. [8] manufacture and tested a jute/vinylester (VE) honeycomb core and found that it failed in a progressive damage due to its typical fibre composite failure mechanisms. The authors also shown that the jute/VE cores having comparable specific compressive strength when comparing with commercially available core, such as Hexcel HRH 10 Nomex.

This paper aimed to expand the capability of corrugated structure made of eco-friendly material. The focus is on the effect of the unit cell number as well their length on the compression properties.

2. METHODOLOGY

Initially, the mould to make the corrugated core was designed using a commercial design software CATIA V5 and fabricated using CNC machineThen, the cores were manufactured using compression moulding method. Here, the material used is pre-preg woven flax reinforced polylactide acid (flax/PLA) supplied by Easy

Composites. The flax/PLA fabric was pressed in the corrugated mould with a dimension of 300 x 300 mm. The manufacturing process was set to 190°C and pressed for approximately 15 minutes.

As for the skin, the similar manufacturing process was used, but using a two identical flat mould. To fabricate the sandwich corrugated structure, both skins and core are attached together using an epoxy resin through the simple hand lay-up method and were left for about 24 hours to be cured. Finally, the complete sandwich corrugated structures were tested under compression loading using Instron 3366 machine following the ASTM C365 standard. The crosshead displacement rate was set to 2 mm/min and stop until the structures completely crushed. Here, three layers of flax/PLA is prepared for both core and skins. Figure 1 show the complete shape of the corrugated structure. This study focuses on investigating the effect of number of unit cell as well their width length.

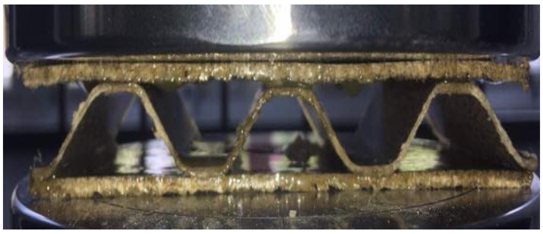

Figure 1 Corrugated core structure.

3. RESULTS AND DISCUSSION

3.1 Compressive Properties

Figure 2 presents the load-displacement exhibited from 3-unit cell with a width length of 48 mm. The curve has been divided into three regions; elastic linear, progressively nonlinear, plateau plastic and densification region. The sample were tested until it completely crushed. Upon loading, the structure facing a nonlinear response during the initial loading stage. This could be influenced by the skins that is not parallel to each other, where the machine is straightening those skins. After the initial stiffness, a linear fashion occurred up to the first peak (region A). Here, a small buckling is observed with the structure deform into a symmetrical shape about the axis of the loading. As the loading continued, the structure reaches its maximum value before started to lose its stability and the strength of the structure is decreasing. As a result, a progressing nonlinear response occurred (region B). During this stage, the web strut at the bottom part of the core structure exhibit a failure breakage. Following this, the breakage of the web strut continues to deform into triangular shape. This is where the core start to resist the applied loading again due to formation of additional triangular shape, which can be seen at region C. Finally, at region D, it is showing a flattened corrugated core and skins, meaning the structure has been completely densified. In some cases, the edge sides of the core are found to having a debonding from the skins.

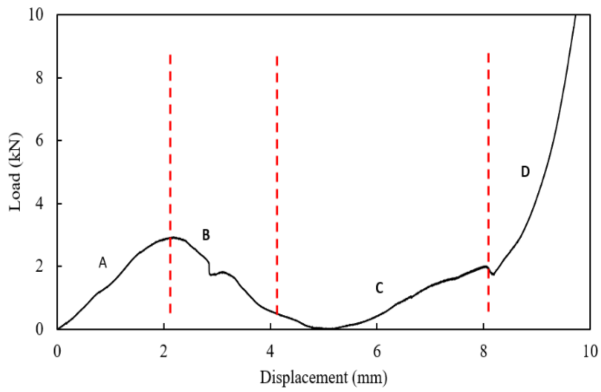

Figure 2 Typical load-displacement for 3-unit cell with width length of 48 mm.

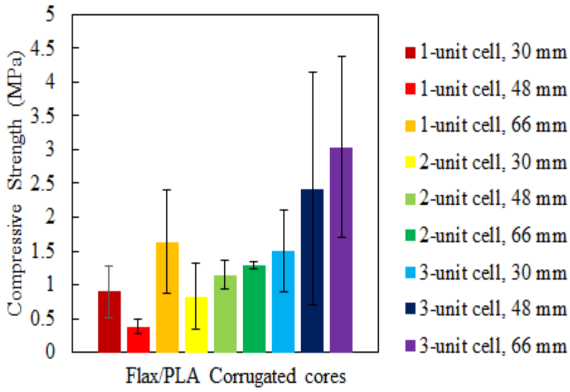

Figure 3 The variation compression strength of the corrugated structures

In Figure 3, a total of nine type of samples were examined. Here, the 3-unit cell with a length of 66 mm sample provide the higher compression strength value. The sample exhibit a maximum value of approximately 3 MPa. It is observed that the wider length of core structure required a large force to deform the samples structure before it is totally crushed. Interestingly, the 1-unit cell with a length of 48 mm showed the lowest value of compression strength than those exhibited by the 1-unit with 30 mm. The reason is unclear; however, it is believed that it could be related to the bonding between the core and skins. As expected, as the length of the structure increasing, the strength is increased.

Close observation on the sample of 2-unit cell (both 48 mm and 66 mm) showing no significant result compare to the 3-unit cell of 30 mm wide length. Is it also found that a 1-unit cell with wider length exhibited a higher value than that offered by the 2-unit cell (for all width length) and 3- unit cell with width length of 30 mm. A similar trend can also be observed in Zhou et al. [9].

Sandwich structure is well known with their energy absorption capability. In this study, the comparison between the cores are conducted in terms of their specific energy absorption (SEA) value. This is done by calculated the energy under the load-displacement graph and divided by the mass of the core. The energy is taken up to its onset densification point, which has been used by several authors [10,11]. The results of SEA are presented in Figure 4. An opposite trend is seen compared to the results in Figure 3. All samples showed a decreasing value of SEA as the width length increase. The 2-unit cell with 48 mm length exhibit a similar value to those offered by the 3-unit cell with same width length. Meanwhile, very small percentage of difference is observed at the 3-unit cell with 48 mm and 66 mm. The core with 1-unit cell shows the highest and lowest value of SEA, at 30 mm and 66 mm, respectively.

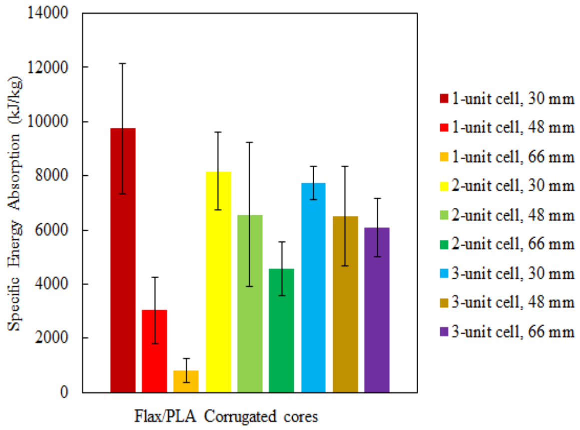

Figure 4 The variation specific energy absorption of each the corrugated structures.

3.2 Deformation failure

During the compression testing, the deformation of corrugated structure seen at 3-unit cell can be characterized as follows; at first, no deformation is observed during the initial loading, but it is believed a flattening occur at the skins due to uneven level of the structure. Then, a small wrinkling can be seen at the bottom part of the surface core, where the web strut gives a force toward the inside area at both sides. As the force increase, the bottom surface started to crack and failed as composite breakage. Due to this breakage, the web strut loses its stability and occurring a localized buckling near to the bottom surface area. On close observation at the bottom skin, a 'convex upward' bending shape is seen. This is suggested that it could be due to a perfect bonding of the skins to core.

A small bending shape also observed at the top skin between the top peak surface of the core. From the displacement of 6 mm to 8 mm, a triangular shape was formed as a result of the composite breakage from the localized buckling at the bottom area (Figure 5). Again, at the displacement of 8 mm, the bottom skin exhibited a small bending, which is caused from the symmetrical shape of bending at both end of the unit cell of the corrugated core. Similar style of failures also occurred for another unit cell, from localized buckling to composite breakage. However, there is also an evident at some sample that a debonding at the edge of the core, which largely related to the insufficient resistance offered by the polymer matrix.

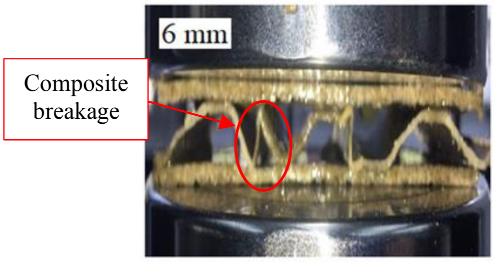

Figure 5 Deformation failure at a displacement of 6 mm.

4. CONCLUSIONS

A range of corrugated core structures made of flax/PLA composite were fabricated and tested. Effect of number of unit cell size as well their width length of the core structures on the compression properties were investigated. The following conclusion can be drawn:

- The increasing number of unit cell and wider length will resist greater force resulted to higher compressive strength.
- Specific energy absorption value will decrease as the number of unit cell and width length is increased.
- A typical breakage failure of composite materials can be observed at the flax/PLA corrugated structures. Here, the corrugated core failed from localized buckling to composite breakage.
- This environmentally friendly corrugated structure could be a good potential use in a low-end engineering application.

ACKNOWLEDGEMENT

The authors would like to thanks to Universiti Putra Malaysia for supporting the work through the Putra Grant (GP-IPM/2016/9499400). Gratitude also expressed to Mr. Muhammad Wildan Ilyas Mohamed Ghazali for his assistance in conducting the experimental testing.

REFERENCES

[1] M.S. Salit, "Tropical natural fiber composite; properties, manufacture and applications". 1, 2014.
[2] L. Yan, N. Chouw, X. Yuan, "Improving the mechanical properties of natural fibre fabric reinforced epoxy composites by alkali treatment". Reinforced Plastics & Composites, 31(6), pp.425-437, 2012.
[3] A. El-Sabbagh, "Effect of coupling agent on natural fibre in natural fibre/polypropylene composites on mechanical and thermal behavior". Composites: Part B, 57, pp.126-135, 2014.
[4] A. Atiqah, M. Jawaid, S.M. Sapuan, M.R. Ishak, M.N.M. Ansari, R.A. Ilyas, "Physical and thermal properties of treated sugar palm/glass fibre reinforced thermoplastic polyurethane hybrid composites". Materials Research and Technology, article in press, 2019.
[5] M.R. Sanjay, G.R. Arpitha, B. Yogesha, "Study on mechanical properties of natural-glass fibre reinforced polymer hybrid composites: A review",

Materials Today: Proceedings, 2(4-5), pp.2959-2967, 2015.

[6] J. Pflug, F. Xinyu, B. Vangrimde, I. Verpoest, "Development of a sandwich material with polypropylene/natural fibre skins and paper honeycomb core", Proceedings of 10th European Conference on Composite Materials (ECCM-10), Belgium, 3-7 June 2002, pp.331.

[7] G. Petrone, S. Rao, S. De Rosa, B.R. Mace, F. Franco, D. Bhattacharyya, "Initial experimental investigations on natural fibre reinforced honeycomb core panels", Composites Part B: Engineering, 55, pp.400-406, 2013.

[8] A. Stocchi, L. Colabella, A. Cisilino, V. Álvarez, "Manufacturing and testing of a sandwich panel honeycomb core reinforced with natural-fiber fabrics", Materials and Design, 55, pp.394-403, 2014.

[9] J. Zhou, Z.W. Guan, W.J. Cantwell, "Scaling effects in the mechanical response of sandwich structures based on corrugated composite core", Composites Part B: Engineering, 93, pp.88-96, 2016.

[10] T. Xinbang, Z. Daiyu, N. Yunhui, "Mechanical and energy absorption properties of foamed concrete under one-dimension strain compression", Modern Applied Science, 10(7), pp.195-207, 2016.

[11] D. Li, W. Liao, N. Dai, Y.M. Xie, "Comparison of mechanical properties and energy absorption of sheet-based and strut-based gyroid cellular structures with graded densities", Materials, 12(13), 2183, 2019.

Application of Electro-Mechanical Impedance Responses for Damage Detection in Metal Structures

Duc-Duy Ho[1,*], Thanh-Canh Huynh[2], Minh-Tuan Ha[3]
[1)] Ho Chi Minh City University of Technology, VNU-HCM, Ho Chi Minh City, Vietnam
[2)] Duy Tan University, Da Nang, Vietnam
[3)] Ho Chi Minh City University of Technology (HUTECH), Ho Chi Minh City, Vietnam
[*]Corresponding e-mail: hoducduy@hcmut.edu.vn

ABSTRACT – In this study, application of electro-mechanical impedance responses for damage detection in metal structures is presented. Firstly, impedance-based structural health monitoring (SHM) method is briefly outlined. Secondly, feasibility verification of numerical impedance simulation by using several examples such as steel beams, aluminum round plates. Finally, a numerical simulation of steel column connection is carried out to evaluate the applicability of the proposed SHM method.
Keywords: bolted connection; damage detection; electro-mechanical impedance; metal structures; numerical simulation.

1. INTRODUCTION

In the age of industry 4.0, automation and data exchange using smart technologies are inevitable trends. Besides, the occurrence of damages is inevitable during service life of metal structures. If the damages are not detected timely, they will cause catastrophic incidents for the safety of not only self-structures but also the humans and society. One of the promising ways to guarantee the structural safety and integrity is to enact structural health monitoring (SHM) in a regular periodic manner and to detect critical damage in its early stage [1]. Recently, impedance-based damage monitoring technologies have been widely used in SHM applications. The impedance-based SHM methods are useful to detect damage in critical local members [2–7].

This study presents an impedance-based damage detection of metal structures by numerical simulation. Firstly, impedance-based damage alarming method is briefly outlined. Secondly, feasibility verification of numerical impedance simulation by using several examples such as steel beams, and aluminum round plates. Undamaged steel beams are simulated to compare to experimental impedance responses. Aluminum round plates with PZT (Lead Zirconate Titanate) patch in center are simulated to investigate sensitive range of impedance responses. Finally, a numerical simulation of steel column connection is carried out to evaluate the applicability of the proposed SHM method for bolt-loosening detection.

2. IMPEDANCE-BASED DAMAGE ALARMING

The electro-mechanical (E/M) impedance response is based on the coupling of mechanical and electrical characteristics [2]. As shown in Figure 1, the host structure is described as the effects of mass, stiffness, damping, and boundary condition. The PZT (Lead Zirconate Titanate) patch is modeled as a short circuit powered by a harmonic voltage or current. When a PZT patch is surface-bonded to a structure, the electrical admittance (the inverse of E/M impedance) of the patch is a combined function of the mechanical impedance of the host structure and that of the piezoelectric patch. The mechanical impedance of the host structure is a function of mass, stiffness and damping. Therefore, any changes in dynamic characteristics of the structure could be represented in the change in E/M impedance. In order to quantify the change in impedance signatures due to structural damage, a simple index which is root mean square deviation (RMSD) of impedance signatures is used [3]

$$RMSD\left(Z,Z^*\right)=\sqrt{\sum_{i=1}^{N}\left[Z^*(\omega_i)-Z(\omega_i)\right]^2 \Big/ \sum_{i=1}^{N}\left[Z(\omega_i)\right]^2} \qquad (1)$$

where $Z(\omega_i)$ and $Z^*(\omega_i)$ are the impedance signatures measured before and after damage for the i^{th} frequency, respectively; and N denotes the number of frequency points in the sweep. The RMSD is larger than 0 if damage, and vice versa.

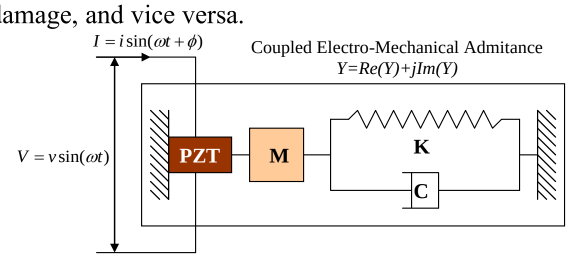

Figure 1. E/M interaction between piezoelectric patch and host structure

3. FEASIBILITY VERIFICATION

In order to demonstrate the applicability of the impedance-based SHM method, numerical simulations are carried out on steel and aluminum structures. COMSOL 4.0 software which is efficient for E/M impedance simulation was employed to estimate models. Steel beams and aluminum round plates were simulated to compare to experiments and to diagnosis occurrence of cracks. A bolted connection in steel column was model to monitor bolt-loosening. In the finite element (FE) models, solid element was used for host structure, and piezoelectric element was used for PZT patch.

3.1 Uncracked steel beams

Four uncracked steel beams which are different from dimensions were simulated to compare to experimental results from [8], as shown in Figure 2. The beams' dimensions were: beam 1 of 100×8×2.6-mm, beam 2 of 100×8×5.2-mm, beam 3 of 100×19.6×2.6-mm, and beam 4 of 100×19.6×5.2-mm. A thin 7-mm square PZT 5-A patch was boned on each beam. The distance from left end of beam to PZT patch was 40 mm. A voltage

2 V was applied to PZT patch. The beams' properties and PZT patch's properties are same as [8]. In the experiment, impedance signals measured by HP 4194A Impedance Analyzer was performed in the 1 ~ 30 kHz range. The boundary conditions of beams were free. Figure 3 shows the FE model of the beams.

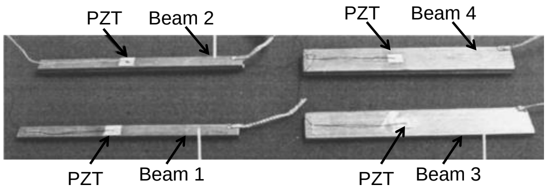

Figure 2. Experimental specimens

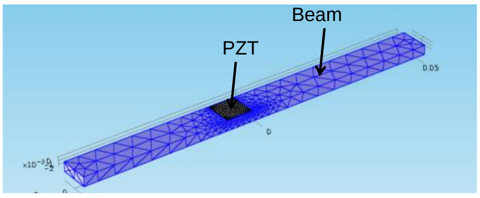

Figure 3. FE model of steel beams

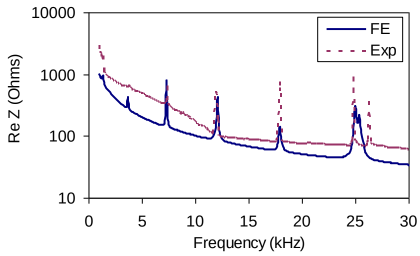

(a) Beam 1

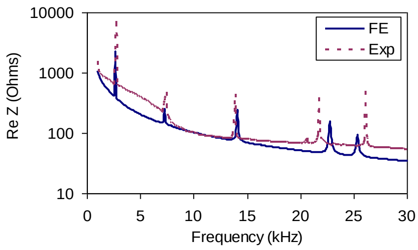

(b) Beam 2

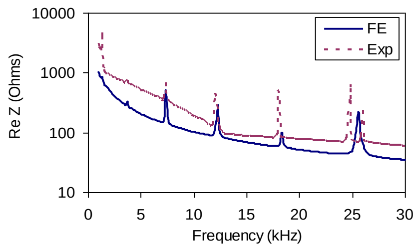

(c) Beam 3

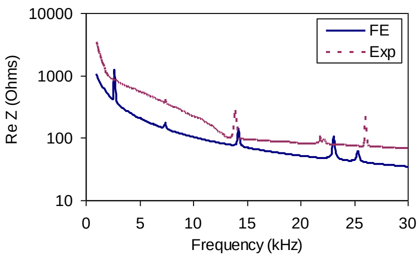

(d) Beam 4

Figure 4. Real impedances of steel beams

The comparisons between FE model and experiment are showed in Figure 4. The resonant frequencies increase proportionally to the thick of beam. The numerical impedance responses are good match with the experimental ones. The differences of resonant frequency are 0.1 ~ 5.1%. Therefore, COMSOL is reliable software for simulation of impedance responses.

3.2 Round aluminum plates

Round aluminum plates were simulated to diagnosis of cracks and to investigate sensitive range of impedance responses. The FE models of five plates were simulated the same to the experiments from [5]. The diameter of each plate was 100 mm and the thickness was 0.8 mm. Each plate was bonded a 7-mm diameter PZT patch at its center. Group 0 was uncracked; groups 1 ~ 4 were cracked with decreasing distance from the PZT patch. A 10-mm circumferential slit was used to simulate the crack. The radial positions 40, 25, 10, and 3 mm from the PZT patch were considered. In the experiment, the plates were placed on foam for free boundary conditions, as shown in Figure 5. A voltage 1.5 V was applied to each PZT patch. The plates' properties and PZT patch's properties are same as [5]. The impedance signatures were measured by HP 4194A Impedance Analyzer for three frequency ranges: 10 ~ 40 kHz, 10 ~ 150 kHz, and 300 ~ 450 kHz. Figure 6 shows the FE model of the plates.

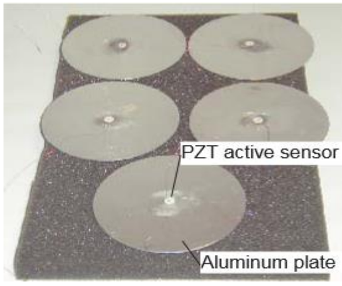

Figure 5. Round aluminum plates

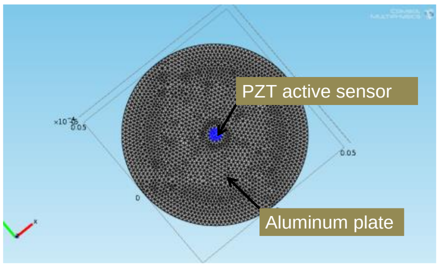

Figure 6. FE model of round aluminum plates

As shown in Figure 7, the numerical and experimental impedances are well agreement. The errors of resonant frequencies are less than 10%. The numerical peak frequencies shift to left side in comparison to experimental ones. Figure 8 shows the real impedance responses for numerical simulations (Group 0 ~ Group 4). An appropriate frequency range should be selected to get reliable SHM results. In this study, frequency range 300 ~ 450 kHz was selected to computed RMSD of impedance signatures by Eq. (1). As shown in Figure 9, it is observed that the RMSD of impedance increases as the crack distance decreases. The results are similar to experiments from [5].

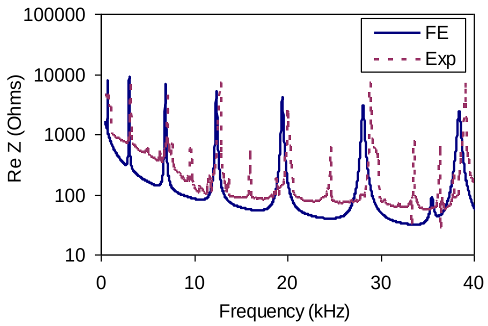

Figure 7. Real impedance of Group 0

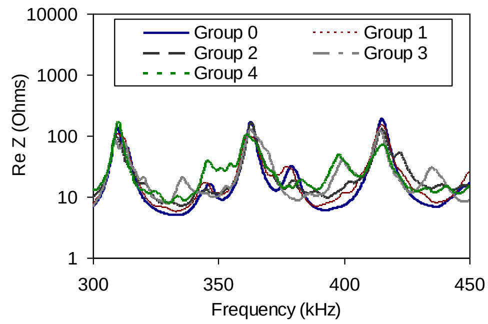

Figure 8. Simulation impedance signatures

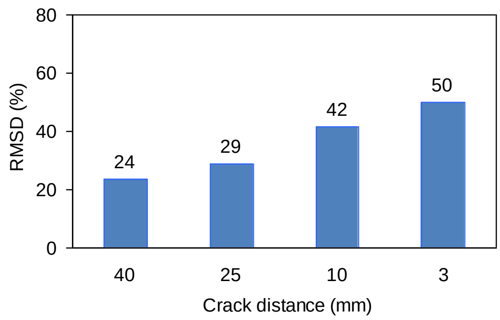

Figure 9. RMSD vs crack distance

3.3 Bolt-loosening monitoring for steel column connection

For steel structures, bolted connections are widely used and bolt-loosening is an important target for SHM. In this study, a bolted connection in steel column was simulated to monitor the bolt-loosening issue. The connection which used to connect two sections H-330×220×8×10 mm included two plates 470×220×10 mm, four stiffeners 220×70×8 mm, four stiffeners 220×100×8 mm, and eight bolts M18. Material properties of steel were defined as modulus of elasticity E = 200 GPa, mass density ρ = 7850 kg/m^3, Poisson's ratio ν = 0.33, and damping coefficient ζ = 0.01. A 20×20×0.2-mm PZT-5A patch was bonded at each bolt. Material properties of PZT patch were defined as modulus of elasticity E = 67 GPa, mass density ρ = 7750 kg/m^3, Poisson's ratio ν = 0.31, and damping coefficient ζ = 0.023. A voltage 5 V was applied to each PZT patch.

FE model is shown in Figure 10. Bolt-loosening of each bolt was simulated at three levels 10%, 25%, and 50%. The fastener tension forces were calculated from the corresponding torque [10]. In the FE model, the bolt-loosening levels were simulated by reducing the assigned forces on corresponding washers, as shown in Figure 10(c). The impedance signatures were analyzed in range 1 ~ 12 kHz with increment step of 200 Hz. Figure 11 shows the real impedance signatures of PZT1 and PZT2. The RMSD of impedance signatures computed by Eq. (1) for frequency range 3 ~ 7 kHz are summarized in Table 1 and shown in Figure 12.

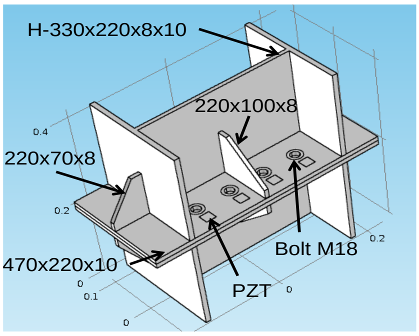

(a) Steel column connection

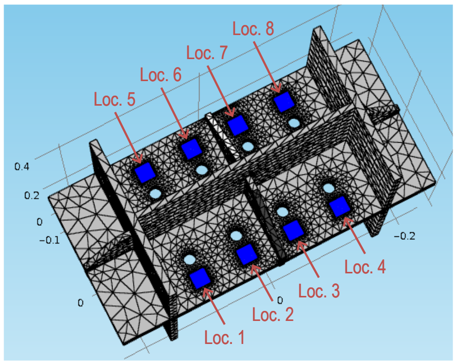

(b) Location of bolts and PZTs

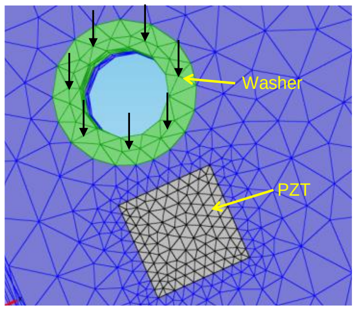

(c) Assigned force

Figure 10. FE model of steel column connection

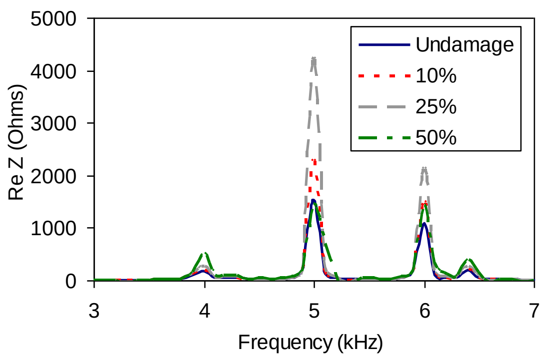

Figure 11. Real impedance signatures

Table 1. RMSD vs bolt-loosening

Level	PZT1	PZT2	PZT3	PZT4	PZT5	PZT6	PZT7	PZT8
Bolt 1-loosening								
Level	**PZT1**	PZT2	PZT3	PZT4	PZT5	PZT6	PZT7	PZT8
10%	**46**	5	6	10	4	2	3	4
25%	**151**	15	17	24	9	5	9	9
50%	**48**	38	35	41	18	9	18	17
Bolt 2-loosening								
Level	PZT1	**PZT2**	PZT3	PZT4	PZT5	PZT6	PZT7	PZT8
10%	9	**15**	7	11	5	3	4	4
25%	23	**38**	18	26	11	7	11	9
50%	46	**166**	37	44	20	12	21	18
Bolt 3-loosening								
Level	PZT1	PZT2	**PZT3**	PZT4	PZT5	PZT6	PZT7	PZT8
10%	10	7	**16**	7	5	4	4	5
25%	24	19	**38**	16	11	9	11	13
50%	43	38	**160**	30	22	20	22	24
Bolt 4-loosening								
Level	PZT1	PZT2	PZT3	**PZT4**	PZT5	PZT6	PZT7	PZT8
10%	9	6	4	**45**	4	3	4	5
25%	21	17	11	**95**	10	8	10	12
50%	37	34	23	**54**	20	16	20	23
Bolt 5-loosening								
Level	PZT1	PZT2	PZT3	PZT4	**PZT5**	PZT6	PZT7	PZT8
10%	3	2	3	4	**45**	6	7	10
25%	8	5	8	10	**125**	16	18	23
50%	15	10	17	19	**56**	40	38	41
Bolt 6-loosening								
Level	PZT1	PZT2	PZT3	PZT4	PZT5	**PZT6**	PZT7	PZT8
10%	3	5	5	4	11	**32**	9	14
25%	10	7	10	10	22	**40**	20	25
50%	18	12	20	20	45	**158**	41	44
Bolt 7-loosening								
Level	PZT1	PZT2	PZT3	PZT4	PZT5	PZT6	**PZT7**	PZT8
10%	5	4	4	5	10	7	**17**	6
25%	11	9	10	13	24	20	**38**	15
50%	22	19	21	25	43	41	**161**	29
Bolt 8-loosening								
Level	PZT1	PZT2	PZT3	PZT4	PZT5	PZT6	PZT7	**PZT8**
10%	5	3	4	5	9	7	4	**41**
25%	11	8	9	13	21	18	12	**89**
50%	21	16	19	24	38	36	25	**63**

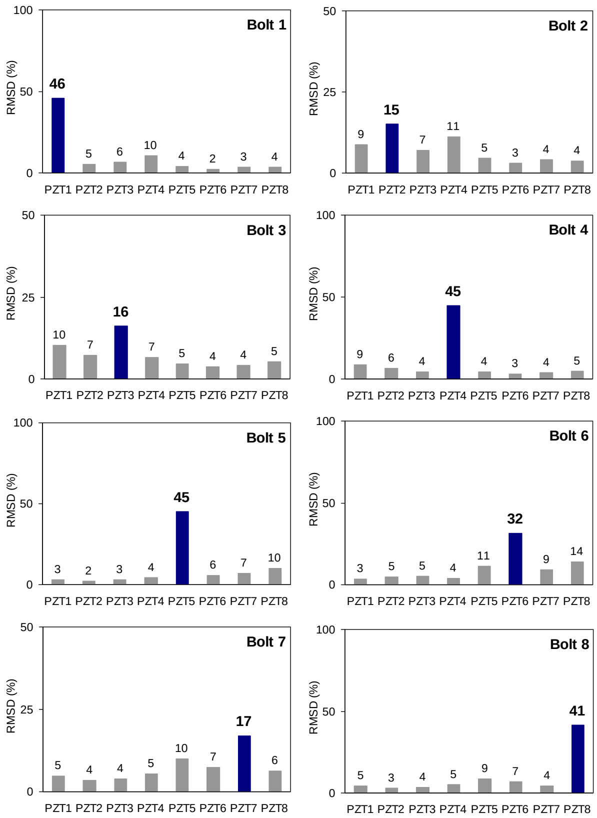

Figure 12. RMSD vs bolt-loosening 10%

The RMSD index is highest at the corresponding bolt-loosening. When the level of damage increases, the RMSD increases. Due to the sensitivity of PZT patches bonding near loose bolt, the corresponding RMSD indices are not equal 0; however, these values are much less than the RMSD index at damaged location. Additionally, the stiffness of H-columns and stiffeners also effect to the sensing of PZT patches on connection.

In summary, the bolt-loosening issue in the bolted connection in steel column was successfully detected by using impedance responses.

4. CONCLUSIONS

Feasibility verifications were successfully performed for impedance-based damage detection in metal structures. The following conclusions have been drawn from the results: (1) numerical simulations of E/M impedance responses were well estimated; (2) the impedance responses were good agreement between numerical results and experimental ones; (3) the damages were accurately detected by using impedance-based SHM method. Numerical results show that impedance responses are potential for damage detection in metal structures.

ACKNOWLEDGEMENT

The authors thank the AUN/SEED-Net project (Phase 4) for the support.

REFERENCES

[1] C.R. Farrar, “Historical overview of structural health monitoring”. Lecture Notes on Structural Health Monitoring Using Statistical Pattern Recognition, Los Alamos Dynamics, Los Alamos, NM, 2001.

[2] C. Liang, F.P. Sun, and C.A. Rogers, “Coupled Electro-Mechanical Analysis of Adaptive Material Systems-Determination of the Actuator Power Consumption and System Energy Transfer”. Journal of Intelligent Material Systems and Structures, Vol. 5, pp. 12-20, 1994.

[3] F.P. Sun, Z. Chaudhry, C. Liang, and C.A. Rogers, “Truss Structure Integrity Identification Using PZT Sensor-Actuator”. Journal of Intelligent Material Systems and Structures, Vol. 6, pp. 134-139, 1995.

[4] G. Park, H. Sohn, C. Farrar, and D. Inman, “Overview of piezoelectric impedance-based health monitoring and path forward”. The Shock and Vibration Digest, Vol. 35, pp. 451-463, 2003.

[5] V. Giurgiutiu, and A. Zagrai, “Damage Detection in Thin Plates and Aerospace Structures with the Electro-Mechanical Impedance Method”. Structural Health Monitoring, Vol. 4, No. 2: 0099–20, 2005.

[6] J.T. Kim, J.H. Park, D.S. Hong, and W.S. Park, “Hybrid health monitoring of prestressed concrete girder bridges by sequential vibration impedance approaches”. Engineering Structures, Vol. 32, pp. 115-128, 2010.

[7] D.D. Ho, “Multi-scale smart sensing of vibration and impedance for structural health monitoring of cable-stayed bridge”. Ph.D. Dissertation, Pukyong National University, Korea, 2012.

[8] V. Giurgiutiu, and A.N. Zagrai, “Embedded Self-Sensing Piezoelectric Active Sensors for Online Structural Identification”. ASME Journal of Vibration and Acoustics, Vol. 124, pp. 116-125, 2002.

[9] X. Liu, and Z. Jiang, “Design of a PZT patch for measuring longitudinal mode impedance in the assessment of truss structure damage”. Smart Materials and Structures, Vol. 18, ID125017, 2009.

[10] S.A. Nassar, G.C. Barber, and D. Zuo, “Bearing friction torque in bolted joints”. Tribology Transactions, Vol. 48, pp. 69-75, 2005.

Performance Evaluation of A Light Rail Vehicle on Curve with Track Twist Irregularities

Yunendar Aryo Handoko[1*], Andi Isra Mahyuddin[1], Arif Sugiharto[1], Yunus Sinaga[1], Prasetya Adi Nugraha[2]

[1)] Faculty of Mechanical and Aerospace Engineering, Institute of Technology of Bandung, Jl. Ganesha 10, Bandung 40132, Indonesia
[2)] PT Industri Kereta Api Persero (PT INKA)
Jl. Yos Sudarso 71, Madiun 63122, Indonesia

[*]Corresponding e-mail: yunendar@ftmd.itb.ac.id

ABSTRACT – The paper reports the evaluation of the performance of a light rail vehicle during negotiating small radius curve with track twist irregularity. The evaluation was done by setting up a comprehensive vehicle-track interaction model in a multibody dynamic software platform. The results show that the designed vehicle has a proper safety margin against derailment.

Keywords: light rail vehicle; curving performance; track twist

1. INTRODUCTION

In the design stage, the dynamics performances of a railway vehicle when running on the track need to be evaluated. One of the important characteristics to be evaluated is its safety against derailment when negotiating small curve with track twist irregularity. In such condition the possibility of flange-climbing derailment increases as the high lateral force in the point of contact combines with the reducing of the vertical force due to canted track geometry as well as track irregularity [1].

To investigate the sensitivity against derailment of a rail vehicle, two parameters are commonly analyzed. The first is the derailment coefficient, which is stated in form of the lateral force (Y) generated at the contact point between the wheel and the rail divided by the vertical force (Q) as shown in Figure 1. If the derailment coefficient is lower than critical value calculated using Nadal's equation, then the derailment is justified to be "unlikely happen". The second parameter is wheel off-loading ratio, which is a ratio between the current load change ΔQ on the wheel being investigated and the average static wheel load Q_i. Discussion on these two parameters and their relation to the derailment sensitivity of railway vehicle can be found in many literatures [2-5].

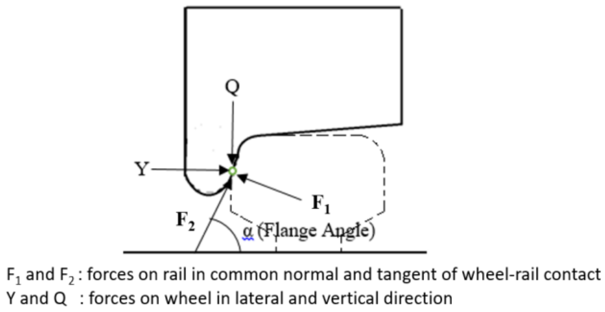

Figure 1 Forces at flange contact point.

From literatures described in the above paragraph, the critical value for derailment coefficient Y/Q depends on the flange angle and friction coefficient μ according the following formulation.

$$(Y/Q)_{crit} = \frac{\tan\alpha - \mu}{1 + \mu\tan\alpha}$$

For the wheel profile used in this study, which is the common wheel profile used in Indonesia, the calculated critical value is 1.2, however for design purpose 0.8 is taken as the maximum value allowed. For wheel off-loading dQ/Q_i, 0.6 is considered as a limit value.

2. METHODOLOGY

The evaluation was done by setting up a comprehensive vehicle-track interaction model in a multibody dynamic software Universal Mechanism [6]. The software has a capability to perform time-series simulation to investigate the vehicle dynamics performances. The full vehicle model with curve track is shown in Figure 2. The inputs for the simulation are mass of the vehicle, suspension stiffness and damping characteristics, wheel and rail profiles, track stiffness, track geometry and operational speed. The expected outputs are wheel-rail contact forces which are then used to calculate the derailment coefficient and wheel off-loading.

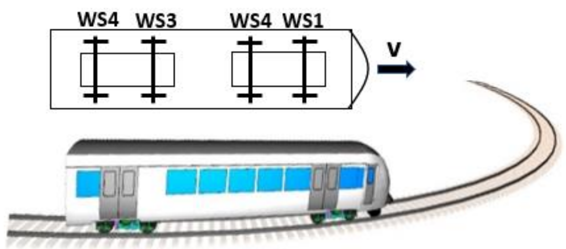

Figure 2 Vehicle model.

The multibody model of the vehicle and the track consists of 11 bodies - including the left and the right rails which is modelled as separate bodies with 3 degree of freedom each (vertical, lateral and rotation about longitudinal axis). To make the model as close as possible to the real vehicle, non-linearities in the suspension elements characteristics such as friction element, clearance with stopper, and non-linear stiffness and damping of the air springs, are put into account. Non-linear stiffness and damping characteristics of the air spring are input into the model in the form of non-linear correlation between forces and displacement or velocity. The carbody to bogie connection involves friction on the pivoting disk and bump-stop elements to represent slack and clearance in the connection. The bump-stop is modelled as a general contact element with clearance that consider the normal contact force as well as the tangential force due to friction. The wheel-rail contact forces are calculated using Kik and Piotrowski method [7], which improves Kalker's contact formulation [8], and consider more than one point of contact.

The vehicle was run at the speed of 10 km/h on the track with the geometry as shown in track curvature diagram in Figure 3. Studies has concluded that the rail vehicle is more vulnerable to the wheel climb derailment when running at low speed on the sharp curve with twisted track geometry [9]. This condition is adopted by railway standards for testing requirement of the new vehicle before it is put into service.

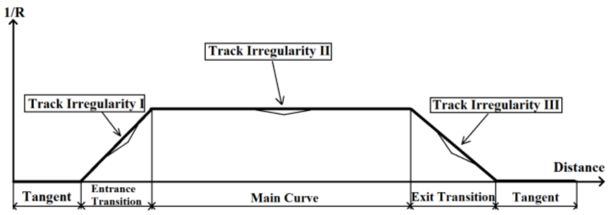

Figure 3 Track curvature diagram

As exhibited in the Figure 4, the vehicle started running in the straight track and entered the entrance transition curve before negotiating the main curve with 80 m constant radius. The length of the transition curve depends on the cant height. After passing the main curve the vehicle entered the exit transition curve with the same length as entrance transition curve and then came out from the curve back to the straight track.

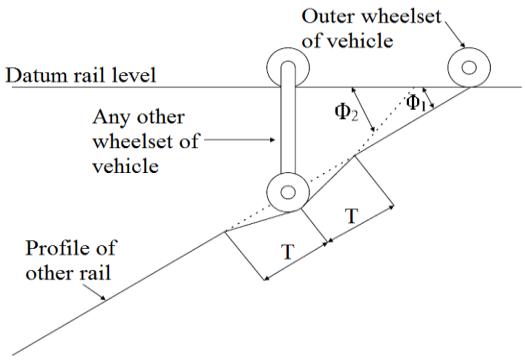

Figure 4 Track Twist

Track twist irregularities are applied in transition curves as well as in the main curve. The positions of the track twist irregularities were setup to induce biggest twist to the vehicle. The track twist configuration is shown in the diagram in Figure 4. Beside the track twist due to the change of track-cant in the transition curve there is also additional twist due to vertical irregularity at one of the rails. The parameters ϕ_1 and ϕ_2 are the twist angles due to the change of track-cant and the vertical irregularity respectively which are defined in radian, while T is the semi-span of track vertical irregularity which is defined in meter. The magnitude of, T, ϕ_1 and ϕ_2 are taken from the GM/RT 2141 standard provided by Rail Safety Standard Board, UK [10].

3. RESULTS AND DISCUSSION

Figure 5 exhibits the wheel-rail interface diagram of all wheelsets in 80 m radius curving with track geometry as explained in the previous section. It can be seen that the flange contact happens in the outer wheel of the leading wheelset of both bogies. As the occurrence of flange contact is the beginning of the wheel climbs on rail, we can conclude that the leading wheels have bigger risk to experience derailment. Thus, in this study more attention is given to the leading wheelsets of both bogies (WS1 and WS3).

It is also interesting to see that the trailer wheelset on both bogies tend to move inward against the inner rail, which is not a proper position to pass the curve. This condition can cause excessive wear on the wheel tread. Some optimizations to the primary suspension stiffness may be needed to improve the curving performance of the vehicle.

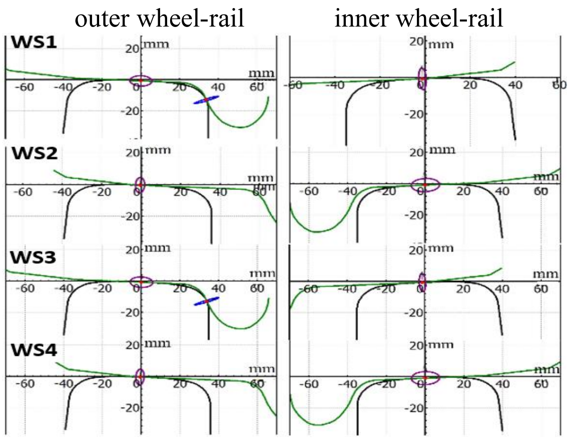

Figure 5 Wheel rail interface on curve

Figure 6 and Figure 7 present the derailment coefficient and the wheel off-loading ratio of the outer wheels of the front wheelset of both bogies which shows the highest derailment coefficient occurred in the outer wheel of the front wheelset of the leading bogie. These confirm the situation of the wheel-rail interface shown in Figure 5 where the flange contact occurred in leading wheelset of both bogies.

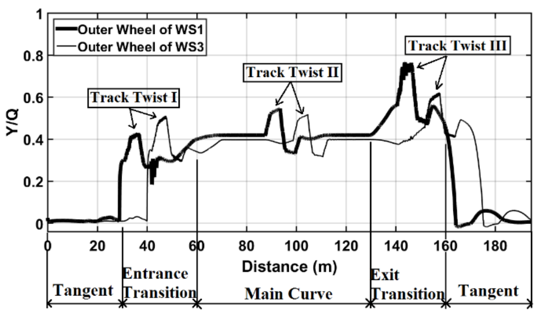

Figure 6 Derailment coefficient

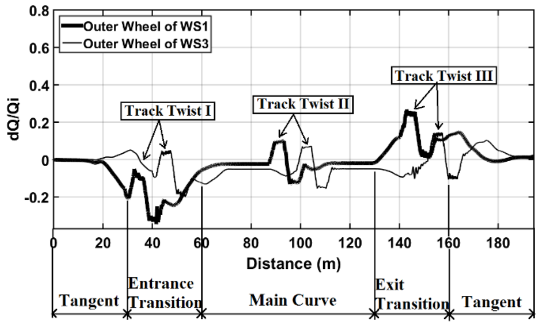

Figure 7 Wheel off-loading ratio

Next, the effect of the irregularity in the outer and inner rail that cause track twist when the vehicle negotiating curves with 70 mm and 100 mm cant height are studied. As presented in Figure 8 and Figure 9, for all cases, the maximum derailment coefficient happened in the outer wheel of the front wheelset of the leading bogie. This fact is consistent with the finding that the flange contact happens in outer wheel of the front wheelset.

It is also found that the cant height does not significantly affect the derailment coefficient as the simulations done at very low speed of 10 km/h - where the vehicle passing the curve at cant excess. However, in the exit transition curve the irregularities in the outer rail cause bigger derailment coefficient compared to the irregularities in the inner rail. It can be explained by the fact that in the exit transition curve the irregularities in outer rail add more twist to the vehicle while the irregularities in inner wheel cause the opposite.

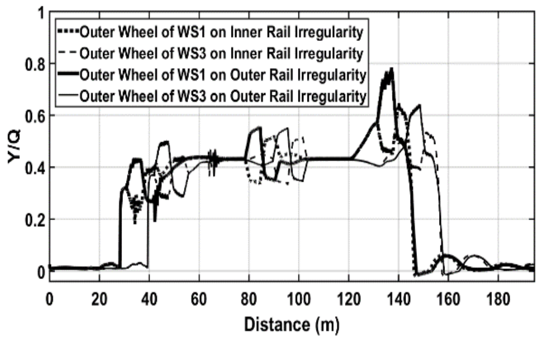

Figure 8 Derailment coefficient at 70 mm cant

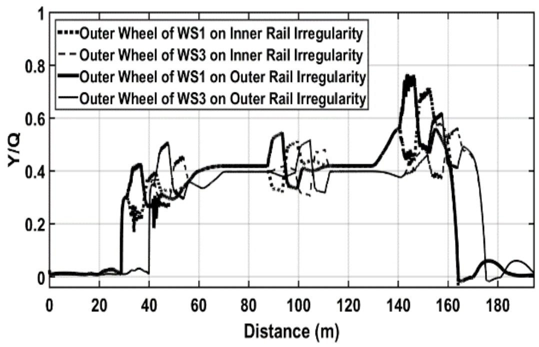

Figure 9 Derailment coefficient at 100 mm cant

Figure 10 and Figure 11 present the wheel off-loading ratio of the outer wheels of the leading wheelset of both bogies for cant height of 70 mm and 100 mm respectively. Positive value means the reducing of the wheel load, while the negative value means the increasing of the wheel load. Both figure show that the maximum reducing of load at the outer wheel occurred at the exit transition curve. This is also related to the twist track irregularity that cause maximum twist to the vehicle, which at the end increase the larger derailment coefficient.

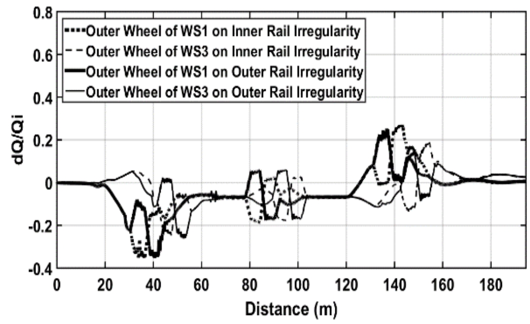

Figure 10 Wheel off-loading at 70 mm cant

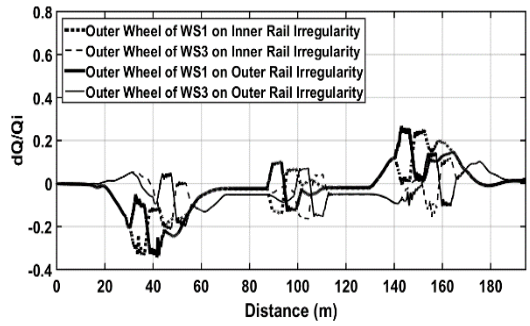

Figure 11 Wheel off-loading at 100 mm cant

The value of the maximum derailment coefficient and corresponding wheel off-loading ratio on each leading wheelset due to the irregularities are resumed in Table 1.

Table 1 Maximum value of derailment coefficient and wheel off-loading

Irregularities	Cant Height (mm)	Outer wheel WS1		Outer wheel WS3	
		Y/Q max	dQ/Q_i	Y/Q max	dQ/Q_i
Inner Rail	70	0.65	0.27	0.55	0.18
	100	0.67	0.25	0.56	0.15
Outer Rail	70	0.77	0.25	0.64	0.15
	100	0.76	0.26	0.62	0.14

4. CONCLUSIONS

The curving performance of a light rail vehicle involving track twist irregularities has been investigated by using computer simulation. The results show that the maximum derailment coefficient is 0.77 with the corresponding wheel-off loading is 0.25, which is lower than design criteria. This condition occurred when the vehicle passing the exit transition curve with irregularity in the outer rail which cause maximum twist to the vehicle. From the results it can be concluded that the designed vehicle has proper safety margin against derailment. However, to improve the curving performance of the vehicle, some optimizations to the primary suspension stiffness may be needed.

ACKNOWLEDGEMENT

Many thanks are addressed to PT Industri Kereta Api (Persero) for providing the vehicle design data for simulation input.

REFERENCES

[1] S. Iwnicki, *Handbook of Railway Vehicle Dynamics* CRC, Boca Rotan, FL, 2006.
[2] X. Jun and Z. Qingyuan, “A study on mechanical mechanism of train derailment and preventive measures for derailment” Vehicle System Dynamics Vol. 43, No. 2, pp. 121-147, 2005
[3] Dan Barbie, “On Derailment-Worthiness in Rail Vehicle Design”, Doctoral Thesis, KTH, Sweden, 2007.
[4] C.M. Kuo, C.C. hiang Lin, “Analysis of derailment criteria”, Rail and Rapid Transit, pp.1-6, 2015.
[5] Y. Nagumo, K. Tanifuji, J. Imai, “A Basic Study on Wheel Flange Climbing using Model Wheelset” International Journal of Railway Vol. 3, No. 2, pp. 60-67, 2010.
[6] Universal Mechanism, “User’s Manual”, Bryansk State Technical University, 2015.
[7] W. Kik, J. Piotrowski, “A fast approximate method to calculate normal load at contact between wheel and rail and creep forces during rolling”, Proceedings of 2nd Mini-Conference on Contact Mechanics and Wear of Rail/Wheel Systems, pp. 338-340, 1996.
[8] J. J. Kalker, “Wheel-rail Rolling Contact Theory”, Wear, pp. 243-261, 1991
[9] H. Iijima, H. Yoshida, K. Suzuki, Y. Yasuda, “A Study on the Prevention of Wheel-Climb Derailment at Low Speed Ranges”, JR EAST Technical Review-No.30, pp. 21-24, 2014
[10] Rail Safety Standard Board, UK, GM/RT 2141 issue-3, Resistance of Railway Vehicles to Derailment and Roll-Over, 2009

Examination of Multimodal Transportation to Enhance the Logistics Efficiency in Thailand: A Case Study of Cassava Products

Thanwadee Chinda[1,*], Pornsiri Punyatara[1], Pitipatara Sukyai[1], and Marisa Ratanakisadatan[1]

[1)] School of Management Technology, Sirindhorn International Institute of Technology, Thammasat University, Bangkadi, Muang, Pathumthani, 12000, Thailand

[*]Corresponding e-mail: thanwadee@siit.tu.ac.th

ABSTRACT – Being the second largest cassava producer in the world, Thailand aims to increase the export amount to neighboring and other countries around the world. Attempting to reduce the logistics and transportation costs, the government initiates various projects to support the multimodal transportation. This study develops the dynamics model of multimodal transportation of cassava products utilizing the system dynamics modeling approach. The model consists of six saving and four cost elements. The simulation results reveal that the project becomes feasible at the end of year 10 with the internal rate of return of higher than the minimum of 12%. The results also show that the saving in truck rental cost and the product damaged cost are the most important saving and cost elements, respectively. The developed dynamics model can be used as a guideline for the agricultural industry and government to effectively plan for the multimodal transportation in the long-term.

Keywords: Cassava, logistics, multimodal transportation, system dynamics modeling, Thailand

1. INTRODUCTION

The agricultural product industry is the one of main export industries of Thailand. According to BOI [1], cassava is one of Thailand's most important economic crops, with the supply of 67% of the global market or 33 million tons in 2016. The export trend of cassava starch in Thailand increases by an average of 8.5% per year or from 3.08 million tons in 2012 to 4.22 million tons in 2016 (see Figure 1) [2]. The highest cultivated area of cassava in Thailand is located in the North Eastern, accounting for 52.3 % of the total cultivated area. With that, 32.86% of the total yield in the North Eastern provinces is in Nakhon Ratchasima province [3].

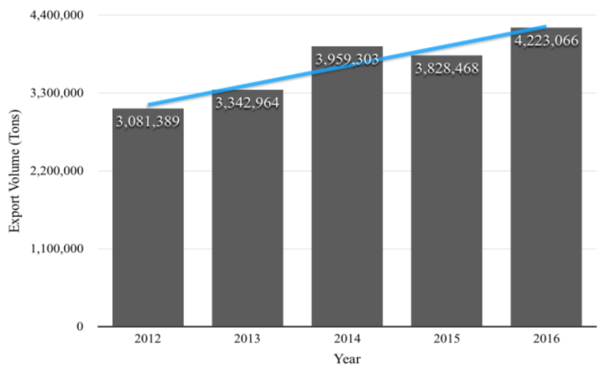

Figure 1 The export volume of cassava starch in Thailand from 2012 to 2016 [2]

Thailand is turning into a major logistics hub in the ASEAN, setting up the production base and sales network in Indochinese Peninsula. In order to develop the country's transportation infrastructure, and prepare for ASEAN Community, the Ministry of Transport comes up with the Infrastructure Development Plan (2015-2022) by integrating all platforms – rail, air, road, and water transportations into multimodal transportation to reduce logistics and transportation cost [4]. Despite being the major mode of transportation in Thailand, road transportation is the most expensive mode among the three modes, including road, rail, and ship, with an average logistics cost of two to three times higher [5]. Better transportation is required to reduce logistics and transportation cost. It is expected that the use of multimodal transportation will help reduce logistics and transportation costs, and diminish problems, such as traffic congestion, high fuel prices, air pollution, and high accident rate caused by the road transportation.

With the government's dual track system project around the country, it is expected that cassava products will gain benefits of using the combination of road and rail transport to reduce the logistics and transportation costs. This research study, therefore, aims to examine the trend of multimodal transportation of cassava products utilizing the system dynamics (SD) modelling approach. Main savings and costs of multimodal transportation of cassava products are extracted, and used for the dynamics model development. The net present value (NPV) and internal rate of return (IRR), achieved from the developed dynamics model, are used to examine the trend of multimodal transportation in the long-term. It is expected that the study results provide a guidance to the cassava and transportation industries to effectively plan for cassava transportation to achieve high competitiveness in the global market.

2. METHODOLOGY

2.1 Research flow

The research flow of this study is summarized in Figure 2. Literature review related to cassava transportation is reviewed to identify possible modes of transportation (i.e. truck and train in this study), and the origin and destination used in this study (i.e. Nakorn Ratchasima province to Laemchabang port in this study). Transportation-related literatures are also conducted to identify saving and cost elements affecting multimodal transportation of cassava products in Thailand. Secondary and primary data are collected to be used for the dynamics model of multimodal transportation development. Secondary data are collected through journal papers, conference papers, and company reports, while primary data are achieved from in-depth interviews. The dynamics model of multimodal transportation of cassava products is then developed to examine the trend of multimodal transportation of cassava products in the long-term.

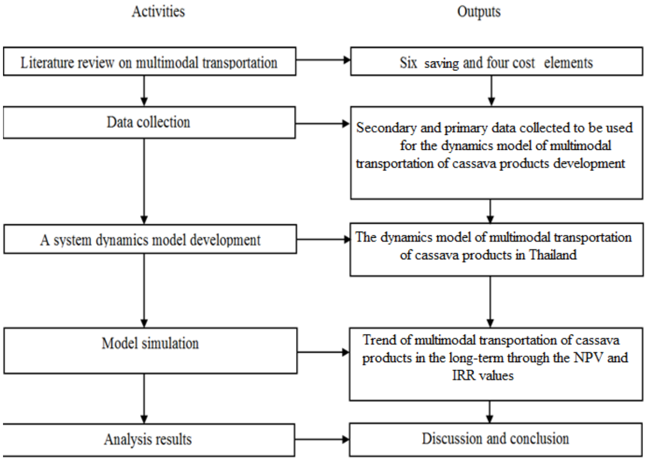

Figure 2 Research flow of this study

2.2 Saving and cost elements

Saving and cost elements related to the use of multimodal transportation of cassava products in Thailand are extracted from a number of literatures. In this study, six savings and four costs are used for the dynamics model development (see Tables 1 and 2). Santisirisomboon et al. [6], for example, mentioned that by using multimodal transportation, the company can also reduce CO_2 emission and carbon dioxide tax. Ministry of Road Transport and Highways [7] stated that the use of multimodal transportation helps reduce chances of accident occurrences, thus reducing the accident and reimbursement costs. The use of multimodal transportation also requires less trucks, leading to lower truck driver and fuel costs [8].

Table 1 Saving elements

Saving element		Value	Unit	Source
Saving in labor cost	Driver wage	18,000	baht/month	In-depth interview
Saving in fuel cost	Fuel price	27.31	baht/liter	[9]
Saving in carbon dioxide tax	Carbon dioxide tax rate	500	baht/ton CO_2	[10]
	Carbon dioxide emission for truck	107.37	g-CO_2/ton-km	[11]
	Carbon dioxide emission for train	13.37	g-CO_2/ton-km	[11]
Saving in truck rental cost	Truck rental price	22,500	baht/day	In-depth Interview
Saving in reimbursement cost	Reimbursement for minor injury	50,000	baht/person	[12]
	Reimbursement for major injury	200,000	baht/person	[12]
	Reimbursement for death	200,000	baht/person	[12]
Saving in accident cost	Truck accident rate	3.5	time/year	[7]
	Probability of minor injury in road accident	96.69	percent	[13]
	Probability of major injury in road accident	2.74	percent	[13]
	Probability of death in road accident	0.57	percent	[13]

Table 2 Cost elements

Cost element		Cost	Unit	Source
Handling cost	Crane cost	17,500	baht/working time	In-depth interview
	Lift on and lift off cost	475	baht/time	In-depth interview
Tariff cost	Tariff cost	246 - 279	baht/ton	[15]
Delay cost	Train delay time	2	hour/day	In-depth interview
	Product return	1	percent of product return	[16]
	Train capacity	570	ton/train	In-depth interview
Damage cost	Product damage	4.18	percent of product shipment	[16]

Seo et al. [8], on the other hand, mentioned that handling and tariff cost caused by mode changing is one of the major costs of multimodal transportation. Products can also be damage during mode changing. The reliability of rail and ship modes in Thailand is still low compared with the truck mode; this sometimes causes delay and product return [14].

3. RESULTS AND DISCUSSION

3.1 The dynamics model of multimodal transportation of cassava products

SD modeling approach is utilized to develop the dynamics model of multimodal transportation of cassava products. It is the computer-aided methodology to represent the causal structure of a system through stock-and-flow feedback structures. It is used in many transportation-related studies, Rawal and Devadas [17], for example, utilized the SD modeling to analyze the impact of road transportation and developing plausible policy decision for sustainable development in Kanyakumari district. Oiu et al. [18], on the other hand, developed a system dynamics model for simulating the logistics demand dynamics of metropolitans in Beijing, China. Yu et al. [19] analyzed the impact of different transportation levels and the proportion of road and railway investment on the land transportation systems in a port city in Tianjin, China.

The dynamics model of multimodal transportation of cassava products consists of 10 sub-models, as follows.

3.1.1 Saving in labor cost sub- model

Labor cost is considered in term of truck drivers in the delivery process (one truck driver per truck). With the use of multimodal transportation, less trucks are required, leading to less labor cost, see Figure 3 and Equations 1 and 2 where LCS = saving in labor cost (baht/year), TSPY = less trucks required per year (trucks), LCPY = labor cost per year (baht/person/year), TTPY = trucks required per year using road mode (trucks), and TMPY = trucks required per year using multimode (trucks).

$$LCS = TSPY \times LCPY \quad (1)$$

$$TSPY = TTPY - TMPY \quad (2)$$

3.1.2 Saving in fuel cost sub- model

Fuel cost consists of fuel price, fuel consumption rate, and travel distance. When the multimodal transportation is implemented, less trucks are required, leading to less fuel cost, see Figure 4, and Equations 3 and 4, where FCS = saving in fuel cost (baht/year), FCTPY = fuel cost per year using truck mode (baht/year), FCMPY = fuel cost per year using multimode (baht/year), FCMLBPY = fuel cost per year to Laemchabang port using multimode (baht/year), and FCMCYPY = fuel cost per year to container yard using multimode (baht/year).

$$FCS = FCTPY - FCMPY \quad (3)$$

$$FCMPY = FCMLBPY + FCMCYPY \quad (4)$$

3.1.3 Saving in carbon dioxide tax sub- model

Train mode releases less CO_2 than truck mode by around eight times. The use of multimodal transportation, thus, helps reduce the amount of CO_2 emission, resulting in less carbon dioxide tax (see Equations 5 and 6, and Figure 5), where CTS = carbon dioxide tax saving (baht/year), CTTPY = carbon dioxide tax per year using truck mode (baht/year), CTMPY = carbon dioxide tax per year using multimode (baht/year), CTMLBPY = carbon dioxide tax per year to Laemchabang port using multimode (baht/year), CTMCYPY = carbon dioxide tax per year to container yard using multimode (baht/year), and CTMRPY = carbon dioxide tax per year using train in multimode (baht/year).

$$CTS = CTTPY - CTMPY \quad (5)$$

$$CTMPY = CTMLBPY+CTMCYPY+CTMRPY \quad (6)$$

3.1.4 Saving in truck rental cost sub- model

According to in-depth interviews, trucks used in the transportation are rent to avoid maintenance problems. When multimodal transportation is utilized, number of trucks used are reduced, leading to less truck rental cost (see Equation 7 and Figure 6), where RCS = saving in truck rental cost (baht/year), TSPY = less trucks required per year (trucks), RCPY = truck rental cost per year (baht/truck/year).

$$RCS = TSPY \times RCPY \quad (7)$$

3.1.5 Saving in reimbursement cost sub- model

Three levels of road injury are considered in this study: minor, loss of organs, and death, see Figure 7 [12]. Based on Ministry of Road Transport and Highways [7], the probabilities of injury in minor, loss of organs, and death are 96.69 %, 2.74 %, and 0.57 % of total accident occurrences, respectively. By using the multimodal transportation, it is expected that the reimbursement can be saved due to less road accidents (see Equation 8), where RBS = saving in reimbursement cost (baht/year), RBMPY = saving in reimbursement cost from minor injuries (baht/year), RBOPY = saving in reimbursement cost form losses of organs (baht/year), and RBDPY = saving in reimbursement cost from deaths (baht/year).

$$RBS = RBMPY+RBOPY+RBDPY \quad (8)$$

3.1.6 Saving in accident cost sub- model

Accidents not only imply a direct cost, but also reduce the competitiveness of exports. Accidents, when occurred, cause product damage. In this study, less accidents result in less products damaged (see Equation 9 and Figure 8), where ACS = saving in accident cost (baht/year), ACRPY = accident reduction per year (times/year), TCap = truck capacity (tons/time), and CVP = cassava price (baht/ton).

$$ACS = ACRPY \times TCap \times CVP \quad (9)$$

3.1.7 Handling cost sub- model

Crane and lift on and lift off costs are included in this study to transfer from truck to train modes. Crane charge is considered based on working hours, total load, and load sizes. Lift on and lift off equipment are equipped with cranes to load and unload cargoes (see Equation 10 and Figure 9), where HLC = handling cost (baht/year), CRCPY = crane cost (baht/year), and LLCPY = lift on and lift off cost (baht/year).

$$HLC = CRCPY+LLCPY \quad (10)$$

3.1.8 Tariff cost sub- model

Tariff cost incurs when train mode is used. It is considered from three container yard stations (i.e. Chira, Kutchik, and Ban Kradone stations) to Laemchabang port (see Equation 11 and Figure 10), where TFC = tariff cost (baht/year), TFCRPY = tariff cost from Chira station (baht/year), TFKCPY = tariff cost from Kutchik station (baht/year), and TFBDPY = tariff cost from Ban Kradone station (baht/year).

$$TFC = TFCRPY+TFKCPY+TFBDPY \quad (11)$$

3.1.9 Product return cost sub- model

In this study, product return cost is calculated based on amount of products that cannot be delivered on time due to the delay (see Equation 12 and Figure 11), where PRC = product return cost (baht/year), PRPY = product return (trains/year), and CVR = cassava cost per train (baht/train).

$$PRC = PRPY \times CVR \quad (12)$$

3.1.10 Product damaged cost sub- model

Transshipments may cause product damage (see Equation 13 and Figure 12), where PDC = product damaged cost, PDCH = chance of having product damaged (%), and CVPY = cassava shipment per year (baht/year).

$$PDC = PDCH \times CVPY \quad (13)$$

3.2 Simulation results

The dynamics model of multimodal transportation of cassava products is simulated, and the results are as shown in Figure 3. In the initial year (year 0), the dual track project is invested to initiate the multimodal transportation to increase the efficiency of train mode. Once the dual track is fully operated in three container yard stations (in years 5, 8, and 11), the savings increase, leading to higher NPV. It takes 10 years for the project to be feasible at IRR of 12%, which is the minimum IRR used in Thai government projects (see Figure 4). This is consistent with Yachiyo Engineering and Japan International Consultants for Transportation [20] that it takes 13 years for the high speed railway project in Indonesia to be feasible.

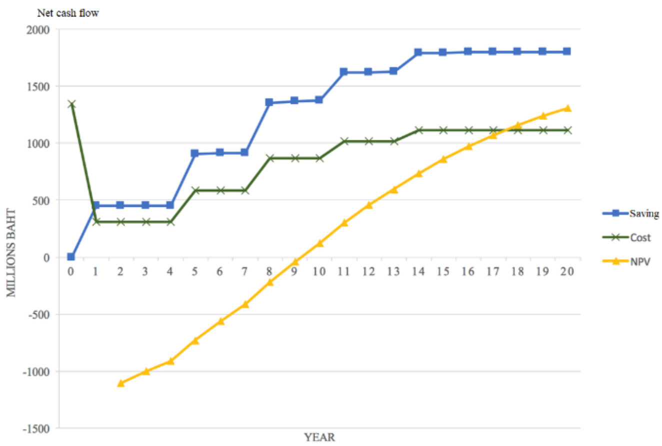

Figure 3 Simulation results

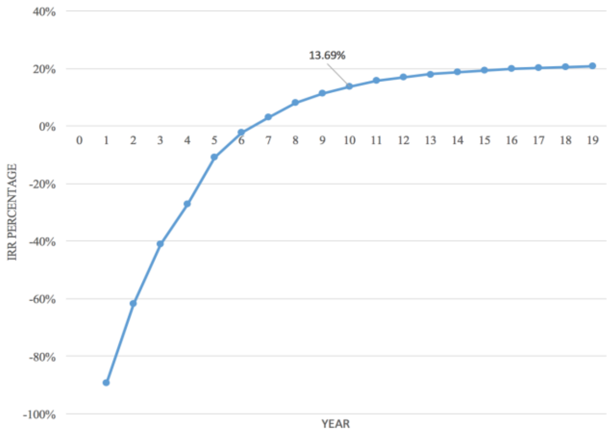

Figure 4 IRR of the project

Figures 5 and 6 show the savings and costs of the multimodal transportation. Saving in truck rental cost is the most important saving element, while product damaged cost is the highest cost. By using less trucks, the company can also reduce the fuel and accident costs. However, products may be damaged during the transshipment processes.

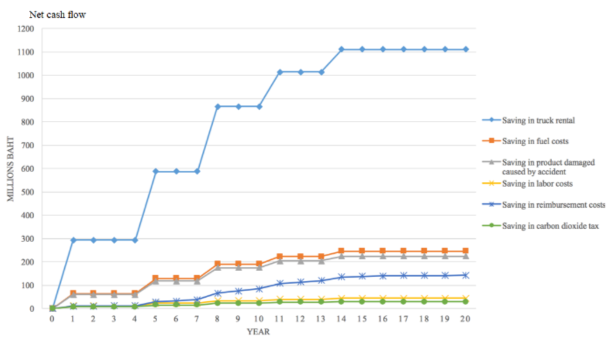

Figure 5 Benefit elements

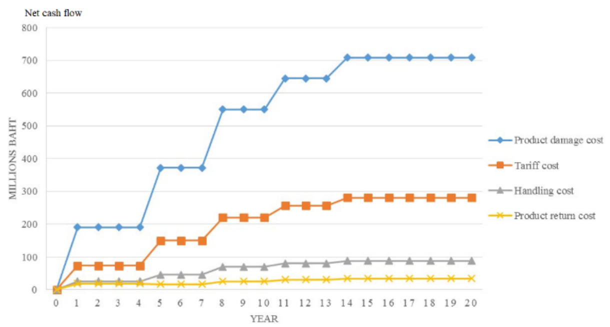

Figure 6 Cost elements

4. CONCLUSIONS

This study examines the use of multimodal transportation of cassava products in Thailand, utilizing the SD modeling. The developed dynamics model consists of six saving and four cost elements. The model is simulated, and the simulation results reveal that at the initial years, net cash flow is negative due to high investments in the dual track railway project. Once the project is implemented, the savings increase, specifically the saving in truck rental cost and saving in fuel cost. Nevertheless, the multimodal transportation implementation incurs costs, especially the product damaged and tariff costs. It takes 10 years for the project to be feasible at the IRR of 13.69%, which is higher than the minimum acceptable rate of 12%. This confirms that the use of multimodal transportation provides long-term benefits to the project.

The dynamics model of multimodal transportation of cassava products can be used as a guideline for the agricultural industry and the government to plan for the multimodal transportation to reduce the logistics and transportation costs in the long-term. Other modes of transportation, such as inland water and road modes, and rail and inland water modes may be studied to further plan for more effective transportation in the future. Data may also be adjusted to suit with different environments.

REFERENCES

[1] BOI, “Leading the world in cassava production”. Thailand Investment Review. 27(9), pp. 1-12, 2017.

[2] The Thai Tapioca Trade Association, “Export volume of cassava products 2007-2016”. Available from http://ttta-tapioca.org/Exportation/ [in Thai], 2016.

[3] Office of Agricultural Economics, “Cassava factory: cultivated area, harvested area, productivity, and productivity per rai: total country, regions, provinces and districts”. Available from http://aginfo.oae.go.th/ewtnews/amphoe_casava.html [in Thai], 2016.

[4] P. Vimolsiri, “Enhancing Infrastructure Development for Thailand's Future Growth”, Thai-Chinese Business Forum 2015, Bangkok, 17 December 2015, pp. 1-36, 2015.

[5] C. Wongsanguan, “The logistics and supply chain”. Available from: https://tma.or.th/2016/uploads/file/FIIS%202018%20-%20Nov%205%20-%20The%20Logistic%20and%20Supply%20Chain%20-%20Mr.%20Chalat%20 Wongsanguan.pdf, 2018.

[6] J. Santisirisomboon, B. Limmeechokchai, and S. Chungpaibulpatana, “Impacts of biomass power generation and CO_2 taxation on electricity generation expansion planning and environmental emissions”, Energy Policy. 12, pp. 975-985, 2001.

[7] Ministry of Road Transport and Highways, *Road Accidents in India – 2016*, New Delhi, India, Transport Research Wing, Government of India.

[8] Y.J. Seo, F. Chen, and S.Y. Roh, “Multimodal transportation: the case of laptop from Chongqing in China to Rotterdam in Europe”, The Asian Journal of Shipping and Logistics. 3, pp. 155-165, 2017.

[9] PTT Public Company Limited, “Retail price of Bangkok and suburbs in 2018”. Available from http://www.pttplc.com/th/media-center/oil-price/pages/bangkok-oil-price.aspx, 2017.

[10] A. Wattanakuljarus, “Carbon taxes to cool earth”, NIDA Case Research Journal, 4, pp. 1-40, 2012.

[11] A. Protopapas, C. Kruse, and L. Olson, *Modal Comparison of Domestic Freight Transportation Effects on the General Public,* Texas, USA, Texas Transportation Institute; 2012.

[12] S. Rungaree, “Coverage of Car Accident Victims Protection Act”. Available from http://www.kawasakimotoaholic.com/single-post/2017/03/13/Coverage-of-car-accident-

victims-protection-act [in Thai], 2017.
[13] S. Siripanich, P. Meanpoung, and A. Sangchatip, "Trends and characteristics of occupational injuries in Thailand, 2002-2010", OSIR, 7(3), pp. 8-15, 2014.
[14] PADECO, *Thailand: Improvement of Railway Passenger Services*, Technical Assistance Consultant's Report, Asian Development Bank.
[15] State Railway of Thailand, "Freight rate". Available from http://www.railway.co.th/main/service/freight/rate-freight.html [in Thai], 2017.
[16] NESDB, "Thailand's logistics report", Office of the National Economic and Social Development Board. Available from http://www.nesdb.go.th/ewt_dl_link.php?nid=3390, 2015.
[17] T. Rawal and V. Devadas, "System dynamics modeling for transportation planning in Kanyakumari district, Tamil Nadu", System Dynamics Society of India Conference, IIT Bombay, At Mumbai, 2015.
[18] Y. Qiu, X. Shi, and C. Shi, "A system dynamics model for simulating the logistics demand dynamics of metropolitans: a case study of Beijing, China", Journal of Industrial Engineering and Management, 8(3), pp. 783-803, 2015.
[19] B. Yu, C. Zhang, L. Kong, H. Bao, W. Wang, S. Ke, and G. Ning, "System dynamics modeling for the land transportation system in a port city", Simulation: Transactions of the Society for Modeling and Simulation International, 90(6), pp. 706–716, 2014.
[20] Yachiyo Engineering and Japan International Consultants for Transportation, *Study on the High Speed Railway Project (*Jakarta-Bandung Section), Republic of Indonesia, Final report, Ministry of Economy, Trade, and Industry, 2012.

Implementing Lean for Improvement of Productivity and Efficiency of some Garment Factories in Industrial Zones, Yangon Region

Yin Yin Tun[1*], Htay Htay[2], Oo San Yee[2]

[1)] Department of Mechanical Engineering, Yangon Technological University
Yangon, Myanmar
[2)] Department of Textile Engineering, Yangon Technological University
Yangon, Myanmar

[*]Corresponding e-mail: yinyintun.ytu@gmail.com

ABSTRACT –The ready-made garment manufacturing in Myanmar is developing. But most of the factories are working as Cut-Make-Pack (CMP). The productivity and efficiency depend on the skill of the workers, absenteeism and staff turnover. The quality problem occurs due to lack of skilled labour. The nonconforming products foil the productivity and cause the higher production cost due to reworks. The absenteeism causes the unstable of production and inability to reach the daily target. In this study, two cases were analysed, the productivity and efficiency of product with large order quantity and frequently-change-style of product. Two factories were observed and studied for productivity and efficiency. The frequently changing the style of garment affects on productivity of the line due to varying of job assigned for operator. For applying lean approach to improve the productivity and efficiency, the operation procedures of bottle-neck stations were studied and the better operation procedures were developed and applied at the station. The capacity for production line were increased and the imbalance efficiency was improved.
Keywords: lean, productivity, efficiency, garment, large order quantity, frequently-change-style

1. INTRODUCTION

The ready garment manufacturing is developing in Myanmar. According to SMART Myanmar report in 2015, the status of garment exports from Myanmar to the world is increasing 0.7 billion USD in 2011 to 1.6 billion USD in 2014. From 2003 to 2012, the quality and product complexity were increased, but overall production efficiency went down [1].

In Myanmar, the garment industries are 400 garment companies employed 400000 garment workers (2016) [2]. But most of the garment factories are having challenges to sustain and maintain. After the law enforcement of minimum labour wages setting, it is more crisis between factories operation teams and workers. The garment industries are facing the problems such as much of work-in-progress in the sewing line, non-value-added activities, much of rework, and setting line with not proper work-breakdown and with longer lay-out-setting time for next style of garment. Besides, the high-number of labour turnover and absenteeism are also one of the sources of accepting unskilled labours causing the low-productivity with low-quality products. But investing in garment sector in Myanmar is still a good business.

To improve the work-environment in the garment sector in Myanmar, the MYPOD project was launched in Yangon in 2018. It is funded by the Danish Market Development Partnerships fund, and the project is carrying out with the collaboration with the Danish Ethical Trading Initiative, the British Ethical Trading Initiative, Holch Povlsen family-owned Danish fashion company BESTSELLER, the Danish trade union 3F and Aalborg University, Denmark. The local stakeholders are SMART Myanmar, Yangon Technological University and local trade unions, Industrial Workers Federation of Myanmar (IWFM) and UNICEF's Multiple Indicator Cluster Survey (MICS) project [3].

As the first batch of project, the 6 garment factories in industrial zones in Yangon Region were studied baseline. In the first phase of implementation the project, the focus is about the productivity of the specified garment production line implementing lean with OHS (Occupational Health and Safety) benefits. The core team and operation team are set by the garment factories to collaborate with the expert team which is formed with the professors and teaching staff of Aalborg University and Yangon Technological University.

2. METHODOLOGY

The 6 garment factories of first batch were studied as baseline for factory information, the 5S conditions in the factory, the OHS: ergonomics (working posture of the workers), the condition of the work-environment in the factory such as room temperature, general light and local light at workstation, the noise and ventilation, the status of the machine facility (adjustable height, auto-machine/motorized, safety for eye, needle, belt) and chair for worker (adjustable height, with back-rest, swivel), the situation of communication between workers and supervisor who is in charge of the specific line, among the workers to understand the state of participation of workers.

After baseline study and forming core team and operation team, the staffs are assigned by factories, and visit the factories regularly, observe the imbalance of the work breakdown, and determine the bottleneck workstation. After analysis and study the cause of the imbalance, make better workload balance by work sharing or by avoiding non-value-added activities and train the station operator and teach the line supervisor, operation team the solving strategy.

Among the 6 factories assigned for implementation the intervention, two factories will be analysed for the line imbalance, the productivity and the efficiency of the operation line. Factory One is situated in Pale Myothit, and the another one, Factory Two is in the Industrial Zone (1), South Dagon Township. The Factory One is owned by local citizen, and the Factory Two is being run by foreigner.

There are number of key performance indicators for understanding the performance of the factory. Among them line efficiency, man to machine ratio and lost time percentage are mainly considered in this study. These are the status of utilization of machine and manpower in factory.

The layout of the garment making section, the flow of the workpiece is in-line layout, and some of the processes are in a cell arrangement. To balance the workloads in the production line, at the junction of the process flow of the two parts of the workpiece should also be balanced, so that work-in-progress (WIP) in the line will be eliminated.

Garment standard allowed minute (SAM) is defined as the total time which a garment should be produced in the production line at standard performance. The basic time is calculated by multiplying the cycle time with the performance rating of the operator. The performance rating of the operator depends on the operator's movement and workspeed. It is between 70% to 100% depending on the work-environment status, and the skill of the operator. Bundle allowance is ranged up to 10%, and the machine and personal allowances is up to 20% of the basic time [4].

Basic Time = Observed Cycle Time × Performance Rating

SAM = Basic time + Bundle allowances + Machine and personal allowances.

The input into the line is the total manpower-minutes in an hour, the output of the line is time value of the available garment output.

$$total\ minute\ input\ to\ the\ line = number\ of\ operators\ \times 60$$

$$total\ minute\ produced = line\ output\ \times garment\ SAM$$

The efficiency of the line is:

$$Line\ Efficiency = \frac{Line\ Output \times Garment\ SAM}{Number\ of\ Operators\ \times 60} \times 100$$

Man to machine ratio is defined as number of total manpower per sewing machine utilized in the line.

$$man\ to\ machine\ ratio = \frac{\text{total manpower}}{\text{total number of utilized machines}}$$

The lost time is non-productive time. The lose time occurs due to line setting, no feeding, machine breakdown and power cut. It can affect on the efficiency of the factory. The lost time percentage is used to determine to control and improve machine and operator utilization [4].

$$lost\ time\ percentage = \frac{\text{total time lost in a day}}{\text{daily working hour } \times \text{ number of operators}} \times 100$$

2.1 *The production of the Factory One*

The product making in the Factory One was the lady-wear trouser with 2 back pockets and front zipping. The 41 workers were in the production line, and there were two quality inspectors. Among 41 workers, five were helpers. Among the helpers, four were trimming the residual threads in the garment, one was opening the pocket holes and matching the back-part and front-part for assembling. Three were ironing. Some operators handled two machines, and some operators had same operations. Two piping machines, three numbers of 5-thread over-locking machines, three numbers of 3-thread over-locking machines and one interlocking machine for bottom hem were used in the line. Two special machines for hook and clip attachment were used. Twenty-five numbers of single needle machines were used. Total number of sewing machines used in the line was 36 and man-to-machine ratio was 1.083. Total takt time was 42.445 minute observed. Performance rating was 90 per cent and the allowance factor was taken as 0.05 for standard minute value for each operation. The standard minute value was 40.11 minute. The available output capacity was 38 units/hour determined by the minimum capacity of the line. There were 4 serial lines making garment and there were cell groups of processing for parts, front-side making, back-side making, assembling front- and back-parts, making belt and belt-loop, attaching belt and belt-loop, total 46 break-down operations. The theoretical efficiency was 59.2%. The total minute loss by the all operators was 1053.2 minutes in one hour, and the maximum was 64.8 minutes. The average minute loss for each operator was 24.49 minutes in every hour.

The style of product was changed before 20 days of data record. The line has frequently changed for style, the previous style was blouse and the style for this case study was lady trouser. The operators were in just learning period for the operations.

The frequently changing style takes time for layout change. It is also one type of waste time. Totally change style, for example from trouser to blouse, is more taking time to setting layout and taking long training time, it is difficult for assigning job for operator.

2.2 *The production of the Factory Two*

The garment producing in the Factory Two was the combat pant. 59-manpower were in the production line. There were 14 helpers for marking on garment, trimming the residual threads. Two were ironing. Total 53 machines were in the line. Single needle machines were 40, two-needle sewing machine 3 number, one cutter machine, one snapping machine, one overlocking machine, two number of 3-thread overlocking machine, one interlocking machine, one piping machine, one button-hole making machine, two bar-tacking machines. Man-to-machine ratio was 1.113. Total takt time was 34.53 minute observed. Performance rating was 60% and the allowance factor was taken as 0.05 for standard minute value for each operation. The standard minute value was 36.25 minute. The available output capacity was 42 units. The total minute loss by the all operators was 1331.7 minutes, and the average minute loss for each operator was 23.78 minutes in one hour. The minute loss due to waiting time for starving, the maximum was occurred 106 minutes at attaching flap to knee, 2 operators were doing same operation, the individual minute lost was 53 minutes each in one hour. The theoretical efficiency of the line was 44.79 per cent.

The garment has been producing for a long and the operators have settled for the operations. The product has been produced for 48 days continuously. This style is frequently ordered and made in this production line. The operators have qualified skill for this garment style.

2.3 Making analysis on two factories

By comparing two factories, both of the factories have nearly the same of man to machine ratio. The average operation time for operator was 59.22 sec and 61.66 sec respectively. The theoretical efficiencies were 59.2% and 44.79%. The average minute losses were 24.49 minute and 23.78 minute in one hour. The effective allowance for two factories were taken as 94.5% and 63.6%. Performance rating of the operator of the Factory Two was better than the Factory One.

If the line is not properly break-down the work-load, there will be imbalance occurred, the number of work-in-progress in the line will be high. The waiting time at stations will be longer. In Fig. 3, the Front Side Pieces were waiting for the Back-Side pieces at the ironing station. The Front Side Making took 7.78 minutes and the Back Side Making took 8.93 minutes. In the Front Side Making, the cell capacity was 51 units/ hour but in the Back Side Making cell, the capacity was only 38 units/ hour. Therefore, in every hour 13 unit of Front Side were waiting for assembly. It needed to level out the workload on Front Side Making and Back Side Making. The actual productivity of the Factory One is 37 units/hour at 12:15 to 13:15 on 30th April, 2018.

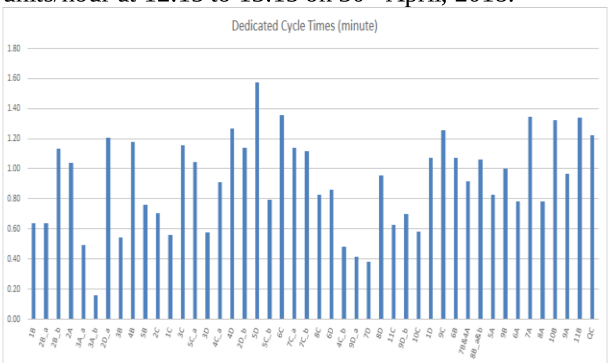

Figure 1 The Imbalance Sheet of Production Line for Factory One

The actual production of the Factory Two was 30 units in 40 minutes. The hourly production rate was 41.38 units. The actual efficiency of the line was 44.65 per cent.

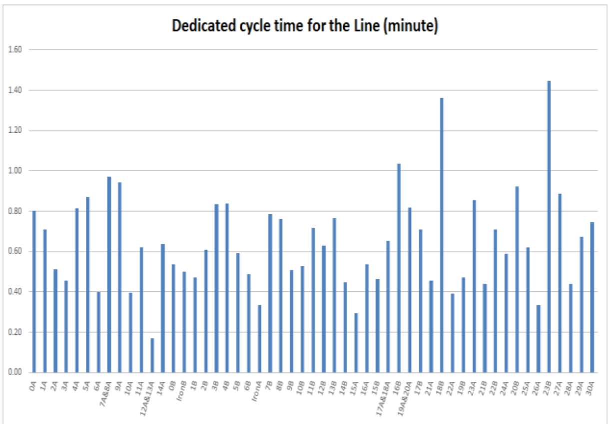

Figure 2 The Imbalance Sheet of Production Line for Factory Two

3. RESULTS AND DISCUSSION

To apply lean method to eliminate the waste, another factory was studied. The Factory Three is situated in Hlaing Tharyar Township. The product produced in the line was jacket with hood. After studying the imbalance of workloads, the bottlenecks stations were determined. Three-most-bottlenecks were studied for improvement. New ideas for better operation removing non-value-added activities were developed and applied at bottleneck-stations.

The line was running with cycle time about 110 sec with 30 units/hour productivity running with 39 operators. The SMV for the jacket was 47.67 min and the efficiency was 61% with total time loss 905.4 min in one hour. One of the stations was taking cycle time 140 seconds. The station was sewing without T-guide, that's why the operator had to take care the sewing line and it took time with extra bursts. The consultant made a T-guide for better operation and the cycle time reduced to 50 sec. The three operations were levelling out the workload, so that the cycle times were balanced, the line output was increased to 33 units/hour, SMV reduced to 47 min. The efficiency was increased to 65% and total time loss was reduced to 812.4 min in one hour.

Eliminating the waste is the basic idea of the Lean approach. Workload balancing, and training were the keys for the better efficiency and productivity.

4. CONCLUSIONS

Lean is the technology that eliminates the non-value-added activities. Non-value-added activities are caused by improper line-layout, waiting time as starving the jobs due to imbalance of the workload sharing, doing with non-standard operation procedure.

Two factories were observed and studied for productivity and efficiency. The frequently changing the style of garment also can effect on productivity of the line due to unstable of job assigned for operator.

One factory has applied the lean approach to improve the productivity and efficiency of line.

ACKNOWLEDGEMENT

The author wishes to express her sincere and gratitude to expert team of the MYPOD project from Aalborg University, Denmark, and the Pro-Rector Dr. Khin Than Yu for the guiding and for their valuable support. The author is thankful to the team members of the Yangon Technological University.

REFERENCES

[1] *https://www.myanmar-migration-nexus.org/en/projects/aung-myin-hmu-project-industry-solutions-safe-employment*

[2] *https://www.fibre2fashion.com/news/apparel-news/danish-project-for-myanmar-s-garment-sector-welfare-229544-newsdetails.htm*

[3] https://clothingindustry.blogspot.com/2017/11/calculate-sam-garment-industry.html

[4] Prasanta Sarkar, *Garment maker's key performance indicators, Why to measure and how to measure*, 2016.

Development of Gasification and Catalyst Technologies to Convert Biomass Resources into Liquid Fuel, a Report for Gasification Performance.

Kanit Wattanavichien[1,*] Tharapong Vitidsant[2]

[1)] Department of Mechanical Engineering, Faculty of Engineering, Chulalongkorn University, Phayathai Rd., Patumwan, Bangkok, 10330, Thailand
[2)] Department of Chemical Technology, Faculty of Science, Chulalongkorn University, Phayathai Rd., Patumwan, Bangkok, 10330, Thailand

[*]Corresponding e-mail: kwattana@gmail.com

ABSTRACT – The Project for Comprehensive Conversion of Biomass and Waste to Super Clean Fuels by new Solid Catalysts aims to create renewable energy resources as an alternative to fossil fuels by developing gasification technologies to obtain gas from such agricultural residues and catalyst technologies to convert the gas to liquid fuel. The main task of the project is to develop synthesis gas production system using non-edible biomass waste resources in order to get stable and reliable synthesis gas production. The scopes of development are 1) Biomass gasifier, 2) Tar reformer and synthesis gas purification unit, and 3) High pressure buffer unit of synthesis gas. This paper shows successful performance of gasification, with continuous operation. The unit can deliver gas flow rate of 6.0 Nm^3 /h with $[H_2]$ / [CO]: approx. 1.83 and $[H_2]$ + [CO]: approx. 93.4%

Keywords: Biomass to liquid; gasification; synthetic fuels

1. INTRODUCTION

In a tropical agricultural country, large amounts of agricultural residues including those from processing of agricultural products are being wasted. The Project for Comprehensive Conversion of Biomass and Waste to Super Clean Fuels by new Solid Catalyst under support from JICA-JST grant aims to create renewable energy resources as an alternative to fossil fuels by developing gasification technologies to obtain synthetic gas from such agricultural residues and catalyst technologies to convert the synthetic gas to liquid fuels. Alternative fuels to fossil fuels and chemical products from abundant biomass resources will be produced in Thailand. The obtained biofuels will serve to improve Thailand's energy self-sufficiency ratio, promote agriculture and rural communities, and conserve the environment of Thailand. In the future, it will also contribute to the development of fuel production from biomass that does not compete with the food supply and prevent global warming by the use of alternative fuels to fossil fuels in all tropical agricultural country. This activities will not only develop technologies for characterization of resources, conversion to synthetic gas suitable for catalytic reaction, and catalytic conversion of gas to diesel, gasoline, LPG or methanol, but will also build a platform for the social implementation of these technologies through verification of product utilization characteristics as well as human resource development.

2. BIOMASS GASIFICATION AND BUFFER PROCESS

The main earlier task of the project is to develop synthesis gas production technology from non-edible biomass waste resources, eucalyptus, rubber tree, cassava root, and corn corp, in order to get stable and reliable synthesis gas and biofuel production. The scopes of development are 1) Biomass gasifier, 2) Tar reformer and synthesis gas purification unit, and 3) High pressure buffer unit of synthesis gas.

The target condition of synthesis gas is expected as follows:

- flow rate 6.0 Nm^3 /h
- $[H_2]$ / [CO]: approx. 2
- $[H_2]$ + [CO]: approx. 80%

The gasifier will be operated about ten (10) days to produce gas for the FT/MT reactor.

The details of the process are shown in Figure 1.

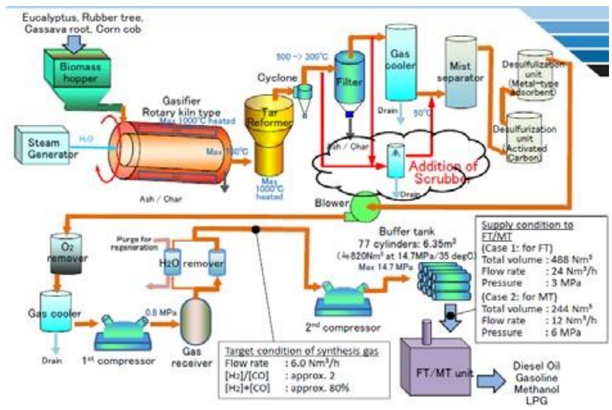

Figure 1 Gasification process illustration

This paper shows commissioning results to check the performance of gasification bench facilities. Objectives are to operate the gasification facilities from gasifier to gas purification unit for 8 hours, and to confirm the planned performance at Saraburi campus in Thailand.

3. SYNTHETIC FUELS PRODUCTION

In this project, different methods to produce each fuel will be used as follows:

a) Biodiesel: The new FT catalyst, which is called as "bimodal catalyst", has an excellent reaction with solid catalysis and will be used in order to get the high-speed compressing of the conversion of biomass into

diesel. It expects the biodiesel will be produced from rubber wood.
b) Bio-gasoline: The new designed capsule catalyst with the combination of FT reaction will produce the premium bio-gasoline. This method will directly convert the bio-synthesis gas to bio-gasoline.
c) Bio-methanol: A new low-temperature methanol synthesis method will be applied.
d) Bio-LPG: A hybrid catalyst combining methanol synthesis catalyst and zeolite catalyst will be applied.

The overall goal of social implementation is that the technologies for alternatives to fossil fuel are utilized for creating as bases to industrialization.

4. RESULTS OF GASIFICATION PERFORMANCE TEST

The synthesis gas production from non-edible biomass waste resources, rubber tree pellet, with new developed gasification unit was first time operated in Thailand at the Center of Fuel and Energy from Biomass, Chulalongkorn Univeristy, Saraburi Research Campus. It can produce stable and reliable synthesis gas. The performance of gasification, with continuous operation for period of 5 days, was evaluated. Approximately more than 20 hours/day operation of gasification bench facilities was successfully verified. However some un-continuous operation was achieved because of the deposition of light tar in the process caused by rubber tree pellet that need to do some maintenance. During the operation, a certain and minimum flow of N_2 is introduced into the gasifier due to equipment protection and the safety reason.

Table 1 Analytical data of Gasification's Performance and Product synthetic gas

No.	1	2	3	4	5	6	7	8	Ave.
Sampling time	12:00	13:00	14:00	15:00	16:00	17:00	18:00	19:00	
Biomass (kg/hr)	2.25	2.25	2.25	2.25	2.25	2.25	2.25	2.25	2.25
Steam (kg/hr)	0.7	0.7	0.7	0.7	0.7	0.7	0.7	0.7	0.7
H2/CO	1.72	1.62	1.68	1.64	1.68	1.73	1.78	1.83	1.83
Biomass/Steam	3.21	3.21	3.21	3.21	3.21	3.21	3.21	3.21	3.21
H2 (dry%)	58.38	57.74	58.22	57.64	58.10	58.68	59.33	60.03	58.51
O2 (dry%)	0.0	0.0	0.0	0.0	0.0	0.0	0.0	0.0	0.0
N2 (dry%)	0.44	0.41	0.4	0.41	0.40	0.39	0.38	0.38	0.40
CH4 (dry%)	7.19	6.92	6.82	6.84	7.00	6.99	6.90	6.83	6.94
CO (dry%)	33.99	34.93	34.56	35.11	34.49	39.95	33.37	32.74	34.89
H2+CO	92.37	92.67	92.78	92.75	92.59	98.63	92.70	92.77	93.40

5. CONCLUSIONS

The Biomass gasification and buffer process can achieve its target conditions of synthesis gas as follows:

- flow rate 6.0 Nm3 /h
- [H2] / [CO]: approx. 1.83
- [H2] + [CO]: approx. 93.4%

The gasifier had been operated about ten (10) days to produce gas of 77 cylinders for the FT/MT reactor.

ACKNOWLEDGEMENT

The financial support from JICA-JST must be acknowledged here.

REFERENCES

Journal articles

[1] Reubroycharoen, P., Yoneyama, Y., Vitidsant, T., and Tsubaki, N. "Catalytically Active Supercritical Fluid to Accelerate Methanol Synthesis", Fuel 82, 2003, 2255- 2257.

[2] Reubroycheroen P., Vitidsant, T., Yoneyama Y., and Tsubaki N. "Development of a new low-temperature methanol synthesis process", Catalysis Today 89, 2004, 447- 454.

[3] Reubroycharoen, P., Yamagami, T., Yoneyama, Y. Ito, M., Vitidsant, T. and N. Tsubaki, N., "A new low-temperature methanol synthesis process from low-grade syngas" Studies in Surface Science and Catalysis, 147, 2004, 409- 414.

[4] Reubroycharoen, P., Vitidsant, T., Asami, K., Yoneyama, Y., and Tsubaki, N. "Accelerated Methanol Synthesis in Catalytically Active Supercritical Fluid" Catalysis communication, 4, 2003, 461-464. history: operational performance". Ocean. Eng. 83, pp. 111–124, 2014.

[5] Thongkam, M., Yang, G., Vitidsant, T., and Tsubaki, N., "Novel Three-component Zeolite Capsule Catalyst for Direct Synthesis of Isoparaffin" Journal of the Japan Petroleum institute, 52(4), 2009, 216-217.

[6] Yang, G., He, J., Zhang, Y., Yoneyama, Y., Tan, Y., Han, Y., Vitidsant, T., and Tsubaki, N. "Design and Modification of Zeolite Capsule Catalyst, A Confined Reaction Field, and its Application in One-Step Isoparaffin Synthesis from Syngas" Energy & Fuels; 22(3), 2008.

Mirror-Like Surface of the Workpiece by Using Diamond and Polymer Slurry as a Polishing Agent

Valerio de Sousa GAMA[1], Ikuo TANABE[1*], Estevão Daniel SOARES[2]

[1,2)] Department of Mechanical Engineering, Faculty of Engineering, Science and Technology, Universidade Nasional Timor Lorosa'e,
Avenida Hera, Cristo Rei, Dili-Timor Leste
[1*)] Professor, Mechanical engineering, Nagaoka University of Technology,
1603-1, Kamitomioka-machi, Nagaoka-city, Niigata prefecture, 940-2188 JAPAN

e-mail: valerio.gama@untl.edu.tl

ABSTRACT - Nowadays, the improvement of product with high quality and high accuracy such as mirror-like surface is needed. Several machines with linear motor were developed in case of high speed, high acceleration and constant behavior of feed in each machine in order for mirror-like surface product necessity. But those methods are not enough yet, because of the highly cost of equipment and high production system. Therefore, in this paper, the use lapping slurry of diamond and polymer polyethylene oxide (PEO_{-8}) as a polishing agent is investigated and evaluated. In this system, the linear motor driver such as shaving device was applied to NC milling machine and used for the polishing system is developed and evaluated. Polypropylene (PP) was used for the polishing head. The optimum polishing conditions were investigated in several experiments and several methods. As a result, mirror-like surface can be obtained easily with a lower costly.

Keywords: Polymer, slurry, mirror-like surface, linear motor

1. INTRODUCTION

Nowadays, the increasing of machine tools using linear motor is important and needed, due to the rapid feed, high fast acceleration or deceleration characteristic and low vibration drive [1-2]. The use of those machines in order to speed up the polishing processes for fine parts of productivity. Therefore, the production with high quality and high accuracy of productivity is obtained easily, but the highly cost for this production system is needed. On the other hand, the capable of NC milling machine can be used for producing mirror-like surface with a lower costly and simple production system by utilizing the effectiveness of the polishing agent is mostly required.

Therefore, in this research, the use polishing agent is more effective for producing product such as mirror-like surface easily and with the lower costly. In this method, high speed polishing system using miniature motor drive for polishing mirror-like surface in micro parts is developed and evaluated. The shaving machine was developed for applying to NC milling machine. The saving machine is suitable for polishing micro parts because of low amplitude (1μm). In this process, polypropylene (PP) was used such as polishing head because of gripping force. The diamond and polymer Polyethylene oxide (PEO_{-8}) were used for the polishing agent, in order to maintain the diamond distribution uniform. Finally, mirror-like surface is obtained easily by using automatic polishing system and manually polishing system. The effectiveness of this system was evaluated by several experiments.

2. METHODOLOGY

Producing product with high quality and high accuracy were used diamond and polymer for lapping slurry is investigated and evaluated. The effectiveness of lapping slurry was proved by automatics and manual polishing system. Automatic polishing system was used compact linear motor is applied to machine tools, and manually polishing system was used hand finger polishing. Both methods were produced mirror-like surface in different polishing time.

The automatic polishing system was used compact linear motor for high speed polishing micro part is Panasonic's ES-LV 5B [3], the use of this linear motor because of overall part is compact, lightweight, low price, available in everywhere and easily apply to any conventional milling machine and use according to the their necessity special for polishing. Therefore, the conventional machine also could be used for producing mirror-like surface.

Table 1 shows the characteristic of this compact linear motor and also the other linear motor [4-9]. The frequency of the shaver was 0.233 kHz and the frequency of the ultrasonic motor were 28 kHz - 60 kHz. On the other hand, the amplitude of shaver was 1000μm and bigger than amplitude of ultrasonic motor

Table 1 Characteristic of compact linear motor and others linear motor

Specification				
		Frequency kHz	Amplitude μm	Average speed mm/min
Shaver[1)]		0.233	1000	28000
Ultrasonic motor	I[2)]	35	2	8400
	II[3)]	60	2	1440
	III[4)]	38.4	4	18426
	IV[5)]	28	7.5	25200
	V[6)]	60	1	7200
	VI[7)]	39	1	4704

[1)];[3], [2)];[4], [3)];[5], [4)];[6], [5)];[7], [6)];[8], [7)];[9], is around 1µm - 7.5µm. So, the average speed is 28000 mm/min, is higher than the speed of ultrasonic motor is around 4740 mm/min - 25200 mm/min. Because of high speed driving characteristic, therefore this compact motor drive was appropriate for polishing system and the precision was measured and evaluated.

Schematic view of the experiment setup is shown in Fig.1. The high speed camera is 10.25 µm and frame rate 1000 fps was used for measuring the accuracy of linear motor. The accuracy were measured in X-axis is the vibration direction, Y-axis is the depth direction and Z-axis is the vibration in the vertical direction. In the X-direction, the position at both ends of the stroke was plotted. The positioning accuracy of linear motor strokes at both ends was 24µm to the right and 22µm to the left side. This result shows that it reciprocates with accuracy within the range of ± 24µm for a stroke of 1.317 mm. In the Y-axis direction, in the range of the stroke (1.317 mm) of the compact linear motor, the maximum variation in the Y-axis direction was 30.75µm. In the Z-axis direction was the amount of fluctuation from the position where the linear motor first took place at a certain time that is shown. In the range of the stroke (1.317 mm) of the compact linear motor, the variation amount was 41µm. These are important factors affecting the dimensional accuracy and the shape accuracy as well as important for precisely limiting the polishing portion of the fine parts. The variation of the Z-axis direction of compact linear motor was affected to the processing pressure. The experimental setup measured in the previous Y-axis direction variation and the positioning accuracy (X-axis direction) at both ends of the stroke was used. As the polishing terminal and the workpiece are not contacted via the lapping agent, this straightness does not directly transfer the workpiece, but the variation in the Z-axis direction of the polishing terminal affects the magnitude of the polishing pressure, which in turn affects the incision into the workpiece of abrasive grains in the lapping agent.

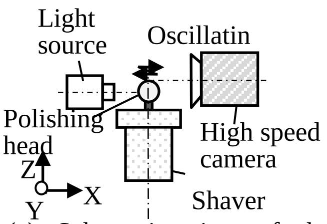

(a) Schematic view of the experimental setup

(b) Photograph of experimental the setup

Figure1 schematic view and photograph for accuracy measurement of compact linear motor

The four control factor used in the experimental design method and their levels is shown in Table 2. The lapping agents are mixed of diamond, tap water and PEO_{-8}. Based on past experimental results[10] the PEO_{-8} concentration as the weight ratio of PEO_{-8} to tap water was set to 0.25 wt%, 0.5 wt%, 1 wt%, 2 wt%, 3 wt% and 4 wt%. The diamond concentration as the weight

Table 2 Parameters used in the orthogonal table to obtain the optimum polishing

Control factors	Levels					
	1	2	3	4	5	6
PEO ratio wt%	0.25	0.5	1	2	3	4
Diamond ratio wt%	1	2	4			
Polishing pressure MPa	5	10	20			
Feed speed mm/min	200	700	1500			

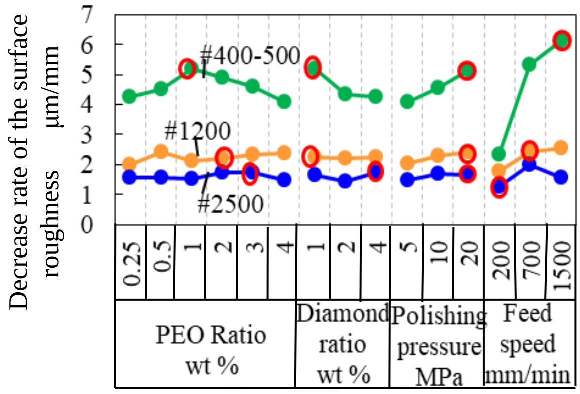

(a) Decrease rate of surface roughness

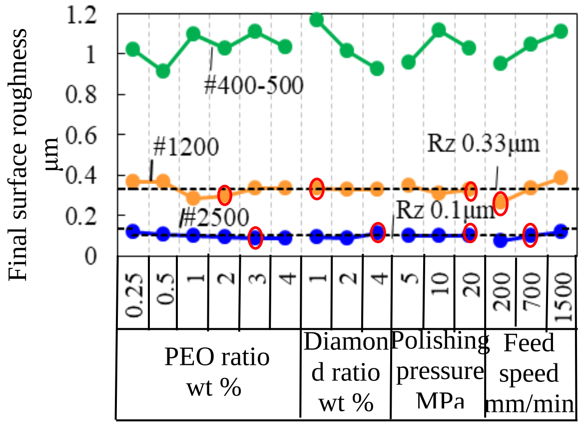

(b) Surface roughness observed under the orthogonal array multiple polishing condition

Figure 2 Factor effect plot from the used orthogona array

Table 3 lapping slurry specification

Abrasive grain diameter	Levels			
	PEO ratio wt%	Diamond ratio wt%	Polishing pressure MPa	Feed speed mm/min
#400-500	1	1	20	1500
#1200	2	4	20	200
#2500	3	1	20	700

ratio of diamond to tap water was set to 1wt%, 2 wt% and 4 wt%. The polishing pressure was set to 5 MPa, 10 MPa and 20 MPa. The feed speed was set to 200 mm/min, 700 mm/min and 1500 mm/min as the processing condition are used for the automatic polishing system. In order to make the surface roughness of the workpiece reached a *Rz* 0.1 µm, the diamond grain size of #400-500, #1200, and #2500 are used. Based on past machining experiments [11] for each abrasive grain, the surface roughness of improvement rate and the critical surface roughness were examined to determine the optimum lapping agent and optimum machining conditions. From figure 2, it is selected for each diamond particle diameter such as a lapping agent condition and a processing condition that the surface roughness improving rate is as high as possible and the critical surface roughness is as small as possible. Processing was performed in the diamond particle grain size #400-500, #1200, #2500 and the others parameter such as feed speed, polishing pressure, diamond ratio and PEO_{-8} ratio for each diamond grain size is marked with the red circle. For diamond grain size # 400-500 and others were selected so that the surface roughness improving rate became faster considering productivity improvement as an initial stage of processing. For diamond grain size #1200 and others parameters, considering both the surface roughness improving speed and the critical surface roughness at the same time, the processing condition was set so that the critical surface roughness reached a value lower than Rz 0.33 µm and the surface roughness improving speed was maximized as much as possible. The last stage for critical surface roughness was less than Rz 0.1 µm, therefore the diamond grain size #2500 and others parameter were used in this process. It is summarizes, the selected processing conditions and compounding conditions of the lapping agent. In the subsequent processing, we decided to use the lapping agent shown in Table 3 for each diamond particle size that used.

The developed polishing system and the specifications of NC milling machine, polishing tool and lapping agent is shown in Fig.3 and Table 4. The polishing tool with the polishing head that attached to the shaving machine was mounted on the existing NC milling machine. Place the polishing container on the table of the NC milling machine, clamp the workpiece with the vice in the container, and place the workpiece fully immersed in the lapping agent. The linear motor drive is turned on, the workpiece is automatically machined by NC control by completely immersing the workpiece with a lapping agent, and it was designed to cope with a long time automatic lapping operation. By feeding, the workpiece and the polishing head intermittently by using the feed in the Z-axis direction of the NC milling machine, new diamond abrasive grains (cutting edge) can be taken in the polishing head. For this reason, each time when a new cutting edge is constructed, it became a process that allows dressing of the tool during processing. At the same time, chip removal is also performed, so the same working process similar dressing and cleaning in grinding can be performed during processing. The machining procedure for determine the optimum machine condition is shown in Fig.4.

The size was machined 3 mm^2. Three steps of polishing process. The first step was used lapping slurry of particle grain size #400-500, second step was #1200 and third step was #2500. In this research, since fine parts are subject to polishing, NC milling drive and linear motor drive are superimposed, for example, positioning work was performed with a NC milling cutter and high speed polishing was performed with a linear motor. However, when applying the pressure in the Z-direction, the used shaver fluctuates by 0.209 mm in the Y-axis direction due to the swinging mechanism, which affects the dimensional accuracy in the Y-axis direction

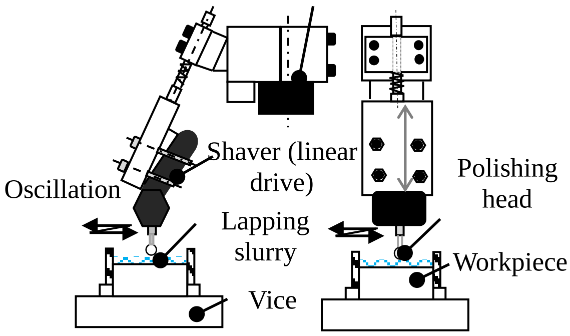

Figure 3 Schematic of view of experimental setup

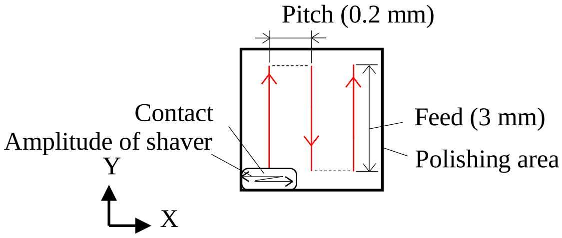

Figure 4 Machining procedure for determine optimum machine condition

Table 4 Experimental specification of NC milling machine, polishing tools and lapping slurry

NC milling machine	
Table working surface mm	550×160
Table movement stroke X-axis mm Y-axis mm Z-axis mm	 400 145 413
Spindle speed min^{-1}	0
Feed speed mm/min	200,700,1500
Polishing tool	
Area of polishing head	ϕ 4.8
Material of polishing head	Polypropylene
Frequency kHz	0.233
Average speed mm/min	28000
Lapping slurry	
Abrasive material	Diamond
Grain size #	400-500,1200,2500
PEO Ratio wt%	1,2, 3
Diamond ratio wt%	1, 4

For the manually polishing system, the lapping Slurry consisted of diamond grain size #2500, PEO ratio 3wt%, Diamond ratio 1wt% and Tap water. In this process, the lapping slurry was applied to the object of workpiece, and then hand finger as a polishing tools.

3. RESULTS AND DISCUSSION

The measurement result of the experiment is shown in Fig.5. Carbide V 10 was used for a workpiece material. The measuring instrument was Surftest SJ-210. Figure 5(a) shows the result of automatic polishing system, the surface roughness reached a *Rz* 0.1 µm with polishing time was 27 sec for square shape 3 mm^2. It`s about 1/2 processing time of automatic polishing when compared with the ultrasonic polishing machine (ex. amplitude 2µm, frequency 60 kHz [12]). Figure 5(b) shows the result of manually polishing, the surface roughness reached a *Rz* 0.1µm with polishing time was 360 sec. The polishing slurry of diamond particle grain size (#400-#500, #1200,#2500) and polymer PEO_{-8} is mostly reliable for polishing agent. The photograph surface roughness of the workpiece of automatic and manually polishing system are shown in Fig.6(a),(b).

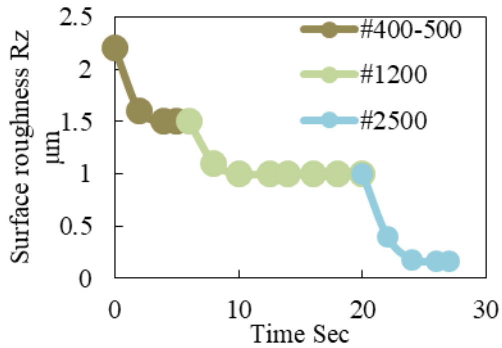

(a) Automatic polishing

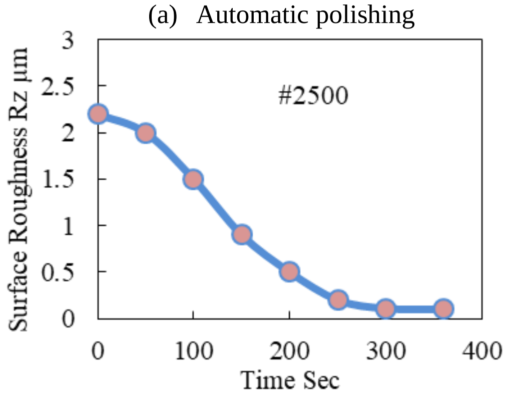

(b) Manual polishing

Figure 5 Relationship of polishing time and surface roughness

(a)Automatic polishing (b)Manually polishing

Figure 6 Photograph of surface roughness of the workpiece

4. CONCLUSIONS

The results of this study are summarized as follows: The NC milling machine could be used to produce the production with high quality and high accuracy with low costly and simple processing system. Polymer PEO_{-8} and diamond are used for the lapping slurry. High-speed polishing processing in the range of several mm was possible and Mirror-like surface processing with Rz 0.1µm or less was possible. The effectiveness of lapping slurry was proved by manually polishing as well.

5. ACKNOWLEDGEMENT

This research work has been supported by JICA CADEFEST project phase II in the Faculty of Engineering, Science and Technology, UNTL, Dili-Timor Leste.

6. REFERENCE

[1] Tsutomu M., Spread of machine tool driven linear motors, The Journal of the Institute of Electrical Engineers of Japan, Vol.121, No.9, pp.620-623, 2001.

[2] Karita, M., High performance technology in linear motor, Journal of Japan Society for Precision Engineering,Vol.61, No.3, pp347-350, 1995.

[3] Panasonic, Men's shever specifications, available from <http://panasonic.jp/shaver/p-db/ES-LV52_spec.html> (accessed on 12 October, 2016)

[4] Suzuki, K.,Uematsu, T., Iwai, M. and Makizaki, T., Ultrasonic grinding utilizing a stator of an ultrasonic motor, The Japan Society of Mechanical Engineers, Manufacturing & Machine Tool Conference,Vol.2 ,pp.183-184, 2000.

[5] Hara, K.,Isobe, H.,Kyusojin, A. and Okada, M., Ultrasonically assisted grinding of die steel using diamond electroplated tools, The Japan Society for Abrasive Technology,Vol.52,No.1, pp.46-51, 2008

[6] Suzuki, N., Yan, Z.,Haritani, M., Yang, J., Hamada, S., Hino, R. and Shamoto, E., Ultraprecision machining of tungsten alloy by applying ultrasonic elliptical vibration cutting, The Japan Society for Precision Engineering, Vol.73, No.3, pp.360-366, 2007

[7] Soutome, T. and Sato, K., Study on superposition superfinishing (4th report, Smoothing of surface roughness by superposition vibration cutting),Transactions of Japan Society of Mechanical Engineers,Vol.76,No.767, pp.1850-1858, 2010

[8] Suzuki, K.,Uematsu, T. and Makizaki, T.,Ultrasonic grinding development of the ultrasonic ellipse vibration grinding stone, Ultrasonic Tehnology, Vol.11,No.7, pp.36-40, 1999

[9] Yamamoto, T., Torii, A., Ueda, A. and Hane, K., Vibration measurement of an ultrasonic motor using stroboscopic phase-shift interferometry, Bulletin of Aichi Institute of Technology Part B, No.36,pp.9-14, 2001

[10] Iyama, T., Tanabe, I. and Takahashi, T., Optimization of lapping slurry in automatic lapping system for dies with cemented carbide and its evaluation, Transactions of the Japan Society of Mechanical Engineers Series C, Vol.75, No.749, pp.210-215, 2009

[11] Iyama, T. and Tanabe, I.,Mirror-Like finishing of soft materials using a polishing tool with controllable hardness by heat softening,Transactions of the Japan Society of Mechanical Engineers Series C, Vol.77, No.775, pp.1154-1160, 2011

[12] Hara, K.,Isobe, H.,Kyusojin, A. and Okada, M., Ultrasonically assisted grinding of die steel using diamond electroplated tools, The Japan Society for Abrasive Technology,Vol.52,No.1, pp.46-51, 2008

Analysis of Machine Availability at Surface-mount Technology (SMT) Line Using WITNESS Simulation

Kam Sheng Mak and Hasnida Ab-Samat*

School of Mechanical Engineering, Engineering Campus, Universiti Sains Malaysia (USM), 14300 Nibong Tebal, Seberang Perai Selatan, Pulau Pinang, Malaysia.

*Corresponding e-mail: hasnida@usm.my

ABSTRACT – In the competition to excel in Industrial 4.0 race, companies especially in Semiconductor Industry, strive to attain efficiency by removing process bottlenecks, improving productivity and increasing machine availability during operation. As so, this research was conducted to analysed the machine's availability based on various preventive maintenance (PM) scheduling. A model was developed in WITNESS 14 Manufacturing Performance Edition software to imitate the Surface-mount Technology (SMT) line in a manufacturing system. The model was build based on a serial layout of five machines which are screen printer, glue dispenser, chip shooter, pick and place and reflow oven. Then, the simulation was run to study the availability of each machine with relation to different stoppages intervals and duration based on the selected PM schedule. The findings of this project show that PM for a SMT line should be carried out every week with 30 minutes PM duration to achieve high machine availability and minimal machine downtime.

Keywords: Availability; Preventive Maintenance (PM); Surface-mount Technology (SMT); WITNESS; Simulation

1. INTRODUCTION

Exponential advances in technology have pushed companies to its limits in delivering innovative and quality products at the lowest cost possible. Therefore, one of the effective solutions is by minimising machine downtime in manufacturing operations, which provides a range of benefits like maximised efficiency and higher profits. Machine stoppages and downtime is a major factor that hinders the attainment of manufacturing efficiency [1]. It leads to the held-up of the manufacturing process and disrupts the workflow. The cost for the machine downtime is enormous when calculated based on the cost of labour rendered idle by the unavailability of the machinery. The company also needs to pay the overtime cost for maintenance personnel. In some cases, the company may be forced to delay its product shipments because of machine breakdown; hence, the surcharges will be applied for the lateness. The situation is critical and can be viewed as in Surface-mount technology (SMT) line which runs in series and continuous configuration.

SMT is an assembly process of complex circuitry fitting in small spaces. The process is used to mount electronic components on the surface of printed circuit boards [2]. The components need to be directly mounted onto the printed circuit board rather than wired or inserted through holes enabling more electronics components to be inserted into small spaces hence reducing devices size and weight. SMT produces Surface-mount Devices (SMDs) which are widely used in today's industry. In SMT line, five different machines are connected to each other by conveyors. Since the process of SMT is a continuous process, the whole production line will stop when one of the machine breakdown [3]. This will cause the other machines goes into an idle state. Therefore, reducing machine availability and affecting production output.

Since the production line must run smoothly without breakdown, proper maintenance is essential for today's production systems [4]. Machine downtime will affect the throughput in the production line. If machine is idle, then the products not being produced, this will certainly affect the business's bottom line. Minimizing downtime also affects a company's profits, making it crucial that the maintenance system was designed to reduce both maintenance and inventory-related costs [5]. Therefore, effective maintenance planning is one of the methods to achieve high productivity and breakdown prevention [1]. To keep the system in good condition and increase machine availability, maintenance management is an important policy in a repairable system [6].

Maintenance is practice in various techniques and strategies as reviewed by [3]. Maintenance recovers and improves equipment performance, and is an important part of a product life cycle [7]. From the information that get from the computer system, maintenance workers can do their own works effectively. For instance, the worker can prepare the spare parts that needed in the maintenance time. Thus, they can save a lot of time when doing maintenance. For this project, the scope of work focus on Preventive Maintenance (PM) scheduling as it is the most common and basic maintenance technique practiced in the industry.

PM is defined as regularly scheduled maintenance actions based on average failure rates. An optimize implemented preventive maintenance strategy can provide many benefits to an organization in terms of extending equipment life and machine availability. Properly scheduled PM can help to maintain the production system in top operating conditions in order to minimize operating costs [8]. According to [9] impact of PM on the service level of degrading manufacturing systems will affect the completion time and delivery dates of customer orders. In the majority of maintenance scheduling studies, the machines were assumed continuously available with perfect maintenance. However, the resources are subject to stoppages and downtime periods because of various planned resources such as PM duration and interval.

Meanwhile, in the age of Industry 4.0, simulation modelling is an important method of analysis, which can be used easily to verify, communicate and understood the real system. Simulation is the “imitation of the real world process or system overtime” which is sufficient enough demonstrate and illustrate the real industry using software with certain adequate accuracy [2]. Computer simulation is used in industry to conducting the experiments on a real system that is impossible or impractical. Many costs and times can be saved through the simulation. This is because the simulation is less expensive than building and testing hardware prototypes. According to simulation output, the production process can be verify by conducting the additional experiment [10].

Simulation can also be used to forecast the future behaviour of a system and investigate what can be done to influence that future behaviour. Therefore, necessary changes can be identified to improve the system. Other benefits of using simulation software are such as risk-free environment, save money and time, visualization, insight into dynamics, increased accuracy and handle uncertainty. The use of simulation to verify and validate process automation systems, perform software acceptance tests and train operators provides numerous benefits to companies in the manufacturing industries [11]. Analysis based on simulation can reduce the risk of unplanned machine breakdown where the researcher can plan and schedule operation based on the simulation analysis [7]. Hence, simulation enables the user to illustrate the condition to schedule and predict the maintenance system without interrupting the operation.

2. METHODOLOGY

In order to achieve the research objectives, a process flow of research methodology was developed as shown in Figure 1.

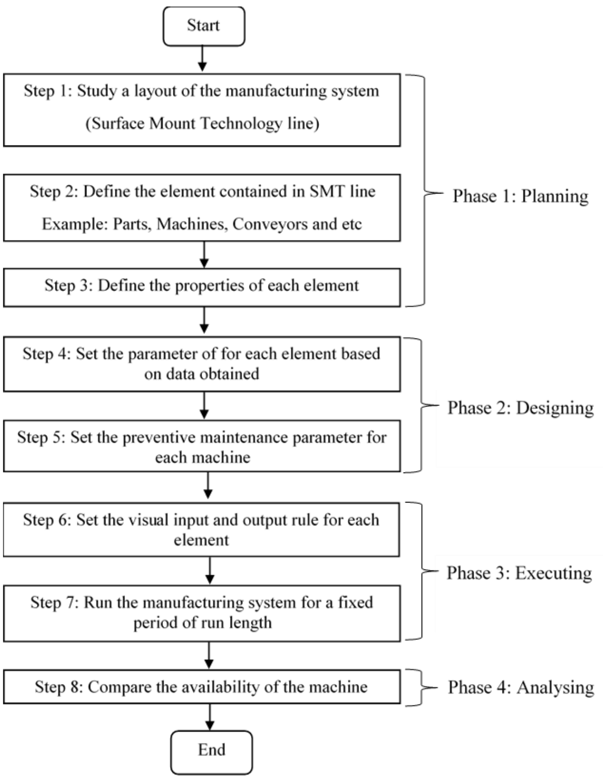

Figure 1 Steps in four phases of research methodology

This research was conducted in four phases with eight steps. Phase 1 focuses on studying and understanding PM scheduling and the SMT operation, and Phase 2 conducted to collects data like machine and maintenance parameters to design the model in WITNESS simulation. Then, Phase 3 involves imitating the operation with a few options in PM schedules. Simulation application is fundamental for enhancing production systems and reduction of bottleneck occurrences [4] and to achieve the result in term of production output, machine downtime and availability function. Finally, Phase 4 involves steps in analysing the results from the previous phase to achieve the research objectives.

The software package used to simulate the model was Witness Simulation Educational Version Release 14 (Build 2124) by Lanner group. Witness is a simulation tool for dynamic process simulation of manufacturing and business process in 2D or 3D models. The benefits of using Witness software enables users to develop a feature of model rapidly, analyse business environments to deliver improved process performance, optimized use of resources and conduct comprehensive experimentation, optimization & reporting framework. The software helps to decrease the risk with enabling model the work environment and simulate consequences of different decisions. User can propose the right solution for a company with displaying in virtual reality environment and information change with the present of the Witness simulation tool. Witness software also helps the user in predicting and solving problems related to production bottlenecks, overly idle resources [4].

The simulation of the model of this research is based on the SMT line which located in Business Unit Innovation Centre, School of Mechanical Engineering, Universiti Sains Malaysia. Table 1 shows the elements of the SMT line and Figure 2 shows the processes in the SMT line and layout of the model in witness software.

Table 1 Types of elements

Designer Element	Characteristics
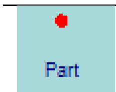	Part representing Printed Circuit Board (PCB) produced.
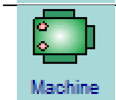	In this research, there are a total of five machines used in SMT line which is, Solder Paste Screen Printer, Glue Dispenser, Chip Shooter, and Place Machine and Reflow Oven.
	There are two types of labour: • The operator that in charge of the minor issues such as feeder problem. • Maintenance team that in charge when performing PM.
	Conveyors used to connect all the machines and to transfer the part between each machine and made the process continuous.

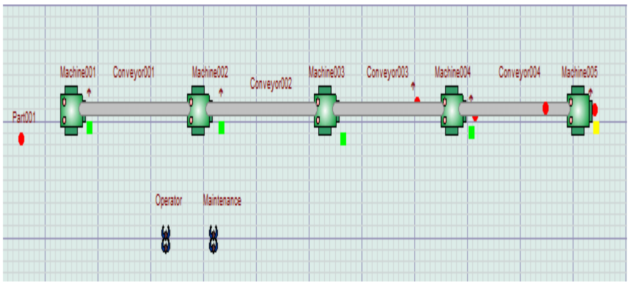

Figure 2 Layout of the model in Witness Software

The cycle time data were obtained from many sources such as machine manual and analogous manufacturing company and as shown in Table 2.

Table 2 Process Parameter for each Machine

Machine	Cycle time (min)
Machine 001- Screen Printer	0.25
Machine 002- Glue Dispenser	0.25
Machine 003- Chip Shooter	0.24
Machine 004- Pick and Place	0.23
Machine 005- Reflow Oven	1.61

It is crucial to have access to accurate and timely data to be able to understand the extent of downtime and its roots causes. There are two types of downtime: planned downtime and unplanned downtime. Planned downtime involves important stoppages like for setup, changeover, breaks, etc., but unplanned disruptions in the production can end up costing significant time and money [1]. The company needs to implement a regular maintenance schedule to prevent machine stoppages and breakdown. In demanding factories, regular maintenance will be easily neglected due to high production. To prevent this, PM scheduling must be a practise to personnel in the company. If a company want a delivery that has 24/7 availability, minimizing downtime as much as possible is necessary.

Availability is a metric that combines the concepts of reliability and maintainability. Availability deals with the duration of up-time for operations and is a measure of how often the system is alive and well. Hence, the run length in simulation for this research was set as three months (129600 minutes). In this project, there are few options used in the simulation which are 1 month 2 days PM, 2 weeks 1 day PM, 10 days half day PM, 1 week 30 minutes PM, twice a week 30 minutes PM and 1 day 15 minutes PM. Table 3 details the breakdown interval and PM duration set in this research.

Table 3 Breakdown Interval and PM duration

Breakdown Interval (min)	**PM duration (min)**
1 month (43200)	2 days (2880)
2 weeks (20160)	1 day (1440)
10 days (14400)	Half day (720)
1 week (10080)	30
Twice a week (5040)	30
1 day (1440)	15

The simulation method is used in this research to estimate a system availability and its associated measures. These include the number of failures and the number of expected maintenance needed. A simulation model of the system could be developed that emulates the random failures and repair times of the components in the system, thus researcher can analyse the suitable time and duration for effective maintenance in operation. In Witness simulation, Mean Time between Failure (MTBF) and Mean Time to Repair (MTTR) were used to set the maintenance parameter that represented the time between machine failure and repair time [12]. For example, a long breakdown needed for the machine that run for a very long duration. When the machine runs for a long time, the PM time will be higher since the tool wear is higher. Therefore, optimisation should be done to get the suitable PM time.

3. RESULTS AND DISCUSSION

The purpose of this research is to reduce machine stoppage and downtime. Thus, the results were based on machine downtime and machine availability. In theory, the availability of machine will decrease with the increase in machine stoppage. Figure 3 shows the operating time and various situation for the machines in the SMT line. Meanwhile, Figure 4 shows the percentage of total machine availability in relation to different PM frequencies and intervals as listed in Table 3 previously. The SMT line is continuous running form first machine to the last machine. Therefore, the availability of machine must be calculated from the first machine until the last machine.

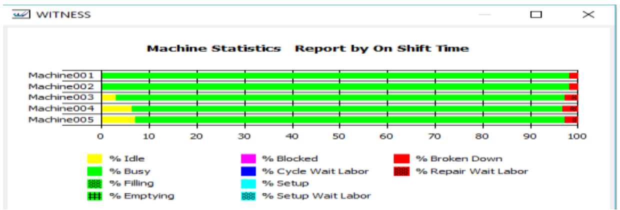

Figure 3 Statistics from Witness Simulation

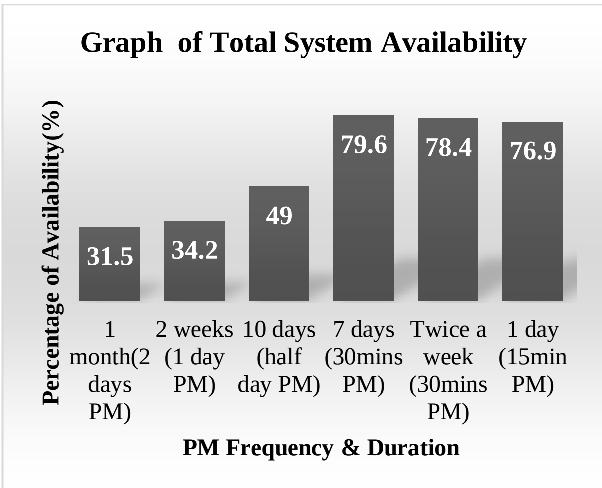

Figure 4 Total SMT line availability based on PM frequency and duration

Total system availability showed the highest percentage of availability is 79.6% that is every one week 30 minutes PM. The lowest percentage of availability is

31.5 % that is every one month 2 days PM. This is because when the machine didn't do the maintenance for a long period, a long time is needed for doing the maintenance. Production stops for two days will cause the machine to idle for a long time. The products that produce will low due to the long breakdown time. The availability is 34.2 % for every 2 weeks 1 day PM, 49% for every 10 days 12 hours PM, 78.4% for twice a week 30 minutes PM and every one day 15 minutes PM. In order to get the highest machine availability, optimisation of scheduling preventive maintenance must be carried out. A too frequency of preventive maintenance can also impact machine availability. From the simulation results, the optimal preventive maintenance is every one week 30 minutes PM due to the highest machine availability shown.

Initially the hypothesis for this research is that frequent PM activities will lower the machine's availability. However, results from simulation shows the opposite as PM reduce unplanned stoppages and downtime. Therefore, optimization of PM is very important for production line. The PM scheduling must be plan wisely to get the highest availability of machine. In comparison, the highest overall equipment efficiency that get from previous research is 95.10% by using the 10000 minutes breakdown interval and 135 minutes PM [7]. This also means that the availability using this approach should be the highest. However, the availability calculated from simulation is 74.06%, which is less than the optimum maintenance scheduling. There is availability difference of 5.54% compare to the optimum maintenance scheduling. Based on the simulation results, the availability from previous research have some difference due to the previous research is based on the wafer fab company. Different field of manufacturing system will have different PM scheduling. Thus, maintenance schedule for every field should be carry out in simulation before implement.

4. CONCLUSIONS

Machine breakdown and stoppage always happened in the industry if the maintenance schedule were not arranged properly. For most manufacturers, downtime is the single largest source of lost production time. Focusing improvements effort on the constraint ensures optimal use of the resources and is the most direct route to improved productivity and profitability. Therefore, companies need good maintenance systems to prevent machine breakdown and stoppage. This research project has brought the insight of the series SMT production line with the focus on various PM scheduling intervals and durations to increase machine availability. The critical issue with SMT line is a single machine breakdown automatically lead to whole production line halt and loss of operation. In summary, the most optimal scheduling has been carried out by using the simulation. A frequent PM not necessary is the lowest availability of this research. Every machine has a lifecycle, hence the maintenance must plan to make the machine long lasting. Based on the simulation, the results showed that every one week 30 minutes PM is the optimize maintenance schedules. The longest PM time has caused the machine availability to become the lowest since the machine did not perform maintenance for a long period.

ACKNOWLEDGEMENT

The authors would like to thanks Universiti Sains Malaysia for the grant (304.PMEKANIK.6315112) that resulting in the success of this project.

REFERENCES

[1] H. Ab-Samat, S. Kamaruddin, I.A. Azid, "Maintenance performance measurement: a review". Pertanika Journal of Science and Technology. 19(2), pp. 199-211, 2011.

[2] S.M. Tan, J.Q. Hwang, H. Ab-Samat, "WITNESS simulation of preventive and corrective maintenance for Surface Mounted Technology (SMT) line". IOP Conference Series: Materials Science and Engineering. 505(1), pp. 012047, 2019.

[3] E.I. Basri, I.H. Abdul Razak, H. Ab-Samat, S. Kamaruddin, "Preventive maintenance (PM) planning: a review". Journal of Quality in Maintenance Engineering. 23(2), pp.114-143. 2017.

[4] P.L. Markt, M.H. Mayer, "WITNESS simulation software". Proceedings of the 29th Conference on Winter Simulation – WSC. 97, 1997.

[5] R. Sarker, A. Haque, "Optimization of maintenance and spare provisioning policy using simulation". Applied Mathematical Modelling. 24(10), pp. 751-760, 2000.

[6] H. Xu & W. Hu, "Modelling and analysis of repairable systems with preventive maintenance". Applied Mathematics and Computation. 224, pp. 46-53, 2013.

[7] A. Charles, I. Floru, C. Azzaro-Pantel, L. Pibouleau, S. Domenech, "Optimization of preventive maintenance strategies in a multipurpose batch plant: Application to semiconductor manufacturing". Computers & Chemical Engineering. 27(4), pp. 449-467, 2003.

[8] G. Liao, "Optimum policy for a production system with major repair and preventive maintenance". Applied Mathematical Modelling. 36(11), pp. 5408-5417, 2012

[9] A. Angius, M. Colledani, L. Silipo, Yemane, A. "Impact of Preventive Maintenance on the Service Level of Multi-stage Manufacturing Systems with Degrading Machines" IFAC-PapersOnLine. 49(12), pp. 568-573, 2016.

[10] B. Bako, P. Božek, "Trends in Simulation and Planning of Manufacturing Companies". Procedia Engineering. 149, pp. 571-575, 2016.

[11] E.M. Frazzon, L.D. Silva, M.C. Pires, "Simulation-based performance evaluation of a concept for integrating intelligent maintenance systems and spare parts supply chains". IFAC-PapersOnLine. 49(12), pp. 1074-1079, 2016.

[12] A.K. Jain, "An Optimal Preventive Maintenance Strategy For Efficient Operation Of Boilers In Industry". International Institute for Science, Technology and Education. 2(4), pp. 1-3, 2012.

Mixed Integer Linear Programming for Permutation Flow Shop

Banhan Lila[1*], Jakrawarn Kunadilok[1*]

[1)] Department of Industrial, Faculty of Engineering, Burapha University,
169 Long-Had Bangsaen, T. Saensuk, A. Muang, Chonburi, Thailand

[*]Corresponding e-mail: blila@eng.buu.ac.th, jakrawarn@eng.buu.ac.th,

ABSTRACT – Scheduling is a mandatory decision for a manufacturing system that jobs need to be processed using the same set of work stations. This paper presents the new mixed integer linear programming (MILP) for scheduling a permutation flow shop that was specifically formulated to be solved using the OpenSolver with the Gurobi engine. The real data of the motorcycle assembly factory where a maximum of 41 jobs per day need to be processed by a 4 stages serial system was utilized to demonstrate the application of the MILP. The optimal solutions based on makespan were found within 5 minutes of the Excel based OpenSolver computation time for small problems. For larger problems, the MILP returned more respectable results compared with the NEH algorithm. Thus, it can be concluded that the MILP can be used to create schedules that yield minimum makespans conveniently with the help of an Excel based designed algorithm.

Keywords: scheduling; permutation flow shop problem (PFSP) problem; mixed integer programming; OpenSolver

1. INTRODUCTION

In a manufacturing system where jobs need to be processed using the same set of work stations or processors, sequences and scheduling of operations should be planned carefully to complete all jobs efficiently [13, 14 and 11]. Variety of indexes such as makespan, mean flow time, number of tardy jobs, for example, can be used to measure efficiency of the planned schedules [11,15]. Pinedo [14] confirmed that among the many parameters that are being optimized, the makespan optimization is the choice of a good number of researchers in recent years.

A processing system in which a sequence of each job is fully specified, and all jobs visit the work stations in the same order is known as a flow shop [2]. The flow shop processing systems are often found in practices of the production systems [3,5,10] with standardized processes. Other systems may include a flexible flow shop (FFS) [7,8], a job shop (JS) [6], and parallel processing systems [11, 13, 15], for example.

Number of techniques have been proposed to schedule jobs thru these systems. Soon Lee and Ying-Tai [8] provided extensive review of the FFS. They classified the FFS research into two categories based on system characteristics/constraints of the problem and performance of the scheduling techniques. Zhang et al. [6] also reviewed more than 100 papers that concern the JS problems. They classified the problems based on number of machines, supporting resources, plants and factory technology. Zhang et al. [6] suggested that different type of problems requires different algorithm and target measure to search for optimal schedule. Ramos and Tupia [2] found that the Differential Evolution (DE) is a stand out algorithm in generating generate better results regarding flow shop scheduling problems. Sawik [7] demonstrated that the mixed integer programming can be developed and applied to solve for an optimal scheduling of flexible flow shops but the commercially available software is needed.

Focusing on the permutation flow shop problem (PFSP), there is a vast literature mentioned the Johnson's algorithm, (Campbell, Dudek and Smith) algorithm, the NEH (Nawaz, Enscore and Ham) algorithm and other modifications algorithems [1, 4]. Johnson's algorithm gives the minimum makespan of a two work stations flow shops with n jobs [11,15]. CDS is the extension of Johnson's algorithm which selects the minimum makespan out of the (m-1) enumerations [9]. NEH selects the first two jobs, after arranging the jobs in the descending order of their total processing times, as the initial partial sequence and other jobs are inserted one by one from the third job to obtain a final optimal makespan and its corresponding sequence [9]. [1 and 4] reported that the NEH algorithm is regarded as one of the best available constructive heuristics.

However, creating a schedule for the PFSP using mathematical model, heuristics or algorithms need a programmer who possess sufficient knowledge about these algorithms to develop a logic program with appropriate program languages or a commercial software. The created program normally not easy to adapt in coping with any changes of problem environment. Additionally, results from such program may need to transform into a format that can be understood by practitioners. Moreover, practitioners are typically not familiar with the special type software that not widely available.

Fortunately, the spreadsheet based program like Excel is most certainly available with any standard computers and its computational power has drastically improved in recent years [9,12]. Most practitioners acquaint with how to use it, thus, it is highly possible to adjust any setting, that may require, to cope with changes. To alleviate the shortcomings of using special software's and complexity of heuristics for scheduling problems, this research presents the mixed integer linear programming (MILP). The model was specifically formulated to determine the optimal schedule of the PFSP using OpenSolver on Microsoft Excel. The problem considered by Sawetsutcharitkul [10] was used to test the model. Results were compared. Details are given in the next section.

2. PROBLEM AND METHODOLOGY

Problems MILP model was formulated for a general PFSP with n jobs that need to pass thru m stations, orderly as shown in figure 1.

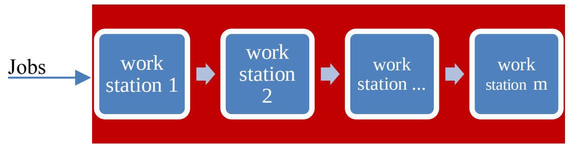

Figure 1. General Problem Scheme of PFSP

The flow shop shown in figure 1 is a typical scheme of the PFSP. The MILP model was developed to determine the optimal sequence of *n* jobs to be processed on *m* work stations in the same order. The PFSP requires the same job sequence on all the work stations with the constraint that a work station can only process one job at a time and a job can be processed by only one work station at a time. No workstation is allowed to remain idle when a job is ready for processing. Such problems are NP-Complete and hence optimal solutions are not guaranteed but the MILP, that was specifically formulated to be solved using the OpenSolver on Microsoft Excel, would yield optimal solutions for small problems and good working solutions for bigger problems within acceptable computation time.

MILP Formulation

The model was formulated to determine the minimum makespan for a PFSP with n jobs and m work stations defining decision based on operations sequence of jobs on all work stations to ease the setting of a spreadsheet model when it is solved. To clarify, the example of number of operations are demonstrate in table 1. Indexes, set, parameters and decision variables are defined as below.

Table 1 defining operations of jobs on work stations

		work stations				
		1	2	3	…	m
Job number in a sequence	1	1	2	3	…	m
	2	m+1	m+2	m+3	…	2m
	3	2m+1	2m+2	2m+3	…	3m
	…	…	…	…	…	…
	n-1	(n-2)m+1	(n-2)m+2	(n-2)m+3	…	(n-1)m
	n	(n-1)m+1	(n-1)m+2	(n-1)m+3	…	mn
	Set, S_k	S_1	S_2	S_3	…	S_m

From table 1, operations *i*, or *j* are defined based on the order each job is processed on the flow shop work stations corresponding to its place in a sequence. For example, if jobs 1 and 2 are placed the first and second, respectively, in a sequence, operations 1 to m are operations of job 1 on work stations 1 to m. The operation numberings continue for job 2 starting from m+1 to 2m, and so on. All operations performed on work stations 1, 2, 3,…,m are members of set S_1, S_2, S_3,…, S_m, respectively, will be referred to as set S_k.

Indexes and Set:

i,j : operations i or j ; i,j = 1,2,3,…mn

k: set of work station ; k = {1,2,3,…,m}

S_k: set of operations performed on work stations k

Parameters:

P_i or P_j : processing time for operation i or j

Decision Variables:

$$x_{ij} = \begin{cases} 1 \; if \; operation \; j \; is \; scheduled \; next \; to \; operation \; i \\ 0 \; otherwise \end{cases}$$

c_i or c_j = completion time of operations i or j

c_{max} = makespan

The MILP Model is expressed using Equations (1) to (11) as below.

Objective function:

$$Minimize \; z = c_{max} \tag{1}$$

Constraints:

$$\sum_{i \in S_1} x_{0i} = 1 \tag{2}$$

$$\sum_{\substack{j \in S_1 \,U\, \{mn+1\} \\ j \neq i}} x_{ij} = 1 \; ; i \in S_1 \tag{3}$$

$$\sum_{\substack{i \in S_1 \,U\, \{0\} \\ i \neq j}} x_{ij} = 1 \; ; \; j \in S_1 \tag{4}$$

$$x_{0j} - x_{0j+l} = 0 \quad ; j \in S_1 \text{ and } l \in k - \{m\} \tag{5}$$

$$x_{ij} - x_{i+l,j+l} = 0 \quad ; i,j \in S_1, \; i \neq j and \; l \in k - \{m\} \tag{6}$$

$$c_j - P_j + M(1 - x_{0j}) \geq 0 \; ; \; j \in S_1 \tag{7}$$

$$c_j - c_{j-1} - P_j \geq 0 \; j \in S_1' \tag{8}$$

$$c_j - c_i - P_j + M(1 - x_{ij}) \geq 0 \quad ; i,j \in S_1, S_2, S_3, \dots, S_m \text{ and } i \neq j \tag{9}$$

$$c_{max} - c_j \geq 0 \quad ; j \in S_m \tag{10}$$

$$c_{max} \text{ and } c_j \geq 0 \quad ; \text{real numbers} \tag{11}$$

The objective expressed in Equation (1) is the minimization of the makespan which defined as the maximum of c_j's. Equation (2) to (4) and (7) are for scheduling of operations on the 1st work station. Equation (2) ensures that only one operation, either 1, m+1, 2m+1,…,(n-1)m+1, can be chosen as the starting operation. Equation (3) forces that only one operation that represents the first operations of each job, except for the one that was placed as the first operation, will be scheduled next. Equation (4) makes certain that only one operation i can be scheduled preceded operations j. Equation (7) determines the completion time of the starting operation. Equations (5) and (6) deal with the 2nd to the (m-1)th operations. Equations (5) ensures that the starting operations at each work station, after the first one, must belong to the same job as the operation at the starting point and Equation (6) makes sure that operations are sequenced in the same pattern. Equation (8) ensures that each operation, besides the first operation of each job, cannot start before its preceding operation finished. Equation (9) forces that each operation cannot start before its preceding operation on the same work station finished. Equation (10) calculates makespan. The last one, Equation (11) defines c_{max} and c_j.

The MILP model was applied to a set of problems of the permutation flow shop as explained in the next section.

3. NUMERICAL EXAMPLE AND RESULTS

The problem represents the PFSP with a maximum of 41 jobs per day that must be processed by 4 serial work stations represented a packing process in a motorcycle factory. This problem was originally studied by Sawetsutcharitkul [10] and was exploited to demonstrate the application of the MILP. The add-in OpenSolver (Gurobi engine) to Microsoft Excel was utilized on a lap top computer with 16 GB of RAM.

A total of 22 problems was applied and grouped according to numbers of jobs as shown in table 2.

Table 2 Problems groups

Number of jobs	Number of problem	Problem name
9	5	A, B, C, D, E
12	4	F, G, H, I
22	5	J, K, L, M, N
28	3	O, P, Q
31	2	R, S
41	3	T, U, V

The problems that consist of 9 and 12 jobs are defined as small problems. The medium and large problems are the ones with 22, 28 and 31 jobs, and 41 jobs, respectively. The computation times are reported. Results in terms of makespan from the MILP were compared with that from the original NEH and are given in tables 3, 4 and 5. Running time allowed for Gurobi to find the solution was set at 300, 900 and 1200 seconds for small, medium and large problems, respectively.

Table 3 Results of small problems

Size	Name	# of jobs	MILP		NEH	Diff*** (%)
			CPU Time* (sec.)	Makespan (mins)	Makespan (mins)	
Small	A	9	0**	503	503	0.0
	B	9	0**	461	461	0.0
	C	9	0**	462	462	0.0
	D	9	0**	488	488	0.0
	E	9	0**	462	462	0.0
	F	12	1	409	409	0.0
	G	12	3	401	401	0.0
	H	12	30**	395	403	2.0
	I	12	2	387	387	0.0
Average			4.0	440.9	441.8	0.0

From table 3, the MILP found global optimal solutions for most problem with very short CPU time (0 seconds of CPU time indicates very fast), except problems F, G and I. For the medium and large problems, Gurobi could not find optimal solutions within the allowing run time but the MILP returned 4.4%, on average, shorter makespan than that of from NEH for the medium problems (table 4). There was no significant difference between the MILP and NEH for the large problems. However, with the limited number of large problems in this study, the MILP still be the better option as seen in problem V. Thus, more problems of large size may provide better comparison between the MILP and the NEH.

Table 4 Rsults of medium problems

Size	Name	# of jobs	MILP		NEH	Diff*** (%)
			CPU Time* (sec.)	Makespan (mins)	Makespan (mins)	
Medium	J	22	141	521	534	2.5
	K	22	337	498	516	3.6
	L	22	116	520	546	5.0
	M	22	105	520	529	1.7
	N	22	196	546	574	5.1
	O	28	14	475	482	1.5
	P	28	97	452	481	6.4
	Q	28	592	458	511	11.6
	R	31	798	539	561	4.1
	S	31	50	497	512	3.0
Average			244.6	502.6	524.6	4.4%

Table 5 Results of large problems

Size	Name	# of jobs	MILP		NEH	Diff*** (%)
			CPU Time* (sec.)	Makespan (mins)	Makespan (mins)	
Large	T	41	1037	589	589	0.0
	U	41	8	567	564	-0.5
	V	41	181	544	557	2.4
Average			408.7	566.7	570.0	0.0

Remarks:

* represents the time that Gurobi returned solutions

** indicates that Gurobi found optimal solution

*** Diff. = 100%* (NEH-MILP)/MILP

4. DISCUSSIONS

From the results of the examples, it can be confirmed that the NEH algorithm still be the powerful constructive heuristics since it is used to produce the same optimal results as the MILP for small PFSP in minimizing of makespan. Nevertheless, the MILP outperforms the NEH for Medium size problems. For the large size problems, the MILP tends to generate schedules with slightly shorter makespan than the NEH.

Comparison in this study relied on the 4 serial work stations examples of the PFSP. The number of variables and constraints of the MILP will exponentially increase for larger systems, in terms of a number of work stations. Subsequently, solving for respectable scheduling will take a longer time. The findings of this study, thus, do not promise the comparison results. Testing the performance of the MILP is suggested when the environment of problems changed.

5. CONCLUSIONS

The MILP for scheduling a permutation flow shop that was specifically formulated to be solved using the OpenSolver with the Gurobi engine. The real data of the motorcycle assembly factory with a maximum of 41 jobs per day was utilized to demonstrate the application of the MILP. The optimal solutions based on makespan were found within 300 seconds of the Excel-based OpenSolver computation time for small problems. For larger problems, the optimal solutions were unable to guarantee but the MILP still returned good working solutions. The MILP also yielded 4.4%, on average, shorter makespan for problems with 22-31 jobs compared to the results provided by Sawetsutcharitkul [10] in which the original NEH was applied. This study also found that the computation time to create optimal schedules was less than 30 seconds for the problems with up to 12 jobs which was relatively short. The computation time was between 8 seconds to 1037 seconds for problems with 22-41 jobs which was still acceptable in this application, even though the optimal solution could not be guaranteed. Therefore, it can be concluded that the MILP can be used to create schedules using the Excel-based OpenSolver and returns the results in such an understandable format for practitioners.

REFFERENCES

Journal articles

[1] A. Baskar, "Revisiting the NEH algorithm- the power of job insertion technique for optimizing the makespan in permutation flow shop scheduling". International Journal of Industrial Engineering Computations. 7, pp. 353–366, 2016.

[2] A. Ramos, M. Tupia, "A Systematic Review for Solving Flow Shop Scheduling Problem Using Differential Evolution Algorithm". International Journal of Applied Science and Technology. 3, pp. 64–74, 2013.

[3] B. Eksioglu, S. D. Eksioglu, P. Jain. "A Tabu Search Algorithm for the Flowshop Scheduling Problem with Changing Neighborhoods". Commputer & Industrial Engineering. 54, pp. 1-11, 2008.

[4] E. Singhal, S. Singh, A. Dayma, "An Improved Heuristic for Permutation Flow Shop Scheduling". International Journal of Computational Engineering Research. 2(6), pp. 95-100, 2012.

[5] J. Kamburowski. "On three-machine flow shop with random job processing times". European Journal of Operations Research., 125,pp. 440-449, 2000.

[6] J. Zhang, G. Ding, Y. Zou, S. Qin, J. Fu, "Review of job shop scheduling research and its new perspectives under Industry 4.0". Journal of Intelligent Manufacturing. 30, pp.1809-1830, 2019.

[7] T. Sawik, "Mixed Integer Programming for Scheduling Flexible Flow Lines with Limited Intermediate Buffers", Mathematical and Computer Modelling, 31, pp. 39-52, 2000.

[8] T. Soon Lee, L. Ying-Tai, "A review of scheduling problem and resolution methods in flexible flow shop'. International Journal of Industrial Engineering Computation, 10, pp. 67-88, 2019.

Conference papers

[9] A.J. Mason, OpenSolver – An Open Source Add-in to Solve Linear and Integer Programs in Excel, Operations Research Proceedings 2011, Springer Berlin Heidelberg: 401-406; 2012.

[10] A. Sawetsutcharitkul, Job Scheduling in a Packaging Process, Master Thesis of Industrial Engineering, Burapha University, 2012.

Books

[11] B. Lila, *Production Planning and Control*, Top Publishing, Bangkok, Thailand, 2010.

[12] C.T. Ragsdale, *Managerial Decision Modeling*, South-Western, Cengage Learning, .2011

[13] D.D. Bedworth, J.E. Bailey, *Integrated Production Control Systems*, John Wiley and Sons, p. 469, 1987.

[14] M.L. Pinnado, *Scheduling: Theory*, Springer Science & Business, 2012.

[15] P. Chutima, *Scheduling Techniques for Operations*, Chulalongkorn University Press, Bangkok, Thailand. 2012.

Analysis of Bus Passenger Head Injury using Finite Element Method

Satrio Wicaksono[1*], Wandi Prasetia[1], Sandro Mihradi[1], Andi Isra Mahyuddin[1], Arif Sugiharto[1]

[1)] Faculty of Mechanical and Aerospace Engineering, Institut Teknologi Bandung,
Jl. Ganesa 10, Bandung 40132, Indonesia

[*]Corresponding e-mail: satriowicaksono@ftmd.itb.ac.id

ABSTRACT – The number of bus especially in Indonesia keeps increasing every year, which was followed by the increase in the number of accidents involving buses. One of the most common and deadly accidents involving bus is frontal collisions. This collision can cause injury in the range of minor to death on passengers. One of the most common injuries in a frontal collision is a head injury. The severity of head injury can be evaluated from the Head Injury Criterion (HIC) value, which has the maximum allowed value of 700. In the current study, a full-scale barrier test was simulated in LS-DYNA and the HIC of the bus passenger was analyzed. The results of the current study clearly show the advantage of the full-scale barrier simulation over the sled test simulation in the case of large deformation on the floor structure.

Keywords: Finite element analysis; frontal crash; bus; head injury; full-scale barrier test

1. INTRODUCTION

The number of bus keeps growing every year, as it is one of the main transportation modes, especially in Indonesia. Unfortunately, the increase in the number of bus is not directly followed by improvement in the safety aspect and it also followed by the increase in number of accidents involving bus [1]. One of the deadliest accidents involving bus is frontal collision [2]. Thus, the study on the bus safety against frontal collision is very important. One of the most common injuries in a frontal collision is a head injury. The severity of head injury can be evaluated from the Head Injury Criterion (HIC) value, as mentioned in FMVSS 208 [3]. Based on FMVSS 208 the maximum allowed HIC value is 700 [4].

In 2001, Mitsuishi et al. [5] has conducted research on the optimization of passenger's seats distance using a sled test for seat configuration with lap seatbelt. Martinez et al. [6] has performed similar optimization but for seat configuration with lap and shoulder belt. Sled test, although reducing the computation cost significantly but disregard some important aspects such as floor structure deformation and seat anchorage strength, as both structures are modeled as rigid bodies in the sled test. In order to model the deformation of the floor structure and seat anchorage accurately, full-scale barrier simulation must be performed.

In the current study, full-scale barrier simulation will be performed in LS-DYNA software. The bus model used is All-New Legacy SR-2 made by PT Laksana Karoseri. The HIC value of the bus passenger then will be analyzed. The simulation will be performed on two different seatbelt configurations: no seatbelt and lap seatbelt, in order to study the effect of seatbelt configurations in bus frontal collision.

2. FINITE ELEMENT ANALYSIS

The finite element model of the bus superstructure was based on All New Legacy SR-2 bus model made by PT Laksana Karoseri. The finite element model was constructed to have mass distribution as close as possible to the actual bus. The dummy was modified to represent the average Indonesian male anthropometry and was placed on aisle seat at row number 8 from the front. In the lap seatbelt case, lap seatbelt was added to the model and was tied to the seat structure. The simulation was performed at a vehicle's speed of 48 km/h. The convergence test was then performed to the full bus model, resulting in a 5.6 % relative error for the final model used. Figure 1 shows the final model used in the current analysis.

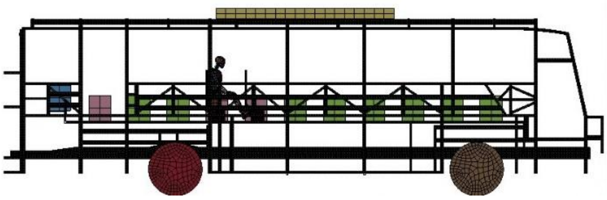

Figure 1 Final model

3. RESULTS AND DISCUSSION

The front collision simulation result of the no seatbelt case shows that the dummy's chin hit the front seat and the movement continues until dummy's chest hitting the same seat. The highest head acceleration happened at the time dummy's chin hitting the front seat as shown in Figure 2. The HIC was also recorded at the same time as shown in Figure 3, with the value of 2604.

In the case of simulation with lap seatbelt, the highest head acceleration was achieved when the dummy's face hit the front seat as shown in Figure 4. The HIC was recorded at the same time as shown in Figure 5, with the value of 2292. Slight improvement in the HIC value was achieved when lap seatbelt was used, but the HIC value was still higher than the maximum allowed value of 700. Thus, resulting in a 60% possibility of fatal accident and a 90% possibility of critical accident, although lap seatbelt has already been used. Detailed observation shows that this condition was caused by the deformation of the floor structure. The floor structure was deformed in such a way that makes the dummy's seat rotated forward and the front seat rotated back, which practically reduced the distance between the dummy's head and the front seat. As a result, even for the case with lap seatbelt, the HIC value was still very high.

Figure 2 No seatbelt case: dummy position when HIC is recorded.

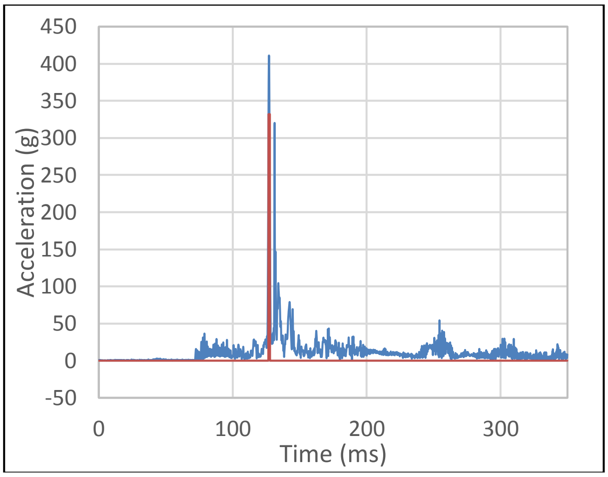

Figure 3 No seatbelt case: head acceleration (blue) and HIC recording (red).

Figure 4 Lap seatbelt case: dummy position when HIC is recorded.

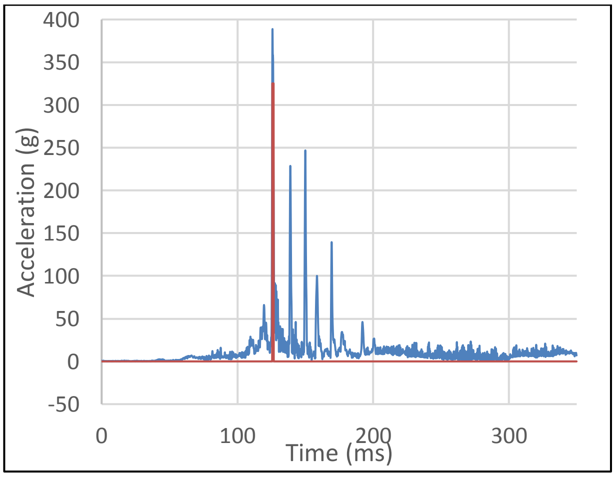

Figure 5 No seatbelt case: head acceleration (blue) and HIC recording (red).

4. CONCLUSIONS

The full-scale barrier simulation was successfully performed to analyze the head injury of the bus passenger in frontal collision. The simulation results show that the usage of the lap seatbelt only slightly reduced the HIC value, which results in a 60% possibility of fatal accident and a 90% possibility of critical accident. This condition was due to the deformation of the floor structure which practically reduced the distance between the dummy's head and the front seat. This special condition will not be able to be captured by the sled test simulation which assumed a rigid floor structure. This result highlight the advantage of full-scale barrier simulation over the sled test simulation when the floor structure deformed quite prominently.

ACKNOWLEDGMENT

This research was funded by Kementrian Riset Teknologi dan Pendidikan Tinggi Republik Indonesia (Penelitian Dasar Unggulan Perguruan Tinggi/PDUPT).

REFERENCES

[1] Transportation Ministry Secretariat General, "Transportation Statistics 2015", Transportation Ministry Secretariat General – Data and Information Center, Jakarta 2016. (Text in Indonesian)

[2] National Highway Traffic Safety Administration, "NHTSA's Approach to Motorcoach Safety", US Department of Transportation, 2007

[3] National Highway Traffic Safety Administration, Updated Review of Potential Test Procedures for FMVSS No. 208, 1999.mv

[4] National Highway Traffic Safety Administration. Federal Motor Vehicle Safety Standards: Motorcoach Definition, Occupant Crash Protection. NHTSA-2010-0112, RIN 2127-AK56, 2010.

[5] Hiroyuki Mitsuishi, Yoshihiro Sukegawa, dan Fujio Matsukawa, Research on Bus Passenger Safety in Frontal Impacts, Japan Automobile Research Institute, Japan, 2001.

[6] Luis Martinez, Teresa Vicente, Antonio Garcia, Enrique Alcala, dan Fransisco Aparicio, Analysis of Coaches Rows Seats Distance Influence on The Passengers Comfort and Safety, Polytechnic University of Madrid, Spain, 2015.

Effective Strategy of Modeling Helmholtz Equation of State

KAN Koemleng[1,*], I Made Astina[2]

[1)]Department of Mechanical and Industrial Engineering, Institute of Technology of Cambodia, CAMBODIA
[2)]Faculty of Mechanical and Aerospace Engineering, Institut Teknologi Bandung, INDONESIA

*Corresponding e-mail: koemleng001@yahoo.com

ABSTRACT – Potential strategy of modeling Helmholtz equation of state for several refrigerants along with the same functional form was well accomplished by employing genetic algorithm optimization along with weighted least square regression analysis. The process starts with finding the optimal functional form with theories approach for multiple linear property data, then use that form to fit the nonlinear data such as speed of sound, isobaric specific heat, and saturation specific heat. This method was successfully applied for developing Helmholtz equation of state for butane (R-600) and isobutane (R-600a). The equation of state is not only accurately, but also reasonable to present extrapolation behaviors, and ideal curves characteristic. The method can also be explored with several refrigerants.

Keywords: simultaneous; genetic algorithm; helmholtz

1. INTRODUCTION

As an outstanding part of thermal engineering field, thermodynamic properties have been carefully assessed for simulation design of thermal system. Since experimental data are limited, thermodynamic property models for various applications have notable interest for scientist. They mostly model equation of state that available to calculate reliable and accuracy property data. Enhancement knowledge of thermodynamic modelling strategy is catching up the attention of engineering due to the modelling process taking time. Developing equation of state for several refrigerants along with the same functional form have been proposed by reason of empirical equation with the same structural form is more reliable.

Astina and Sato [1] established a simultaneous cybernetic optimization on thermodynamic modeling. The method was proposed to conduct the functional form of saturation equation including vapor-pressure, saturated-liquid density, and saturated vapor-density. Not only for saturation equation, but it is also successfully applied for single optimization of Helmholtz equation of state. Taking above background into account, we extended the method from Astina and Sato [1] to simultaneously optimize the functional form of Helmholtz equation of state. Beside this method, Span et al. [2] implemented the modified stepwise regression to a general functional form of thermodynamic model. Despite the method are success to find the optimal functional form, but the modelling took too much time to obtain the results. Regarding to the method of Astina and Sato [1], the number of population and generation are limited. Therefore, it is very important to propose a method of modeling to enhance the model development.

2. DATA PREPARATION

Simultaneous optimization of Helmholtz equation of state, property data such as *PVT* in single-phase region, isobaric specific heat capacity, isochoric heat capacity, saturated heat capacity, saturation property measurements including Maxwell criteria, second and third virial coefficients, and speed of sound have been used as the input data for the model development. The main properties including universal gas constant, mass molar, critical temperature and density, critical pressure, and triple point criteria are needed in the optimization process.

3. METHODOLOGY

Simultaneous optimization to get the same functional form of Helmholtz equation of state in this research, non-analytic functional form is empirically and numerically finalized from experimental measurement as a result of employing genetic algorithm with weight least square regression analysis. The target of the simultaneous optimization is to find a best structural form along with thermodynamic theory and extrapolation behaviors for several refrigerants. The optimization procedure is illustrated in figures 1 and 2.

To facilitate the optimization process, effective technique was proposed to enhance the modeling framework with time consuming. Generally, the strategy is divided into two parts, trial functional form and selected functional form. Initially, modeling work starts with trial functional form of Helmholtz equation of state by using genetic algorithm optimization, then continue with weighted least square regression analysis of multiple property of linear data such as, PVT (Pressure, Volume, and Temperature), PVT-saturation, second and third virial coefficients, Maxwell criteria, and isochoric specific heat capacity to fit the coefficients of first refrigerant. To obtain the same functional form, the previous function form was used again for other refrigerants and perform regression until the last object refrigerant. The method was implemented in a computer program with object-oriented programing language C++ from Astina in 2003. Not only function form that has influence on the quality of property model as results of weighted least square regression process, but also weighting factor has significant. In the case, improvement by iteration of weighting factor of fluids may be considering to obtaining desire deviation of the model from the input data.

After obtained a good functional form, analysis of regression of multiple property including nonlinear data such as speed of sound, isobaric specific heat, and saturated specific heat were introduced again as shown in figure 2. This concept is very effective and fast for developing residual part of Helmholtz equation of state.

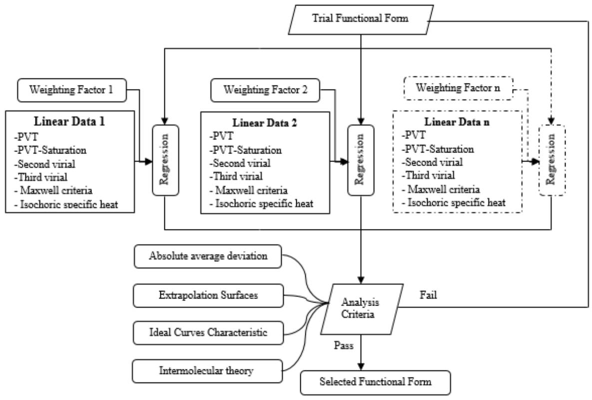

Figure 1 Trial functional form

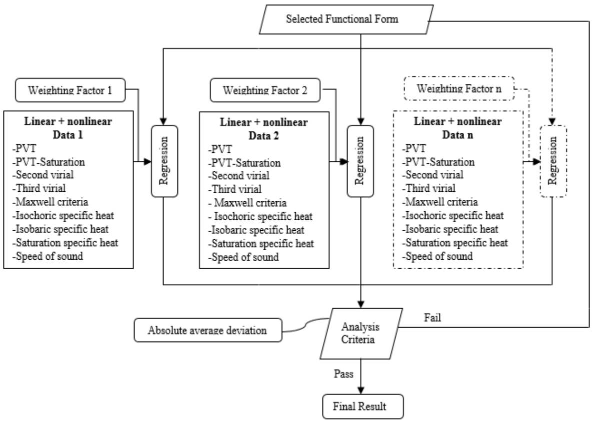

Figure 2 Selected functional form

3.1 OBJECTIVE FUNCTION OF THE MODEL

In the process of developing residual part of Helmholtz equation, will be obtained from the iteration of using genetic algorithm optimization method combing with weighted least square regression. The objective function is given in equation (1).

$$\chi^2 = \sum_{i=1}^{N} w_i \left(y_i - \sum_{j=1}^{m} a_{i,j} x_j \right)^2 \tag{1}$$

Where:

w_i is the weighting factor.

General form of residual part,

$$\alpha^r(\delta,\tau) = \sum_{i=1}^{n} N_i \delta^{d_i} \tau^{t_i} \exp\left[-m_d(\delta - s_d)^{d_e} - m_t(\tau - s_t)^{t_e}\right] \tag{2}$$

Where:

$t_i, m_d, s_d, d_e, m_t, s_t$, and t_e are the predicted parameters and N_i is the numerical coefficients.

After the predicted parameters are obtained from the genetic algorithm, optimal numerical coefficients will fit from regression as written in equation (3).

$$Y = AX + E \tag{3}$$

Where:

Y is the independent variable matrix.
A is the dependent variables matrix.
X is numerical coefficients matrix.
E is deviation matrix of calculated data and input data.

In order minimize E, sum of square of E is minimized by differing respect to unknown coefficients in matrix X. Minimization of the sum of the square obtained from this manipulation can be written in equation (4).

$$A^T Y = A^T A X \tag{4}$$

Saturation and ideal part equations were also prepared before starting the modelling in the development of residual part. Saturation equations are adopted from previous work [3]. Below equation is the matrix that will be entered by input data for establishing the residual part. Explanation of symbols is described in section 4.

$$\begin{bmatrix} p,\rho,T \\ p_s,\rho',T_s \\ p_s,\rho'',T_s \\ p_s,\rho',\rho'',T_s \\ B,T \\ C,T \\ C_v,\rho,T \\ C_p,\rho,T \\ w,\rho,T \\ C_s',\rho',\rho'',T_s \end{bmatrix} = \begin{bmatrix} 1-\delta\alpha_\delta^r \\ 1-\delta'\alpha_{\delta'}^{r} \\ 1-\delta''\alpha_{\delta''}^{r} \\ ln\frac{\delta'}{\delta''}-(\alpha^{r'}-\alpha^{r''}) \\ \lim_{\delta\to0}\alpha_\delta^r \\ \lim_{\delta\to0}\alpha_{\delta\delta}^r \\ \tau^2(\alpha_{\delta\delta}^o+\alpha_{\delta\delta}^r) \\ C_v(\delta,\tau)/R-(1+\delta\alpha_\delta^r-\delta\tau\alpha_\delta^r)^2/(1+2\delta\alpha_\delta^r+\delta^2\alpha_{\delta\delta}^r)^2 \\ 1-2\delta\alpha_\delta^r-\delta^2\tau\alpha_{\delta\delta}^r-(1+\delta\alpha_\delta^r-\delta\tau\alpha_{\delta\tau}^r)^2/(C_v(\delta,\tau)/R) \\ \frac{c_v(\delta',\tau_s)}{R}-\frac{\left(1+\delta'\alpha_\delta^{r'}-\delta'\tau_s\alpha_{\delta\tau}^{r\,'}\right)^2}{\left(1+2\delta'\alpha_\delta^{r'}-\delta'^2\tau\alpha_{\delta\delta}^{r\,'}\right)}\left\{1+\delta'\alpha_\delta^{r}{}'-\delta'\tau_s\alpha_{\delta\tau}^{r}{}'-\frac{dp_s(\delta',\delta'',\tau_s)}{R\rho_c\delta' dT}\right\} \end{bmatrix} \times \begin{bmatrix} N_i \end{bmatrix}$$

4. RESULTS AND DISCUSSION

The effective concept above was successfully applied for finding the optimal functional form of residual part of Helmholtz equation of state for R-600 and R-600a. The results are not only accuracy, but also reasonable to derive the extrapolation behaviors. The ideal curves characteristic including intermolecular potential theory were assessed in this section. The statistical analysis and extrapolation behaviors of the equation of state will be reported in two papers of Koemleng and Astina [4]. The residual and ideal parts of Helmholtz equation of state for both fluids can be written in equations (5) and (6). The functional constants with numerical coefficients of equation for R-600 and R-600a are separately given in two papers [4] and [5].

$$\alpha^r(\delta,\tau) = \sum_{i=1}^{11} N_i \delta^{d_i}\tau^{t_i} + \sum_{i=12}^{13} N_i \delta^{d_i}\tau^{t_i}\exp(-\delta) + \sum_{i=14}^{14} N_i \delta^{d_i}\tau^{t_i}\exp(-\delta^2) + \sum_{i=15}^{17} N_i \delta^{d_i}\tau^{t_i}\exp(-\delta^3) \tag{5}$$

$$\alpha^0(\delta,\tau) = \ln\tau + N_1^0 + N_2^0\tau + N_3^0\ln\tau + \sum_{i=4}^{8} N_i^0 \ln\left[1-\exp\left(-\eta_i^0\tau\right)\right] \tag{6}$$

In each correlation $\tau = T_c/T$ and $\delta = \rho/\rho_c$ including main properties of equation are prepared section 2.

The proposed technique is capable to find the ideal curves characteristic for modeling equation of state. The ideal curves are judge reasonable fluids surface of equation of state. Figure 3 shows the characteristic of ideal curve derived from the new simultaneous optimization. The consistency of fundamental thermodynamic equation of state with the intermolecular potential was investigated with the behaviors of the second and third virial coefficients derived from the fundamental EOS. Second and third virial coefficients for R-600 and R-600a are shown in figures 4 and 5; figures 6 and 7, respectively.

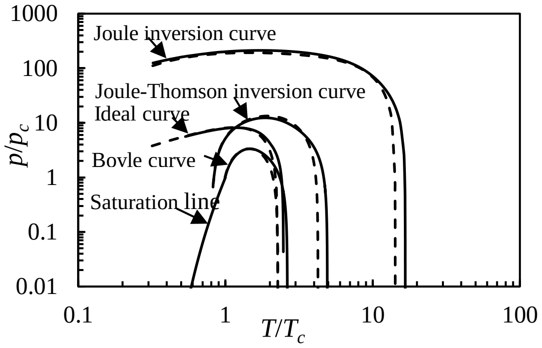

Figure 3 Ideal curves characteristic from the new simultaneous equation of state. (---) R-600; (—) R-600a Koemleng and Astina [4], [5].

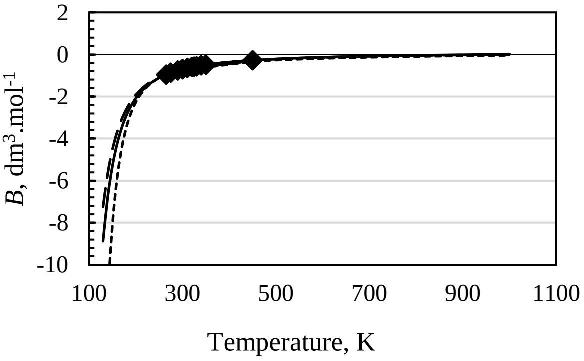

Figure 4 Second virial coefficients for R-600. (♦) Glos et al. [11]; (——) Koemleng and Astina [4]; (---) Sarin et al. [6] ; (· · ·) Miyamoto and Watanabe [9].

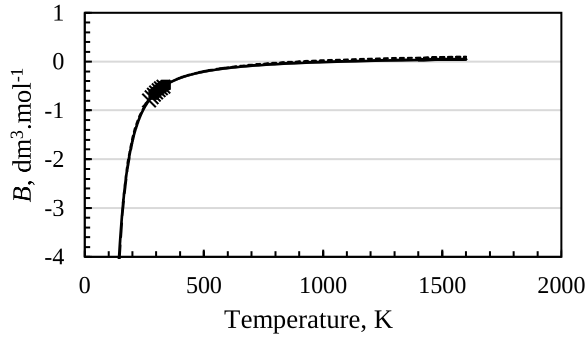

Figure 5 Second virial coefficients for R-600a. (×) Liu et al. [10]; (♦) Glos et al. [11]; (– – –) Koemleng and Astina [5]; (---) Sarin and Astina [7]; (——) Miyamoto and Watanabe [8].

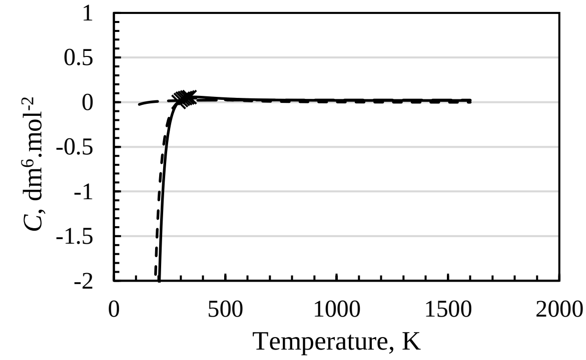

Figure 6 Third virial coefficients for R-600. (■) Glos et al. [11]; (——) Koemleng and Astina [4]; (---) Sarin et al.[6]; (– – –) Miyamoto and Watanabe [9].

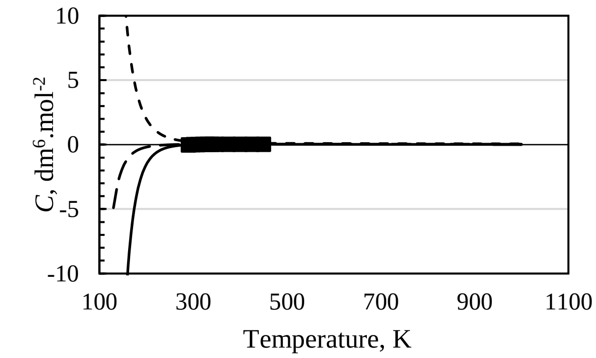

Figure 7 Third virial coefficients for R-600a. (×) Glos et al. [11]; (——) Koemleng and Astina [5]; (– – –) Sarin and Astina [7]; (---) Miyamoto and Watanabe [8].

All thermodynamic property models can be calculated from thermodynamic relations when independent parameters are known.

Compressibility and Pressure:

$$Z\,(\delta,\tau) = p(\delta,\tau)/(\rho RT) = 1 + \delta\alpha_\delta^r$$

Ideal gas isobaric specific heat:

$$c_p^0(\tau)/R = 1 - \tau^2\alpha_{\tau\tau}^r = 1 + c_v^0/R$$

Isochoric specific heat:

$$c_v(\delta,\tau)/R = -\tau^2(\alpha_{\delta\delta}^o + \alpha_{\delta\delta}^r)$$

Isobaric specific heat:

$$c_p(\delta,\tau)/R = -\tau^2(\alpha_{\delta\delta}^o + \alpha_{\delta\delta}^r) + \frac{(1 + \delta\alpha_\delta^r - \delta\tau\alpha_\delta^r)^2}{(1 + 2\delta\alpha_\delta^r + \delta^2\alpha_{\delta\delta}^r)}$$

Saturation properties:

$$p_s(\delta',\tau)/(\rho' RT) = 1 + \delta'\alpha_\delta^r$$

$$p_s(\delta'',\tau)/(\rho'' RT) = 1 + \delta''\alpha_\delta^r$$

$$p_s(\delta',\delta'',\tau)/(RT)(1/\rho'' - 1/\rho') - \ln(\delta'/\delta'') = \alpha^r(\delta',\tau) - \alpha^r(\delta'',\tau)$$

Speed of sound:

$$w(\delta,\tau)^2 M/RT = 1 + 2\delta\alpha_\delta^r + \delta^2\tau\alpha_{\delta\delta}^r + \frac{(1 + \delta\alpha_\delta^r - \delta\tau\alpha_{\delta\tau}^r)^2}{c_v(\delta,\tau)/R}$$

Virial coefficients:

Second virial: $B(\tau)\rho_c = \lim_{\delta\to 0} \alpha_\delta^r$

$$\text{Third virial: } C(\tau){\rho_c}^2 = \lim_{\delta\to 0} \alpha^{r}_{\delta\delta}$$

Internal energy:

$$u(\delta,\tau)/RT = \tau(\alpha^o_\tau + \alpha^r_\tau)$$

Enthalpy:

$$h(\delta,\tau)/RT = \tau(\alpha^o_\tau + \alpha^r_\tau) + 1 + \delta\alpha^r_\delta$$

Entropy:

$$s(\delta,\tau)/R = \tau(\alpha^o_\tau + \alpha^r_\tau) - (\alpha^0 + \alpha^r)$$

Abbreviations:

$$\alpha_\delta = \frac{\partial\alpha}{\partial\delta}; \alpha_\tau = \frac{\partial\alpha}{\partial\tau}; \alpha_{\delta\delta} = \frac{\partial^2\alpha}{\partial\delta^2}$$

$$\alpha_{\tau\tau} = \frac{\partial^2\alpha}{\partial\tau^2}; \alpha_{\delta\tau} = \frac{\partial^2\alpha}{\partial\delta\partial\tau};\ \delta = \frac{\rho}{\rho_c}; \tau = \frac{T_c}{T}$$

5. CONCLUSION

An effective technique of modeling simultaneous Helmholtz equation of state has proposed for R-600 and R-600a. The method is not only successful and faster for simultaneous development of two refrigerants, but also for more refrigerants. The method is capable to optimize the functional form with number of parent's more than 100 and large number of generation by reason of taking less time.

NOMENCLATURE

M	molar mass
p	pressure
B	second virial coefficient
c	specific heat
w	speed of sound
T	temperature
C	third virial coefficient
R	gas constant
ρ	density
τ	inverse reduced temperature
α	reduced Helmholtz free energy
δ	reduced density
Subscripts	
c	critical parameter
p	process at constant pressure
v	process at constant volume
t	triple point
S	saturation
Superscripts	
o	ideal part
r	residual part
‘	saturated-liquid state
“	saturated-vapor state

ACKNOWLEDGEMENT

The authors would like to thank to AUN/SEED-net program (ASEAN University Network/Southeast Asia Engineering Education Development Network) for financial support on the research.

REFERENCES

[1] I M. Astina, H. Sato, "Implementation of Simultaneous Cybernetic Optimization on Thermodynamic Modeling", J. Teknik Mesin 1(2), pp 51–60, 2006.

[2] R. Span, H-J. Collmann, W. Wagner, "Simultaneous Optimization as a Method to Establish Generalized Functional Form for Empirical Equation of State", Int. J. Thermophys. 19, pp. 491–500, 1998.

[3] K. Koemleng, I M. Astina, P S. Darmanto, "Simultaneous Optimization of Saturation Equation for two Hydrocarbons and four Hydrofluoroolefins refrigerants". International Conference Aerospace, Mechanical and Mechatronic Engineering (CAMME), Malaysia, 21-24 February 2019.

[4] K. Koemleng, I M. Astina, "Helmholtz Equation of State for Normal Butane", Submitted to ITB J. Eng. Sci (2019).

[5] K. Koemleng, I M. Astina, "Thermodynamic Equation of State for Wide-Range Fluid Phase Isobutane", Submitted to Fluid Phase Equilibria (2019).

[6] C. Sarin, I M. Astina, P S. Darmanto, H. Sato, "Thermodynamic Property Model of Wide-Fluid Phase n-Butane", J. Teknik Mesin. 22, 44–54, 2007.

[7] C. Sarin, "Development of Thermodynamic Equations of State for Alternative Refrigerants R-600 and R-600a", Master Thesis, Institut Teknologi Bandung, Indonesia; 2006.

[8] H. Miyamoto, K. Watanabe, "A Thermodynamic Property Model for Fluid-Phase Isobutane", Int. J. Thermophys. 23(2), pp. 477–499, 2002.

[9] H. Miyamoto, K. Watanabe, "A Thermodynamic Property Model for Fluid-Phase n-Butane", Int. J. Thermophys. 22(2), pp. 459–475, 2001.

[10] Q. Liu, X. Feng, K. Zhang, B. An, Y. Duan, "Vapor pressure and gaseous speed of sound measurements for isobutane (R600a)", *Fluid phase equilibria.* 382, pp. 260–269, 2014.

[11] S. Glos, R. Kleinrahm, W. Wagner, "Measurement of the (p, ρ, T) Relation of Propane, Propylene, n-Butane, and Isobutane in the Temperature Range from (95 to 340) K at Pressure up to 12 MPa Using an Accurate Two-sinker Densimeter", J. Chem. Thermodyn. 36, pp. 1037–1059, 2004.

Wind Tunnel Experiments on Smoke Structure Dispersed from a Chimney in a Cross Flow

Nobumasa Sekishita[1*], Xangpheuak Inthavideth[1], Sounthisack Phommachanh[2]

[1)] Department of Mechanical Engineering, Toyohashi University of Technology,
1-1 Hibarigaoka, Tempaku-cho, Toyohashi, Aichi, 441-8580, Japan
[2)] Department of Mechanical Engineering, Faculty of Engineering, National University of Laos,
Lao-Thai Friendship Rd, Sisattanak District, Vientiane Capital, P.O.BOX: 3166, Lao PDR

*Corresponding e-mail: seki@me.tut.ac.jp

ABSTRACT – The present study aims to investigate the patterns of smoke dispersion from a chimney and its occurrence conditions in large-scale turbulence generated by an atmospheric wind tunnel with an active turbulence generator [1]. Six kinds of the smoke structures are distinguished. The smoke in the large-scale turbulence is dispersed more widely by meandering motion with high jet velocity and low cross flow velocity. This fact can be considered that large-scale turbulent eddies effectively contribute to the meandering smoke dispersion. Compared in an unheated jet, the meandering smoke structure in a heated jet with higher temperature occurs in the case of the lower jet velocity and the higher cross flow velocity. On the other hand, the smoke structures in grid turbulence have the five kinds of structures: bifurcated vortex tubes with and without strongly mutual interaction, connected hairpin-type vortices, the mixture of the coherent vortices and turbulent vortices and downwash-type structure.

Keywords: Smoke dispersion, large-scale turbulence, air pollution, environment, wind tunnel

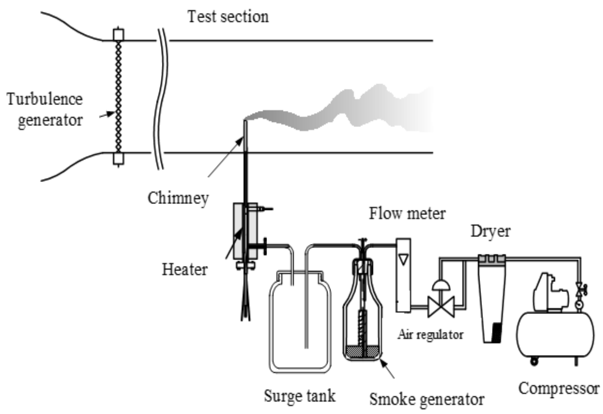

Figure 1 Wind tunnel and smoke generation system

Table 1 Experimental condition

Temperature difference $\Delta\theta$ [K]	0, 100, 200
Jet velocity U_j [m/s]	0.5, 0.6, 0.8, 1.0, 1.2, 1.4
Cross flow velocity U_0 [m/s]	0.3, 0.4, 0.6, 0.8, 1.0

1. INTRODUCTION

Air pollution including particle dispersion from industrial factories, motor vehicles, ordinary houses where coal is used for heating apparatus, etc., seriously affects ecosystems and human health for which the several millions of people die every year due to the atmospheric pollution. It is strongly demanded year by year to more precisely assess the particle diffusion like PM 2.5 for the mitigation of grave air pollution problems. The heat and mass transfer including the smoke in a jet flow from a chimney is remarkably related to turbulence dispersion which has one of particular interests of turbulence researchers. In order to investigate the mechanism of the turbulence diffusion of the smoke, it is made in laboratory experiments by using a wind tunnel. It is necessary for its wind tunnel testing to realize the smoke dispersion which is similar in an actual atmospheric boundary layer.

Many researches [2-8] on the smoke dispersion from a chimney were conducted by using a wind tunnel. Extensive results into these wind tunnel experiments were presented and compared with theory, field measurement and numerical simulation results. Said et al. [6] used particle image velocimetry, PIV, to investigate coherent structures in the near-wake region of a turbulent round jet ejected perpendicularly from a chimney into a cross flow. They elucidated the Kelvin–Helmholtz vortex structures, the downwash phenomena and the effect of the height of the chimney. Huang and Hsieh [7] classified the jet structure by the momentum ratio between the cross wind and the jet velocity. Four characteristic types of flows with apparent differences were identified: downwash, cross wind dominant flow, transitional flow and jet dominant flow. Majeski et al. [8] proposed a phenomenological model for the prediction of the size of low-momentum jet diffusion flame diluted with an inert gas in a cross flow.

However, it is difficult to reproduce an atmospheric turbulence phenomenon like the smoke dispersion in an ordinary-size wind tunnel by using high-drag strakes, roughness blocks, a turbulence grid, etc. The wind tunnel experiments of a buoyancy jet with the smoke vertically ejected in high Reynolds number turbulence which has the large-scale turbulent eddies are

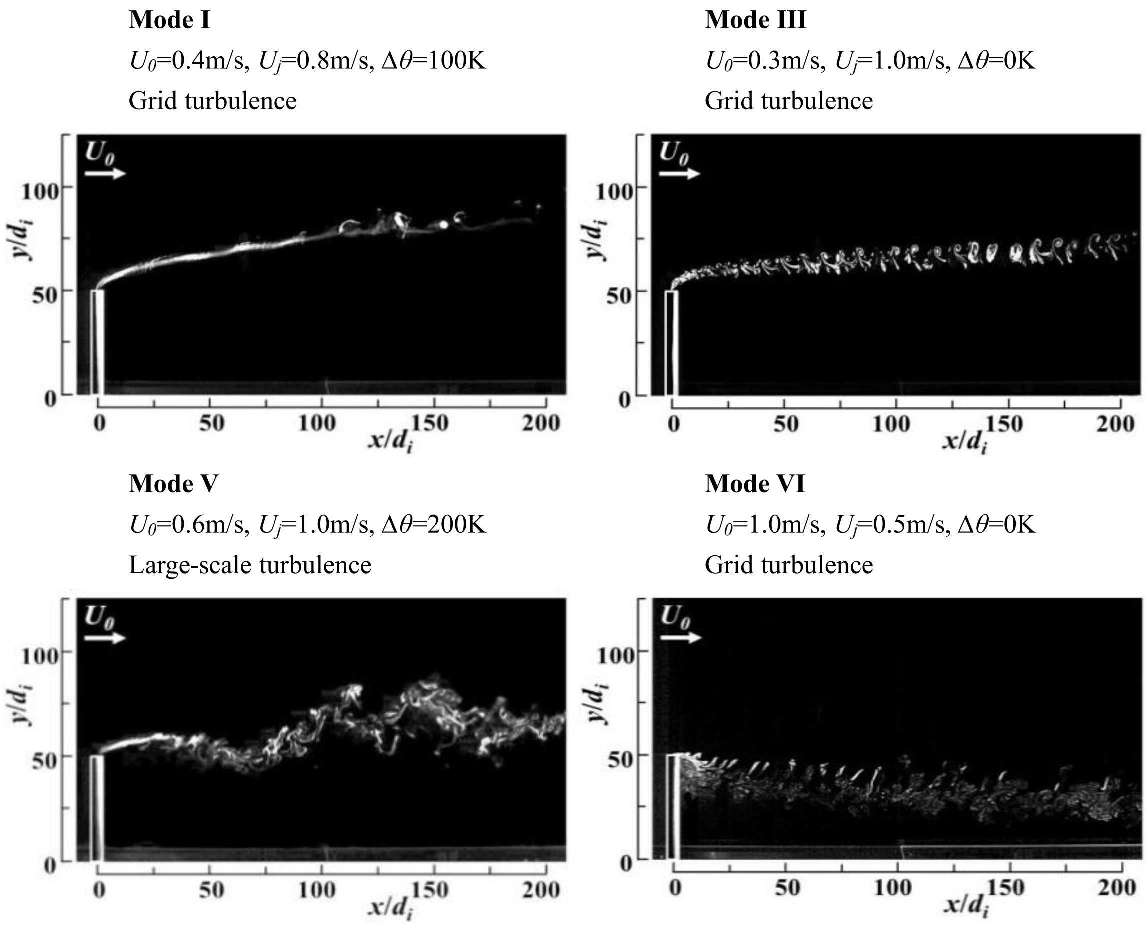

Figure 2 Dispersion structures of smoke ejected from chimney

essential for the investigation and the precise estimation of the smoke dispersion. Our final goal is to construct a turbulence diffusion model for the environmental assessment and the prediction of atmospheric dispersion from a point source like a chimney. The purpose of the present paper is to investigate the structures of the smoke dispersion from the chimney and its occurrence conditions in the large-scale turbulence and the grid turbulence by using an atmospheric wind tunnel with an active turbulence grid.

2. EXPERIMENT DEVICES AND METHOD

A blown-type atmospheric wind tunnel was employed and it had a test section of $0.7 \times 0.7 m^2$ in cross section and 6m in length [1]. A Makita-type active turbulence generator equipped just upstream of the test section can generate the large-scale turbulence having the high turbulence Reynolds number, $R_\lambda \sim 390$ at U_0=5m/s, the large integral scale, large turbulence fluctuations, the wide inertial subrange in the energy spectra of velocity fluctuations.

The chimney model of d_i=4mm in inside diameter, 8mm in outside diameter and 200mm in height was placed on the floor of the wind tunnel test section. The smoke generation system for ejecting heated or unheated air with the smoke from the chimney was composed of an air compressor, an air dryer, an air regulator, a flow meter, a smoke generator which was to smoke by using Ondina oil, a surge tank, a heater for generating the buoyancy jet and the chimney as shown in Figure 1. The cross sectional average velocity of the jet at the chimney exit was controlled by the air regulator. The patterns of the smoke dispersion were visualized by a high-speed camera (Photron FASTCAM SA3, 1000frame/s) and a halogen light.

The present experiments were carried out in the experimental conditions of temperature difference between the cross wind and the jet from the chimney, $\Delta\theta$, the jet velocity at the center of the chimney exit, U_j, the mean velocity of the cross wind, U_0, as shown in table 1. That is, the velocity ratio between the jet velocity and the cross wind velocity, r, was from 0.5 to 4.7, its momentum ratio, R, was from 0.145 to 21.8 and the density ratio between the heated jet and the cross wind, S, was 0.59, 0.74, 1.00. The vertical mean velocity profile of the cross flow was uniform around the height of the chimney exit. Turbulence intensity, u_{rms}/U_0, was from 9.5% to 11.0% in the large-scale turbulence and from 2.9% to 3.5% in the grid turbulence. The origin of a coordinate system was the center of the chimney on the floor in the wind tunnel test section. The cross wind direction was x, the vertical direction which is the direction of the jet velocity at the chimney exit was y and the span-wise direction was z.

Table 2 Occurrence condition of each mode in large-scale turbulence
mode V: meandering dispersion, mode VI: downwash dispersion

		$\Delta\theta$=0K						$\Delta\theta$=100K					
		Jet velocity, U_j [m/s]						Jet velocity, U_j [m/s]					
		0.5	0.6	0.8	1.0	1.2	1.4	0.5	0.6	0.8	1.0	1.2	1.4
Cross wind velocity U_0 [m/s]	0.3	**VI**	**V**	**V**	**V**	**V**	**V**	**V**	**V**	**V**	**V**	**V**	**V**
	0.4	**VI**	**VI**	**V**	**V**	**V**	**V**	**V**	**V**	**V**	**V**	**V**	**V**
	0.6	**VI**	**VI**	**V**	**V**	**V**	**V**	**VI**	**V**	**V**	**V**	**V**	**V**
	0.8	**VI**	**VI**	**VI**	**V**	**V**	**V**	**VI**	**VI**	**V**	**V**	**V**	**V**
	1.0	**VI**	**VI**	**VI**	**VI**	**VI**	**V**	**VI**	**VI**	**VI**	**VI**	**V**	**V**

3. RESULTS AND DISCUSSION

So as to get a direct qualitative aspect of the smoke structures in the large-scale turbulence and the grid turbulence, the smoke structures can classify six kinds of the smoke dispersion patterns, modes I-VI. Figure 2 shows the typical smoke structures diffused from the chimney in the case of the temperature difference, the cross wind velocity and the jet velocity. The mode V structure is affected of the meandering motion by the large integral scale in the large-scale turbulence. The smoke structure of the mode V is dispersed more widely by the meandering motion which can not be realized in a usual-size wind tunnel with roughness blocks, a conventional turbulence grid, etc. This fact can be noticed that the turbulent eddies corresponding to the integral scale effectively contribute to the meandering smoke diffusion. The mode VI structure in the large-scale turbulence is a downwash with the hairpin vortices due to the wake of the chimney. Thus, the smoke does not rise above the chimney exit. This is the serious situation for an actual chimney.

On the other hand, by the buoyancy force in the grid turbulence, the structures of modes I and II are composed of two longitudinal vortex tubes whose one end of are connected to the chimney exit. For the mode I, the two vortex tubes are disconnected each other. For the mode II, these two vortex tubes are strongly interacted by the strong buoyancy and its cross section is like the inverse shape of heart-type. The mode III structure is comprised of connecting hairpin-type vortices generated by the Kelvin-Helmholtz instability near the jet exit where the velocity shear is large. The mode IV structure is composed of the developed coherent vortices and the turbulent vortices by the turbulent motion.

Table 2 shows the occurrence conditions of each mode in the large-scale turbulence. Only the modes V and VI occur in the large-scale turbulence. The mode V, the meandering smoke diffusion, appears by the large-scale turbulent motion in the case of the low cross wind and the high jet velocity both in the heated and the unheated jet. It means that the effect of the turbulent motion is more dominant than of the buoyancy force. In the case of the lower jet velocity and the higher cross flow velocity, the meandering smoke structure in the heated jet with high temperature is generated more certainly than in the unheated jet. The mode VI, the downwash dispersion, occurs in the condition of the high cross wind and the low jet velocity both in the heated and the unheated jet due to the wake flow of the chimney.

Besides in the large-scale turbulence, the modes I-IV and VI occur in the gird turbulence. The mode I, the bifurcation diffusion, appears by the buoyancy force in the case of the low cross wind and the low jet velocity only in the heated jet with $\Delta\theta$=100K. The mode II, the bifurcation dispersion by the buoyancy, is generated with increasing the temperature difference, $\Delta\theta$. The mode III, the hairpin-type dispersion, is founded in the unheated jet. In addition, the mode III in the heated jet occurs in the higher cross wind and the higher jet velocity. Only for the heated jet with $\Delta\theta$=200K due to the increase of disturbance, the mode IV appears in the case of U_0=0.3m/s with the all jet velocity conditions and the low jet velocity. For the mode VI, the downwash diffusion occurs also in the grid turbulence in the case of the high cross wind and the low jet velocity both in the heated and the unheated jet.

4. CONCLUSIONS

The structures of the smoke dispersion from the chimney were investigated in the large-scale turbulence with the turbulence intensity, u_{rms}/U_0=9.5~11%, and the grid turbulence with u_{rms}/U_0=2.9~ 3.5%. The flow visualization experiments by using the high-speed camera elucidated the following conclusions.

(1) The present experiment succeeded in the realization of the meandering smoke dispersion which can be observed in an actual atmospheric boundary layer. This meandering smoke dispersion was realized in the large-scale turbulence generated by the atmospheric wind tunnel with the active grid. The smoke diffused more widely by the meandering motion in the case of the high jet velocity and the low cross flow velocity in the high Reynolds number turbulence. Compared in the unheated jet, the meandering smoke structure in the heated jet with higher temperature occurred in the condition of the lower jet velocity and the

higher cross flow velocity.

(2) The structures of the smoke dispersion were divided into the six modes. The mode V, the meandering dispersion, occurred in the large-scale turbulence. On the other hand, the modes I-IV appeared in the grid turbulence. The mode VI, the downwash dispersion, occurred both in the large-scale and the grid turbulence.

(3) For the modes I and II, the two longitudinal vortex tubes were generated without and with strongly mutual interaction, respectively. The bifurcation structure was produced by the buoyancy force near the jet exit, when the buoyancy was dominant. For the mode III, the hairpin-type vortices occurred by the Kelvin-Helmholtz instability. For the mode IV, the structure was comprised of the developed coherent vortices and the turbulent vortices. For the mode V, the meandering structure was affected of the turbulent motion. For the mode VI, the downwash structure occurred behind the chimney. This smoke diffusion was depended on the turbulent motion, the inertia force, the buoyancy force, etc.

REFERENCES

[1] H. Makita. Realization of a large-scale turbulence field in a small wind tunnel. Fluid dynamic research. 8, pp. 53-64, 1991.

[2] R.S. Roaman and S. Ramachandran. Annual and seasonal variability of ambient aerosols over an urban region in western India. Atmospheric Environment. 44, pp. 1200-1208, 2010.

[3] A. Leelossy, F.Jr. Molnar, F. Izsak, A. Havasl, I. Lagzl, and R. Meszaros. Dispersion modeling of air pollutants in the atmosphere: a review. Central European Journal of Geosciences. 6(3), pp. 257-278, 2014.

[4] S.G. Taylor. The present position in the theory of turbulent diffusion. pp, 101-112.

[5] F. Gifford. Statistical properties of a fluctuating plume dispersion model. pp. 117-137.

[6] N.M. Said, H. Mhiri, G.L. Palcc, and P. Bournot. Experiment and numerical analysis of pollutant dispersion from a chimney. Atmosperic Environment. 39, pp. 1727-1738, 2005.

[7] R.F. Huang and R.H. Hsieh. An experimental study of elevated round jets deflected in a crosswind. Experimental thermal fluid science. 27, pp. 77-86, 2002.

[8] A.J. Majeski, D.J. Wilson, and L.W. Kostiuk. Predicting the length of low-momentum jet diffusion flame in cross flow. Combustion Science and Technology. 176:12, pp. 2001-2025, 2010.

The droplet characteristics on micropillar surface during the dewetting process

Bambang Arip Dwiyantoro[1,*]

[1)] Department of Mechanical Engineering, Institute of Technology Sepuluh Nopember
Kampus ITS, Surabaya, Indonesia

[*]Corresponding e-mail: bambangads@me.its.ac.id

ABSTRACT – In this study, we theoretically investigate the dynamic behavior of microdroplet formation on the micropillar surface after the dewetting process. Dimensional analysis is used to determine independent dimensionless groups to characterize the time of droplet formation i.e. the Ohnesorge number (Oh), the Capillary number (Ca), the dimensionless liquid thickness (*H*). The simulation results show that the dynamic of microdroplet formation on the top surface of micropillar depends on the parameters in the dewetting process.
Keywords: *microdroplet; micropillar; dewetting process*

1. INTRODUCTION

Dynamic molecular combing (DMC) is a commonly used approach for guiding the assembly by flow. It relies on the meniscus in the wetting or dewetting process. When a solid substrate (glass or PDMS) is dished in a solution that contains soft molecules (such as DNA), one or both ends of each molecule are uncoiled at the receding air–water–solid contact line and may combine with the substrate surface. To generate a DNA nanowire array, a PDMS stamp with microwells or micropillars is placed on the DNA solution and peeled up from one end to allow the solution de-wet the stamp surface. DNA wires form immediately on this surface. To generate high quality arrays of stretched DNA, the microwells must be filled with DNA solution when the microwell stamps are used. However, for micropillar stamps, care should be taken to avoid filling the space between micropillars. On the micropillar stamp, continuous DNA wires reside on each column of micropillars. Long nanowires and diagonally oriented short nanowires can be formed on a microwell stamp by through adjusting the dewetting conditions, such as the speed and direction of peeling. Figure 1 gives the schematic illustration of droplet formation on micropillar stamps. In the de-wetting of a micropillar stamp, which is filled with air in the space between the pillars, the solution recedes faster on the air cushion (highly hydrophobic) than on the micropillars (less hydrophobic). As a result, a droplet is left behind on a micropillar but it is connected to the main body of the receding solution by a “liquid bridge”. As the liquid bridge breaks, the solution can be trapped in two separate bodies of liquid and are uncoiled by dynamic molecular combing, forming a suspended nanowire between the two pillars. The nanowire then extends onto the surface of micropillar as the droplet shrinks.

The developments of microfluidic systems which allow in engineering applications for the microdroplet formation have been done. Xu et al. [1] investigated the droplet formation in T-junction microfluidics devices in three typical regimes. The numerical results show the growth of droplet at various inlet velocities depending on the Capillary number and the dynamic break-up process. Some studies [2-3] on the formation of droplet in the dewetting of surface have been also done.

The dewetting process was performed by peeling the coverslip from a micro-featured substrate. Microdroplets were first formed on the top of micropillars. A droplet is created on the top surface of micropillar after the recoiling of captive wet region. Figure 2(a) shows the nanoparticles left on micropillar stamps after a dewetting process by the peeling technique proposed in [4]. However, the correlation between the droplet characteristics, i.e. the size of droplet and its formation time, and the operation parameters, such as the size of micropillar and fluid property was not extensively studied in previous studies. The objective of this paper is to investigate the dynamic behavior of droplet formation on micropillar surface and its correlation to operation parameters governing the dewetting process.

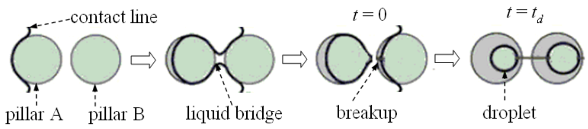

Figure 1. Schematics illustration of the processes for the generation of droplets on micropillar stamps (top view).

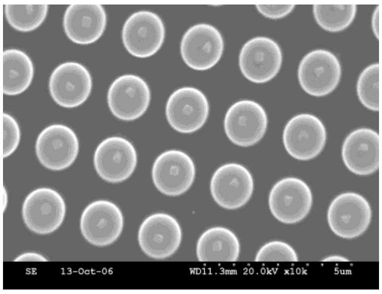

(a)

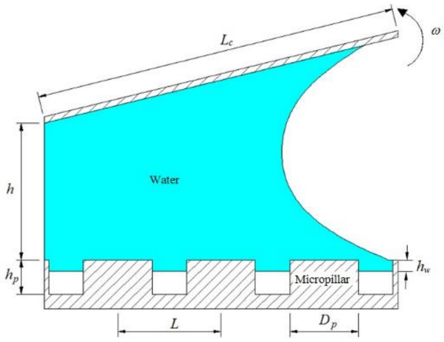

(b)

Figure 2. (a) Image of microdroplets left on micropillar stamps [3] (b) Schematic illustration of the dewetting process of micropillars.

2. METHODOLOGY

The dewetting on micropillars adopted in this research can be described as the evolution of receding water meniscus located between two parallel solid surfaces that caused by the rotation of the upper one. Figure 2 (b) schematically illustrates this process, where D_p represents the hydraulic diameter of micropillar, h_p the height of micropillar (=0.5 D_p), L the center to center distance between micropillars, L_c the length of upper substrate, h the liquid thickness between the top surface of micropillar and the upper substrate, h_w the water submergence depth among micropillars (=0.1 D_p), and ω the peeling speed of the upper substrate.

The governing equations to describe the moving-front flow phenomenon, i.e. the continuity equation and the Navier–Stokes equation, can be expressed in the integral form over a control volume V:

$$\frac{\mathrm{d}}{\mathrm{d}t}\int_V \rho \mathrm{d}V + \int_S \rho(\mathbf{v}-\mathbf{v}_\mathrm{S})\cdot \mathrm{d}S = 0 \qquad (1)$$

$$\frac{\mathrm{d}}{\mathrm{d}t}\int_V \rho\mathbf{v} \mathrm{d}V + \int_S \rho\mathbf{v}(\mathbf{v}-\mathbf{v}_\mathrm{S})\cdot \mathrm{d}S = \int_S \mathbf{f}\cdot \mathrm{d}S + \int_V \rho\mathbf{g}\mathrm{d}V \qquad (2)$$

where the control volume V is bounded by a closed surface S, $\mathbf{v}$ denotes the flow velocity, $\mathbf{v}_S$ the surface velocity of S, ρ the fluid density, t the time, $\mathbf{f}$ the external force acting on S and $\mathbf{g}$ the gravitational acceleration. The surface velocity $\mathbf{v}_\mathrm{S}$ was then determined by the third governing equation to avoid the errors caused by the direct calculation of surface velocity from the face centre displacement:

$$\frac{\mathrm{d}}{\mathrm{d}t}\int_V \mathrm{d}V + \int_S \mathbf{v}_\mathrm{S}\cdot \mathrm{d}S = 0 \qquad (3)$$

The last governing equation is to describe the position of front:

$$\frac{\mathrm{d}}{\mathrm{d}t}\int_V c\mathrm{d}V + \int_S c(\mathbf{v}-\mathbf{v}_\mathrm{S})\cdot \mathrm{d}S = 0 \qquad (4)$$

where c represents the volume fraction of fluid, i.e. $c = 0$ for cells by air and the case of $0 < c < 1$ for cells by both fluids and $c = 1$ for cells are filled by liquid.

In this study, the continuity and momentum equations are solved by using *COMET©* software. The numerical scheme used to solve these coupled governing equations is based on a finite volume discretization. All vector quantities, such as vector position, velocity and moment of momentum, are expressed in Cartesian coordinates. A non-staggered arrangement is adopted to define the dependent variables: all physical quantities are stored and computed at the center of cell. The practice of second-order interpolation accuracy is adopted to calculate the field variables at the center of cell-face.

The integral form of governing equation obtained through a finite volume discretization of governing equations is given as follows:

$$\int_V \rho\frac{\partial\phi}{\partial t}\mathrm{d}V + \int_S \rho\phi(\mathbf{v}-\mathbf{v}_S)\cdot\mathbf{n}\mathrm{d}S = \int_S \Gamma(\nabla\phi\cdot\mathbf{n})\mathrm{d}S + \int_V S_\phi \mathrm{d}V \qquad (5)$$

where ϕ the generic field variable, Γ the generic diffusion coefficient, S_ϕ the generic source term. The convective flux of the variable ϕ through the internal cell-face j represents the rate at which it is transported into the control volume by the fluid motion relative to the boundary of cell. Using the Picard iteration method, the generalized convective flux term C_j at cell face j is approximated by the following equation:

$$C_j = \int_S \rho\phi(\mathbf{v}-\mathbf{v}_S)\cdot\mathbf{n}\mathrm{d}S \approx \dot{m}_j\phi_j \qquad (6)$$

where $\dot{m}_j$ the mass flux across the cell face j, ϕ_j represents the generalized field variable at the cell face j. Deferred correction approach is used to calculate the convection term by blending the upwind and central difference schemes to obtain a diagonally dominant matrix after the discretization of the governing equations and computation domain. The blending factor is chosen close to unity to ensure a second-order approximation.

Finally, SIMPLE algorithm is adopted to separate the coupling velocity and pressure, followed by solving the transport equation of front. The liquids in a cell are treated as single effective fluid, whose physical properties vary in space and are calculated in accordance with the volume fraction of liquid in the cell. For example, the density and viscosity are determined by the linear interpolation of the volume fraction in the cell, namely $\varphi = \varphi_l + (1\text{-}c)\varphi_g$ where φ is fluid property in the cell and the subscripts l and g stand for the corresponding liquid and gas property, respectively. Fluids sharing a cell (i.e. $0 < c < 1$) is considered to have the same velocity, pressure, and other properties. Since both liquids are calculated, the grid used to discretize the calculation domain extends over both liquid and gas. The front is implicitly defined at $c = 0.5$. The surface tension is modeled by a continuum surface force model, which employs gradient c to determine the normal vector on the interface pointing from gas to liquid. The determination of surface tension follows the following approach:

$$\mathbf{f}^\sigma = -\sigma\left[\nabla\cdot\left(\frac{\nabla c}{|\nabla c|}\right)\right]\nabla c \qquad (7)$$

where σ indicates the surface tension depending on the working fluids and is considered constant along the interface. The correct prediction of the sharpness of the interface requires an accurate estimate of the convection term in the transport equation of front, where a two-stage scheme is applied to the calculation of the convection term. Details of the mathematical and the numerical scheme can be referenced in our previous work [5].

The fluid properties of water are $\rho = 998.3$ kg/m^3, the viscosity $\mu = 1.002\times10^{-3}$ N s/m^2, and the surface tension $\sigma = 0.074$ N/m, while the air properties are $\rho = 1.188$ kg/m^3, $\mu = 1.824\times10^{-5}$ N s/m^2. The typical grid density is 0.7×10^6 hexahedral cells to discretize the computational domain for a row array arrangement consisting of five micropillars. A body-fitted grid is employed to discretize the computational domain, which is regenerated at every time step to exactly match the computational domain defined by the peeling movement of upper substrate. The deformation of liquid-gas meniscus is then tracked by an interface-capturing approach, in which the numerical grid extends over both liquids and the front is implicitly defined by the location of volume fraction equals to 0.5. The typical time step used in numerical simulations is in tens of nanoseconds to ensure the required numerical stability.

3. RESULTS AND DISCUSSION

Figure 3(a) illustrates the evolution of water front in the case with D_p = 7 µm and ω = 10 rad/s, where microdroplets with similar size are sequentially formed from right to left on the top surface of each micropillar during the dewetting process. In this process, the fluid originally located between the upper substrate and the top surface of micropillar moves upward shortly after the peeling starts. The small amount of water initially filled among micropillars quickly sweeps away by the moving front, which obviously possesses sufficient inertia to overcome the capillary force along the wetted contact line. The dewetting of water occurs from the edge of the top surface of micropillar and results in an island-like fluid region behind the main front. The island-like region is finally detached from the main front because of the surface tension. The fluid remaining on the column of micropillar, which completely detaches from the micropillar edge, slows down its velocity because of the viscous damping of contact surface. Since the surface roughness of micropillar is very small (≈0.17 nm), the difference between advancing and receding contact angles can be ignored [2]. Thus the effect of contact angle hysteresis is neglected in this study. Figure 3(b) shows the calculated time series of velocity vectors for water front moving across micropillar array in the case with D_p = 7 µm and ω = 10 rad/s. The numerical simulations reveal that water above two successive micropillars (right to left) flows in the peeling direction only before the detachment of meniscus. The water left on the top surface of micropillar (right) begins to flow in the opposite direction after the detachment of meniscus, which is explained by the recoiling process due to surface tension effect. Figure 3(c) gives time series of pressure for water front moving across micropillar array in the case with D_p = 7 µm and ω = 10 rad/s. The pressure inside the microdroplet is apparently larger than the ambient pressure. The pressure inside the microdroplet is clearly higher than that of the fluid behind the main front and a relatively high pressure region occurs in the liquid bridge before the detachment. This high pressure region still remains in the microdroplet even after the breakup, where is mainly because of the strong capillary effect of microdroplet with small size.

Figure 4 shows dimensionless of the growth of droplet diameter d_x ($=D_x/D_p$) as function the dimensionless time t^* ($=t\omega$) for different the Ca numbers. The value of d_x reduces with the increases of t^*, where the value of d_x becomes saturated after reaches an equilibrium shape of microdroplet. In the breakup phase, the growth of droplet is mainly determined the surface tension and the inertia force of fluid due to the dewetting process. Then, at the droplet formation phase, the fluid remaining on the column of micropillar slows down its velocity because of the viscous damping of contact surface. The dimensionless time of droplet formation (t_d^*) grows with the increases of

Capillary number. When the value of Ca increases, the viscous force on the top surface of micropillar magnifies, which slows down the movement of water front attached to the top surface of micropillar. Thus, the capillary force is prone to need a long time on microdroplet formation.

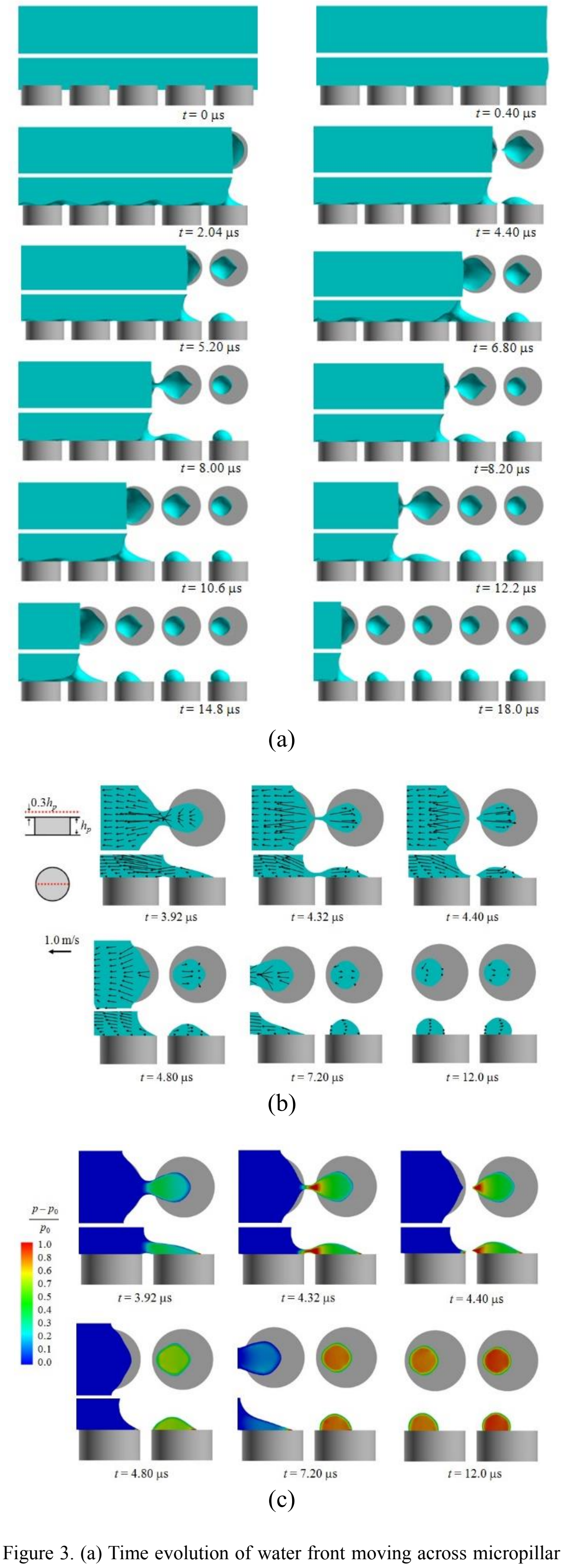

Figure 3. (a) Time evolution of water front moving across micropillar array. (b) Time series of velocity vectors for water front moving across micropillar array. (c) Time series of pressure for water front moving across micropillar array. (top and side views, D_p = 7 µm and ω = 10 rad/s).

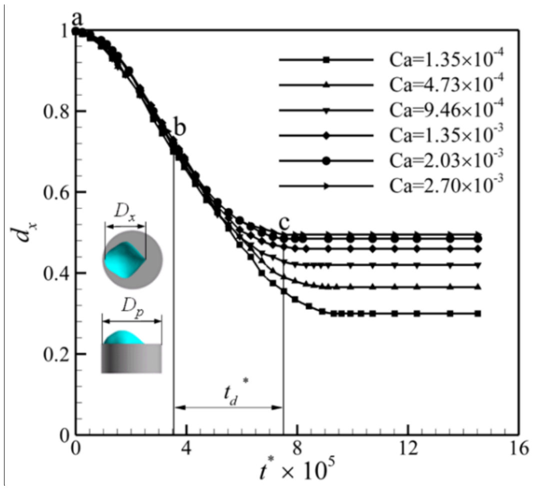

Figure 4. Dimensionless of the growth of droplet diameter as function t^* for the case of D_p= 7 μm

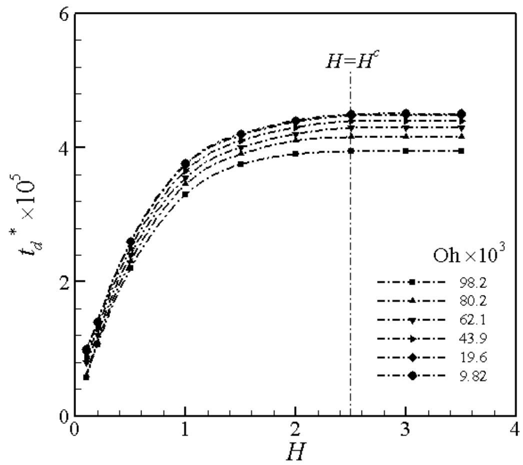

Figure 5. Dependence of t_d^* on H and Oh at Ca=1.35×10^{-3}.

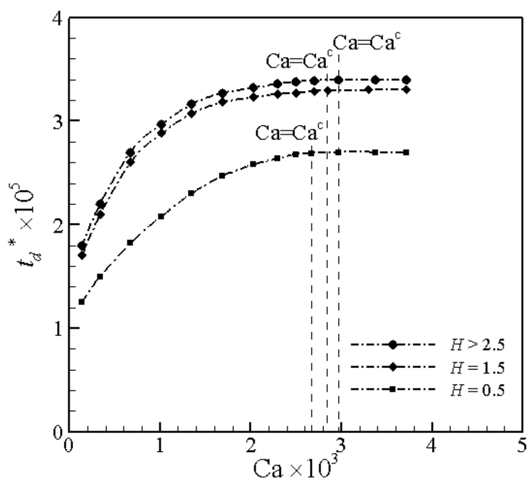

Figure 6. Dependence of t_d^* on Ca and H at Oh=4.39×10^{-2}.

In the dewetting process, the time of droplet formation (t_d) left on the top surface of micropillars mainly depends on D_p, h, ω, L_c, L, ρ, μ, σ, and the contact angle (θ). With the help of dimensional analysis, the dimensionless time of droplet formation (t_d^*) can be expressed as the function of dimensionless group as follows:

$$t_d^* = f(\mathrm{Oh}, \mathrm{Ca}, H, l, \theta) \tag{8}$$

where $t_d^* = t_d\omega$, $\mathrm{Oh} = \mu/(\rho\sigma D_p)^{1/2}$, $\mathrm{Ca} = \mu L_c\omega/\sigma$, $l = L/D_p$, and $H = h/D_p$.

Figure 5 depicts the dependence of dimensionless formation time (t_d^*) on the dimensionless liquid thickness (H) for different Ohnesorge numbers at Ca=1.35×10^{-3}. The value of t_d^* increase with H for small liquid thickness at a given Ohnesorge number, where t_d^* approach to asymptotic values provided H reaches a critical value (H^c) of 2.5. For small H, fluid meniscus is apparently influenced by the top surface of micropillar, as well as the upper coverslip. This results in small droplets with short formation time, because of the competition of capillary effect between micropillar and coverslip. As H increases, the influence of upper coverslip on droplet formation diminishes, and it directly leads to the growth of droplet diameter and the increase in formation time. For sufficiently large H, the influence of the upper substrate on fluid meniscus in the vicinity of micropillar becomes negligible. For a given liquid thickness, the microdroplet size increases with the decline of Oh number, which is the direct consequence of prevailing capillary effect over the viscous damping at small Oh number. This leads to the growth of droplet formation time.

Figure 6 demonstrates the dependence of t_d^* on Capillary numbers at Oh=4.39×10^{-2}. The dimensionless formation time (t_d^*) increase with Capillary number, where their values varies little provided Ca reaches a critical value (Ca^c). At large capillary number, the main meniscus already detaching from micropillar moves much faster than the meniscus on the micropillar, which causes a large captive region on the top surface of micropillar. This clearly gives large volume of fluid on the micropillar behind the main meniscus and hence has positive impact on the size of droplet. When the top surface of micropillar is completely captive, the diameter of droplet will reach its maximum value, so the formation time of droplet also will reach its maximum value, which implies Ca = Ca^c. For H < 2.5, the critical Capillary number (Ca^c) grows with the dimensionless liquid thickness (H), while for H ≥ 2.5, Ca^c is almost independent of H.

Simulation results show the time of droplet formation on the column of micropillar depends on the parameters in the dewetting process. Using the least square fitting method, the critical Capillary number (Ca^c) and the dimensionless time of droplet formation (t_d^*) can be expressed as

$$\mathrm{Ca}^c = f_3(\mathrm{Oh})\, g_3(\theta)\, h_3(H^*) \tag{9}$$

$$t_d^* = f_4(\mathrm{Oh})\, g_4(\theta)\, h_4(H^*) C_4(\mathrm{Ca}^*) \tag{10}$$

where $H^* = H/H^c$, $\mathrm{Ca}^* = \mathrm{Ca}/\mathrm{Ca}^c$, and the functions f_3, g_3, h_3, f_4, g_4, h_4, C_4, expressed as a sixth-degree polynomial. The influence of l on the time of droplet formation in a linear arrangement is negligible.

Figure 7 shows the theoretical calculation of the dimensionless time of droplet formation (t_d^*) expressed as function of H^*, where the accuracy of the present numerical model is verified by available measurements of the dimensionless droplet diameter [6,7].

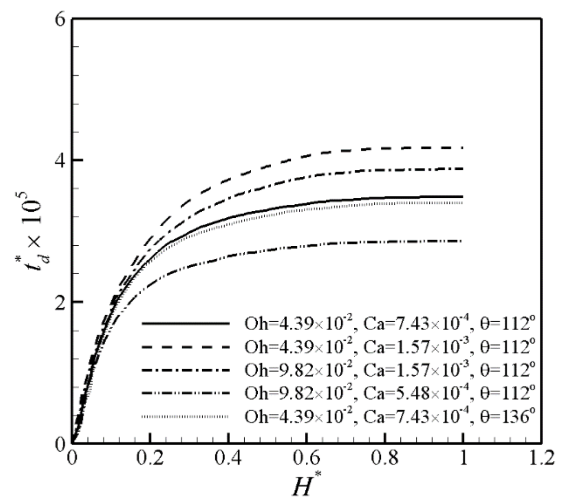

Figure 7. The calculations results of the dimensionless time of droplet formation.

4. CONCLUSIONS

We theoretically investigate the dynamic behavior of microdroplet formation on micropillar surface. The simulation results show that the time of microdroplet formation depends on the parameters in the dewetting process. Using least square fitting method, the equation of dimensionless droplet formation time can be determined by the product of functions of Oh, θ, H^*, and Ca^*. Successful numerical prediction of microdroplet size and its formation time on the dewetting process not only offers insights to the mechanism of microdroplet formation but also reveals its great potential as a design tool for creating microdroplets for device development.

REFERENCES

[1] J. H. Xu, S. W. Li, J. Tan, and G. S. Luo, “Correlations of droplet formation in T-junction microfluidic devices: from squeezing to dripping,” *Microfluid Nanofluid*, vol. 5, no. 6, pp. 711-717, 2018.

[2] Z. Wang, P. Zhang, B. Kirkland, Y. Liu, and J. Guan, Microcontact printing of polyelectrolytes on PEG using an unmodified PDMS stamp for micropatterning nanoparticles, DNA, proteins and cells, S*oft Matter, v*ol 8, no 29, pp. 7630-7637, 2012.

[3] C. H. Lin, J. Guan, S. W. Chau, S. C. Chen, and L. J. Lee, “Patterning nanowire and micro-/nanoparticle array on micropillar-structured surface: Experiment and modelling,” *Biomicrofluidics*, vol. 4, no. 1, pp. 034103-1-034103-15, 2010.

[4] C. H. Lin, J. Guan, S. W. Chau, and L. J. Lee, “Experimental and numerical analysis of DNA nanostrand array formation by molecular combing on microwell patterned surface,” *Journal of Physics D: Applied Physics*, vol. 42, no. 2, pp. 025303-1-025303-8, 2009.

[5] B.A. Dwiyantoro and S.W.Chau, ”The dependence of microdroplet size on the parameters governing the dewetting process on circular micropillar arrays,“ *Journal of Mechanical Science and Technology*, vol 27, no. 7, pp. 2005-2013, 2013.

[6] J. Guan, B. Yu, and L. J. Lee, “Forming highly ordered arrays of functionalized polymer nanowires by dewetting on micropillars,” *Advanced Materials*, vol. 19, pp. 1212-1217, May 2007.

[7] J. Guan, N. Ferrell, B. Yu, D. J. Hansford, and L. J. Lee, “Simultaneous fabrication of hybrid arrays of nanowires and micro/nanoparticles by dewetting on micropillars,” *Soft Matter*, vol. 3, pp. 1369-1371, 2007.

Overdriven Transmission System for Reducing Carbon Dioxide Emission from Vehicles

Harwin Saptoadi

Department of Mechanical and Industrial Engineering, Universitas Gadjah Mada,
Jl. Grafika 2, Yogyakarta 55281, Indonesia

*Corresponding e-mail: harwins@ugm.ac.id

ABSTRACT – The research is aimed to reveal the advantages of overdriven transmission systems, which is able not only to reduce fuel consumptions during high speed run but also to lower CO_2 emissions. Data are collected from a typical city car on a chassis dynamometer while its torque, power and AFR (air-fuel ratio) are recorded. The calculations are carried out at normal speeds (using 3rd gear) and overdriven speeds (using 4th and 5th gears). Two types of gasoline, with RON (research octane number) of 88 and 92, are used. After determining the fuel consumption, the emitted CO_2 can be predicted. It is advisable to switch the gear up because the CO_2 emission will be lowered. The decrease varies 31% - 35% if the 4th gear is used instead of maintaining the 3rd gear, while such emission drops amount to 45% - 50% if the 5th gear is applied rather than the 3rd gear. In the same gear position, higher speed will result in more CO_2 emission according to a linear correlation. However, the quantity of emitted CO_2 per kilometer does not change with the car speed, but with the gear position. They amount to around 400 g/km at the 3rd gear, about 273 g/km at the 4th gear, and only 220 g/km at the 5th gear.

Keywords: CO_2 emission, Dynamometer, Fuel consumption, Gear switch-up, Overdriven transmission.

1. INTRODUCTION

Transportation of persons and goods requires fuels and energy. Unfortunately, energy consumption is always proportionally related to emission of greenhouse gases, especially CO_2 (carbon dioxide), due to combustion of hydrocarbon fuels. CO_2 emission from gasoline engines dominates over that of diesel engines in urban areas, accounting for 80% - 90% of the total, whereas diesel engines are relatively more important in rural areas by contributing 30% - 40% of the whole [1]. Another case shows that around 2.4 million private cars produce approximately 26,372 tons of CO_2 per day, which is about 88% of the total CO_2 emission from motorized vehicles in the city [2]. Another research group has compared CO_2 emissions of light-duty vehicles during rush hour and work zone congestions with those in free-flow conditions. The emission factors of CO_2 during work zone congestions, rush hour jams and free-flow traffics are 339 ± 19 g/mi, 293 ± 17 g/mi and 287 ± 17 g/mi, respectively [3]. Most recently, the OTAQ releases a fact sheet regarding CO_2 emission from a typical passenger vehicle, which mentions that the average emission is 404 g/mi (251.034 g/km) and 8,887 g/gallon (2,347 g/l) [4].

In order to cope with the GHG problem, car manufacturers introduced some proven technologies. One example is utilization of gasoline-ethanol blends. The higher the ethanol fraction, the more gasoline will be saved and the more CO_2 emission can be avoided. Using E10, for instance, the avoided CO_2 emission amounted to 13,102 tons in 2007 [5]. Another effort is application of light-weight materials, such as fiberglass-reinforced thermoplastics, for automobile body and chassis. The lighter the vehicle, hence less power is required, smaller quantity of gasoline will be burned and less CO_2 emission will be produced. Reducing weight by 20% causes a significant decrease of CO_2 emission up to 28% [6].

The main theme of this work is application of a fuel-saving power transmission system, called overdriven transmission system, assembled in almost all automobiles. Overdrive allows the engine to operate at lower speed for a given car velocity [7]. Lower engine speed will lead to less air brought to the cylinders and proportionally less fuel and emission as well. A previous research employed a chassis dynamometer to identify fuel consumptions of a typical city car during normal and high velocities. The former commonly use the 3rd gear, while the latter apply either the 4th or the 5th gears [8]. The present study deals further with CO_2 emissions from the city car. The research is aimed to reveal quantitatively the advantages of overdriven transmission systems in most vehicles. It is expected that the research result will contribute for convincing car drivers to behave more efficiently and environmental friendly.

2. METHODOLOGY

A city car with a 1000 cc gasoline engine and 5-speed manual transmission, is selected as a sample. The car is run statically on an AWD 1200 chassis dynamometer at various engine speeds and 3 gear positions, i.e. the 3rd, 4th and 5th gears. Gear ratio at the 3rd gear is 1.25, whereas at the 4th and 5th gears are 0.865 and 0.707, respectively. The two highest gears are called overdriven, since their gear ratios are less than 1. The test delivers engine performance characteristics, such as torques, powers and AFR (air-fuel ratio) as a function of engine rotational speed (as well as vehicle speed) and gear position. Two locally available gasolines are used, i.e. RON 88 and RON 92 [8].

The air consumption $\dot{m}_a$ strongly depends on the number of suction, which is effected by the piston movement and proportional with the engine rotation N. It is calculated with the help of the equations:

$$\dot{m}_a = \eta_V \rho_a V_d \frac{N}{2} \quad (1)$$

$$\dot{m}_f = \frac{\dot{m}_a}{AFR}, \quad (2)$$

Gasoline consists of numerous hydrocarbon compounds, however it is a common practice to regard it as a single compound for convenience. Normally octane (C_8H_{18}) is selected to represent the fuel [9]. Complete combustion is assumed because there is always excess air supplied to engine cylinders.

$$2\ C_8H_{18} + 25\ O_2 \rightarrow 16\ CO_2 + 18\ H_2O \quad (3)$$

$$228\ \text{kg}\ C_8H_{18} + 800\ \text{kg}\ O_2 \rightarrow$$

$$704\ \text{kg}\ CO_2 + 324\ \text{kg}\ H_2O \quad (4)$$

$$\dot{m}_{CO2} = 3.0877\ \dot{m}_f \quad (5)$$

3. RESULTS AND DISCUSSION

The measurement results are displayed. The figures reveal the performance at various gear position using different fuel. It is obvious that higher wheel power can be produced at higher speed. A maximum power occurs in a certain speed at the 3rd gear only, while at the 4th and 5th gears the measurements end before the maximum power is discovered. At the 5th gear the average torque is higher (around 80 Nm) compared to that of the 4th gear (about 76 Nm) and also the 3rd gear (roughly 72 Nm). It is apparent that in all cases the AFR is initially higher (between 13 and 14), but with the increase in speed the AFR becomes normal (slightly changes between 12 and 13). High AFR indicates fuel economy due to lean mixture, i.e. fuel fraction in the reactants is relatively less than it should be, however the generated power will be consequently lower. Subsequently, after several calculations using the Equations 1, 2 and 5, the results are shown in the Figures 1, 2 and 3, along with Table 1. It is observable that there is no substantial difference between RON 88 and RON 92 gasolines in producing CO_2. The more expensive RON 92 gasoline is not necessarily better.

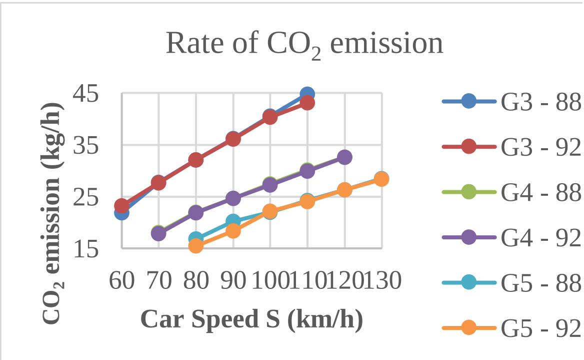

Figure 1 CO_2 emission rate vs. car speeds

The rate of CO_2 emission as a function of the vehicle speed is displayed. The dependencies seem to be almost linear and can be represented by simple equations appeared in the Table 1. It is noticeable that the 3rd gear drives always emit higher rate of CO_2 emission, whereas switching-up to the 4th gear can reduce it between 31% and 35%, but if the 5th gear is selected instead of the 4th the improvement can be even better, i.e. between 45% and 50%. Thus the advantages of overdrive transmission system can be demonstrated quantitatively. It is apparent as well that if the gear position is maintained, higher car speed S will release carbon dioxide more intensively. Therefore, lower speed is desired.

Table 1: CO_2 emission as a function of car speed S

No	Gear – RON	Equation	Correlation coef-ficient
1	G3 – 88	$\dot{m}_{CO2}$ = 0.448 S – 4.220	0.996
2	G3 – 92	$\dot{m}_{CO2}$ = 0.402 S – 0.511	0.995
3	G4 – 88	$\dot{m}_{CO2}$ = 0.285 S – 1.331	0.995
4	G4 – 92	$\dot{m}_{CO2}$ = 0.286 S – 1.520	0.994
5	G5 – 88	$\dot{m}_{CO2}$ = 0.225 S – 0.711	0.992
6	G5 - 92	$\dot{m}_{CO2}$ = 0.256 S – 4.517	0.985

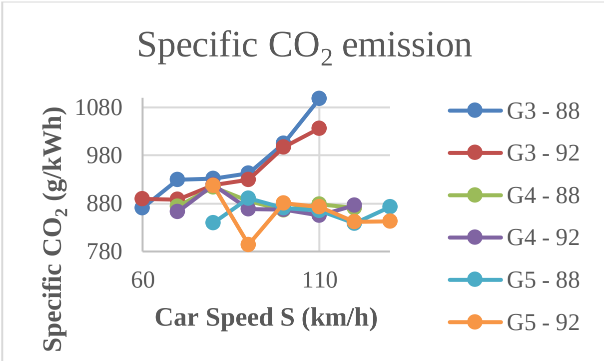

Figure 2 CO_2 per generated power vs. car speeds

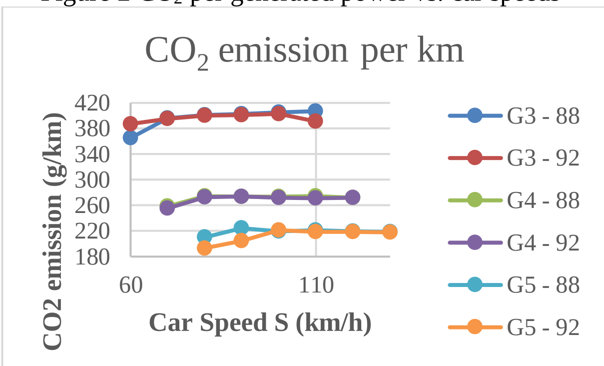

Figure 3 CO_2 emission per traffic distance vs. car speeds

Figure 2 is presented because it is important to consider Specific CO_2 emission which shows the amount of CO_2 emission for each unit of generated power. Here the amount of CO_2 emission from running vehicles is represented by specific CO_2 emission (g/kWh) rather than just CO_2 emission (kg/h). Information regarding CO_2 emission only may mislead, because it will certainly low if engines produce low power (at low speed). In the reality, car drivers demand high power in order to drive rapidly and consequently the CO_2 emission will be high. At normal speeds (between 60 – 90 km/h, using the 3rd gear) the specific CO_2 emissions amount to between 880 g/kWh and 930 g/kWh, but after shifting up to the 4th gear it is apparently reduced to around 880 g/kWh again, otherwise it will go up to > 980 g/kWh. Further shifting up to the 5th gear does not improve the specific CO_2 emissions significantly, except at velocities of > 120 km/h, which is not recommended for safety reason.

It is equally critical to state the total amount of CO_2 emission per kilometer travelled distance, as displayed by Figure 3. Initially, at low speeds, the emission is lower, but then it increases slightly with higher speeds before achieving a nearly constant value. Yet again, the 3rd gear presents the highest CO_2 emission per kilometer, i.e. around 400 g/km when $S \geq 70$ km/h. The 4th gear will be definitely better, because it emits about 273 g/km when $S \geq 80$ km/h, which is an approximately 32% reduction. Unfortunately, the suggested value for a typical passenger vehicle is 251 g/km, which is still lower than those. The best one is the 5th gear, which produces roughly 220 g/km when $S \geq 100$ km/h and thus acceptably below the suggested limit. Probably, this is one of the reasons why the 5th gear is provided in the car.

4. CONCLUSIONS

Based on those investigations, the following essential phenomena can be mentioned:

1. The RON (Research Octane Number) does not play any significant role in the CO_2 emission. The more expensive RON 92 gasoline is not essentially better.
2. The highest overdriven position, i.e. the 5th gear, emits the least CO_2, whereas another overdriven position, i.e. 4th gear, produces more CO_2. The normal 3rd gear position generates the largest amount of CO_2. The 5th gear is therefore preferable.
3. The rate of CO_2 emission is a positive function of vehicle speeds. The correlation seems to be linear and can be represented by simple equations. In order to reduce the speed, higher gear position should be applied when possible.
4. The amount of CO_2 emission per kilometer travelled distance is nearly constant. Likewise, the 3rd gear produces the highest, while the 4th gear is definitely better, and the best one is the 5th gear. The CO_2 emission with the 5th gear is below the suggested limit.

ACKNOWLEDGEMENT

The author appreciates the research assistant and also his former bachelor student, Fadhli Akbar, who cautiously carried out the measurements. The research is generously supported by the Department of Mechanical and Industrial Engineering, Universitas Gadjah Mada.

REFERENCES

[1] B.C. McDonald, Z.C. McBride, E.W. Martin, R.A. Harley, “High-resolution mapping of motor vehicle carbon dioxide emissions”. J. Geophysical Res.: Atmospheres, 119, pp. 5283-5297, 2014.

[2] A. Kakouei, A. Vatani, A.K Idris, “An estimation of traffic related CO_2 emissions from motor vehicles in the capital city of Iran”. Iranian J. Environ. Health Sci. Eng., 9 (1), 13, 2012.

[3] K. Zhang, S. Batterman, F. Dion, “Vehicle emissions in congestion: Comparison of work zone, rush hour and free-flow conditions”. Atmospheric Environment, 45, pp. 1929-1939, 2011.

[4] OTAQ (Office of Transportation and Air Quality), US-EPA, *Greenhouse gas emissions from a typical passenger vehicle*. EPA-420-F-18-008, 2018.

[5] D. Surroop, Z. Soheea, “Carbon dioxide emissions reduction estimates: Potential use of biofuels in Mauritian transport sector for cars and dual cars”. University of Mauritius Research Journal, vol. 16, pp. 512-527, 2010.

[6] A. Elalem, M.S. El-Bourawi, “Reduction of automobile carbon dioxide emissions”. Int. Journal of Material Forming, vol. 3, Suppl. 1, pp. 663-666, 2010.

[7] K. Pimparkar, M. Rajput, C. Sonawane, A. Sonawane, V. Randive, “Automatic kinematic linkage transmission using overdrive”. Int. Journal of Advances in Scientific Research and Engineering, vol. 3, issue 4, pp. 145-149, 2017.

[8] H. Saptoadi, “Fuel efficiency of vehicles during normal and overdriven speeds”, 5th Putrajaya International Built Environment, Technology and Engineering Conference, Kuala Lumpur, 26 November 2018. e-ISBN: 978-967-2072-30-0.

[9] Y.A. Cengel, M.A. Boles, *Thermodynamics: An engineering approach*, 4th edition. New York, McGraw-Hill; 2002.

Thermodynamic Analysis of Supercritical Organic Rankine Cycle with Propane (R-290) as a Working Fluid

Harmen[1,2,*], Willy Adriansyah[1], Abdurrachim[1], Ari Darmawan Pasek[1,*]

[1)] Faculty of Mechanical and Aerospace Engineering, Institut Teknologi Bandung, Jl. Ganesha no. 10, Bandung (40132), Indonesia
[2)] Department of Mechanical Engineering, Universitas Lampung, Jl. Sumantri Brojonegoro no. 1, Gedongmeneng, Bandarlampung (35145), Indonesia

[*]Corresponding e-mail: harmen.1969@eng.unila.ac.id and aripasek@gmail.com

ABSTRACT – Propane is a potential working fluid for supercritical ORC that has lower critical temperature than other hydrocarbons and environmentally friendly. In this paper a thermodynamic analysis is carried out to investigate performance of SORC system with propane as working fluid. Specific isentropic net power output and thermal efficiency of system are calculated for various sub- and super-critical pressures (0.75Pcrit – 1.25Pcrit) and various turbine inlet temperatures (80°C – 150°C). The system is analyzed to obtained higher power and efficiency. The power and efficiency were also compared with SORC system that used R-1270, R-134a and R-227ea as working fluid. The results show that the performance of system using propane is better than the system using R-1270, R-134a and R-227ea. The maximum power and efficiency of the system using propane is 71.15 kJ/kg and 15.08% while by using R-1270 is 67.61 and 14.81%; 37.00 kJ/kg and 15.42% for R-134a and 24.72 kJ/kg and 13.39% for R-227ea.

Keywords: Propane; Hydrocarbon; Organic fluid; Supercritical; Organic Rankine cycle.

1. INTRODUCTION

Supercritical organic Rankine Cycle (SORC) systems are one step ahead in terms of power generation technology of low-grade heat resources. One of the reasons for this, beside the higher thermal efficiency [1], is the thermal match of heat source and working fluid inside the heat exchanger [2].

Due to its good thermal performance and environmental friendliness, hydrocarbons are widely used as working fluid in the ORC systems. In supercritical ORC systems, the use of hydrocarbons is also highly considered because the critical temperature is higher than hydrofluorocarbons [3].

This work is propose a thermodynamic analysis for propane (R-290) as a working fluid in a subcritical ORC (ORC) and supercritical ORC (SORC) system. The main purpose of the research is to investigate thermodynamic performance especially net specific isentropic power output and isentropic thermal efficiency of SORC system. The thermodynamic performance is also compare with propylene (R-1270), R-134a and R-227ea as working fluid.

2. METHODOLOGY

In this study four refrigerants or organic fluids were chosen as working fluids in the ORC and SORC system as presented in Table 1. The critical temperature of the four organic fluids is not much different, which is around 100 °C. So that it can be used for SORC systems with low temperature heat sources (< 150 °C).

Table 1 Critical pressure and temperature of the working fluid [4] and environment properties [5].

Fluids	p_{crit}, MPa	T_{crit}, °C	GWP	ODP
Propane	4.25	96.74	3	0
Propylene	4.56	91.06	2	0
R-134a	4.06	101.06	1430	0
R-227ea	2.93	101.75	3580	0

Environment impact (GWP and ODP) of fluids are adopt from fifth assessment report of IPCC 2014, too.

Thermodynamic analysis of ORC and SORC system are doing based on simple ORC as illustrated in Figure 1 and its *T-s* diagram is shown in Figure 2.

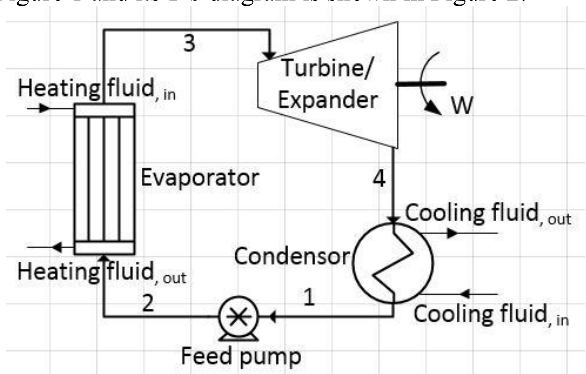

Figure 1 schematic diagram of simple supercritical/subcritical ORC

The changes of state of the working fluid in the ORC and SORC system are the same as in the Clausius-Rankine cycle with water as the working fluid. In the ideal condition, these are:

- 1 – 2: Isentropic pumping process
- 2 – 3: Isobaric heat addition
- 3 – 4: Isentropic expansion
- 4 – 1: Isobaric heat rejection

In this thermodynamic investigation we want to obtain the net specific isentropic work and isentropic thermal efficiency of the both sub and supercritical ORC system. Equations 1-6 we used for analysis.

Pump work, $$w_p = h_2 - h_1 \tag{1}$$

Heat input, $q_{in} = h_3 - h_2$ (2)
Turbine work, $w_t = h_3 - h_4$ (3)
Heat realease $q_{out} = h_4 - h_1$ (4)
Net specific work, $w_{net} = w_t - w_p$ (5)
Thermal efficiency, $\eta_{th} = \frac{w_{net}}{q_{in}} = \frac{q_{in}-q_{out}}{q_{in}}$ (6)

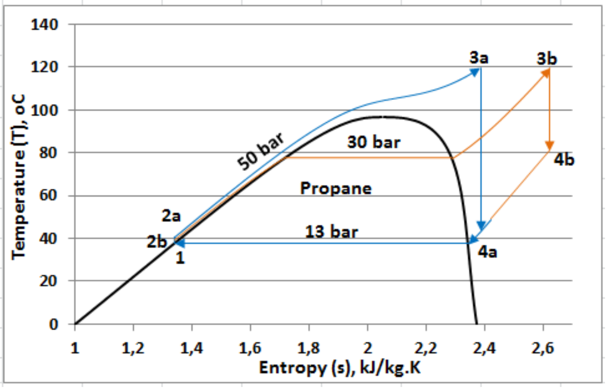

Figure 2 *T-s* diagram for simple supercritical (blue line) and subcritical (orange line) ORC of propane.

Thermodynamic performances of systems are calculated for various sub- and super- critical evaporation pressure ($0.75P_{crit}$ – $1.25P_{crit}$) and turbine inlet temperatures is vary around 80°C – 150°C. Evaporation pressure is increase gradually in the range of $0.05P_c$ Condensation pressure of the ORC system for each working fluid is determined based on its condensation temperature whose value is not less than 37.5 °C. Then, the performances for each specific pressure, temperature, and working fluid is compared to each other to find the optimal condition of ORC system.

3. RESULTS AND DISCUSSION

3.1 Net specific isentropic power output

Figure 3 shows the influence of evaporation pressure and inlet turbine temperature to net specific isentropic power output of ORC system with propane as working fluid.

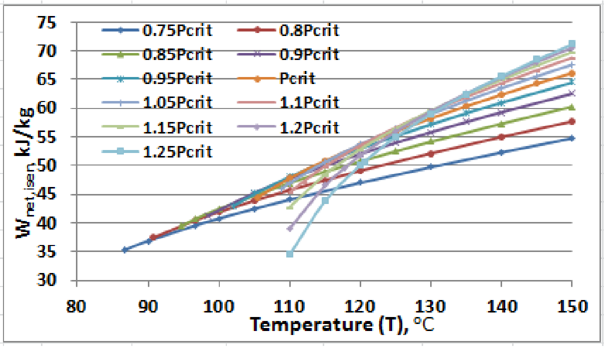

Figure 3 Net specific isentropic power output of ORC and SORC systems with propane as working fluid for various evaporation pressure and turbine inlet temperature.

From the Fig. 3, it can be seen that increasing evaporation pressure and the inlet turbine temperature will increase the net specific work of ORC system. It should be noted that net specific work output will drop if the working fluid quality exits the turbine at the mixture state condition. Therefore, the entropy of the working fluid entering the turbine must be higher than the saturated entropy at the condensation pressure.

The highest net specific isentropic work is 71.15 kJ/kg which is obtained in evaporation pressure of 1.25 P_{crit} or 5.314 MPa and in the temperature of inlet turbine is 150 °C. The minimum net specific isentropic work is 34.45 kJ/kg, its found in evaporation pressure of 5.314 MPa too and in the temperature of inlet turbine 110 °C. The net specific work is fall due to quality of vapor exit the turbine is bad (quality = 0.78)

The comparison of net specific isentropic work of the ORC and SORC systems using R-290, R-1270, R-134a, and R-227ea as working fluid to turbine inlet temperature are shown in Figure 4. From the Figure 4 it can be seen that the specific net power output of the ORC system with the propane as working fluid is better than propylene, R-134a, and R-227ea, respectively. Vetter et. al. [6] carried out thermodynamic analyzes of R-290, CO_2 and various refrigerants, for geothermal sources with temperatures below 150 °C they also concluded that propane is the best working fluid. The maximum net specific isentropic work for R-1270 is 67.61 kJ/kg, 37.0 kJ/kg for R-134a, and 24.72 kJ/kg for R-227ea.

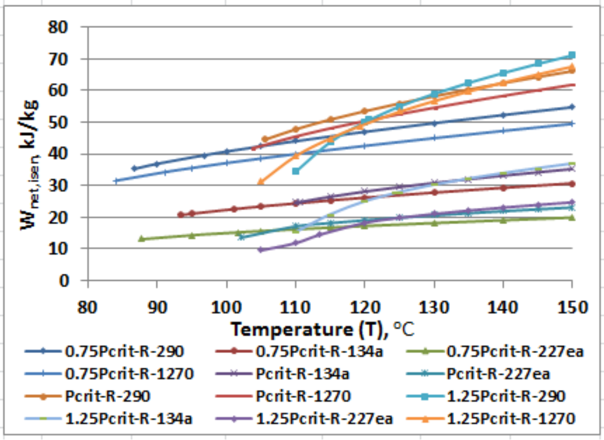

Figure 4 Comparison of the net specific isentropic work of ORC system for different working fluid.

3.2 Isentropic thermal efficiency

The isentropic thermal efficiency of the ORC system with propane as working fluid for each evaporation pressure are shown in Figure 5. Increased evaporation pressure will increase thermal efficiency of the system. The efficiency of system for pressure below the critical pressure tends to stagnant and goes to decrease. While for the pressure above the critical pressure, the efficiency of the system still continues to increase with increasing fluid temperature at inlet turbine.

The maximum efficiency is 15.08% that found at the pressure and temperature of inlet turbine $1.25P_{crit}$ and 150 °C, respectively. The minimum value of efficiency is 10.17% at subcritical pressure $0.75\%P_{crit}$ and temperature of inlet turbine 86.63 °C.

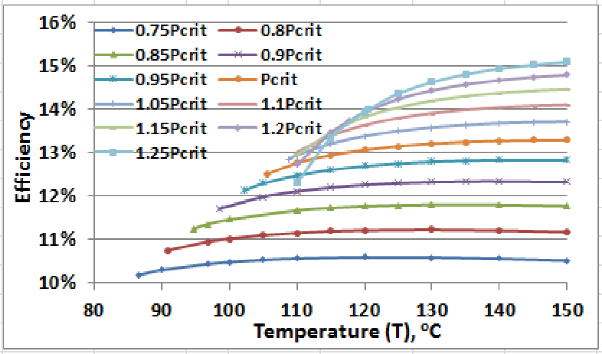

Figure 5 Efficiency of the ORC and SORC system with R-290 as working fluid for various evaporation pressure and turbine inlet temperature.

Figure 6 shows comparison of the thermal efficiency of ORC system for different working fluid for the evaporation pressure of $0.75P_{crit}$, P_{crit} and $1.25P_{crit}$.

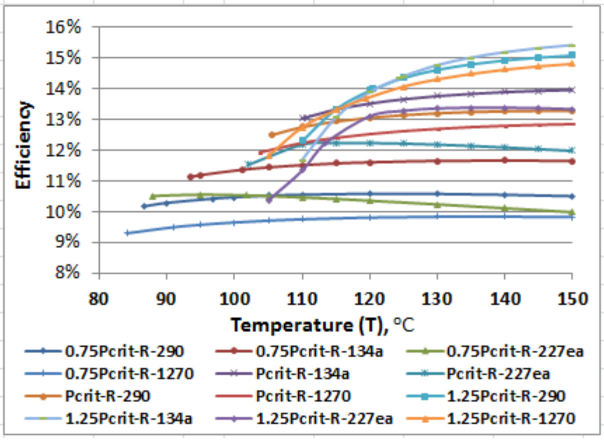

Figure 6 Comparison of the thermal efficiency of ORC system for different working fluid

The thermal efficiency of SORC with R-134a as the working fluid is the highest among the three other working fluids. Its isentropic thermal efficiency reaches 15.42%. the maximum thermal efficiency of others fluid is 15.08% for R-290, 14.81% for R-1270 and 13.39% for R-227ea.

4. CONCLUSIONS

This paper present thermodynamic analysis of four organic fluid as working fluids with almost the same critical temperature for both subcritical and supercritical ORC system. Generally the supercritical ORC system provides better both net specific isentropic work and thermal efficiency than the subcritical ORC system. For heat sources with low temperatures, less than 150 °C, the SORC system with propane as working fluid deliver better net specific isentropic work and thermal efficiency than the ORC system that using propylene, R-134a, and R-227ea as working fluids.

In this study, it was concluded that increased the evaporation pressure and temperature inlet of the turbine will increase both the net specific isentropic work and thermal isentropic efficiency. The net specific isentropic work and thermal isentropic efficiency will drop dramatically if the state of working fluid exit of the turbine, come to in the saturation dome. So, the entropy of the working fluid enter the turbine must be greater than the saturated vapor entropy at the condensing pressure.

ACKNOWLEDGEMENT

Authors would like to acknowledge to the Indonesian Ministry of Research, Technology, and Higher Education for the PTUPT research grant (contract No. 2/E1/KP.PTNBH/2019), 2019 fiscal year.

REFERENCES

[1] S. Karellas, A. Schuster, “Supercritical Fluid Parameters in Organic Rankine Cycle Applications”. Int. J. of Thermodynamics. 11, pp. 101–108, 2008.

[2] M. Gleinser and C. Wieland, “The Misselhorn Cycle: Batch-Evaporation Process for Efficient Low-Temperature Waste Heat Recovery”. Energies. 9, pp. 337–350, 2016.

[3] X. Dai, L. Shi, Q. An, W. Qian, ”Screening of hydrocarbons as supercritical ORCs working fluids by thermal stability”. Energy Conversion and Management. 126, pp. 632–637, 2016.

[4] E. W. Lemmon, M. O. McLinden, and M. L. Huber, “NIST standard reference database 23: Reference Fluid Thermodynamic and Transport Properties-REFPROP, version 9.1.” National Institute of Standard and Technology, Standard Reference Data Program, The U.S. secretary of Commerce, 2013.

[5] C. Song, M. Gu, Z. Miao, C. Liu, and J. Xu, Effect of Fluid Dryness and Critical Temperature on Trans-critical Organic Rankine Cycle, *Energy*, Vol. 174, pp. 97-109, 2019.

[6] C. Vetter, H. J. Wiemer, D. Kuhn, “Comparison of sub- and supercritical Organic Rankine Cycles for power generation from low-temperature/low-enthalpy geothermal wells, considering specific net power output and efficiency”. Applied Thermal Engineering 51, 871–879, 2013.

Sound Transmission Loss of Multiple Layer Car Dash Panel Insulators

M. Z. Khari[1], N. A. Abdul Jalil[1,*], Z. A. Zulkefli[1]

[1)] Sound and Vibration Research Group, Department of Mechanical and Manufacturing Engineering,
Faculty of Engineering, Universiti Putra Malaysia,
43400 UPM Serdang, Selangor, Malaysia.

*Corresponding e-mail: nawalaswan@upm.edu.my

ABSTRACT – Application of multi-layer with various thicknesses can improve the sound insulation properties of dash panels. The objective of this paper was to measure the Sound Transmission Loss (STL) for a multi-layer dash panel insulator. Three (3) samples of multilayer dash panel insulator were tested – Sample 1 (thickness, t = 25mm), Sample 2 (t = 28mm), and Sample 3 (t = 33mm). Each sample incorporated varying thickness of Ethylene Propylene Diene Terpolymer (EPDM) layer. All samples were tested to measure the STL using an Impedance Tube. The results showed that the measured STL was better for a thicker EPDM layer (Sample 3), when compared to a thinner EPDM layer (Sample 2). The measured STL for Sample 3 was more than 40dB and up to 50dB at frequencies greater than 2kHz and up to 6kHz. The EPDM layer has a more pronounced impact on STL (Samples 2 and 3) when compared to the absence of the EPDM layer (Sample 1).

Keywords: Dash Panel Insulator; Sound Transmission Loss; Impedance Tube Testing

1. INTRODUCTION

A common dash insulator is made up of barrier (i.e. a heavy layer) of Ethyl Vinyl Acetate (EVA), Poly Vinyl Chloride (PVC) or Thermo Plastic Olefin (TPO) materials. The mass of the heavy layer is indicated in terms of surface density which is in the range of 1.2 - 7.3kg/m^2 of decouple-layer to boost the performance of the dash insulator. The decouple layer is normally a sound package material such as foams or felts or a mixture of both. The thickness of the decouple layer varies from 6mm to 25mm [1].

One of the properties that determine both sound absorption and sound transmission of a material is the specific flow resistance per unit thickness. It determines how easy air can enter a porous structure, as well as the level of resistance the air meets within the material structure. It is an inherent property of the material, and not related to the area of the tested material. Commonly, when sound travels through these materials, friction will lower its amplitude, as the waves try to move through the tortuous passages within the material, converting sound energy into heat [2 - 5].

According to Jain *et al.* [6], sound transmission loss (STL) is the result of an interplay between mass, stiffness and damping of the material. The STL of a panel is contained by rigidity, double wall resonance dip, mass law, coincidence dip, and damping restricted region. These factors might influence the performance of the barrier and gives poorer performance at all frequency series. Thus, it is crucial to recognize the source frequency range and consider these criteria while designing the firewall assembly.

Transmission loss performance of limp, non-rigid materials are directly related to its surface density or mass, and are governed by the mass law [3]. This means greater amount of energy is required to set it in motion. Doubling of the mass will result in a 6dB reduction in sound level transmitted through it. The firewall assembly made up of steel plate and dash panel insulator, acts as a mass-spring-mass system having the same frequency range as the engine's operational resonance frequency, from 100Hz to 500Hz. The purpose of this arrangement is for the firewall assembly to reduce sound at the resonance frequency, while still maintaining its performance at middle and higher frequencies. The efficiency of noise barrier can be improved to with appropriate selection of decouple, heavy layer density and use of analysis tool [6].

To that end, the objective of this paper was to measure the STL of a multi-layer dash panel insulator, so as to determine the optimum noise barier for car cabin.

2. METHODOLOGY

All the three material construction consist of either two and three decouple layers. The thickness of the decouple layers ranged from 25mm to 30mm. The layers were made up from a combination of needle punched felt blends with two density variations, 750g/m^2 and 1500g/m^2, and Ethylene Propylene Diene Terpolymer (EPDM) with two thickness variations, 1.5mm and 3mm. These are commonly used material for dash panel insulator in cars. Both materials were supplied by a supplier in roll form, with thickness of 10mm to 15mm for needle punched Felt blends, and 1.5mm for the EPDM (see Figures 1 and 2).

During actual production process, these materials will be layered together using adhesive and lamination before being compressed using forming mould. The compressed decouple layer then brought to either trimming or water jet cutting process for making holes or access to surrounding parts. The typical thickness after compression for insulator dash panel ranging from 6mm to 25mm according to Jain *et al.* [1] which varies depending on design and vacant space available between firewall and surrounding parts. For this study, tested sample only consisted of layers of two or three materials without compression. Details of the proposed samples are listed in Table 1. Three test samples for each material construction are cut into 29mm diameter, the same inner diameter with impedance tube body.

Figure 1: Felt in roll form with approximation of 10mm – 15mm of thickness

Figure 2: EPDM in roll form with approximation of 1.5mm of thickness

Details of the test samples are listed in Table 1. Three test samples for each material construction were cut into 29mm diameter (see Figure 3), which is the size of the inner diameter for the impedance tube body.

The impedance tube apparatus was set up based on Sound Absorption coefficient Transmission loss measurement using ASTM E2611 method [7]. The measurements for the ASTM E2611 [7-8] tests were made using a 30mm diameter tube. Four (4) microphones, type MPA416 were used with a spacing of 50mm in the transmission loss measurement setup as shown in Figure 4.

Table 1 Sample specification

Sample	**Decouple layers construction**	**Approximate total thickness, t (mm)**
1	Felt 750 g/m^2 / Felt 1500 g/m^2	25
2	Felt 750 g/m^2 / EPDM t = 1.5mm / Felt 1500 g/m^2	28
3	Felt 750 g/m^2 / EPDM t = 3.0mm / Felt 1500 g/m^2	30

Note: Thickness of Felt 750 g/m^2 is approximately 9 mm, while for Felt 1500 g/m^2 is approximately 17.5 mm (Sample 2) and 18 mm (Sample 3).

Figure 3: Test sample after cutting with approximation of 29mm – 30mm of thickness

The usable frequency range depends on the diameter of the tube and the spacing between the microphone positions. A loudspeaker was located at one end of the tube, generated a broadband random signal over the frequency range of 1000 to 6100Hz, with 2Hz resolution. The frequency response functions between the reference microphone located closest to the loudspeaker and the other measurement positions were measured simultaneously by using a 4-Channel MC3242 data acquisition front end and the Impedance Tube Module (VALab IMP) software running on an attached computer. All of the measurements were made using the two-load method as described in Section 8.5.4.1 of ASTM E2611 [7], with also reference to established methods [8-11].

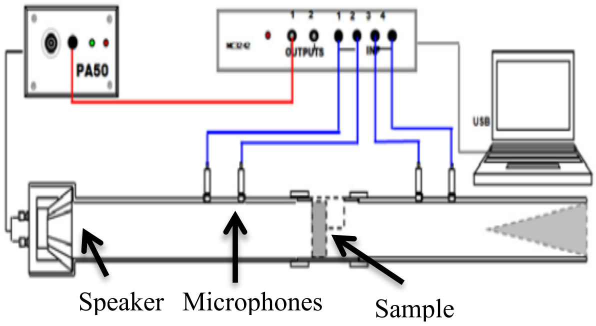

Figure 4: System diagram with for TL measurement using impedance tube

3. RESULTS AND DISCUSSION

Figure 5 shows the STL for all three samples. In general, each sample shows similar trends which are more profound for Sample 2 and Sample 3. Each sample suffered a drop in transmission loss around 500 – 2000Hz before increasing steadily at higher frequencies. The dip in the transmission loss is largest for Sample 2, followed by Sample 3, and least for Sample 1.

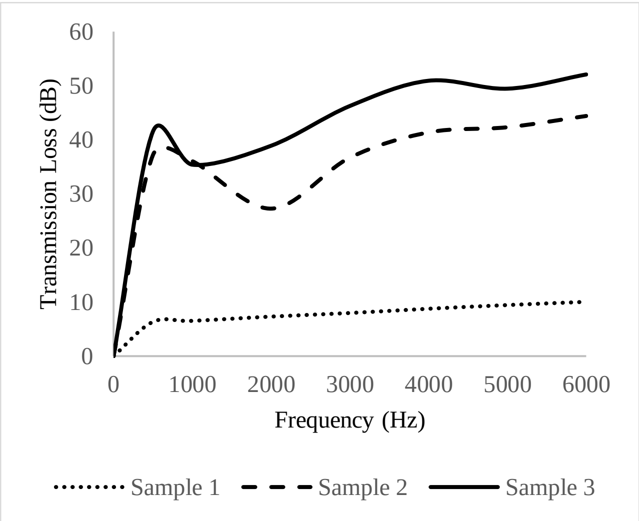

Figure 5: Sound Transmission Loss for all samples

According to Jain *et al.* [6], transmission loss performance of limp, non-rigid materials are directly related to its surface density or mass and are governed by the mass law. This might explains why Sample 3 showed high STL as compared to Sample 1 and Sample 2. There is significant difference in the level of transmission loss between samples with EPDM layer (Sample 2 and Sample 3) when compared to sample without it (Sample 1). This is due to the high total surface density of the samples with the EPDM layer, 3,950 g/m^2 restricting the transmission of the sound level. Although both Sample 2 and Sample 3 have the same thickness of the decouple layers, Sample 3 performed better due to a thicker EPDM layer, resulting in a higher surface density compared to Sample 2.

The test results also showed that there was dip in the STL at around 2000Hz and 1000Hz for Sample 3 and Sample 2, respectively, and after which, the STL increases with increasing frequency. This dip was probably due to the double wall resonance of the felt-EPDM-felt system [2-3]. The difference in the STL dip between Sample 2 and Sample 3 was due to the different thickness of the EPDM layer. The EPDM layer may increase the flow resistivity of the decouple layers and shift the resonance dip to a lower frequency. In addition, Sample 3 showed an additional dip at around 5000 Hz. This dip was significantly less than the initial dip in the STL shown by Sample 3 and could be caused by the downward shift in resonance frequency due to the EPDM layer.

The results also showed that the EPDM layer resulted in an increase in the overall STL of the samples. Sample 1 has the lowest overall STL, while the overall STL for Sample 2, with an EPDM layer, is significantly higher than Sample 1. As the thickness of the EPDM layer is increased by 100% in Sample 3, the overall STL level also increased though not as significantly as the difference in overall STL levels between Sample 2 and Sample 1.

4. CONCLUSIONS

From the STL test, it was concluded that Sample 3 has the best STL performance followed by Sample 2 and Sample 1. The EPDM layer has a more pronounced impact on STL (Samples 2 and 3) when compared to the absence of the EPDM layer (Sample 1).

REFERENCES

[1] S. K. Jain, P. Shravage, M. Joshi, N. V. Karanth, "Acoustical Design of Vehicle Dash Insulator", Symposium on International Automotive Technology India 2011: SAE International, Technical Paper 2011-26-0022.

[2] A. Maria, J. C. Kuczmarski, "Acoustic Absorption in Porous Materials", *NASA*, Technical Paper TM-2011-216995, 2011.

[3] R. H. Randall, *An Introduction to Acoustics*, Mineola, NY: Dover Publications, Inc., 2005.

[4] J. S. Bolton, R. J. Yun, J. Pope, D. Apfel, "Development of a New Sound Transmission Test for Automotive Sealant Materials". *SAE Trans., J. Pass. Cars*, 106: p. 2651–2658, 1997.

[5] J. F. Allard, "Propagation of Sound in Porous Media: Modelling Sound Absorbing Materials", Elsevier, Ireland, 2010.

[6] S. Jain, M. Joshi, P. Yadav, N. Karanth, "Various Parameters Affecting The Acoustical Performance of Firewall Studied Using Experimental Techniques", The 22nd International Congress on Sound and Vibration 2015, Florence, Italy.

[7] Standard Test Method for Measurement of Normal Incidence Sound Transmission of Acoustical Materials Based on the Transfer Matrix Method, ASTM E 2611-09 (International, West Conshohocken, PA, USA, 2009).

[8] S. S. Jung, Y. T. Kim, Y. B. Lee, "Measurement of Sound Transmission Loss by Using Impedance Tubes", *Korean Physical Society,* Vol. 53, No. 2, pp. 596 - 600, 2008.

[9] BSWA TECH. *SW Series Impedance Tube Solutions.* Scantec, Inc., 2015.

[10] J. Kunio, T. Yoo, K. Hou, J. S. Bolton, J. Enok, "A Comparison of Two and Four Microphone Standing Wave Tube Procedures for Estimating the Normal Incidence Absorption Coefficient", INTER-NOISE 2009, Ottawa, Canada.

[11] R. G. Nan, Y. J. Park, Y. J. Kang, C. M. Park, K. S. Chae, "Investigation of STL Measurement Method at The Vehicle Component Level and Correlation Between Measurement and Prediction", International Congress on Sound & Vibration 2007. Cairns, Australia.

The Tensile Strength and Morphology of Fast Food Packaging from Cellulose Material

Irwan Suriaman[1,2,*], Y. Mardiyati[1], Jooned Hendrarsakti[1], Ari Darmawan Pasek[1]

[1)] Faculty of Mechanical and Aerospace Engineering, Institut Teknologi Bandung, Jalan Ganesha No. 10 Bandung-40132, West Java, Indonesia
[2)] Department of Mechanical, Faculty of Engineering, Universitas Pasundan, Jalan Dr. Setiabudhi No. 193, Bandung-40153, West Java, Indonesia

[*]Corresponding e-mail: irwan_suriaman@yahoo.co.id

ABSTRACT – Food packaging material is an important factor for maintaining product quality. Currently, synthetic polymer materials still dominant use for fast food packaging. They are not safety to use because produced from petroleum oil, besides that have of structure is easily degraded which allows them to bond with the structure of food products, specifically for high temperature. This research about of the morphology and tensile strength for fast food wrapping paper made from cellulose material. They have result of scanning electron microscope (SEM) for distribution of fiber diameter is 7.88 µm and tensile strength is 5120 N/m. The product can be used to fast food packaging that are healthy and good quality.

Keywords: Cellulose material, fast food, morphology, synthetic polymer and tensile strength.

1. INTRODUCTION

The renewable, biodegradable, safe for health materials have been developed in various industrial applications [1,2]. currently, materials made from synthetic polymers for packaging fast food have dominated the market. But it needs to be realized that synthetic polymers have disadvantages because they come from petroleum residues that can be degraded, so that the structure can bind to fast food product, that is way it is not safe for health [3,4].

Natural material is a potential that needs to be developed as a source of biodegradable material, healthy, recyclability and environmental safety [5,6]. As an example: cellulose material that grows in almost all space of the world, especially those with tropical climates, such as Indonesia. While they have advantages of easy for processing cellulose material, non-toxic and can absorbing CO_2 during their growth in the word [7,8].

This research was result about the performance of fast food packaging materials produced from cellulose materials, both in terms of morphology and mechanical properties. The hope is that this material can replace synthetic polymer materials that are still dominant in use today.

2. METHODOLOGY

Cellulose material used collected from Garut, West Java. The production of fast food packaging materials is based on TAPPI T.205 standard, with the grammage at 50, 100 and 150 g/m² [9].

The morphological test using scanning electron microscopic (SEM) JEOL JSM-6510, at Balai Besar Tekstil Bandung, West Java. Each sample is cut to size 1cm then attached to an aluminum plate and coated with gold (Au) by using sputter coater JEOL JEC-3000 FC.

Tensile strength is based on SNI ISO 1924-2:2010 at Balai Besar Pupl dan Kertas (BBPK), West Java.

3. RESULTS AND DISCUSSION

The result of SEM obtained various morphology of fast food packaging from cellulose material that can be shown in Figure 1. and Figure 2.

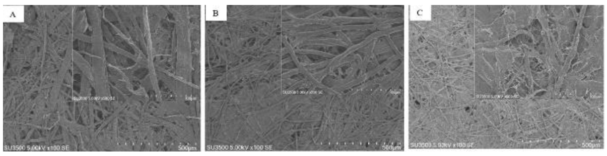

Figure 1. Fast food packaging material for grammage (g/m²): (A) 50; (B) 100; (C); 150, with magnification 100x and 500x.

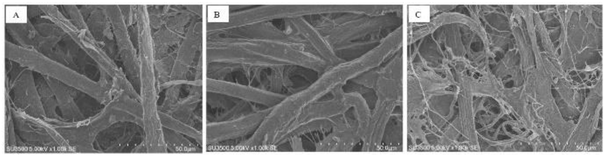

Figure 2. Fast food packaging material for grammage (g/m²): (A) 50; (B) 100; (C); 150, with magnification 1000x.

The morphological of fast food packaging from cellulose fiber can be seen in Figure 1., bundle of fiber formed hydroxyl bond which occurs firmly with increasing grammage values from 50, 100 and 150 g/m². Fibers bind to one another through secondary bonding between the cellulose material compounds that are predominantly from the cellulose element in the form of crystalline element. The higher grammage value of 50, 100 and 150 g/m², as also in Figure 2., it shows that the dense number of fibers that bind to each other, which increased the mechanical properties of the food packaging as well as the lower of porosity can withstand the load of food on it. Furthermore, the increase of grammage can be seen in Figure 3., the diameter distribution of fiber is smaller with the assumption of food bonding between the surface of the fiber that is bind each other [9].

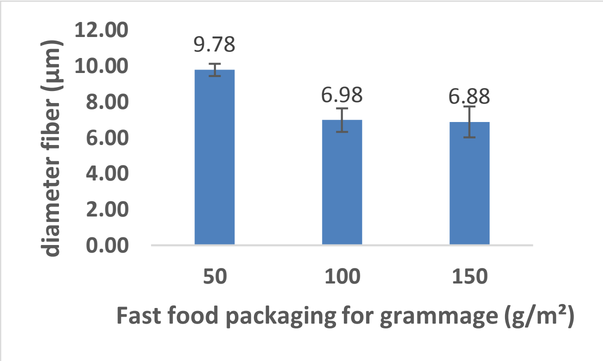

Figure 3. Fiber size distribution of fast food packaging material for grammage: 50, 100 and 150 g/m².

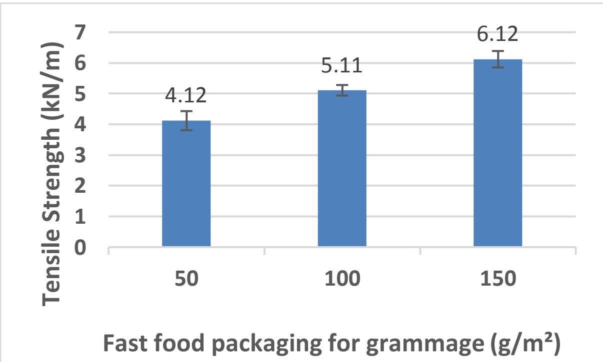

Figure 4. Tensile strength of fast food packaging material for grammage: 50, 100 and 150 g/m².

Mechanical properties of the fast food packaging from cellulose fiber can be seen in Figure 4., as the grammage value increases, the tensile strength of the fast food packaging also increase due to the increasing number of fibers that make a hydroxyl bond. The dominant compounds from the food packaging is crystalline element and little amorphous element that affects to the strength of the food packaging. Moreover, the higher interface area of the cellulose fiber will create greater energy absorption that affect to the tensile strength of the fast food packaging [8,9].

4. CONCLUSIONS

The results of morphology test with SEM obtained distribution diameter average is 7.88 µm and tensile strength average is 5120 N/m. The product can be developed as fast food packaging material for eliminate synthetic polymer.

ACKNOWLEDGEMENT

This study was supported by the program of BUDI-DN Ristek Dikti of Indonesia and Lembaga Pengelola Dana Pendidikan (LPDP).

REFERENCES

Journal articles

[1] Cruz, R. and Fangueiro, R., "Surface modification of natural fibers: A review, procedia engineering, 155, 285-288, 2016.

[2] Omrani, E., Menezes, P. L. and Rohatgi, P. K., "State of the art on tribological behavior of polymer matrix composites reinforced with natural fibers in the green materials word, Engineering Science and Technology, an International Journal, (19) 2, 717-736.

[3] Pickering, K. L., Efendy, M. G. A., and Le, T. M., "A review of recent development in natural fibre composites and their mechanical performance, Compistes Part A: Applied Science and Manufacturing, 83, 98-112.

[4] Rowell, R., M., Han J., S., and Rowel J., S., "Characterization and factors effecting fiber properties". Natural polymers an agrofibers composites, pp. 115–134, 2000.

[5] Sgriccia, N., Hawley M.C., Misra M., "Characterization of natural fiber surface and natural fiber composites". Compositesa, pp. 1632–1637, 2008.

[6] Taalah, B., Guettala A., Guetala S., Kriker A., "Mechanical properties and hygroscopicity behavior of compressed earth block filled by date palm fibers". Conbuildmat, pp. 161–168, 2014

Conference papers

[7] Suriaman, .I, Mardiyati M., Hendrarsakti J., Pasek A.D., "effect alkali treatment of tensile strength and morphology of palm dan coir fiber" SENAMM X Seminar Nasional Metalurgi dan Material, Semarang, 8 November 2017, pp. 6025–6030.

Books

[8] Feller, C., et. al Handbook of Ageing/ Degradation of paper. Stockholan, UK, 1989.

[9] TAPPI Antitrust Policy. Handbook of TAPPI Standards: Regulations and Style Guidelines. 2018.

The Behavior of Cylindrical Natural Bamboo Structures Under Axial Loading Compression

Bambang K. Hadi*, Andi Kuswoyo and M. Rafiqi Sitompul

Faculty of Mechanical and Aerospace Engineering, Institut Teknologi Bandung, Jl. Ganesha 10, Bandung 40132, Indonesia

*Corresponding e-mail: bkhadi@ae.itb.ac.id

ABSTRACT – The paper discusses the failure of cylindrical natural bamboo of the types *Gigantochloa pseudoarundinacea* and *Gigantochloa apus* under compressive loading. Both numerical analysis and experimentation were discussed. There were three types of bamboo structures to be analyzed: without bamboo node, center node and end node. The length of the bamboo structure was 500 mm. Finite element analysis was performed in order to find the buckling strength of the structures. It was found that *Gigantochloa pseudoarundinacea* was able to withstand the first buckling mode up to 80,000 N while the *Gigantochloa apus* was able to carry up to 40,000 N compressive loadings. Experimentation was done in order to compare with the numerical analysis. It was found that the bamboo structures were able to carry post-buckling loads beyond the first buckling strengths. The failure modes were also investigated

Keywords: bamboo structures; compressive loading; finite element analysis.

1. INTRODUCTION

Bamboo is widely found in South East Asia Region and widely used in everyday life. There are more than 1000 bamboo species in the world, mostly in tropical climate in Asia. Bamboo was used mainly for handcrafts and everyday use. However, recent studies have begun to utilize bamboo for structural parts, mainly for civil engineering purposes. Figure 1 shows the bamboo structures and the presence of nodes.

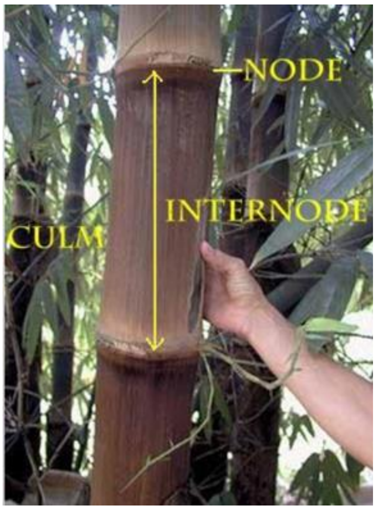

Figure 1 Bamboo structure and their nodes.

Sharma, et al [1] studied the use of bamboo for structural applications. It was shown that bamboo can replace traditional wood for structural applications such as timber and timber products. Nurmadina, et al [2] studied the behaviour of *Gigantochloa apus* based on their flexural properties, while Verma [3] used bamboo for structural laminates and tested their mechanical properties.

The buckling behaviour of bamboo column under compressive load was studied by Yu [4, 5] especially for scaffolding structures. However, their works did not cover the effect of bamboo nodes on the buckling behaviour. The current works will include the presence of bamboo nodes on their buckling characteristics and failure modes.

The present study was part of the greater study on bio-mimetics of bamboo for the design of fuselage structures.

2. METHODOLOGY

Both the numerical analysis and experimentation was carried out. ABAQUS finite element software was extensively used to predict the first buckling load and its buckling mode. The experimental works used 10 tons capacity universal testing machine.

Bamboo is an orthotropic material, therefore for the purpose of finite element analysis, mechanical properties in fiber direction and perpendicular fiber direction should be available. These properties were taken from previous studies [6] and given in Table 1. It should be noted, however, the mechanical properties of bamboo depends on the age and the moisture content. Thefore, a standardize properties should be seek in the future. In this work, the age of bamboo was 10 years without the drying up to remove the moisture.

Table 1. Mechanical properties of bamboo [6]

Material	X_t (MPa)	E_{11} (MPa)	X_c (MPa)
Gigantochloa pseudoarundinacea	397	28029	54.3
Gigantochloa apus	315	16575	36.5

where X_t is the tensile strength of bamboo in fiber direction, E_{11} is the modulus of elasticity in fiber direction and X_c is the compressive strength in fiber direction. It shows that bamboo has excellent tensile strength, while the compressive strength was inferior compared to their tensile strength. This will affect the failure mode of bamboo structures under compressive loadings.

In this study, there are three types of bamboo structures under investigation, based on the location of the bamboo nodes. First is the central node, second is without node and the third is the end node. Figure 2 shows the structures.

Figure 2 Three types of bamboo structures: central node, without node and end node.

3. RESULTS AND DISCUSSION

3.1 Finite element analysis

Figure 3 shows the finite element model for the buckling analysis for the three cases of structures. The dimensions of the specimens are: length 500 mm, outer diameter 100 mm and the thickness is 12 mm. The boundary condition was simply supported for all the bamboo edges.

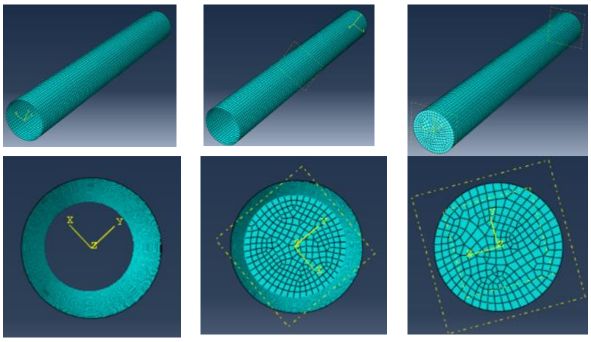

(a) (b) (c)

Figure 3 Finite element model for buckling analysis (a) without node, (b) central node and (c) end node

3.2 Comparisons between finite element analysis and experimental results

a. Failure modes

Figure 4 – 6 show the failure modes comparisons between finite element analysis and experimentation for the case of *Gigantochloa pseudoarundinacea* bamboo.

Figure 4 Buckling mode and ultimate failure of *Gigantochloa pseudoarundinacea* bamboo specimen without node.

Figure 4 shows that the specimen buckled locally, and the specimen split under compressive loading. This is due to the low shear modulus and strength and low compressive strength of typical bamboo. The bamboo can not withstand shear stresses and thus split during compressive loading.

Figure 5 shows the failure mode of bamboo specimen with central node. It shows that the specimen produces two local buckling and the central node was intact with no deformation. The experimental result also shows that the central node was intact, and the specimen split at the end loading.

Figure 5 Buckling mode and ultimate failure of *Gigantochloa pseudoarundinacea* bamboo specimen with central node

Figure 6 shows for the case of end node. It shows that the node provides the clamped boundary conditions for the specimen. The specimen buckled locally, while the nodes at both ends provide support and still intact during compressive loading.

Figure 6 Buckling mode and ultimate failure of *Gigantochloa pseudoarundinacea* bamboo specimen with end nodes

b. Buckling loads

In the experimental works, the specimen was put between two flat-loading-apparatus in the Universal Testing Machine (UTM) and compressed in the rate of 5 mm/second in order to achieve a quasi-static loading. The UTM has a maximum capacity of 100 kN. Figure 7 shows the experimental load-deformation results.

Figure 7 shows load-deformation curve for the three different types of nodes: without node, central node and end nodes. The figure shows that the presence of node did not affect the ultimate failure strength of bamboo column under compressive loading. The low shear and compressive strengths of the bamboo affect more on the behavior of bamboo column under compressive loads. These are confirmed by finite element results that shows that the critical buckling loads of the three types of specimens did not differ significantly. Table 2 shows the critical buckling loads of the specimens taken from the finite element analysis.

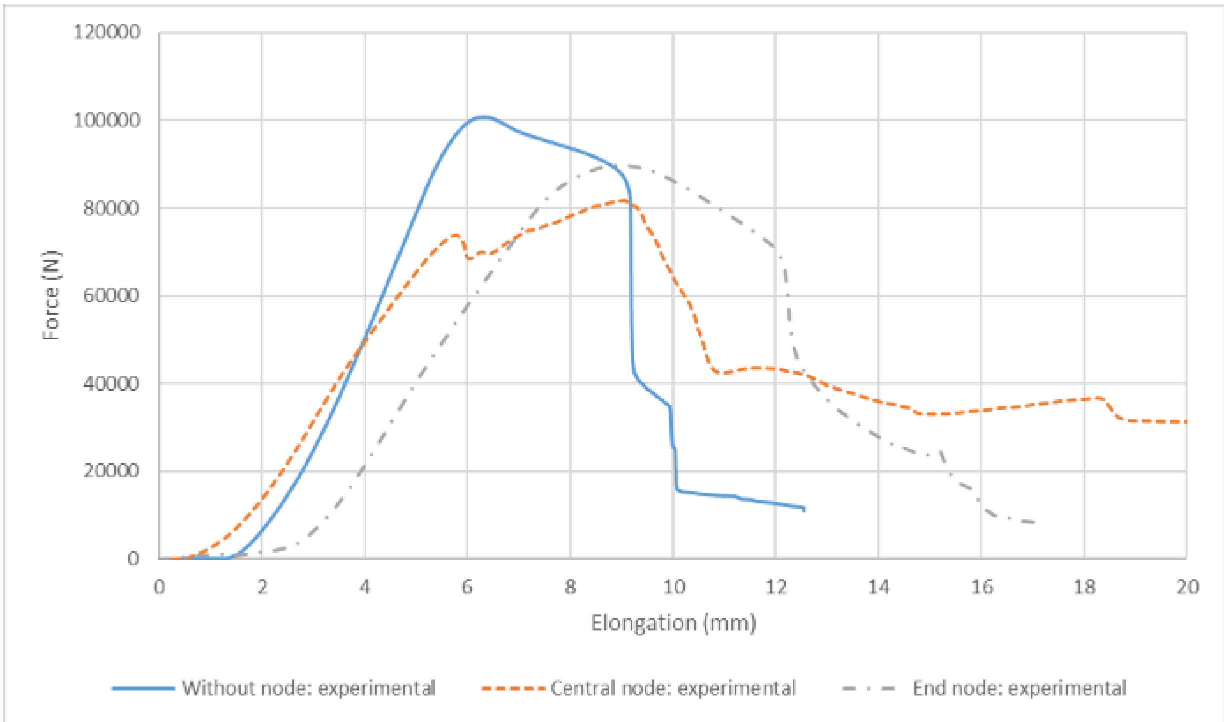

Figure 7 Load deformation curve for *Gigantochloa pseudoarundinacea* specimen under compressive loading

The predicted finite element results of 78,000 N compared well with the experimental results of 80,000 N.

Table 2 Critical buckling finite element results of *Gigantochloa pseudoarundinacea* specimen

	Without node	**Central node**	**End nodes**
First eigenvalue (N)	78526	78568	78532
Second eigenvalue (N)	78574	78578	78572
Third eigenvalue (N)	78605	78642	78606

4. CONCLUSIONS

The present studies investigated the behavior of bamboo column under compressive loading. Buckling was found to be the most critical mode during the studies, for both the numerical analysis and the experimental ones. The presence of nodes did not affect significantly the failure modes and the critical buckling loads. The low shear and compressive modulus and strengths affect more on the critical buckling loads, rather the presence of nodes. The numerical analysis compared well with the experimental ones. The specimens were able to withstand around 80,000 N experimentally, while the numerical analysis showed the critical buckling loads of 78,000 N.

ACKNOWLEDGEMENT

The research was funded by PDUPT year 2019, under the contract no 1388.4/I1.C08.2/PL-DIKTI/2019. The authors wish to thank the Ministry of Research and Higher Education for the generous funding. We also thank the Faculty of Mechanical and Aerospace Engineering for the support during the research.

REFERENCES

[1] B. Sharma, A. Gatoo, M. Block and M. Ramage, engineered bamboo for structural applications, *Construction and Building Materials*, 81 (2015) 66-73.

[2] Nurmadina, N. Nugroho and E.T. Bachtiar, Structural grading of *Gigantochloa apus* bamboo based on its flexural properties, *Construction and Building Materials*, 157 (2017) 1173-1189.

[3] C.S. Verma and V.M. Chariar, Development of layered laminate bamboo and their mechanical properties, *Composite Part B*, 43 (2012) 1063-1069.

[4] W.K Yu, K.F. Chung and S.L. Chan, Column buckling of structural bamboo, *Engineering Structures*, 25 (2003) 755-768.

[5] W.K. Yu, K.F. Chang and S.L. Chan, Axial buckling of bamboo columns in bamboo scaffolding, *Engineering Structures*, 27 (2005) 61-73.

[6] B.K. Hadi, A. Subadra and A. Kuswoyo, Mechanical Properties of Natural Bamboo Due to Tensile and Compression Loadings, *Key Engineering Materials*, 775 (2018) 576-581.

Threshold Current for Arc Free and Short-duration Arc in Hybrid DC Switch

Chomrong Ou[12*], and Koichi Yasuoka[1]

[1)] Department of Electrical and Electronic Engineering, Tokyo Institute of Technology, 2-12-1, S-3-3, Ookayama, 152-8550, Tokyo, Japan
[2)] Department of Electrical and Energy, Institute of Technology of Cambodia, Russian Federation Blvd, P.O. BOX 86, Phnom Penh, Cambodia

[*]Corresponding e-mail: ou@hv.ee.e.titech.ac.jp

ABSTRACT – Automotive applications that uses direct current (DC) to operate its performance becomes interesting because of its economic and environment. Relays and switches in automotive applications are used to switch on or off power. During power switching off, the relays suffer long-duration arc that results in failure of the relay. A hybrid DC switch (HDCS) composing a mechanical switch connected in parallel with semiconductor devices can switch off DC power without arc discharge, and faster than conventional relays. This work presents threshold current for arc-free (without arc) and contact resistance affected by short-duration arc in opening contacts. The experiment was carried out with DC current to 800 A. From the results, the threshold current for arc free was up to 120 A and with short-duration arc for larger current. The contact was eroded by the arc but the contact resistance did not change much with 100 contact opening operations.

Keywords: Hybrid DC switch, arc free, short-duration arc, contact erosion and contact resistance

1. INTRODUCTION

Automotive applications such car, train that uses direct current (DC) to operate its performance becomes popular because of its economic and environment [1-2]. Relays and switches in automotive applications are used to switch on or off power. During power switching off, the relays suffer long-duration arc. Long-duration arc is harmful phenomena that erodes the contacts of the relay that results in failure of the relay. That affected on lifespan of the relays or switches and security of the automotive applications [3].

A hybrid DC switch (HDCS) composing a mechanical switch connected in parallel with semiconductor devices can switch off DC power without arc discharge, and faster than conventional relays. A typical circuit diagram of HDCS consists of a mechanical switch (S), a SiC-MOSFET, and a metal-oxide varistor (MOV) connected in parallel, as shown in Figure 1. An operating diagram of the HDCS is shown in Figure 2. The circuit current from the DC source initially flows power source to automotive applications through the contact S at position (1) under normal conditions. Under fault conditions, the contacts start to separate and the SiC-MOSFET turns on at position (2). The contact voltage increases, which transfers the main current from the contacts to the SiC-MOSFET. After full commutation, the semiconductor carries the current for a while and is turned off afterward. Then, the circuit current flows to the MOV. A surge voltage is induced owing to the inductor when the SiC-MOSFET turns off at position (3). The remaining current caused by the inductor in the circuit is absorbed by the MOV at (4). Then, a successful current interruption is achieved. This work presents performance of a hybrid DC switch associated with threshold current for arc free, and short-duration arc that erodes the contact erosion and resistance opening contacts of a hybrid DC switch.

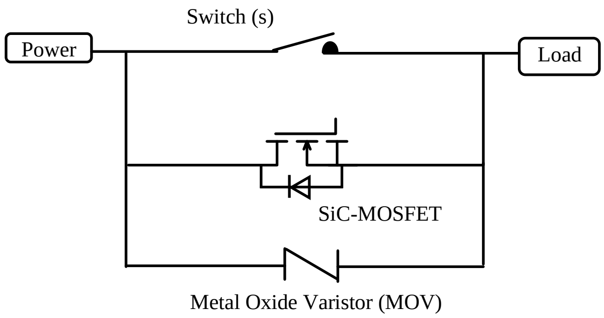

Figure 1 A typical circuit diagram of hybrid DC switch.

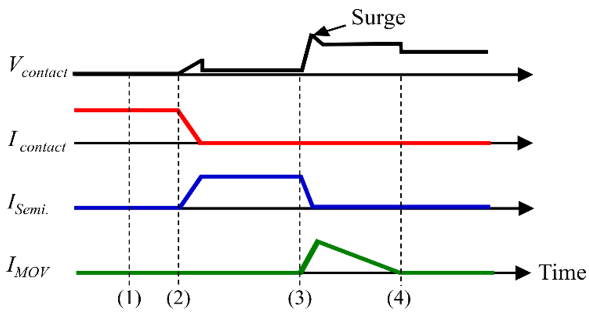

Figure 2 Operating diagram of a hybrid DC switch.

2. METHODOLOGY

The experiment was carrying out in opening contacts. DC supply, a 0.27 Ω resistor, three contact pairs (as switch) and a SiC-MOSFET were used as shown in Figure 3. DC supply flows current up to 800 A through the contacts and SiC-MOSFET was connected in parallel with the contacts. The copper contacts with diameters of 10 mm used in the experiment as shown in Figure 4. The lower contact was fixed, and the upper contact was attached with electric piezo actuator to separate or close the contacts.

The circuit current initially flowed through the contacts. Then, the piezo actuator opened contacts with same time of SiC-MOSFET turning on. During opening the contacts, the current is transferred to SiC-MOSFET. The experiment repeated for 100 times for each cases. The arc voltage and current waveforms were recorded with an oscilloscope. The contact resistance was measured for each experimental run.

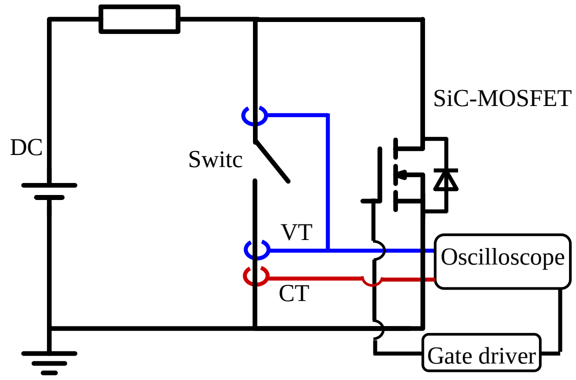

Figure 3 Experimental diagram of hybrid DC switch.

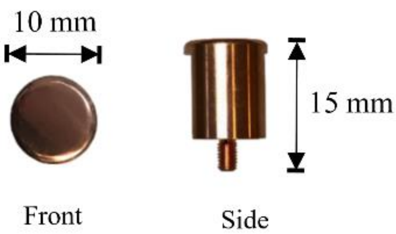

Figure 4 Configuration of copper contacts used in the experiment.

3. RESULTS AND DISCUSSION

A. Arc free in commutation phase

In experiment with the current up 120 A, arc discharge was not found in commutation phase. Figure 5 shows example of contact voltage and current without arc discharge (arc free) for 80 A. The contacts started separating at 100 μs approximately. After separation, contact voltage raised with time and the current flowing through the contacts decreased until to zero. That means I_c transferred from switch to SiC-MOSFET.

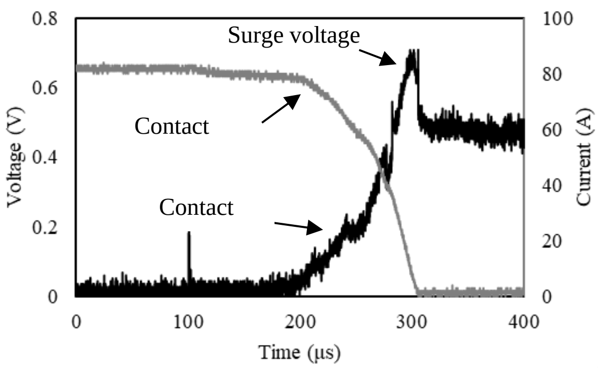

Figure 5 Contact voltage and current waveforms of arc free for 80 A.

V_c raised was due to increasing the contact resistance associated with raising temperature. When the contacts start separating, number of contact a-spots decrease and the current flows through the remain a-sports which results in increasing heating Joule and resistance [4]. Holm [5] expressed the relation of temperature of contact area and contact voltage (T-V) as

$$T_m = \sqrt{\frac{V_c^2}{4L} + T_0^2} \quad (1)$$

where T_m and T_0 is maximum temperature of contact area and temperature in atmosphere, respectively. V_c is the contact voltage. L is Lorenz coefficient, equals 2.4 x10^{-8} $(V/K)^2$.

Table I shows the V_c at melting and boiling temperatures for copper [5].

Table I
Contact voltages at melting and boiling temperatures

Temperature	Melting	Boiling
	1,083 K	2,582 K
Voltage	0.43 V	0.8 V

From the equation, with increasing temperature of the contacts, the contact voltage increases and transferred current to SiC-MOSFET until the current almost reaches to zero value. After the contact raptures, the remaining current at the contact is low that resulting in low surge voltage at shown at 300 μs in Figure 5. The surge voltage is not high enough for arc generation owing to ionization process. In addition, the contact voltage does not reach 0.8 V (boiling voltage), the metal vapor does not release between the contact. With presence of the metal vapor, arc discharge easily to generate because it has lower ionization potential than gas medium [6].

A. Arc discharge in commutation phase

When the current increases from 120 A, short-duration arc was found in commutation phase. Figure 6 shows example of contact voltage and current waveforms with arc discharge for 200 A. The contacts start separating at approximately 20 μs. During separation, the contact voltage increases with time until it reaches 0.8 V. Meanwhile, the current flowing through the contacts decreases. This indicates that partially commutates from the contacts to the SiC-MOSFET. After exceeding 0.8 V, V_c is unstable following the arc discharges at 87 μs, and I_c promptly decreases to zero. After the arc ignition, V_c decays to the voltage of the SiC-MOSFET. V_c raised discontinuously at 0.43 V in Figure 6 was coincided with melting voltage from the calculation in Table I. When V_c exceeds boiling voltage (0.8 V) when contacts rapture, metal vapor releases in narrow gap (below few micrometers). As the gap is narrow, the electric field in the gap is high which leading ionization of the metal vapor with electron stream emitted from cathode. That results in arc generation between the contacts. Figure 7 shows the average total arc duration and number of arcs over 100 operations. The total arc duration for full commutation increases linearly from 4 to 14 μs for a current of 200 to 800 A, respectively. That is much shorter than conventional switch that ignites arc up to several hundred seconds. That can increase lifespan of the switch owing to shorter duration arc. As the arc accelerated commutation current to SiC-MOSFET, the arc duration mainly depended on the current. The number of arc discharges increased slightly with increasing current because larger arc energy splattered a larger amount of molten contacts.

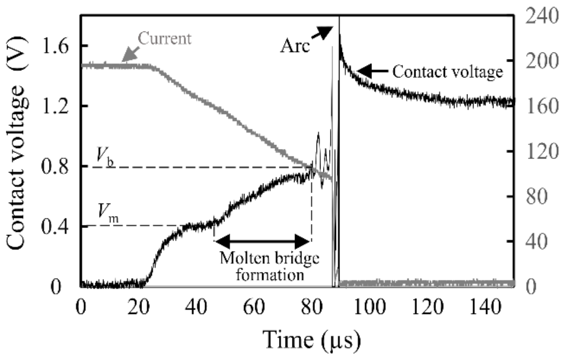

Figure 6 Contact voltage and current waveforms with arc discharge for 200 A.

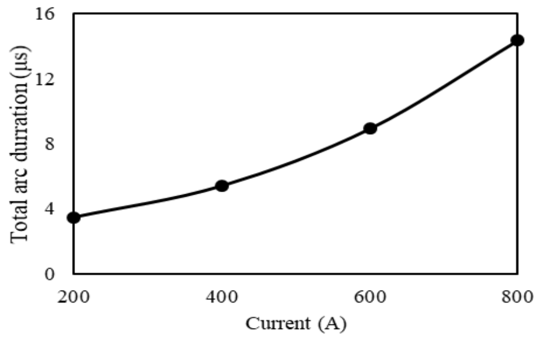

Figure 7 Average of duration with current from 200 to 800 A.

B. Contac resistance

For arc free with current below 120 A, arc discharge and contact erosion due to the arc are not found. We consider that the contact resistance also not change significantly. Therefore, in this section, we only discuss about contact resistance with short-duration arc.

Figure 8 shows the relationship between the contact resistance and the number of opening contact operations with current from 200 A to 800 A. The contact resistance was calculated by the voltage between the contacts divided by the current through the contacts. The initial contact resistance varies from 0.687 to 0.97 mΩ between each case. The contact resistances did not increase or decrease significantly after 100 operations. Interestingly, the contact resistance decreases with the first opening contact operation for all cases as shown in inset of Figure 8. This may be because the oxidized film is removed by large current flows, or because of an increase in the contact area owing to melting. The contact resistance did not change much because contact erosion was not severe and the oxidized film was not deposited significantly on the contact surface. The oxidized film deposited on contact surface caused by a long-duration arc dramatically increases resistance [7].

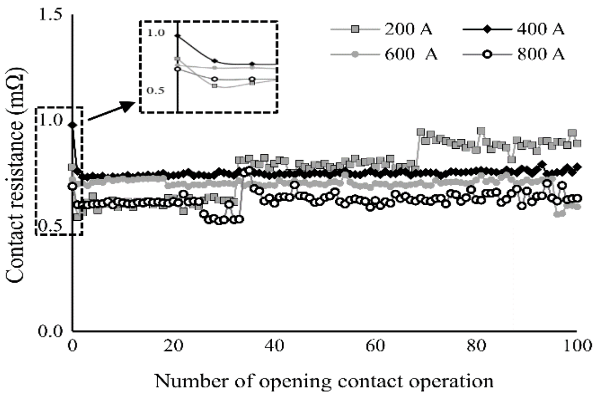

Figure 8 Contact resistance with the number of opening contact.

4. CONCLUSIONS

Arc discharge is a harmful phenomenon which erode the contact surface, which results in increasing power loss. Short lifespan and current interrupting failure. From the results, it was found that arc discharge is not found in current up to 120 A. It was clear that the hybrid DC switch improve lifespan of switch. For current larger than 120 A, short-duration arc is found in commutation phase. The duration and number of arcs increased with increasing current. The total duration of arc increased with increasing current because the arc took a longer time to commutate current to the SiC-MOSFET. However, this arc duration is still much shorter than conventional switch that ignite arc discharge up to several hundred milliseconds. Power loss due to Joule heating is improved because the contact resistance did not much increase by the short-duration arc.

ACKNOWLEDGEMENT

This work was supported by JSPS KAKENHI Grant Number JP18H01420. Authors would like to thank Japan International Cooperation Agency – JICA

REFERENCES

[1] A. A. Isurin, A. Cook, "Step-up DC-DC converter for automotive application", IEEE 18th European Conference on Power Electronics and Applications (EPE'16 ECCE Europe). Karlsruhe, 5-9 Sept. 2016.

[2] N. B. Jemaa, L. Nedelec and S. Benhenda, "Break arc duration and contact erosion in automotive application," IEEE Trans. on Comp. Pack., and Manu. Tech., vol. 19, no. 1, pp. 82-86, Mar. 1996.

[3] T. Øyvang, E. Fjeld, W. Rondeel, and S. T. Hagen, "High current arc erosion on copper electrodes in air," in Proc. IEEE 57th Holm Conf. Elect. Cont., pp. 1–6, Sep. 2011.

[4] W. Ren, H. Wang, C. Chang, S. Xue and Y. Chen, "Experimental investigation and understanding of the intermittent molten bridge phenomena and mechanism of contacts with super low opening speed," Vol. 6, no. 3, pp. 418-423, Mar. 2016.

[5] R. Holm, "Electric contacts: Theory and Application, 4th edition., Springer, 1979.

[6] P. G. Slade, "Electrical Contacts: Principles and Applications," 2nd edit., CRC Press, 2014.
[7] K. Yoshida, K. Sawa, K. Suzuki and K. Takaya, "Effect of arc discharge types on various characteristics and mass change in electrodes for electromagnetic contractor," presented at Tech. Repo. Elec. Devi. Inst. of Elec., Info. and Comm. Engi. (IEICE), vol. 117, no. 312, pp. 13–19, Nov. 2017.

Industrial Application of Exoskeleton Current and Future Research: A Malaysian Context

Raja Ariffin Raja Ghazilla[1*], Sado Fatai[2], Mukhtar Fatihu Hamza[3]

[1,2,3)] Department of Mechanical Engineering, Faculty of Engineering, University of Malaya, Kuala Lumpur, Malaysia

Email: [1*]r_ariffin@um.edu.my

ABSTRACT – Recently there is a growing interest in the application of Exoskeleton in industries, worldwide. In the Malaysian context however the application has yet to gain traction. This could be main due to industrial exoskeleton being perceive as expensive for economic viability standpoint and its poor accommodation of the Malaysian sizing. In addition, falling recognition and balance recovery are not included in most design which can be translated to user insecurity in considering them. Apart from that the user acceptance of wearable robots among Malaysian workers have yet being studied. These are among the challenges that need addressing among the exoskeleton robot research community in Malaysia. Albeit these challenges many research groups in the country have started developing exoskeleton robots in towards expanding and localising its use within the local context. One such research is the development of lower body exoskeleton at Universiti Malaya. The lower limb exoskeleton developed called Exoskeleton for Lower Extremity Augmentation or ExoLEA is an attempt at jumpstarting research industrially applied exoskeleton rather than focus on the more widely researched medical and/or rehabilitation applications. This paper discuses the development of ExoLEA and future challenges of exosksleton development within the scope of industrial application of Malaysian context.

Keywords: Exoskeleton; Fulling recognition; Balance recovery; Industrial application;

1. INTRODUCTION

Exoskeletons are mechanical systems worn by an operator, whose structure mirrors the skeletal structure of the operator's limbs (joints, muscles, *etc.*) [1]. The exoskeleton works in tandem with joints and muscles, and it can be used as power argumentation device, haptic controller, assistive device, or rehabilitation [2]. Until recently, most effort for study and commercialization in exoskeleton domain were focused on the medical rehabilitation and defense sectors, or as mobility aids allowing paraplegics to walk, stand upright, and climb stairs [3, 4]. Exoskeleton technology designed to support customised manufacturing activities in automobile industries are also commercially available [2].

The main reasons that draw the interest in using the exoskeleton towards helping industrial workers prevent work-related injuries and its associated financial penalties. It has been reported that about 44 million workers within the EU suffer from musculoskeletal disorders (MSDs) [5]. The German Federal Institute for Occupational Safety and Health states that 'MSDs account for 23% of the sick days in Germany and lead to an estimated loss in production of e10bn and an annual gross loss of e17bn'.

The MSDs in Malaysia are on the increasing trend as shown in the SOCSO report in 2018. Following the annual report of SOCSO in 2018, the number of reported cases increased sharply from 517 cases in 2013 to more than 2,135 in 2017. Most of the affected workers are from different industries, among which are agricultural industries, construction industries, logistic and shipping industries and various manufacturing industries. The workers in these industries are exposed to repetitive arm motion and static elevation of the arms, repetitive lifting, extended standing, and distance walking and more. [6]. In Malaysia, MSDs is recorded as notifiable work-related diseases in the 3rd schedule of Factories and Machinery Act 1967 and required to be put under NADOPOD (notification of accidents, dangerous occurrence occupational poisoning and occupational diseases) by Malaysian Department of Occupational Safety and Health. Higher rates of MSDs are noticed especially in the forestry, agricultural, demolition, construction, social care, health, shipbuilding and transportation industries. MSDs is expected to continue if care is not taken, as most tasks are not been automated or relieved by robotics. Although many industries have started considering and implementing the use of automation and robotics but in many cases manual task, in which is often with awkward postures, are difficult to avoid as in the case of agricultural and manufacturing industry. The reason is some industries are very complex that involve random and diverse moves that are outside the capabilities of classical robots. Some industries are small scale in which automation is not economical. Exoskeletons can bridge the gap between unassisted human operations and classical robotics, as illustrated in Table 1.

2. CURRENT STATUS

The existing research in Malaysia for application of exoskeleton in industries are very few. One of the is our ExoLEA from centre for product design and manufacturing, University of Malaya shown in Figure 1. Some of the applications of ExoLEA can be seen in https://www.youtube.com/channel/UChpwKDqTrQsOMuagAjfZQxg. It is a lower-limb anthropomorphic device with four degrees of freedom (DOF) on each leg: one active DOF at the hip and knee respectively, and 2 passive DOFs at the ankle for motion on the sagittal plane. The active hip and knee DOFs are actuated by back-drivable, bi-directional brushless DC motors with rated torques 38Nm and 17Nm respectively. The joints are equipped with sensors for torque and position measurement. To ensure firm coupling between the pilot and the exoskeleton, there is provision of four braces attached at

Table 1 Benefit/cost consideration of different material handling methods

Methods	Added capital cost	Operator injury risk	Cost to Employer*
Unassisted human operators	none	High	High
Humans supported with exoskeletons	moderate	Greatly minimised	None/greatly minimised
Classical robots	high	N/A	N/A

* Worker absenteeism, compensation, and loss of productivity

the thigh and shank links. These also facilitate compliance in coupled motion. Upper-body rigid support for the exoskeleton is partly provided by a backpack worn around the shoulder of the operator. Embedded in the backpack is a fairly thin aluminium plate attached on one end to a rigid mechanical bar around the hip, which serve as the torso of the exoskeleton. The exoskeleton communication unit (i.e. the interface between the exoskeleton and the PC) is housed in the backpack [7]. ExoLEA, as a proof of concept, through simulated lifting task experiments has shown to be promising in alleviating risk of MSD due to its capability in reducing fatigue onset as well as augmenting the strength of the operator muscle electromyography results shown in Table 2. None the less, findings from the experimentation have identified several crucial improvements before the technology can be acceptable for industrial application as follows:

1. The prototype does not have the upper limb part and back supports, to reduce the load on the shoulder and back muscles while holding uncooperative postures in the industrial setting be it Manufacturing or agricultural. There is a need for an upper body frame system that can transfer weight from the arms to the outside of the hips, easing the strain of overhead work,
2. The important issues of balance recovery and stability assurance are lacking in the prototype. The stability recovery is crucial for the wearer's safety. The falling recognition strategy and the stability recovery during different phase of falling will be necessary to ensure operator safety.
3. The prototype is heavy, about 16.5kg including the backpack. This need to be improved. Even though during operation ExoLEA, users will not feel the weight but the perception of it being heavy could hinder its application.
4. The discomfort issue is another drawback of the prototype. This can produce musculoskeletal stress and fatigue due to the weight and unnatural or constrained movement of the suit. Thus, there is a need for future prototypes to be more flexible, adaptable and adjustable to the wearer to allow for better synchronization with the natural human movements while providing the needed assistance.
5. Although with the current control strategy, good synchronisation with the operator's movement have been achieved but a smother sync control strategy is needed before the technology can be practical in industrial application such as through the use GRF, EMG for stable admittance control without relying on inverse kinematics. This allows for a better detection of human intention to enable smooth movement.

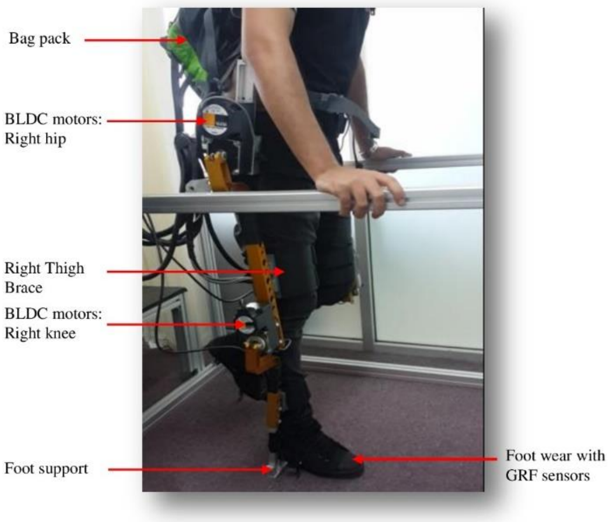

Figure 1: ExoLEA Prototype System

Table 7.1: Summary of the RMSA and MVC means, standard deviations, and percent differences between the 'no Exo assist' and the 'Exo assist' conditions for all the muscles across all participants and treatment conditions

Task	Measure	Vastus Medialis (VM)			Rectus Femoris (RF)			Gastrocnemius (GA)		
		Mode A (w/o Exo) (mV)	Mode B (with Exo) (mV)	% ΔM^1	Mode A (w/o Exo) (mV)	Mode B (with Exo) (mV)	% ΔM^1	Mode A (w/o Exo) (mV)	Mode B (with Exo) (mV)	% ΔM^1
Lifting	RMSA (SD)	0.035 (0.018)	0.017 (0.0066)	51.43	0.043 (0.020)	0.030 (0.015)	30.23	0.032 (0.014)	0.019 (0.007)	40.63
	Peaks (SD)	0.127 (0.083)	0.050 (0.017)	60.63	0.136 (0.065)	0.089 (0.048)	34.55	0.108 (0.068)	0.064 (0.024)	40.74
Lifting & Carrying	RMSA (SD)	0.041 (0.020)	0.023 (0.013)	43.90	0.045 (0.018)	0.028 (0.015)	37.78	0.050 (0.029)	0.021 (0.006)	58.00
	Peaks (SD)	0.121 (0.058)	0.083 (0.037)	31.40	0.131 (0.041)	0.090 (0.041)	31.30	0.169 (0.062)	0.095 (0.035)	43.79

$^1\% \,\Delta M = \%\ muscle\ activity\ reduction = (EMG_{w/o\ Exo} - EMG_{with\ Exo})/EMG_{w/o\ Exo}\ x\ 100$

3. CHALLENGES

The commercially available exoskeletons are few with undetectable technology, this is particularly true for the Malaysian context. The few system that are available in the Malaysia market, most have yet to reach Malaysian shores, are cost prohibitive and may not suit Malaysian workers in term of size. The falling recognition and balance recovery are not included in their design which can be translated as user insecurity.

In addition, the following challenges of the exoskeleton community are still not perfectly solved: wearer security [8], power supply [9], materials [10], actuators [11], joint flexibility [12], power control and modulation, and Adaptation to user size variations [13]. Apart of the technical challenges, the understanding of user perception in the use of exoskeleton among Malaysian worker have yet to be studied. Exoskeleton system in essence are robotics system which requires tandem human co-operation. As with any new technology that requires machine-human cooperation, the perception of safety and compliance to the commands are often a challenge towards is acceptance, which are influence by many factors such as culture, emotion etc.

4. OPPORTUNITIES

Although there seems to be many challenges towards developing and application of exoskeleton technology within the industrial application context of Malaysia but there are justifiable reason it should be pursued due to the opportunities present in the current Malaysian Industrial application. Based on studies conducted by Malaysian National Institute of Safety and Health, in the year 2014 the cost of permanent disability compensation for occupational diseases associated to ergonomics, which in many cases are due to tasks that can be assisted using exoskeleton, was RM25,313 per case which total to RM1.94 million in 2014. This trend is rising with the cost increasing each year. This scenario could be a good economic justification for industries to now consider the application of exoskeleton in the industrial tasks.

The Malaysian Central Bank concluded in a report that Malaysian industries has a high-dependence on imported labour, the palm oil industries alone employs is employ more than 500000 imported labour, in which if left unabated, will weaken the case for automation, suppress overall wages, and deter adoption of productivity enhancing efforts. It will also hinder the creation of high-skilled jobs and adversely shapes Malaysia's reputation as a low-skilled, labour-intensive investment destination. When taken together, these factors trap Malaysia in a low-wage, low productivity bind. The prevalence of large segments of undocumented workers in Malaysia compound the socio-economic costs. Most of the jobs in question relates to job that have low interest from local workers due to its strenuous strength requirements, awkward postures, repetitive in nature and often poses danger to them, which are often difficult to automate. Thus this fact could prove to be an opportunity among the exoskeleton community to pursue the development of exoskeleton increase local worker participation in such jobs, further fuelling the growth of the Malaysian economy.

5. CONCLUSIONS

It has been established that there is a need to continue the pursuit of developing exoskeleton for industrial application which is especially true for the Malaysian context. Exoskeleton technology such as ExoLEA, can minimize the pain of industrial workers and increase in their productivity. The economics justifications discussed above present clear opportunity for the development of exoskeleton but none the less the challenges needs to be addressed so as to increase its uptake within the industrial community.

REFERENCES

1. Zoss, A.B., H. Kazerooni, and A. Chu, *Biomechanical design of the Berkeley lower extremity exoskeleton (BLEEX).* IEEE/ASME Transactions on mechatronics, 2006. **11**(2): p. 128-138.
2. Bogue, R., *Exoskeletons - a review of industrial applications.* Industrial Robot-the International Journal of Robotics Research and Application, 2018. **45**(5): p. 585-590.
3. Zhang, X., Z. Yue, and J. Wang, *Robotics in Lower-Limb Rehabilitation after Stroke.* Behavioural Neurology, 2017.
4. Veneman, J.F., et al., *EMERGING DIRECTIONS IN LOWER LIMB EXTERNALLY WEARABLE ROBOTS FOR GAIT REHABILITATION AND AUGMENTATION - A REVIEW.* Advances in Cooperative Robotics, ed. M.O. Tokhi and G.S. Virk. 2017. 840-850.
5. Bevan, S., *Economic impact of musculoskeletal disorders (MSDs) on work in Europe.* Best Practice & Research Clinical Rheumatology, 2015. **29**(3): p. 356-373.
6. Omar, M.B., *2018 annual repot* in *social security organization*, 18, Editor. 2018: Malaysia.
7. Sado, F., et al., *Exoskeleton robot control for synchronous walking assistance in repetitive manual handling works based on dual unscented Kalman filter.* PloS one, 2018. **13**(7): p. e0200193.
8. Yatsun, A. and S. Jatsun, *Modeling quasi-static gait of a person wearing lower limb exoskeleton*, in *Lecture Notes in Mechanical Engineering*. 2019. p. 565-575.
9. Bogue, R., *Robotic exoskeletons: a review of recent progress.* Industrial Robot: An International Journal, 2015. **42**(1): p. 5-10.
10. Herr, H., *Exoskeletons and orthoses: classification, design challenges and future directions.* Journal of neuroengineering and rehabilitation, 2009. **6**(1): p. 21.
11. Gopura, R., et al., *Developments in hardware systems of active upper-limb exoskeleton robots: A review.* Robotics and Autonomous Systems, 2016. **75**: p. 203-220.
12. Aliman, N., R. Ramli, and S.M. Haris, *Design and development of lower limb exoskeletons: A survey.* Robotics and Autonomous Systems, 2017. **95**: p. 102-116.
13. Gadi, S.K., et al. *Stability analysis and experiments for a force augmenting device*. in *CCE 2012 - 2012 9th International Conference on Electrical Engineering, Computing Science and Automatic Control*. 2012.

Head Injury Analysis of Bus Passenger due to Frontal Crash: Effect of Seat Cushion

Sandro Mihradi [1*], Jerry Setiawan[1], Satrio Wicaksono[1], Andi Isra Mahyuddin[1], Ferryanto[1]

[1)] Faculty of Mechanical and Aerospace Engineering, Institut Teknologi Bandung,
Jl. Ganesa 10, Bandung 40132, Indonesia

*Corresponding e-mail: sandro@ftmd.itb.ac.id

ABSTRACT – As the number of bus increases every year in Indonesia, the safety aspects, unfortunately, has not been improved significantly. Many accidents involving buses that lead to fatality have been widely reported. One of the most frequent ones is frontal crashes. In the event of a frontal crash, the severity of the head injury of the occupants has been widely used as a parameter to evaluate the crashworthiness of the vehicle. In the present study, finite element simulation has been carried out to analyze the head injury of bus passengers due to frontal-crash by measuring the Head Injury Criterion (HIC) value. The analysis was conducted by modeling two conditions: seats with and without cushion. The results show that in general, seat cushion did not have a significant effect in altering the HIC value.
Keywords: Finite element analysis; frontal crash; head injury criterion.

1. INTRODUCTION

In Indonesia, the bus plays a vital role in public transportation. Its number is increasing every year. From the statistic published by Land Transportation Directorate of the Ministry of Transportation, in 2016, the growth was 5.57% [1]. However, the safety aspects still become a primary concern in Indonesia as the number of accidents and fatalities involving buses is considerably high [2].

One type of bus accidents that frequently occurs is frontal-crash [3]. Therefore, the study on bus safety against frontal crashes is critical. The US National Highway Traffic Safety Administration (NHTSA) has issued Federal Motor Vehicle Safety Standard (FMVSS) no 208 that regulates occupant crash protection by specifying vehicle crashworthiness requirements in terms of forces and accelerations measured on humanlike dummies in test crashes, and by specifying equipment requirements for active and passive restraint systems. One of the parameters to be measured is Head Injury Criterion (HIC) value, as a tool to assess the severity of the head injury of the occupants. FMVSS 208 has regulated the maximum allowed HIC_{15} value on humanlike dummies is 700 [4].

There are already several studies regarding passenger safety in frontal impacts by optimizing passenger's seats distance using a sled test [5,6]. In the author's previous work, the effectivity of seatbelt (lap and shoulder belt) has also been studied by conducting a finite element simulation of a frontal crash using two-step simulations [7]. In the current study, the effect of the addition of seat cushion in the seat model will be analyzed using LS-DYNA software. The simulation will be performed by modeling two conditions: seat with and without cushion, and two different seatbelt configurations: no seatbelt and a lap seatbelt.

2. FINITE ELEMENT SIMULATION

Two-step simulations were conducted in the present work. In the first step, the full-frontal barrier crash test without involving dummies was simulated (Figure 1) to measure the deceleration curve of the bus. In the second step (the sled test simulation), only seats and dummy were modeled (Figure 2). Deceleration data obtained in the previous step is used as input in the second step.

In the first step simulation, only the main components of the bus were modeled. The seats and passengers were represented as block masses. The arrangement was made so that the mass distribution of the model was close to the actual one. The superstructure and chassis were made of steel JIS G3445, with yield and ultimate strength of 309 MPa and 667 MPa, respectively. Meanwhile, in the second simulation, the Hybrid III 50th Percentile Male Sitting dummy that represents the average Indonesian male anthropometry, aged between 18 to 40 years old, was utilized. The dummy has a mass of 63 kg and a sitting height of 84 cm [8]. The mechanical properties of the cushion were obtained from the compression test that follows ASTM D 3574.

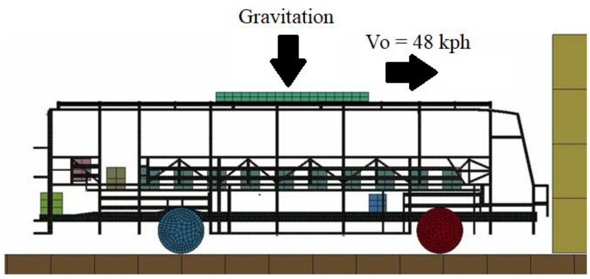

Figure 1 Full frontal barrier crash test.

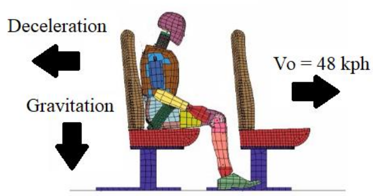

Figure 2 Sled test simulation.

3. RESULTS AND DISCUSSION

Figure 3 shows the results of the full-frontal barrier crash test after 100 and 300 milliseconds. After the impact, the dummy was accelerated to the front. The unbelted dummy was then ejected from the seat, then its knees and head hit the front seat, as depicted in Figure 4. On the contrary, the dummy with seatbelt will still be restrained to the seat, as shown in Figure 5. The typical head acceleration recorded during simulation is given in Figure 6.

Table 1 shows the calculation results of the HIC_{15} values for various dummy conditions. It is seen that HIC_{15} values for the dummy with lap seatbelt are higher than without seatbelt. After looking into simulation results of the unbelted dummy, it is seen that during ejection, the knees of the dummy hit the front seat first, then the seat deformed to the front. Only after that, the head hit the seat. This phenomenon could explain why the unbelted dummy has a lower HIC_{15} value than the belted one. From calculation results, it is also seen that the seat cushion did not have a significant effect in altering the HIC values. It is predicted that the stiffness of the seat has a more significant role in determining the severity of the head injury of the occupants during the frontal crash.

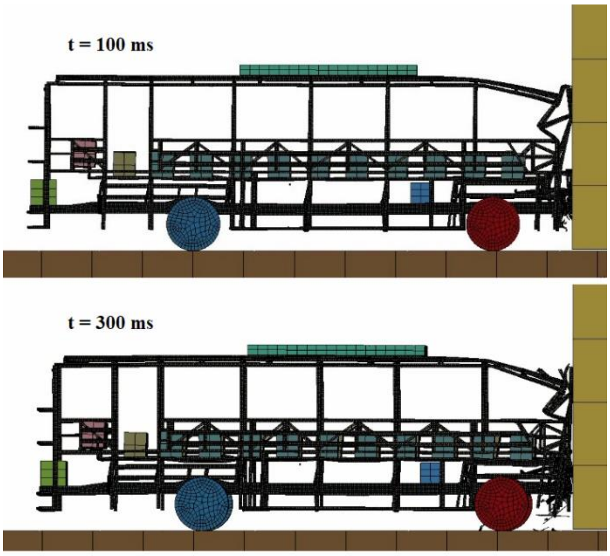

Figure 3 Full-frontal barrier crash test results.

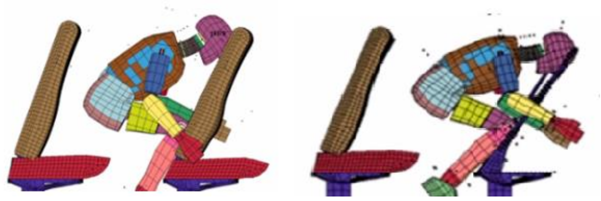

a) b)

Figure 4 Unbelted dummy's ejection to the front seat: a) with cushion, b) without cushion.

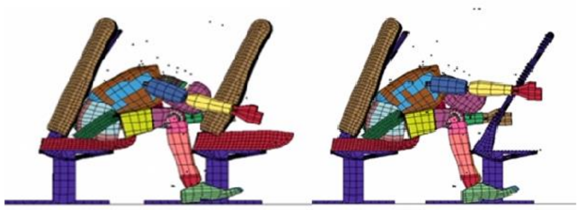

Figure 5 Dummies with lap seatbelt.

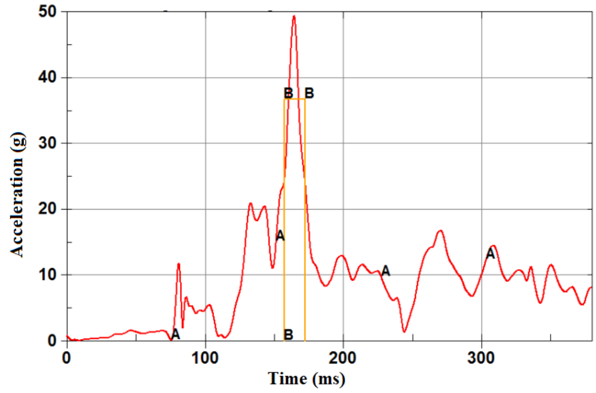

Figure 6 Head acceleration for unbelted dummy (red) and HIC recording (yellow).

Table 1. Calculated HIC_{15} values for various conditions

Seat	unbelted	with lap seatbelt
with cushion	259.3	377.9
without cushion	232.7	375.2

4. CONCLUSIONS

The two-step finite element simulation has been successfully performed to analyze the head injury of the bus passenger in the frontal collision. The simulation results show that the addition of a cushioned model to the passenger seat did not have a significant effect on the HIC values. It is predicted that the other factor such as the seat stiffness plays a more significant role in determining the severity of the head injury of the occupants during the frontal crash.

ACKNOWLEDGMENT

This research was funded by Kementrian Riset Teknologi dan Pendidikan Tinggi Republik Indonesia (Penelitian Dasar Unggulan Perguruan Tinggi/PDUPT).

REFERENCES

[1] Pusat Data dan Informasi Direktorat Perhubungan Darat, "Perhubungan Darat Dalam Angka, Tahun 2016", Land Transportation Directorate of the Ministry of Transportation, Jakarta, 2017.

[2] Direktorat Pembinaan Keselamatan, "Gambaran Umum Kecelakaan Lalu Lintas Angkutan Umum (Bus dan Truk)", Land Transportation Directorate of the Ministry of Transportation, 2018.

[3] Federal Motor Carrier Safety Administration, "Large Truck and Bus Crash Facts 2016", Federal Motor Carrier Safety Administration, United States, 2018.

[4] National Highway Traffic Safety Administration, *Federal Motor Vehicle Safety Standards: Motorcoach Definition*, Occupant Crash Protection. NHTSA-2010-0112, RIN 2127-AK56, 2010.

[5] Hiroyuki Mitsuishi, Yoshihiro Sukegawa, and Fujio Matsukawa, "Research on Bus Passenger Safety in Frontal Impacts", Japan Automobile Research Institute, Japan, 2001.

[6] Luis Martinez, Teresa Vicente, Antonio Garcia, Enrique Alcala, and Fransisco Aparicio, "Analysis of Coaches Rows Seats Distance Influence on The Passengers Comfort and Safety", Polytechnic University of Madrid, Spain, 2015.

[7] Sandro Mihradi, V. M. Puspitaningtias, and Satrio Wicaksono, "Head Injury Analysis of Bus Passenger due to Frontal Crash: Effect of Seatbelt and Seating Position", Asian Conference on Experimental Mechanics, Xi'an, China, October 11-15, 2018.

[8] Perhimpunan Ergonomi Indonesia, *Indonesia Antropometri: The Largest Anthropometry Data in Indonesia*. (https://antropometriindonesia.org/index.php), accessed on 5 August 2019.

Rotary Magnetic Refrigeration Prototype with Active Magnetic Regeneration System: Initiative Research and Prototype Development in Thailand

Ratchatee Techapiesancharoenkij[1,2,3*], Kittiwit Matan[2,4], Yuranan Hanlamyuang[1,2], Weerachai Chaiworapuek[2,5], Jirat Tulyaprawat[1,2], Teetawat Kanluang[1,2], Vichagorn Lupponglung[1,2], Prasertsit Panjatawakup[1,2], Jirattaya Thongjamroon[2,5]

[1)] Department of Materials Engineering, Faculty of Engineering, Kasetsart University, 50 Ngamwongwan Rd., Chatuchak, Bangkok, 10900 Thailand

[2)] Thailand Center of Excellence in Physics (ThEP), Commission of Higher Education, Bangkok, 10400, Thailand

[3)] International Collaborative Education Program for Materials Technology, Education, and Research (ICE-Matter), ASEAN University Network/Southeast Asia Engineering Education Development Network (AUN/SEED-Net), Bangkok, Thailand

[4)] Department of Physics, Faculty of Science, Mahidol University, 272 Rama VI Rd., Ratchatehewi, Bangkok, 10400 Thailand

[5)] Department of Mechanical Engineering, Faculty of Engineering, Kasetsart University, 50 Ngamwongwan Rd., Chatuchak, Bangkok, 10900 Thailand

[*]Corresponding e-mail: fengrct@ku.ac.th

ABSTRACT – A rotary magnetic refrigeration (MR) prototype is designed and developed in this work. The MR prototype consists of (i) the rotary permanent magnet (PM) system (Figure 1), (ii) the active magnetic regenerators (AMR, Figure 4), and (iii) the heat exchange fluid flow controls (Figure 6). The rotary magnet system was designed using COMSOL AC/DC module. The rotary PM system was built and tested with the resultant maximum magnetic field of 0.65 tesla and minimum field of 0 tesla. The AMR bed contains packed magnetocaloric Gd particulates. The temperature of Gd solid refrigerant increases with adiabatic magnetization and decreases with adiabatic demagnetization. Heat exchange fluids must be used to exchange and transport heat from the Gd refrigerants to cold and hot heat exchange units. The preliminary test showed that the MR prototype exhibits the maximum temperature span of 1.4 °C at no thermal load. The demonstration of the MR prototype initiates the development of magnetocaloric materials and magnetic refrigeration in Thailand.

Keywords: Magnetic Refrigeration; Magnetocaloric Effect; Active Magnetic Regenerator; Magnetic Field; Gadolinium

1. INTRODUCTION

Cooling and refrigeration are basic needs for human beings in daily lifestyle. In tropical Asean countries, refrigeration is integrated to their people in everyday life, e.g. household, work, retails, and transport sectors. It has been reported that, in Thailand, the electricity consumption for domestic cooling and refrigeration was accounted for more than 50% of the total domestic electricity consumption [1].

Currently, one of the most commonly-used refrigeration system is a vapour compression cooling (VC). The VC system applies phase-changing refrigerant as a coolant medium. Under pressure change and heat exchange, the refrigerant's temperature changes due to its phase transformation between hot liquid (under high pressure) and cold vapour (under low pressure). The VC system shows good performance for high cooling power and large temperature span. However, the VC system requires the use of a compressor for irreversibly pressurizing the refrigerant, which consumes high energy with low efficiency. Moreover, the refrigerants used in the VC system normally consist of hydrofluorocarbons (HFCs) and hydrochlorofluorocarbons (HCFCs), which damage the ozone layer and increase the greenhouse effect. Therefore, several alternative refrigeration systems that exhibits high energy efficiency and environmental-friendly processes have been proposed and developed.

The magnetic refrigeration (MR) system has gained a lot of attentions, because the MR system replaces environmental-hazardous liquid refrigerant with solid magnetocaloric refrigerants. The refrigeration cycles of the magnetocaloric effect can potentially exhibit high energy efficiency up to 60% of Carnot cycle [2,3]. The magnetic refrigeration is based on the thermodynamics and Maxwell relation of entropic and magnetic states, known as the magnetocaloric effect [3–5]. The temperature of a magnetocaloric material increases under adiabatic magnetization (H field on) and decreases under adiabatic demagnetization (H field off). Therefore, the magnetocaloric solid refrigerants can be used to cool down the system by using the varying magnetic field, e.g. rotating permanent magnet, without the need for a pressurizing compressor.

Active magnetic regenerator cycle (AMR) is commonly used in majority of the reported high-performance MR prototypes [6–12]. For the AMR cooling cycle, a magnetocaloric material performs two roles including (i) a refrigerant whose temperature changes under magnetization/demagnetization, and (ii) a regenerator exchanging heat with water or coolant fluids to expand a temperature span of the cooling cycle [4,13].

For designing a MR prototype, three important components should be considered, including a selection of magnetocaloric materials and an AMR bed structure, a magnetic-field generating system, and a control system of a heat-exchange fluid flow. Gd-based and La-based alloys are one of the most widely-used magnetocaloric materials in reported MR prototypes, because they provide large entropy change under magnetization at near room temperature. For a magnetic field generating system, a permanent magnet system (PM) is more practical than an electromagnet system, since a PM system does not require a large electromagnet coil with high electrical power consumption to generate high field. Normally, a rotating PM setup is commonly applied, as the field at a stationary AMR bed can be varied from 0 to high field with a continuous rotation of the PM structure [14].

In this work, an AMR rotary magnetic refrigeration prototype has been designed and built. A rotary magnet design was studied with the goals for compactness and efficiency. The PM assembly design was first computed using COMSOL AC/DC module. The final PM assembly was then built and tested. Gd particulates were used as magnetocaloric materials in this work. An AMR structure was designed corresponding to the PM assembly constraint. The flow control of a heat-exchange coolant was set to coordinate with the magnetization/demagnetization cycle of the prototype. The purpose of this initiative MR prototype development is for future study of the performance of different magnetocaloric materials and AMR bed designs. The preliminary results of the prototype performance are reported in this presentation.

2. METHODOLOGY

2.1 Permanent magnet assembly design

The PM assemblies were designed and computed using COMSOL AC/DC module. Due to a manufacturing constraint, a PM shape is limited to a simple rectangular shape. With a compact requirement and simple rectangular shape constraint, the PM assembly was designed, based on the design principle from the prior work by Okamura et al. [15,16], Lozano et al.[17], and Monfared, et al. [12]. Different PM assembly designs were investigated and discussed in Ref. [18]. The final PM assembly design is shown in Figure 1. Four rectangular Nd-Fe-B permanent magnets were used to generate magnetic fluxes. Soft-magnetic steels were arranged between the PM to concentrate and guide the flux lines in a complete magnetic flux loop.

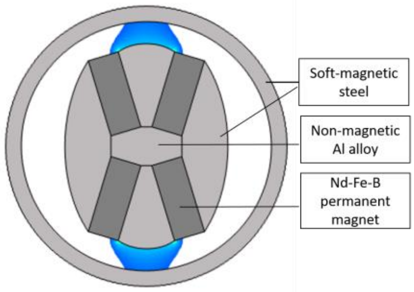

Figure 1 Cross-sectional view of the PM assembly for the MR prototype

Figure 2 shows the simulated results of the magnetic flux density in the gap area between the rotor and stator of the PM assembly. The maximum magnetic flux density in the gap is 0.85 T. The average flux density in the gap is 0.65 T. The flux lines were shown in Figure 2 with the flux lines were generated from the PM and guided through the connected soft magnet pole. The flux lines continue across the gap to the outer stator and returns to the opposite soft magnet pole for magnetic loop completion.

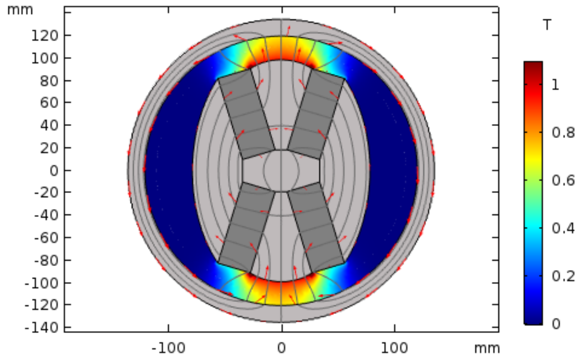

Figure 2 Simulated results of the magnetic flux densities in the gap between the rotor and stator of the PM assembly

2.2 AMR prototype design and assembly

The PM assembly from the design in Figure 1 was assembled with the fixing enclosure and rotating shaft, as shown in Figure 3(a). The PM assembly was fabricated and successfully built as shown in Figure 3(b). The blue plastic structure located in the gap between the rotor and stator is the housing for the AMR beds. As the PM rotor was rotated, the magnetic field on a stationary AMR bed would change resulting in continuous magnetization and demagnetization cycles.

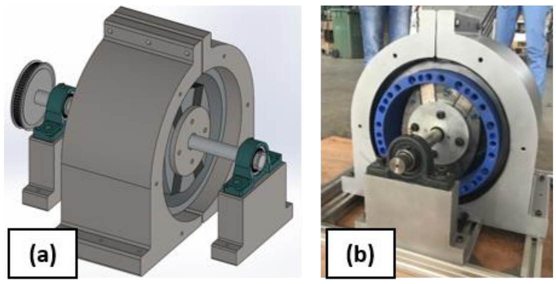

Figure 3 (a) CAD drawing and (b) the actual structures of the total assembly of the PM assembly, enclosure, and rotating shaft.

AMR housing and AMR beds were made of polyamide plastic (PA6) for strength with good thermal insulation. Gd particulates of 200 micron diameter or smaller were packed in a bed. Four AMR packed beds, with length of 8 cm, were inserted in the AMR housing, as shown in Figure 4. A pair of the beds were aligned together, so that both beds were under the same magnetization or demagnetization state. The other pair was aligned orthogonally to the former pair. As a result, when one pair was under magnetization, the other pair was under demagnetization state. The stationary AMR beds were connected with the valves for heat-exchange fluid to flow through.

Automotive coolant (diluted ethylene glycol with corrosion inhibitor) was used as a heat-exchange fluid to ensure that Gd particulates did not corrode over usage.

The flow distribution of the heat-exchange fluid was controlled by solenoid valves. For the AMR beds under magnetization (temperature rise), the fluid flow through the beds from cold heat exchange (CHEX) to hot heat exchange (HHEX). Vice versa, for the AMR beds under demagnetization (temperature drop), the fluid flow through the beds from HHEX to CHEX. A 3-phase motor was used to rotate the magnet rotor via a pulley and belt connection to the shaft. A reciprocating displacement pump, with maximum flow rate of 2.5 LPM, was used to drive fluid flow. The final assembly of the MR prototype is shown in Figure 5.

Figure 4 AMR bed housing and packed AMR bed with Gd particulates

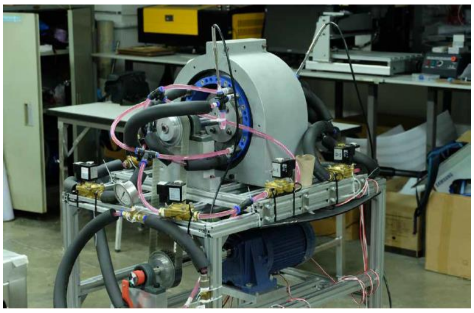

Figure 5 Full assembly of the rotary AMR refrigeration prototype

For the preliminary performance test, the temperature span of magnetic cooling was measured at no thermal load. The pressure drop across the system was limited to 2 bar to avoid the mechanical swelling of the PA6 AMR housing and beds. The temperature span was measured across the AMR bed with four RTD thermocouples were located at 4 points across the AMR bed, as shown in Figure 6. T1 and T4 were the temperatures of the coolant flowing into the bed, from HHEX and CHEX, respectively. T2 and T3 were the temperatures of the coolant flowing out off the bed, to CHEX and HHEX, respectively.

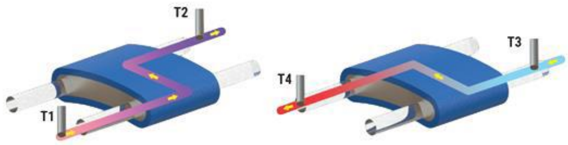

Figure 6 Four locations for temperature measurements across the AMR bed

3. RESULTS AND DISCUSSION

3.1 *Permanent magnet assembly performance*

Figure 7 shows the results of the magnetic flux density in the gap between the rotor and stator of the PM assembly. The magnetic flux density was measured as a function of a rotating angle of the PM rotor pole. In one rotating round of the rotor, two cycles of magnetization and demagnetization were applied on both pairs of the AMR beds. The maximum field strength of 0.65 T was measured at the gap location closest to the rotor pole. At the position closer to the outer stator, the field dropped to 0.55 T. The maximum field was lower than the calculated field of 0.85 T from the COMSOL simulation. The difference is due to the actual magnetic properties of the permanent magnet and soft magnet, e.g. remanence, coercivity, are lower than the input values in the simulation. This may be due to the limitation of the manufacturing processes.

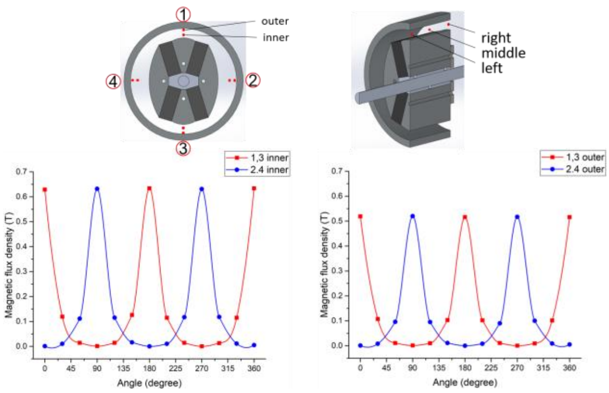

Figure 7 Magnetic flux density as a function of the rotating angle of the PM rotor pole. The top picture shows the 0-degree orientation of the rotor.

3.2 *AMR refrigeration prototype performance*

For the flow rate test, with the control of pressure drop below 2 bar, the maximum flow rate was only 0.5 LPM. The friction loss across the packed AMR beds were large, because the Gd particulates were irregular shapes and small in sized. The fluid flow channels were small and complex, resulting in high pressure drop. Moreover, the automotive coolant (diluted ethylene glycol) also exhibited higher dynamic viscosity than water. As a result, the pressure drop of the system was large resulting in low fluid flow rate for this setup.

The PM rotation was in a step motion with an interval period of magnetization and demagnetization of 3 sec each. Before the MR cycle, the temperature of the heat exchange fluid was controlled at 21 °C by an external chiller and flowed throughout the MR system for 10 minutes to ensure uniform temperature. Then the PM magnet was rotated to generate alternating field of 0 T (demagnetization state) and 0.65 T (magnetization state). The fluid temperature from HHEX (T1) was always controlled at 21 °C, while the fluid temperatures at other locations (T2, T3, and T4) changed by the magnetic cycle processes.

As the MR was on, T2 and T3 slowly decreased from the HHEX temperature (T1 = 21 °C). The temperature span, which is the difference between the HHEX and CHEX temperature (T1 – T2), was recorded. The temperature span as a function of time during MR ON and Off is shown in Figure 8. The maximum temperature span at zero thermal load is 1.4 °C. The cooling temperature span for the current setup is low. It is due to low maximum field and low flow rate. For the ongoing work, the flow rate is improved by using low viscous fluid. The AMR magnetocaloric materials with varying Curie temperature will also be used to increase the temperature span and the MR prototype performance.

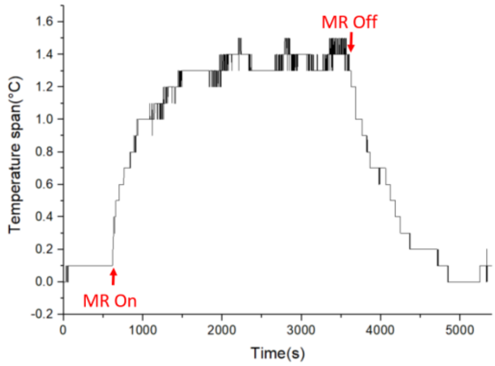

Figure 8 Cooling temperature span as the MR system was on over time. The temperature span was measured at zero thermal load.

4. CONCLUSIONS

The AMR magnetic cooling prototype, using Gd as magnetocaloric solid refrigerant, was designed, built, and tested. The rotary PM assembly generate a cyclic field of 0 to 0.65 T. The flow rate of the heat exchange fluid was limited at 0.5 LPM due to high pressure drop across the system. The MR prototype successfully exhibits cooling capability with the preliminary temperature span at zero thermal load of 1.4 °C.

ACKNOWLEDGEMENT

The research project is funded by Thailand Center of Excellence in Physics (ThEP) under Grant No. ThEP-60-PIP-MU1.

REFERENCES

[1] “Thailand Energy Situation in Year 2017 and Energy Trend in Year 2018,” Energy Policy and Planning Office, Ministry of Energy, 2018.

[2] C. Zimm, A. Jastrab, A. Sternberg, V. Pecharsky, K.G. Jr, M. Osborne, I. Anderson, “Description and Performance of a Near-Room Temperature Magnetic Refrigerator,” in *Advances in Cryogenic Engineering*, P. Kittel, Ed. Springer US, pp. 1759–1766, 1998.

[3] V. K. Pecharsky and K. A. Gschneidner Jr, “Magnetocaloric effect and magnetic refrigeration”. J. Magn. Magn. Mater. 200, pp. 44–56, 1999.

[4] F. C. Chen, R. W. Murphy, V. C. Mei, and G. L. Chen, “Thermodynamic Analysis of Four Magnetic Heat-Pump Cycles”. J. Eng. Gas. Turb. Power. 114, pp. 715–720, 1992.

[5] K. A. Gschneidner Jr. and V. K. Pecharsky, “Magnetocaloric materials”. Annu. Rev. Mater. Sci. 30, pp. 387–429, 2000.

[6] C. Zimm, A. Boeder, J. Chell, A. Sternberg, A. Fujita, S. Fujieda, K. Fukamichi, “Design and performance of a permanent-magnet rotary refrigerator”. Int. J. Refrig. 29, pp. 1302–1306, 2006.

[7] K. Engelbrecht, D. Eriksen, C.R.H. Bahl, R. Bjørk, J. Geyti, J.A. Lozano, K.K. Nielsen, F. Saxild, A. Smith, N. Pryds, “Experimental results for a novel rotary active magnetic regenerator”. Int. J. Refrig. 35, pp. 1498–1505, 2012.

[8] S. Jacobs, J. Auringer, A. Boeder, J. Chell, L. Komorowski, J. Leonard, S. Russek, C. Zimm, “The performance of a large-scale rotary magnetic refrigerator”. Int. J. Refrig. 37, pp. 84–91, 2014.

[9] C.R.H. Bahl, K. Engelbrecht, D. Eriksen, J.A. Lozano, R. Bjørk, J. Geyti, K.K. Nielsen, A. Smith, N. Pryds, “Development and experimental results from a 1 kW prototype AMR”. Int. J. Refrig. 37, pp. 78–83, 2014.

[10] A. Kitanovski, J. Tušek, U. Tomc, U. Plaznik, M. Ozbolt, and A. Poredoš, *Magnetocaloric Energy Conversion*, 1st ed. Springer; 2015.

[11] D. Eriksen, K. Engelbrecht, C.R.H. Bahl, R. Bjork, K.K. Nielsen, A.R. Insinga, N. Pryds, “Design and experimental tests of a rotary active magnetic regenerator prototype”. Int. J. Refrig. 58, pp. 14–21, 2015.

[12] B. Monfared, “Design and optimization of regenerators of a rotary magnetic refrigeration device using a detailed simulation model”. Int. J. Refrig. 88, pp. 260–274, 2018.

[13] W. A. Steyert, “Stirling-cycle rotating magnetic refrigerators and heat engines for use near room temperature,” J. Appl. Phys. 49, pp. 1216–1226, 1978.

[14] R. Bjørk, C. R. H. Bahl, A. Smith, and N. Pryds, “Review and comparison of magnet designs for magnetic refrigeration”. Int. J. Refrig. 33, pp. 437–448, 2010.

[15] T. Okamura, K. Yamada, N. Hirano, and S. Nagaya, “Performance of a room-temperature rotary magnetic refrigerator,” Int. J. Refrig. 29, pp. 1327–1331, 2006.

[16] T. Okamura, R. Rachi, N. Hirano, and N. Nagaya, “Improvement of 100 W class room temperature magnetic refrigerator,” The Second International Conference on Magnetic Refrigeration at Room Temperature, Portoroz, Slovenia, 2007, pp. 377–382.

[17] J.A. Lozano, K. Engelbrecht, C.R.H. Bahl, K.K. Nielsen, J.R. Barbosa Jr., A.T. Prata, N. Pryds, “Experimental and numerical results of a high frequency rotating active magnetic refrigerator”. Int. J. Refrig. 37, pp. 92–98, 2014.

[18] T. Kanluang, Y. Hanlumyuang, and R. Techapiesancharoenkij, “Design and development of magnetic refrigeration prototype for the performance analysis of magnetocaloric materials,” J. Phys.: Conf. Ser. 1144, p. 012065, 2018.

The Implementation of Single-Input Single-Output AutoRegressive Moving Average with eXogenous Input (ARMAX) Modeling in Modal Analysis

Ignatius Pulung Nurprasetio[1,*], Tem Kimleang[2], Tobias Prawira Tumbuan[1], Bentang Arief Budiman[1,3]

[1)] Faculty of Mechanical and Aerospace Engineering, Institut Teknologi Bandung, Jalan Ganesha 10, Bandung 40132, Indonesia
[2)] Institute of Technology of Cambodia, Industrial and Mechanical Engineering, Phnom Penh, 1250, Cambodia
[3)] National Center for Sustainable Transportation Technology, Bandung, Indonesia

[*]Corresponding e-mail: ipn@ftmd.itb.ac.id

ABSTRACT – Modal analysis is an attempt to obtain mathematical model of vibration system based on measurement. Traditionally, Fourier-based method or FBM is the method of choice. Although not new, parametric time domain method such as ARMAX modeling is a better alternative since it incorporates noise. In this paper, a detailed and comprehensive SISO ARMAX based modal analysis procedure is discussed. For numerical experiment, we simulate an underdamped SDOF vibration system excited by a broadband signal. A discrete-time ARMAX is first estimated before it is transformed to the continuous-time domain. In addition, laboratory experiment involving L-shaped beam is also performed, in which the beam is clamped at one end and excited at the other end. All calculations are performed using MATLAB®. Numerical experiment shows that the parametric method is more accurate as compared with the FBM under the presence of noise, whereas for the beam experiment, the results are comparable.

Keywords: ARMAX modeling, noise corrupted observation, parametric modal analysis

1. INTRODUCTION

The idea of implementing time-domain parametric model such as the AutoRegressive Moving Average with eXogenous input or ARMAX model in modal analysis is definitely not new [1]. By modal analysis, we are referring to the effort of obtaining a complete mathematical model of vibration systems, along with all their attributes such as natural frequencies, damping ratios, and mode shapes, from input and output signal measurements [2, 3]. However, reference with a detailed and comprehensive information on the above subject is difficult to find. Since it integrates ideas from system identification, which is defined in discrete-time domain, to obtain parameters of a continuous-time system, we need to select the suitable discrete-to-continuous transformation. In addition, vibration systems are basically deterministic, whereas ARMAX model is a representation of stochastic processes. Therefore the implementation of ARMAX model in modal analysis requires the satisfaction of some requirements such that it may be transformed into a valid vibration system model. In this paper, these requirements is performed in the pre-modeling stage.

The modeling stage will rely on MATLAB® [4]. However, the order of the ARMAX model should follow specific rule that depends on the type of discrete-to-continuous transformation. For zero order hold (ZOH) transformation that is utilized in this paper, the AR and X order depends on the order of the governing differential equation of the vibration system or the number of degree-of-freedom of the system with unit delay [5]. The MA order is the only part of the model that needs to be optimized using standard order determination measure such as the Bayesian Information Criterion (BIC) [6]. Thus, noise dynamics will be accommodated by the MA part.

In the post-modeling stage, the discrete-time model is first validated by looking at the properties of the residuals and, most importantly, by observing the quality of the one-step-ahead prediction [6, 7]. Once validated, the ARX part of the discrete-time model will be altered into continuous-time to form the model of the vibration system through ZOH transformation [5].

The method will be demonstrated numerically as well as experimentally. For the numerical experiment, we simulate a single degree-of-freedom vibration system which is excited by a broadband input. Noise is introduced by adding both the input and output signal by white and colored Gaussian noise. In addition, we also perform a simple laboratory experiment in which an L-shaped beam is excited by a magnetic exciter at one end and clamped at the other end. A force transducer is placed at the tip of the exciter and the measured signal from the force transducer will be regarded as the input signal, whereas the output of an accelerometer placed on the beam will be the output signal.

2. METHODOLOGY

Consider the following governing differential equation of a single-degree-of-freedom (SDOF) vibration system:

$$m\ddot{y} + c\dot{y} + ky = f(t) \qquad (1)$$

In the above equation, y denotes the generalized coordinate [m], m: mass of the vibrating body [kg], c: damping coefficient [Ns/m], k: spring stiffness [N/m], and $f(t)$ the excitation force [N]. Taking the Laplace transform of Equation (1) followed by normalization and parameterization will result in the following relation [8]:

$$Y(s) = \frac{1/m}{s^2+2\zeta\omega_n s+\omega_n^2} F(s) \qquad (2)$$

in which ζ stands for the damping ratio and ω_n is the natural frequency of the system [rad/s]. Upon sampling, the continuous-time system (1) in general will become the following discrete-time system:

$$y[n] + a_1 y[n-1] + a_2 y[n-2] = b_1 f[n-1] + b_2 f[n-2] \quad (3)$$

With the inclusion of noise dynamics, Eq. (3) may be cast into the following SISO ARMAX system [6, 7]:

$$y[t] = G(q^{-1})f[t] + H(q^{-1})w[t] = \frac{B(q^{-1})}{A(q^{-1})} f[t] + \frac{C(q^{-1})}{A(q^{-1})} w[t] \quad (4)$$

In Eq.(4), $G(q^{-1})$ stands for the discrete transfer function of the sampled system, $H(q^{-1})$ is the transfer function of the noise dynamics, and the autoregressive (AR), exogenous (X), and moving average (MA) polynomials are,

$$A(q^{-1}) = 1 + a_1 q^{-1} + \cdots + a_{na} q^{-na} \quad (5)$$

$$B(q^{-1}) = b_0 + b_1 q^{-1} + \cdots + b_{nb} q^{-nb} \quad (6)$$

$$C(q^{-1}) = 1 + c_1 q^{-1} + \cdots + c_{nc} q^{-nc} \quad (7)$$

In Eq. (5)-(7), q^{-1} stands for the backshift operator, i.e., $q^{-1}y[t] = y[t-1]$. Furthermore, the system is assumed to satisfy the generic stability condition, in the sense that all zeroes of $A(q^{-1})$ lie strictly inside the unit circle, and also invertibility condition, i.e., all zeroes of $C(q^{-1})$ strictly lie inside the unit circle [6]. The noise $w[t]$ is also assumed to be Gaussian white noise N(0, σ_w^2).

For ZOH transformation, it is known that upon setting the AR order to be n_a, the X-polynomial will also be of order n_a with unit delay, whereas the MA-polynomial will follow the order determination procedure using a legitimate criterion [6]. In addition, for vibration system, n_a should be an even integer.

The acceptance of a particular ARMAX model as the best discrete-time model representing the measured data is judged primarily on the quality of the one-step-ahead prediction [6, 7], which is calculated as:

$$\hat{y}[t|t-1] = y[t] - \hat{e}[t|t-1] \quad (8)$$

The closer the one-step-ahead prediction to the measured data, the better the fit of the ARMAX model. Once the estimated ARMAX model have been validated, the estimated system transfer function, i.e., $[B(q^{-1}, \hat{\theta}) / A(q^{-1}, \hat{\theta})]$ representing structural dynamics is transformed back to the continuous-time domain using the ZOH inverse transformation [5].

3. NUMERICAL AND EXPERIMENTAL RESULTS

For the numerical simulation, consider the following SDOF vibration system as depicted in Fig. 1, in which we pick a hypothetical set of values: m = 1 kg, c = 4.85 Ns/m, and k = 207025 N/m. Inserting the above values to Eq.(1) results:

$$\ddot{x} + 4.85\dot{x} + 207025x = f(t) \quad (9)$$

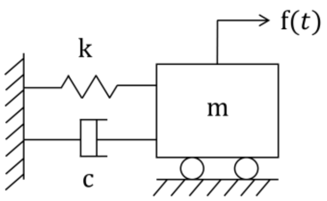

Fig. 1 SDOF vibration system

The system will have theoretical value of damping ratio, ζ, equal to 0.00533 and natural frequency, ω_n, equal to 455 rad/s or f_n 72.415 Hz.

The evaluation of the proposed method will focus on the effectiveness of method to deal with noise corrupted observation in vibration response data with different noise-to-signal ratios (N/S). The simulated response is generated using MATLAB® with sampling frequency 725 Hz and total observation time 12 s. The system is excited with input signal generated by taking the sign of the white Gaussian signal N(0,1) to satisfy the persistently exciting of sufficient order requirement [7]. The numerical test consists of two test cases. For test case 1, the noise-corrupted response is obtained by adding white Gaussian noise (WGN) at 1% and 10% N-S ratio. For test case 2, the noise-corrupted response is obtained by adding colored noise (CLN) at 1% and 10% N-S ratio. N-S ratio is defined as the ratio of the standard deviation of the noise (σ_n) over the standard deviation of the response (σ_s). The white and colored noises are zero-mean and uncorrelated with the excitation. The CLN is generated by passing the white noise through a shaping filter and the filter is a dynamic low pass filter.

Monte Carlo simulations are also performed to investigate the statistical characteristics of the proposed method. For each test case, two 30 recorded data-sets corresponding to the same structural system and N-S ratio are used in Monte Carlo analysis. Each set is analyzed by the proposed approach, and the sample mean values and standard deviations of the estimated modal parameters are then calculated. In addition, to compare the result with the frequency domain method, the same 30 data sets are employed. In this case, periodogram estimator and standard half power bandwidth [9] are used to obtain the modal parameters. The complete results of test case 1 and 2 are presented in Table 1 and Table 2, respectively. The modal parameter estimates (from both tables) are evidently very good and slightly better than the FBM.

Table 1. Test Case 1 Result.

True Par.		1% N/S ratio		10% N/S ratio	
		Prop. Meth.	FBM	Prop. Meth.	FBM
f_n [Hz]	72.415	72.415	72.407	72.415	72.408
ζ	0.0053	0.0053	0.0055	0.0053	0.0056

Table 2. Test Case 2 Result.

True Par.		1% N/S ratio		10% N/S ratio	
		Prop. Meth.	FBM	Prop. Meth.	FBM
f_n [Hz]	72.415	72.415	72.407	72.415	72.408
ζ	0.0053	0.0053	0.0055	0.0053	0.0055

To have a better view, the frequency response plots are also generated for the proposed method and the FBM for the 10% N/S ratio. Figure 1 depicts the results of Test Case 1, while Figure 2 portrays the results of Test Case 2. In both cases, the FBM cannot match the smoothness and accuracy of the proposed approach.

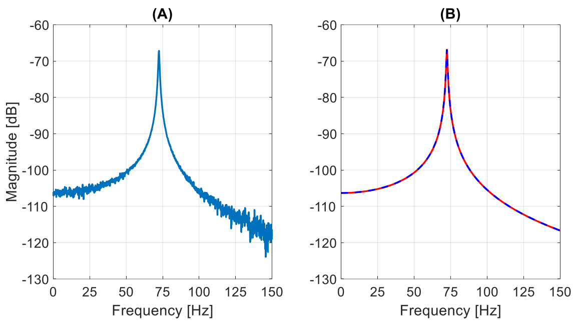

Fig. 1 The frequency response plots of the transfer functions, on the left estimated by FBM based on 8192 data points – Hanning window (N/S = 10%), and on the right, estimated by ARMAX (2, 2, 2) model for Test Case 1.

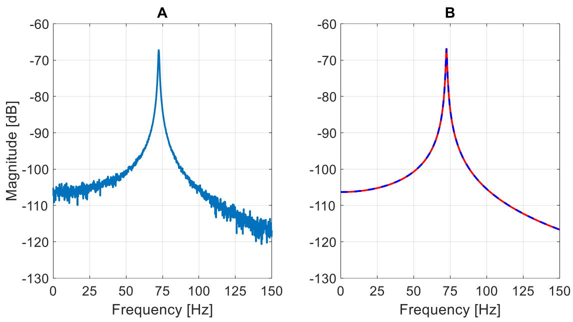

Fig. 2 The frequency response plots of the transfer functions, on the left estimated by FBM based on 8192 data points – Hanning window (N/S = 10%), and on the right, estimated by ARMAX (2, 2, 2) model for Test Case 2.

In addition to computer simulation, a laboratory experiment using an L-shaped cantilever beam is also performed. The set-up is shown in Fig. 3 and Fig. 4. The beam was excited by band-limited (filtered with band pass frequency from 8 to 150 Hz) white Gaussian random, N(0,4), force signal generated by LabVIEW. The signal was applied through an electromagnetic shaker, measured by a load cell. The vibration response were measured through accelerometers at two points on the first leg of the beam as shown in Fig. 4. The frequency range of interest was selected as 0 to 250 Hz. The force excitation and the corresponding response signal were amplified and sampled at sampling frequency 1 kHz by data acquisition system which consists of NI 4472 PCI equipped with antialiasing filter, NI6001, and computer with LabVIEW program installed. The vibration responses and excitation signals were recorded for 600 s. Thirty data sets were collected, each one was considered as an independent experiment and consists of 1024 samples in which 924 was used for estimating the ARMAX parameters and the remaining 100 for model validation.

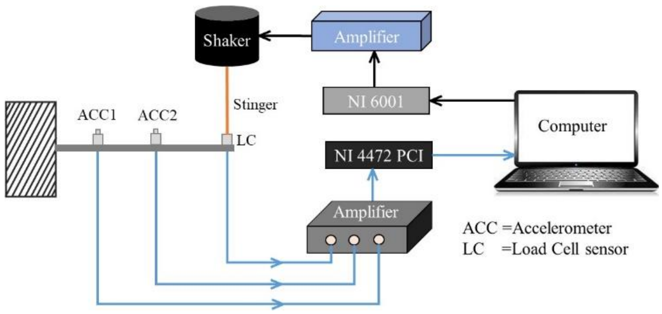

Fig. 3 Schematic diagram of the experimental set-up

Fig. 4 The experimental set-up.

ARMAX modeling resulted in an ARMAX (8, 8, 7). The one-step-ahead prediction test is depicted in Fig. 5.

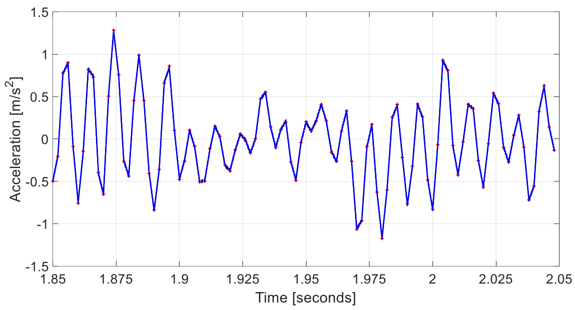

Fig. 5. The one step ahead prediction of the measured vibration acceleration signal results from the estimated ARMAX (8, 8, 7). The solid line represents measured acceleration signal (L-shaped beam experiment) and the + signs is the prediction signal

The perfect match indicates that ARMAX(8,8,7) is the best model. Since the ARMAX (8, 8, 7) model is obtained as the discrete-time system representation, the continuous-time system as the result of inverse ZOH transformation produces up to four natural frequencies and damping ratios. However, after further investigation, mode number four turns out to be extraneous or computational, since the damping ratio is very high as shown in Table 3. The order of damping ratio, which is in one-tenth, can only be obtained by physically installing viscous dampers. It would not be possible to have equivalent viscous damping ratio for structures in the one-tenth range. Therefore, only the first three modes are considered as the actual modes of the L-shaped beam. In lieu of ARMAX(8,8,7), an ARMAX(6,6,x) is probably a better choice to avoid computational mode, at the cost of increased BIC and reduced quality of the one step ahead prediction.

Table 3 Modal parameters of the L-shaped beam as estimated by the ARMAX (8, 8, 7)

Mode	Frequency [Hz]	Damping ratio
1	10.3744	0.003195
2	39.3133	0.002320
3	113.8900	0.000866
4	*179.0938*	*0.15414*

Frequency response curve of the transfer function estimated by the ARMAX (8, 8, 7) is compared to that estimated by Fourier-based method (FBM). The FBM result appears to be quite inaccurate in the low dB region corresponding to the frequency range of 0-6 [Hz] and 220-250 [Hz]. However, it should be noted that to achieve this agreement, much longer data records had to be used for the FBM. Specifically, 35 overlapped segments (50% overlap factor) consist of 16384 samples each were averaged to obtain such an estimated frequency curve. The Frequency Response Function (FRF) results are depicted in Fig. 6. All peak values on the FRF curves for the ARMAX(8,8,7) and the FBM are in excellent agreement. However, the ARMAX model fails to capture the anti-resonance part around 25.97 Hz.

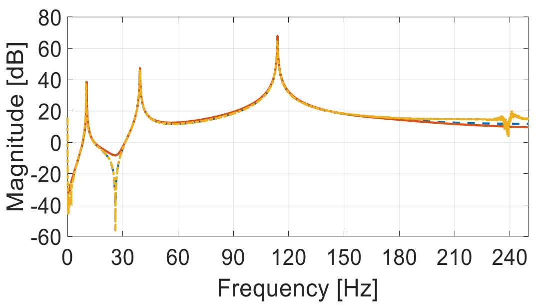

Fig. 6. Frequency response magnitude curves estimated via ARMAX and the FBM. The ARMAX model-based frequency is represented by the blue dashed line, its continuous-time model is represented by the orange solid line, and the FBM is represented by the yellow dashed line

4. CONCLUSIONS

In this paper, an effective and simple structural dynamics system identification based on SISO ARMAX model is elaborated. The performance of the method was evaluated via numerical simulations and laboratory experiment. Comparisons with the classical Fourier-based method (FBM) were made. The results demonstrate that the proposed method may be used to complement the FBM. As the results indicated, the proposed method effectively overcomes the difficulties related to the inadequacy of the FBM in dealing with noisy data and offers high accuracy and resolution even at relatively high noise-to-signal (N/S) ratios. However, there is a problem with model transformation using ZOH in actual experimental data due to the default delay in the model.

ACKNOWLEDGEMENT

The authors wish to acknowledge the financial support of the AUN/SEED-Net that enabled the undertaking of this research work.

REFERENCES

[1] J. He and Z-F Fu, *Modal Analysis*, Butterworth-Heinemann, 2001

[2] P. Avitabile, *Modal Testing – A Practitioner's Guide*, Wiley, 2018

[3] D.J. Ewins, *Modal Testing – Theory, Practice, and Application*, 2nd ed., Wiley, 2009.

[4] L. Ljung, *System Identification ToolboxTM User's Guide—R2017b*, MathWorks, Inc., 2017

[5] K. Baskoro, *Discrete–to–Continuous Transformation Methods Analysis in the Implementation of ARMAX Modeling on Structural Dynamics Parameter Estimation*, Thesis, Mechanical Engineering Study Program, Institut Teknologi Bandung, 2017 (in Indonesian).

[6] L. Ljung, *System Identification – Theory for the User*, 2nd ed., Prentice Hall, 1999.

[7] T. Söderström and P. Stoica, *System Identification*, Prentice Hall, 1989

[8] S.S. Rao, *Mechanical Vibrations*, 5th ed., Prentice Hall, 2011

[9] J.S. Bendat and A.G. Piersol, *Random Data – Analysis and Measurement Procedures*, 4th ed., Wiley, 2010.

Stabilization in Longitudinal Elastic Modulus of Braided Synthetic Fiber Rope for Dynamic Loading

V. Sry [1, 2,*], Y. Mizutani [3], G. Endo[3], A. Todoroki[3]

[1)] Department of Industrial and Mechanical Engineering, Institute of Technology of Cambodia, Russian Federation Blvd, P.O. BOX 86, Phnom Penh, Cambodia
[2)] Department of Mechanical Sciences and Engineering, Graduate School of Tokyo Institute of Technology, 2-12-1, I1-70, I1-457, Ookayama, 152-8552, Tokyo, Japan
[3)] Department of Mechanical Engineering, Tokyo Institute of Technology, 2-12-1, I1-70, I1-457, Ookayama, 152-8552, Tokyo, Japan

[*]Corresponding e-mail: sryvannei@itc.edu.kh

ABSTRACT – This paper discusses the stabilization in longitudinal elastic modulus of braided high modulus polyethylene (HMPE) rope for dynamic loading in tendon-driven robot by mean of preload treatment. Dynamic loading was presented by impact loading which expressed in term of number of drops applied on the rope. Different preload levels were applied on the ropes before they were tested in five consecutive impact loadings in order to investigate the stability of rope modulus. The stabilization of rope modulus was performed based on experimental data of impact loading of the preloaded ropes and the proposed empirical equation which takes number of drop and preload level into account. Based on the empirical equation, the stabilization of the rope modulus could be obtained.

Keywords: Longitudinal elastic modulus, Preload treatment, Number of drop, Preload level, Empirical equation

1. INTRODUCTION

Synthetic fiber ropes with high performances are widely used in mooring systems. In these fields, minimum break load (MBL) and dynamic stiffness of the ropes are very important parameters. Dynamic stiffness of synthetic fiber ropes was extensively studied in both experiment and model [1-8]. Casey and Banfield [1- 2] used large diameter polyester ropes that are applied in mooring lines to determine the dynamic stiffness of the ropes. Davies et al. [3] conducted experiments to determine dynamic stiffness of HMPE and aramid ropes under dry and wet conditions. Francois et al. [4] determined dynamic stiffness of different type of synthetic fiber ropes under different loading conditions then practical model of stiffness was developed. Liu et al. [5] studied the stiffness evolution of polyester, HMPE and aramid under cyclic loading then they proposed an empirical expression for stiffness by taking the mean load, strain amplitude and number of loading cycles into account. Although widely studied, dynamic stiffness of synthetic fiber ropes is not constant and varies with loading conditions and histories because of viscoelastic properties [9-10]. Based on this context, many researches had been conducted to study the effect of loading history applied on the rope so-called bedding-in (preload treatment). Davies et al. [11] found that there is large difference between new rope and preloaded rope in term of load-strain curves obtained from static tensile testing. Weller et al. [12] concluded that preload treatment has great influenced on mechanical property of synthetic fiber rope. Casey et al. [2] confirmed that when the preloaded rope is fully stabilized, the dynamic stiffness of the ropes remains almost constant value. Recently, Lian et al. [13] had investigated the influenced of preload treatment on the mechanical behavior of synthetic fiber rope. They found that the slope of load vs. strain of preloaded rope is significantly larger than that of the virgin rope when the rope is fully stabilized by preload treatment.

Recently, small diameter of high performance synthetic fiber rope such as high modulus polyethylene (HMPE), para-aramid ropes are very popular in robotic fields for example tendon-driven [14-17]. In these fields, there is no specific guideline or study existed for the longitudinal elastic modulus of the rope. All previous researches as mention early were dealt in rope stiffness not in rope modulus which is probably due to difficulty in measuring cross section of the synthetic fiber rope because of presence voids (internal space between strands in the rope) and uneven shape. Furthermore, breaking load and axial stiffness of a rope obviously increase with increasing in rope diameter [18]. To compare the mechanical properties of different fibers, different rope construction and size, a normalization is required. Yet, the normalization of the rope in conventional method is not quite simple as the solid materials due to inconsistency in defining the cross section of the rope which caused by voids between strands in the rope

Therefore, the aims of this paper is to discuss and stabilize the longitudinal elastic modulus of the HMPE rope by preload treatment for dynamic application in tendon-driven robot with the unit of N/tex which is not based on the cross section of the rope. The dynamic application in this study is assumed to be consecutive impact loading in term of number of drops applied on the rope.

2. MATERIAL AND METHODOLOGY

This study examines high modulus polyethylene (HMPE) rope. The HMPE rope was constructed by a braiding method using eight strands. Each strand was made from parallel fibers. The rope was purchased from Hayami (Hayami Industry Co.,LTD, Japan). The minimum break load (MBL) of the rope obtained from the manufacturer was 1765 N. Linear density, expressed in grams per kilometer (1tex =1g/1km) is commonly used in textile engineering due to the presence of voids in the rope. In this study, the linear density of the rope was determined by cutting rope at 1.6m and weighed (Shimadzu AX200) it. Figure 1 shows the braided HMPE rope consisting of eight strands and Table 1 summarizes the material properties of the rope.

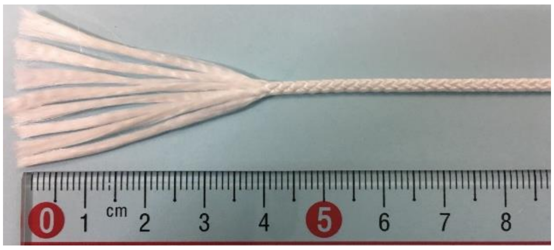

Figure 1 Braided HMPE rope composed of eight strands

Table 1 Material properties of braided HMPE rope

Material	High Modulus Polyethylene (HMPE)
Fiber	IZANAS
Fiber model	DB-60
MBL (static) (N)	1765
Construction	1721* tex, 8 strands braided
Diameter (mm)	2
Supplier	Fiber: Toyobo, Rope: Hayami Industry

* : Obtained by weighting the rope at the length of 1.6 m

An impact tester as shown in Figure 2 was developed to conduct preload treatment and impact testing of the ropes (virgin rope and preloaded ropes). This apparatus contains five main components with the first being the drop mass that is used to generate an impact load. The mass moves along linear guides that are mounted on side poles of the tester. The second part that is located on the side of the drop mass is the steel plate with aluminum disk that is used to fix the fiber rope at the bottom end. The aluminum disk is used to reduce the stress concentration of the ropes at a fixed point. The third component is the rotating winch on the right of the tester that is used to lift and release the drop mass by connecting it with a rope. The fourth component is a load cell (Kyowa, LUK-A-10 KN) that is used to measure the impact load by mounting on top of the tester. The tested rope is fixed to this load cell directly. The fifth component is the draw-wire displacement sensor (Tokyo Sokki Kenkyujo, DP-500E) that is used to measure the rope elongation. Preload treatment was carried out in impact tester by applying dead weight on the rope for 3600 seconds. Preload treatment at different level of loads is shown in Table 2. The preloaded ropes were tested further under five consecutive impact loadings in order to determine elastic modulus of preloaded rope. Impact testing in this study was performed by releasing a 5.1 kg drop mass from 1.03 m. The strain in impact loading was determined using the displacement of draw-wire displacement sensor. Since the linear density of the rope is changed with length of rope when impact loading was applied, then linear density of the rope corresponds to each drop is calculated when discussing about the longitudinal elastic modulus of the rope. When the linear density is used instead of cross section of the rope, the stress in unit of MPa becomes specific stress with unit of N/tex and the longitudinal elastic modulus of the rope becomes longitudinal specific elastic modulus with unit of N/tex.

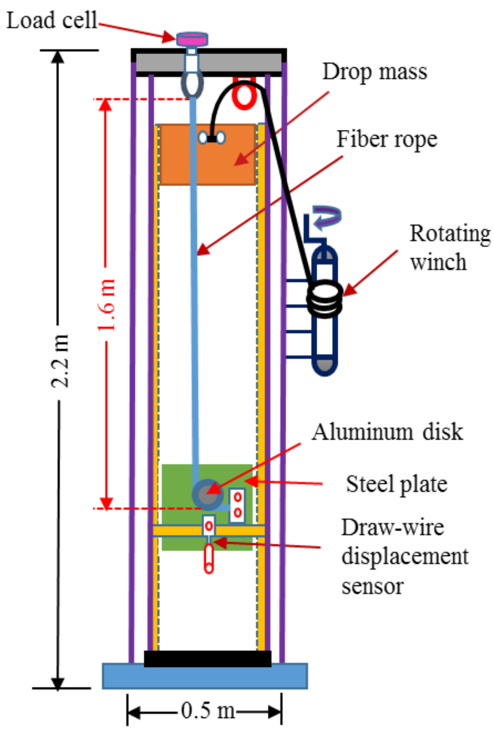

Figure 2 Impact tester for preload treatment and consecutive impact loading

Table 2 Preload treatment condition applied on rope

Preload (N)	P_r= Preload/MBL (%)
172	9.74
220	12.4
363	20.5
607	34.4

3. RESULTS AND DISCUSSION

3.1 Experimental result of virgin rope

Figure 3 shows the results of five consecutive impact loadings of the virgin rope in which abscissa is the strain and ordinate is the specific stress expressed in N/tex. It obviously shows that large strain occurred at the first drop for virgin rope due to large change in construction geometry of the rope when experienced to the first loading [19]. The strain decreases with respect to number of drops as the loading level applied to the rope was the same. The specific modulus at the loading part of virgin rope was determined by fitting the specific stress vs. strain in the linear region. The specific modulus of the virgin rope (second-fifth drop) was determined by using the strain ranging from 0 – 0.4%. For virgin rope at the first drop, specific modulus was calculated based on the strain ranging from 0 – 2% due to large strain in this drop. The summarized of specific modulus for the virgin rope is shown in Table 3. Results clearly show that specific modulus of virgin rope is strongly affected by consecutive impact loading by yielding smallest value at the first drop and subsequently increases in next drops. This variation in specific modulus is undesirable in tendon-driven robot because it causes an unstable in controlling the tendon-driven robot during operation. Therefore, stabilization in rope specific modulus is needed in order to get stable in controlling tendon-driven.

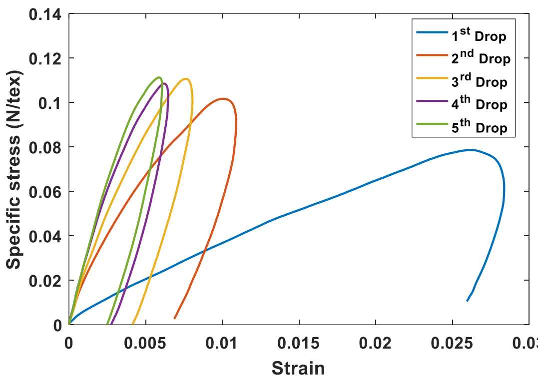

Figure 3 Specific stress-strain curve of virgin rope from five consecutive impact loadings

Table 3 Specific modulus of virgin rope from five impact loadings

N. Drop	Specific modulus (N/tex)
1	3.22
2	14.4
3	18.5
4	21.9
5	23.9

3.2 Experimental results of preloaded ropes

All preloaded ropes were tested in five consecutive impact loadings further in order to determine the specific modulus of the ropes and to investigate the stability in specific modulus of preloaded ropes. The results of five impact loadings of preloaded rope at 9.74%MBL and 34.4%MBL are presented in Figure 4 and 5 respectively. It is obvious that the strain at the first drop depend on the preload level, i.e., if the low preload level applied on the rope, larger strain at the first drop occurred which implies that construction geometry of the rope changes further in impact loading. On the other hand, if higher preload level implemented on rope, construction geometry of the rope changes less since it was already change during preload treatment. Therefore, preload treatment plays an important role in limiting strain of the preloaded ropes as well as the rope specific modulus. The specific modulus of preloaded rope was determined by fitting the specific stress vs. strain in linear region by using the strain data ranging from 0-0.4%. The specific moduli of preloaded ropes for all preload level are given in Table 4.

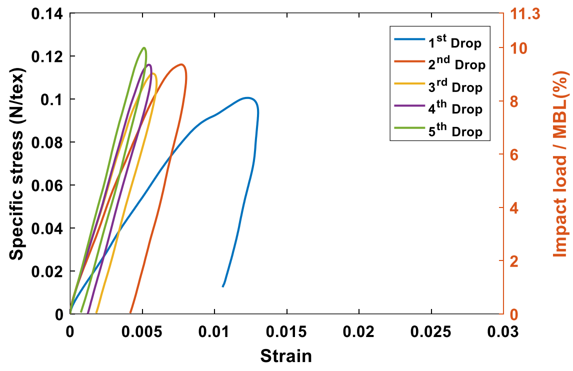

Figure 4 Specific stress-strain curve of preloaded rope at 9.74%MBL from five consecutive impact loading

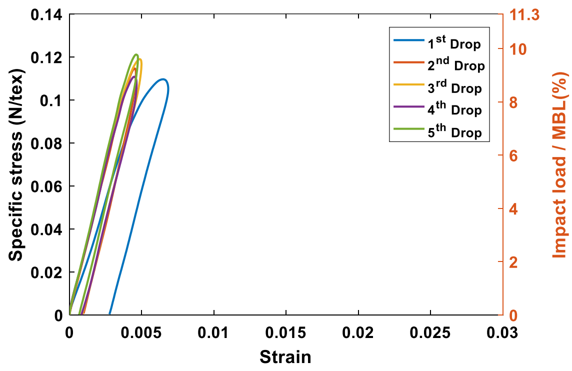

Figure 5 Specific stress-strain curve of preloaded rope at 34.4%MBL from five consecutive impact loading

Table 4 Specific modulus of preloaded rope from five impact loadings

N.	Modulus	Preload level (P_r) (%MBL)			
Drop	(N/tex)	9.74	12.4	20.5	34.4
1	E1	10.7	13.4	18.3	21.1
2	E2	18.0	20.9	24.1	26.9
3	E3	21.6	21.1	24.8	27.3
4	E4	22.7	23.1	24.8	26.6
5	E5	25.7	24.4	24.3	28.3

The specific modulus of preloaded ropes depends on the preload levels and number of drops. The specific modulus of the rope at the first drop has high value when preload level implemented on the rope increases and vice versus. At high preload level, the specific modulus of rope tends to have constant value after the second drop as shown in the case of preload level 20.5 and 34.4%MBL. Whereas at low preload level, rope specific modulus becomes virtually stable from the fourth drop onward as at 12.4%MBL. Because dynamic loading is more severe than that of static, then it is necessary to study stability of the rope specific modulus before utilizing in the robotic fields. Thus, an empirical expression is needed in order to study the trend line specific modulus of the rope and of course the stability of the rope specific modulus. As the modulus for all cases relies on preload level (P_r) and

and number of drops (N). Therefore, a proposed empirical expression for rope specific modulus is presented in Equation (1) as follow:

$$E = a - \lambda exp(-(\alpha P_r + \gamma N)) \qquad (1)$$

where a, λ with unit of N/tex and α, γ with unitless are coefficients that represent the material properties and the construction geometry of the HMPE rope, P_r and N are the preload level and number of drops, respectively. The maximum value of P_r is 1 because P_r is the ratio of preload load with respect to MBL. The term $exp(-(\alpha P_r + \gamma N))$ is responsible for the stability of the rope specific modulus as the number of drops and /or the preload level increases.

The experimental results of impact loading for all preloaded ropes were used to calibrate the coefficients in Equation (1) by fitting specific modulus data. Estimated coefficients in Equation (1) are shown in Table 5. By substituting these coefficients back into Equation (1), specific moduli values for any cases can be obtained. The no preload case is obtained by substituting the preload level P_r=0 into Equation (1). To validate the empirical expression in this study, a comparison between the experimental and the empirical expression was carried out. Table 6 shows the estimated specific moduli of the rope for no preload, and for preload levels of 9.74, 12.4, 20.5, and 34.4% MBL respectively. Figure 6 compares the specific moduli from experimental data and empirical equation for both virgin and preloaded ropes. In overall, the specific moduli obtained from both cases are in good agreement.

Table 5 Value of coefficients in empirical equation (1)

Parameters	a	λ	α	γ
Value	25.1	70.5	5.38	1.12

Table 6 Estimated specific modulus of rope from empirical equation (1)

N. drop	Modulus (N/tex)	Nopreload	Preload level, P_r (%MBL)			
			9.74	12.4	20.5	34.4
1	E1	2.08	11.4	13.3	17.5	21.5
2	E2	17.6	20.6	21.3	22.6	23.9
3	E3	22.7	23.7	23.8	24.3	24.7
4	E4	24.3	24.6	24.7	24.8	25.0
5	E5	24.8	25.0	25.0	25.1	25.1

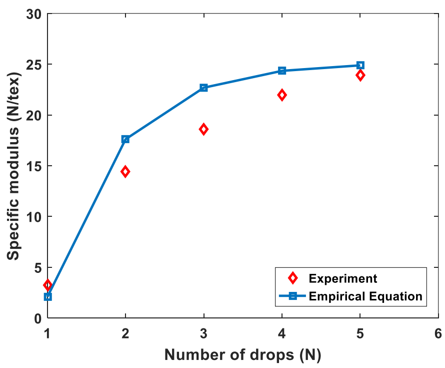

(a) Nopreload

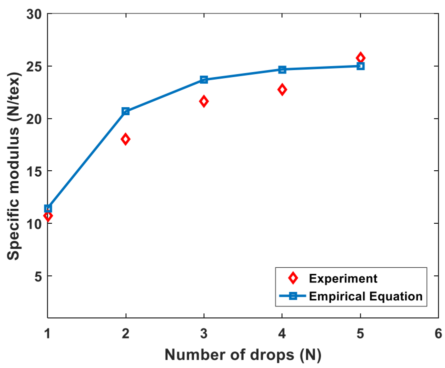

(b) Preloaded at 9.74%MBL

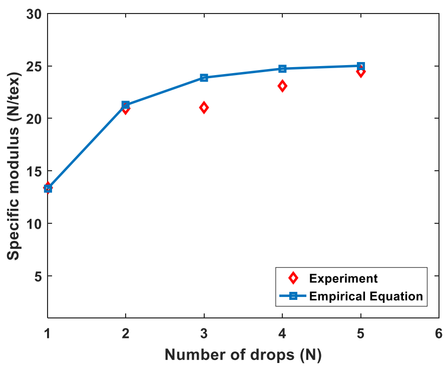

(c) Preloaded at 12.4%MBL

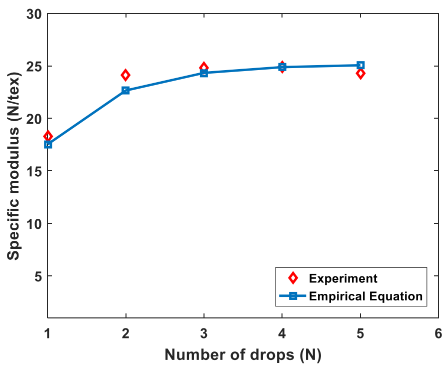

(d) Preloaded at 20.5%MBL

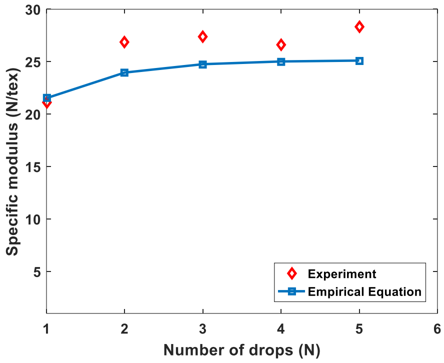

(e) Preloaded at 34.4%MBL

Figure 6 Comparison of specific modulus from experiment and empirical expression

To discuss more detail about the condition to stabilize the rope specific modulus of the HMPE, the relationship between specific modulus and number of drops with a variation in preload levels was calculated by using Equation (1) with the parameters in Table 5. The results are presented in Figure 7. The specific modulus increases as preload level and the number of drops increases. However; when the preload level is high, there is a slight change in specific modulus with respect to the number of drops. For no preload, the specific modulus depends strongly on the number of drops such that at the first drop, the specific modulus is very small and it increases substantially in the next drops. Overall, the specific modulus becomes constant from the tenth drop onward. To examine the influence of preload levels on the rope specific modulus, a plot of specific modulus vs. preload level with a variation in the number of drops (N=1 to 10) was carried out. The results are shown in Figure 8. The specific modulus increases as the preload level increases when the number of drops N equals 1 to 4. The specific modulus of the rope is slightly affected by the preload level when the number of drops increases like the cases N = 6 to 10. The rope specific modulus in all cases becomes harden and stable when the preload level and the number of drops becomes large, except at the first drop (N=1), although it shows that at the preload level of around 90%MBL, the specific modulus has almost constant value. However, in real application, preload treatment at 90%MBL is unrealistic because the rope will be damaged due to very high load in preload treatment. The unstable of the rope specific modulus occurs at the first drop because of small impact loading applied to the rope (7.7 to 9.8% MBL).

Equation (1) is the empirical expression for specific modulus in which only the preload and number of drops is considered. Based on this Equation, there is a possibility that a suitable procedure exists (level of preload and number of drops) for preload treatment to stabilize the rope specific modulus. The specific modulus of the preloaded rope at 40%MBL needs only five consecutive impact loadings in order to achieve the stabilization (Figure 7, 8) while the virgin rope requires tenth consecutive impact loading to become harden and stable.

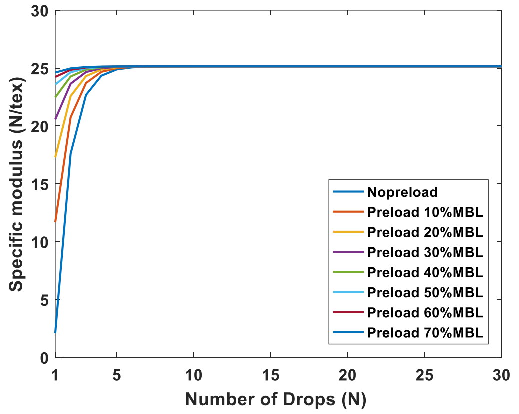

Figure 7 Specific modulus-number of drops obtained from empirical equation

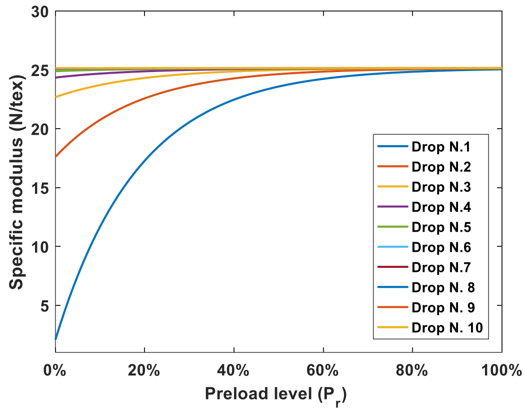

Figure 8 Specific modulus-preload level (P_r) obtained from empirical equation

4. CONCLUSIONS

The summarized of conclusions are given as follows:

- ➢ Consecutive impact loading affects the properties of virgin HMPE rope by changing the modulus from the first to the next drops because of a rearrangement of rope structure that all fibers or strands move towards to the rope axis.
- ➢ Preload treatment is an efficient way to reduce changing rope modulus which resulted from unchanged

in construction geometry of preloaded ropes.

- An empirical equation of modulus was proposed by considering number of drops and preload levels into account. Based on the equation, the stability of virgin rope could be obtained by applying tenth consecutive impact loadings while preloaded rope at level of 40%MBL needs only five consecutive drops in order to achieve stability in modulus.

ACKNOWLEDGEMENT

This paper is based on results from a project commissioned by the New Energy and Industrial Technology Development Organization (NEDO).

REFERENCES

[1] Casey, N.F. and Banfield, S.J. (2002) Full-Scale Fiber Deepwater Mooring Ropes: Advancing the Knowledge of Spliced Systems. Offshore Technology Conference, Texas, USA, 6-9 May 2002, 2189–2201.

[2] Casey, N.F., Banfield, S., (2005). Factors affecting the measurement of axial stiffness of polyester deepwater mooring rope under sinusoidal loading. (OTC 17068) Offshore Technology Conference, Houston, USA, 2-5 May, 2005.

[3] Davies, P., Reaud, Y., Dussud, L. and Woerther, P. (2011) Mechanical Behavior of HMPE and Aramid Fiber Ropes for Deep Sea Handling Operations. Journal of Ocean Engineering, 38, 2208–2214.

[4] Francois, M., Davies, P., Grosjean, F. and Legerstee, F. (2010) Modelling fiber rope load-elongation properties-polyester and other fibers. Offshore Technology Conference, Texas, USA, May, 2010.

[5] Liu, H., Huang, W., Lian, Y. and Li, L. (2014) An Experimental Investigation on Nonlinear Behaviors of Synthetic Fiber Ropes for Deepwater Moorings Under Cyclic Loading. Journal of Applied Ocean Research, 45, 22–32.

[6] Flory, J.F., Ahjem, V. and Banfield, S.J. (2007) A New Method of Testing for Change-in-Length Properties of Large Fiber Rope Deepwater Mooring Lines. Offshore Technology Conference, Texas, 30 April-3 May,2007, 1087-1096.

[7] Flory, J.F. and Ahjem, V. (2013) Testing Polyester Fiber Rope for Six Change-in-Length Properties (6CILP). IEEE Conference, Bergen, 10-14 June 2013, 1-10.

[8] Flory, J. F., Leech, C. M., Banfield, S.J. and Petruska, D. J. (2005). Computer Model to Predict Long-Term Performance of Fiber Rope Mooring Lines. (OTC 17592) Offshore Technology Conference, Texas, U.S.A, 2-5 May, 2005.

[9] Kwan, C. T., Devlin, P., Tan, P. L., and Huang, K. (2012). Stiffness Modelling, Testing, and Global Analysis for Polyester Mooring. Proceeding of the ASME 2012 31st International Conference on Ocean Offshore Arctic Engineering Rio de Janeiro, 1-6 July, 2012, 777-785.

[10] Beltran, J. F. (2006). Computational modelling of synthetic fiber ropes. PhD thesis, The Univeristy of Texas at Austin.

[11] Davies, P., Bouquet, P., Conte, M., Deuff, A., (2006). Tension/torsion behaviour of deepwater synthetic mooring lines. Offshore Technology Conference, Houston, USA. Paper OTC17872.

[12] Weller, S.D., Davies, P., Vickers, A.W., Johanning, L. Synthetic rope responses in the context of load history: operational performance. Ocean. Eng., 2014, 83, 111–124.

[13] Lian, Y., Liu, H., Li, L., Zhang, Y., (2018). An experimental investigation on the bedding-in behavior of synthetic fiber ropes. Ocean Engineering 160, 368-381.

[14] Kitano, S.; Hirose, S.; Endo, G.; Fukushima, E.F. Development of Light-Weight Sprawling-Type Quadruped Robot TITAN-XIII and Its Dynamic Walking. IEEE International Conference on Intelligent Robots Systems (IROS), Tokyo, 3-7 November 2013, pp. 6025–6030.

[15] Mazumdar, A.; Spencer, S.J.; Hobart, C.; Dabling, J.; Blada, T.; Dullea, K.; Kuehl, M.; Buerger, S.P. Synthetic Fiber Capstan Drives for Highly Efficient, Torque Controlled, Robotic Applications. IEEE Robotic and Automation Letters 2017, 2, pp. 554–561.

[16] Horigome, A.;Yamada, H.; Endo, G.; Sen, S.; Hirose, S. (2014). Fukushima, E.F. Development of a coupled tendon-driven 3D multi-joint manipulator. IEEE Inter-National Conference on Robotics & Automation, Hong Kong, May 31- June 7, 2014, pp. 5915–5920.

[17] Kirchhoff, J. and Stryk, O. V. (2017). New Insights in Synthetic Fiber Rope Elongation and its Detection for Ultra Lightweight Tendon Driven Series Elastic Robots. IEEE International Conference on Advanced Intelligent Mechatronics (AIM), Munich, Germany, July 3-7, 2017.

[18] McKenna, H.A., Hearle, J.W.S., O'Hear, N., (2004). Handbook of Fibre Rope Technology, 3ed. Woodhead Publishing Ltd and CRC Press LLC, Abington Cambridge, UK.

[19] Sry, V., Mizutani, Y., Endo, G., Suzuki, Y. and Todoroki, A. (2018). Estimation of the Longitudinal Elasticity Modulus of Braided Synthetic Fiber Rope Utilizing Classical Laminate Theory with the Unit N/tex. Applied Science, 8(7), 1096, 2018.

On-line Detection of Fretting Fatigue Crack Initiation with a Perpendicular Cylindrical Contact by Thermography

Saosometh Chhith[1,*], Wim De Waele[2], Patrick De Baets[2]

[1)] Department of Industrial and Mechanical Engineering, Institute of Technology of Cambodia, Russian Federation Blvd, P.O. Box 86, Phnom Penh, Cambodia
[2)] Department of Electrical Energy, Systems and Automation, Soete Laboratory, Ghent University Technologiepark 903, 9052 Gent, Belgium

[*]Corresponding e-mail: saosometh.chhith@itc.edu.kh

ABSTRACT – Typical fretting fatigue tests under cylindrical plane contact may not be sufficient to validate a robust analytical/numerical model for crack initiation life prediction if the model is to be used for real engineering problems of fretting fatigue. Fretting fatigue experiment of a perpendicular cylindrical contact is therefore performed and monitored on-line by an infrared camera for crack initiation detection. Thermo-elastic temperature amplitude is used as thermal indication of crack initiation. The test is stopped immediately when the thermo-elastic temperature amplitude is increased from a stabilized value, and the sample is inspected for crack depth by off-line optical microscopy. The detection threshold of the crack depth is then discussed for this contact configuration.

Keywords: fretting fatigue, perpendicular cylindrical contact, crack initiation, on-line monitoring

1. INTRODUCTION

Fretting fatigue occurs when two bodies in contact move slightly relative to each other. The amplitude of the reciprocating sliding is in an order of several micrometers. Fretting fatigue can reduce lifetime of materials or components significantly, and it is more likely to occur within mechanical clamps such as: bolt connection, riveting, dovetail connection or press-fitting [1]. To develop understanding of fretting fatigue, fretting fatigue tests with Hertzian contacts such as spherical on plane [2] or cylindrical on plane contact [3] are performed due to thorough existing analytical solutions. Among fundamental features of fretting fatigue, crack initiation remains a big challenge for researchers because fretting fatigue crack occurs in close contact and only recently that on-line detection of crack initiation is made feasible for fretting fatigue tests under cylindrical on plane contact [4], [5]. However, fretting fatigue tests with one single type of contact configuration may not be sufficient to understand crack initiation.

Results of crack initiation lifetime are to be used to validate numerical/analytical models such as multiaxial fatigue criteria, damage mechanics, crack arrest methodologies, etc [6]–[9]. Once validated, the models are expected to be able to predict crack initiation lifetime of real engineering problems like riveting lap joints [6]. even though the contact configuration between the coupon-scale tests and the riveting lap joints is different. The cylindrical on plane contact is non-conformal Hertzian contact while in the riveting lap joint, the contact type is conformal non-Hertzian cylinder-on-cylinder contact (contact area between the holes of the plates and the rivets).

Since it is not clear yet that the mechanism of the crack initiation is solely controlled by the stress/stain states or just the micro-slip amplitude, or their combination as stated in [10], validation of the model with just the coupon scale may not guarantee its accuracy for the real engineering application due to different contact types. In this study, fretting fatigue test under perpendicular cylindrical contact is performed and crack initiation lifetime is determined by the developed thermography methodology [5]. This new contact type offers another validation exam for the models before extending them to the real engineering problems. On the other hand, perpendicular cylindrical contact is a bit more open than the cylindrical on plane contact for the infrared camera to focus on the damage zone. The detection threshold of the crack depth is then expected to be improved.

2. METHODOLOGY

2.1 Experimental set-up and tested specimen

A fretting fixture has been designed and manufactured to equip with the ESH 100 kN servo hydraulic load frame so that fretting fatigue tests could be performed [11]. Its schematic drawing is shown in Figure 1.

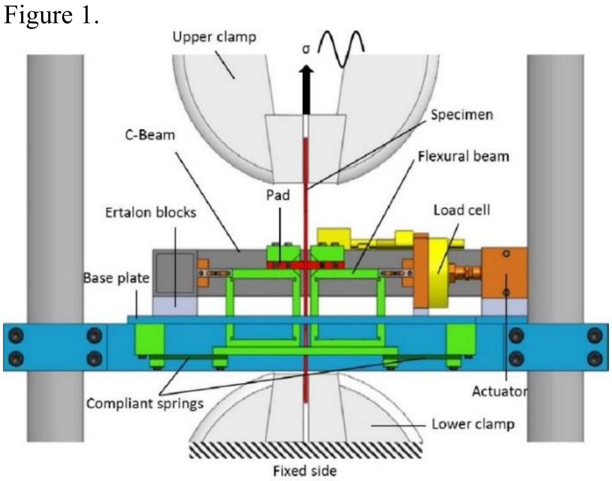

Figure 1 Schematic drawing of the fretting fatigue test rig [12]

The 100 kN hydraulic cylinder of the load frame is used to apply axial dynamic loads on a modified dog-bone specimen. The normal load, P, is applied to the specimen by a separate horizontal hydraulic cylinder via the fretting pads mounted on the flexural beam. The C-beam mounted on the ertalon blocks could float freely on the base plate to ensure that the normal load is applied equally in the opposite direction. The tangential force, Q, between the dog-bone specimen and the pads is generated by the leaf springs due to the elastic deformation of the specimen. The load cell mounted on the C-beam is used to measure directly the contact normal load whereas the tangential force is measured by a calibrated strain gauge attached to the leaf spring.

The specimen and the pad are made of similar materials. The specimen is AL2024-T33511 while the pad is AL2024-T3. Their mechanical properties are shown in Table 1. The specimen is turned from an aluminum rod of 28 mm radius and 340 mm length to a desired radius of 27.5 mm. Then, it is milled to have a cruciform shape with four flanges. Finally, each flange is sawed to get four specimen with one side as planar surface while the other side as cylindrical surface (see Figure 2). Due to the geometry of the specimen, it is more likely that failures occur at the clamping areas outside the fretting location. To avoid these failures, two aluminum sheets are pasted over both end of the specimen before mounting it on the ESH machine. The pad is cut from an aluminum sheet of 5 mm thickness along the rolling direction and milled to have a radius of 10 mm at one side and 200 mm at the other side (see Figure 2). The smaller radius of the pad is selected to have a contact with the planar specimen surface while the larger radius is in contact with the cylindrical surface of the specimen. All the pads consist of a groove (see Figure 2) so that the alignment between the specimen and the pad is easier. With these geometries of the specimen and the pad, contact types of fretting fatigue tests, in this study, are cylindrical plane and perpendicular cylindrical contact at the left and right contacts, respectively. The interest contact type is at the right-hand side so that experimental loading conditions must be selected to simulate fretting fatigue failures from this side.

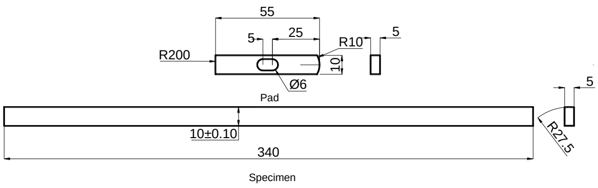

Figure 2 Dimensions of the specimen and the pad

Table 1: Materials properties of the specimen and the pad

Materials	Young's Modulus [GPa]	Yield Strength [MPa]	Ultimate Strength [MPa]
Specimen (AL2024-T3511)	73	450	570
Pad (AL2024-T3)	73	383	506

2.2 Sliding regime

Under fretting, two sliding regimes can occur: partial slip and gross slip, depending on the sliding amplitude or the magnitude of the tangential force. Normally, crack is more dominant as fretting damage for partial slip while fretting wear dominates under gross slip [13]. To determine these sliding regimes, an experimental methodology is adopted from a previous study [13]. A normal load is fixed to a constant value (P = 1 kN), while the amplitude of the cyclic fatigue load is sequentially increased. The duration of each fatigue load level is run for 10^3 cycles since it was mentioned that after this period a partial slip regime is stabilized [1]. The border between the two sliding regime is defined when the tangential force drops while the fatigue amplitude remains increased. Figure 3 illustrates corresponding loading conditions as a function of their sliding regime. One test of fretting fatigue under partial slip regime is tried until final fracture of the specimen and the specimen fracture surface is shown in Figure 4. Crack is initiated from the trailing edge within the contact area and grow further along the width and thickness until the final brittle fracture of the specimen.

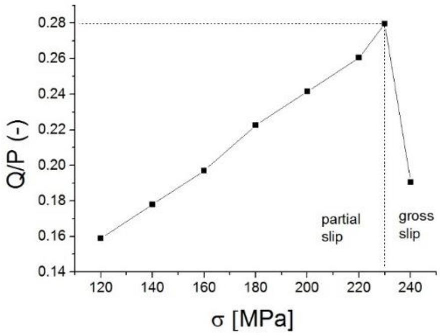

Figure 3 Sliding regime under fretting for the perpendicular cylindrical contact

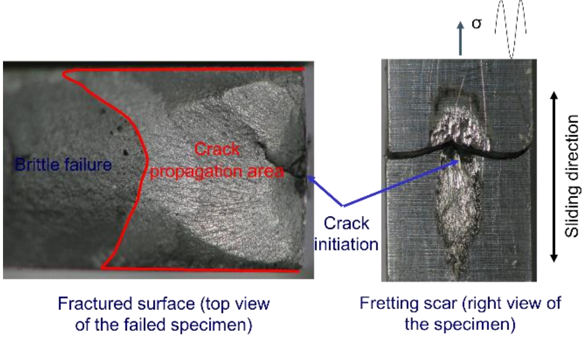

Figure 4 Fretting fatigue failure

2.3 Temperature modulation during fretting fatigue tests

Heat sources in fretting fatigue experiments are fretting friction, plastic dissipation, thermo-elasticity and other noise sources such as environmental temperature variations and heat conduction originating from the testing machine. The temperature variation at the specimen surface can be expressed by Equation (1) [14], [15].

$$T_{exp}(t) = LD(t) + T_1 \sin(\omega t + \varphi_1) + T_2 \sin(2\omega t + \varphi_2) \quad (1)$$

Here T_{exp} is the overall experimental temperature, $T_1 sin(\omega t+\varphi_1)$ is the first harmonic effect (pure thermo-elastic effect), $LD(t)$ and $T_2 sin(2\omega t+\varphi_2)$ are linear drift and second harmonic effect respectively, which account for friction, plasticity and other noise factors [14], [15]. Higher harmonic effects can be neglected. Parameter ω is the angular frequency of the fatigue loading, φ_1 and φ_2 are phase shifts to the controlled sinusoidal force, and t is time.

2.4 Experimental procedures

Fretting fatigue test with the mentioned contact configuration is performed and monitored by an infrared camera. Test conditions are σ_{max}= 220 MPa, f = 5 Hz, R ($\sigma_{min}/\sigma_{max}$) = 0.001, P = 1 kN, Q_{max}/P = 0.26. The camera model is infratec 8300 series with a telephotolens of 50 mm focal length. Example of regions of interest are illustrated in Figure 5 with four regions of interests. Dimensions of each region of interest are 10 by 20 pixels and one pixel corresponds to 65 μm, the minimum size achievable [5]. R_1 and R_2 are at the left and right contact, respectively. Cracks are expected to occur at the perpendicular cylindrical contact at the right side (R_2). R_3 and R_4 are above and below the contact regions, respectivley. They are for references purposes and their temperature difference allows to monitor the tangential force based on a basic thermo-elastic calibration. Average temperature data of all the regions of interest are grabbed and processed on-line with a Matlab script. The on-line processing based on Fast Fourier Tranform is to extract the maximum temperature amplitude which corresponds to the first harmonic frequency or the thermo-elastic frequency or the fatigue loading frequency so that an on-line crack initiation could be detected [5]. No capturing of the thermal image is required which avoids the storage issue of thermography technique. When there is a thermal indication for crack initiaiton, the fretting fatigue test is stopped immediately and the specimen is inspected for crack depth by off-line microscopy.

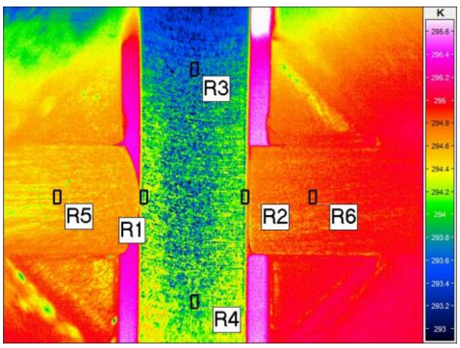

Figure 5 Thermal images with four regions of interest

3 RESULTS

The evolution of the thermo-elastic temperature amplitude is plotted on-line during the fretting fatigue test. The on-line processing is performed every 1024 (2^{10}) data points so that the signal-to-noise ratio is reduced to approximately 2 mK. Figure 6 illustrates the temperature evolution of the test. It begins with a running-in period and reaches a stabilized regime around 25 000 cycles. The stabilized regime continues until 46 586 cycles that the thermo-elastic temperature at R_2 is increased. It is hypothesized that this increase of the thermo-elastic temperature amplitude is due to occurrence of a crack. The test is stopped immediately and the specimen is inspected for a crack depth by an optical microscopy.

The sample is embedded into an acrylic. Then it is ground every 500 μm with a sand paper from the sample surface towards the center of the specimen. At each step, the sample is polished and inspected by an optical microscope. The maximum crack depth along this grinding direction is considered to be the detection threshold. For this test, a maximum crack depth of 221 μm is found at the right side of the contact while zero crack can be found at the left side of the contact (see Figure 7).

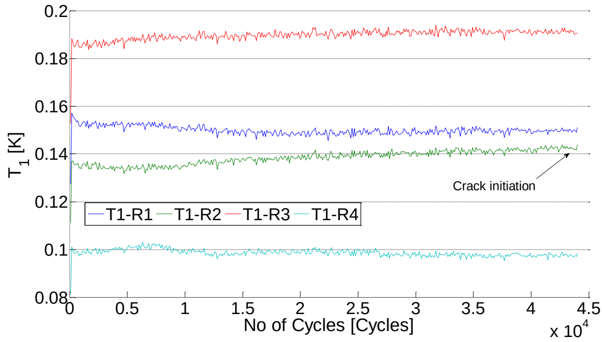

Figure 6 Evolution of thermos-elastic temperature amplitude of the four regions of interest

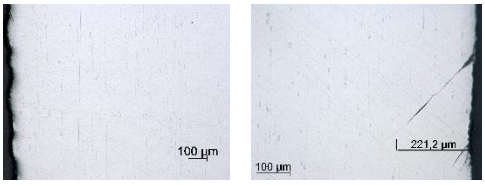

Figure 7 Off-line optical microscopy at left and right contacts.

4 CONCLUSIONS

Fretting fatigue test with a perpendicular cylindrical contact is feasible and monitored by an infrared camera. On-line data acquisition and processing from the infrared camera allows to extract the thermo-elastic temperature amplitude so that an on-line crack detection could be achieved. The detectable crack depth is around 200 μm. This threshold does not improve the detection sensitivity compared to the cylindrical plane contact even though the damage area is open more to infrared camera. The reason can be due to the fact that the crack tends to grow faster along the width than along the thickness as the plane strain location situates along the width more than along the thickness. Anyhow, more data of this perpendicular cylindrical contact will be critical to validate any numerical or analytical model for the prediction of crack initiation time under fretting fatigue.

ACKNOWLEDGEMENT

This project has been funded with support from the European Commission, Erasmus Mundus Action 2 EACEA 2012-2635. This publication reflects the views only of the authors, and the Commission cannot be held responsible for any use which may be made of the information contained therein.

REFERENCES

[1] D. A. Hills and D. Nowell, *Mechanics of fretting fatigue*. Dordrecht: Kluiwer Academic Publishers, 1994.

[2] D. A. Kuno, M., Waterhouse, R. B., Nowell, D., and Hills, "Initiation and growth of fretting fatigue cracks in the partial slip regime," *Fatigue Fract. Eng. Mater. Struct.*, vol. 12, no. 5, pp. 387–398, 1989.

[3] D. Nowell and D. a. Hills, "Crack initiation criteria in fretting fatigue," *Wear*, vol. 136, no. 2, pp. 329–343, Mar. 1990.

[4] J. Meriaux, S. Fouvry, K. J. Kubiak, and S. Deyber, "Characterization of crack nucleation in TA6V under fretting–fatigue loading using the potential drop technique," *Int. J. Fatigue*, vol. 32, no. 10, pp. 1658–1668, Oct. 2010.

[5] S. Chhith, W. De Waele, P. De Baets, and T. Van Hecke, "On-line detection of fretting fatigue crack initiation by lock-in thermography," *Tribol. Int.*, vol. 108, no. October 2016, pp. 150–155, 2017.

[6] M. P. Szolwinski, G. Harish, P. A. McVeigh, and T. N. Farris, "Experimental study of fretting crack nucleation in aerospace alloys with emphasis on life prediction," in *Fretting Fatigue: Current Technology and Practices, ASTM STP 1367*, 2000, pp. 267–281.

[7] M. P. Szolwinski and T. N. Farris, "Mechanics of fretting fatigue crack formation," *Wear*, vol. 98, pp. 93–107, 1996.

[8] J. A. Araújo and D. Nowell, "The effect of rapidly varying contact stress fields on fretting fatigue," *Int. J. Fatigue*, vol. 24, pp. 763–775, 2002.

[9] A. Belloula, A. Amrouche, and N. Benseddiq, "Comparison of the cracking energy density and the Smith – Watson – Topper parameters in predicting fretting fatigue lifetime of a steel / aluminum alloy contact," pp. 1355–1366, 2014.

[10] D. A. Hills and D. Nowell, "Mechanics of fretting fatigue—Oxford's contribution," *Tribol. Int.*, vol. 76, pp. 1–5, Aug. 2014.

[11] J. De Pauw, P. De Baets, and W. De Waele, "Design of a fretting fatigue test rig," *J. Sustain. Constr. Des.*, vol. 4, p. 6 Pages, 2013.

[12] R. Hojjati-talemi, M. A. Wahab, J. De Pauw, and P. De Baets, "Prediction of fretting fatigue crack initiation and propagation lifetime for cylindrical contact configuration," *Tribol. Int.*, vol. 76, pp. 73–91, 2014.

[13] S. Fouvry, P. Kapsa, and L. Vincent, "Quantification of fretting damage," *Wear*, vol. 200, no. 1–2, pp. 186–205, Dec. 1996.

[14] B. Berthel, A.-R. Moustafa, E. Charkaluk, and S. Fouvry, "Crack nucleation threshold under fretting loading by a thermal method," *Tribol. Int.*, vol. 76, pp. 35–44, Aug. 2014.

[15] J. C. Krapez, D. Pacou, and G. Gardette, "Lock-in thermography and fatigue limit of metals," in *Quantitative Infrared Thermography 5*, 2000, no. JANUARY, pp. 277–282.

Investigation on Application of Fish Oil as Binding Material in Biomass Briquetting Process

Porchaing CHOENG[1*], Latin HEANG[2], Kinnaleth VONGCHANH[3], Sarin CHAN[4]

[1*,2,3,4] Department of Industrial and Mechanical Engineering, Institute of Technology of Cambodia,
Russian Federation Blvd, P.O. BOX 86, Phnom Penh, Cambodia
*Corresponding e-mail: choengchaing@gamil.com

ABSTRACT – Binding material is one of important part in briquetting process; fish oil (FO) is new binding material which is focused in this study. In order to clarify that FO can be used as a binder, 5 samples of FO, 100g, 200g, 300g, 400g, and 500g were selected to mix with rice husk (RH), and sawdust (SD) for producing briquette using screw press machine. The experimental work was conducted by mixing FO with SD:RH (1kg:1kg). The results showed that the heating values were not much different within the 5 samples. Energy density and density were experimentally obtained 22.05 - 22.9 GJ/m^3, 1161.89-1197.42 kg/m^3, respectively. Water and impact resistance tests and ash content were also discussed in this paper. However, the less amount of fish oil caused briquette failed in the water resistance test.

Keywords: Briquette, fish oil, binding material, rice husk, sawdust, Biomass properties.

1. INTRODUCTION

Every year, millions tons of waste are burnt or destroyed in many ways without usefulness of the materials while it can be recycled and used as renewable source of energy [1]. Waste to energy and renewable energy are encouraged by many stakeholders; biomass briquette from rice husk, sawdust, baggass, etc. are included in renewable energy sources. Total rice production quantity in Cambodia, especially paddy, was approximately 10.35 million ton [2] and 22% of rice husk was obtained [3]. Besides the available of the saw dust is found as one of waste in Phnom Penh. It was not always reused according to the actual observation. The RH and SD are good energy sources if it is changed form into high energy density such as biomass briquette; thus, binder is required during briquetting process. Thus, fish residue was considered to be a binding material. After many experimental works, to reused of fished residue, fish fat, which was extracted for fish oil, was selected.

Therefore, this paper aimed to investigate possibility on applying fish oil in different ratio from 100 to 500 g to be binder in biomass briquette using screw press by referring to values of the moisture content, density, impact resistance, water resistance, ash content, fixed carbon.

2. METHODOLOGY

2.1 Material

Rice husk (dimension 3mm-6mm) and sawdust (size ≤ 8mm) was obtained from Kampong Cham province and waste from furniture shop in Phnom Penh, respectively. The freshwater fish residue (the fat and intestine parts) was obtained from the local market in Phnom Penh.

2.2 Material Preparation

Fish oil (FO) was extracted from fish fat (FF) of 4 kg was added in the pressurized port and placed on electric stove at 2000 W, for 60 mins. Finally, the fish oil was obtained for 3 kg. Five samples, with fish oil of 100g, 200g, 300g, 400g, and 500g, were prepared for mixing with raw materials, RH and SD.

First, RH and SD with ratio 1:1 were mixed using motor (Multifunction electrical drill) then added fish oil per each sample. After that, the mixed/composited material material was placed at the hopper of the screw press machine (gear motor: 3 phases, gearbox: 100:1). The briquette mole was wraped with heater at the outer surface with temperature controller with 300°C depicted in Figure **1**.

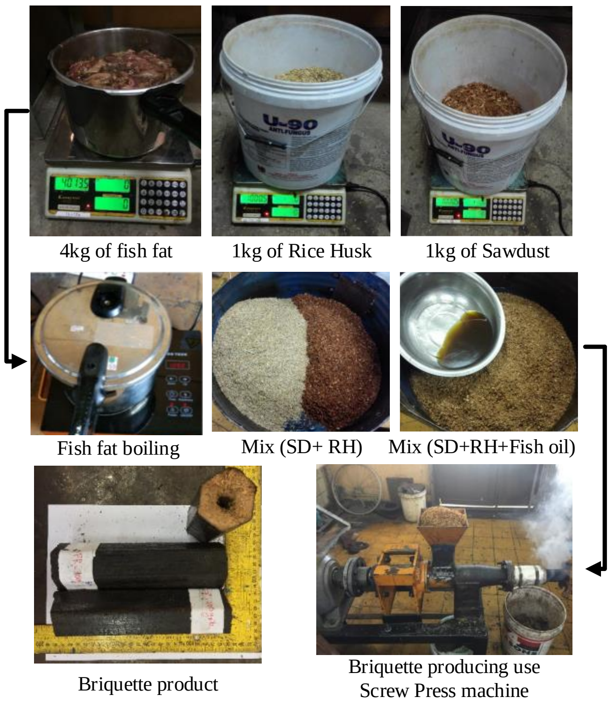

Figure 1 Process of producing briquette

2.3 Biomass briquette properties' investigation

a. Density

The standard DIN 52182 (additional standard DIN 51731) also defines the testing method for briquette density. [4]

$$\rho = \frac{m}{V} \quad (1)$$

m: mass of briquette [kg]
V: volume of briquette [m^3]
ρ: density of briquette [kg/m^3]

b. Impact Resistance

Impact resistance test is considered to be the best general diagnostic of briquette strength [5].

$$IRI = \frac{100 \times Average\ number\ of\ drops}{The\ average\ number\ of\ pieces} \quad (2)$$

c. Water Resistance

Sample immersion-in-water test on a single briquette was adopted to evaluate the resistance of briquette against the water absorption and disintegration in 30 mins [5].

$$WRI = 100 - \%\text{water absorbtion} \quad (3)$$

d. Moisture Content (MC)

Moisture content tests were performed on the as-received sample by the oven-drying method, ASTM-D 3173-73 (American Society for Testing and Materials) [6] [7]. Moisture content has an important role to play as it facilitates heat transfer [1].

Moisture content measurement can be estimated according to Ref. TP7/1, Eq.4, [8].

$$\%MC = \frac{m_0 - m_{n+1}}{m_0} \times 100 \quad (4)$$

m_0: mass of initial sample, [g]
m_1: mass of sample after first drying, [g]
m_n: mass of sample after n^{th} drying, [g]
m_{n+1}: mass of sample after $(n+1)^{th}$ drying, [g]

e. Heating Value (HV)

The heating value is understood to be the amount of heat released with the complete oxidation of fuel without taking into consideration the condensation heat of the water vapor present in the smoke (i.e. the gaseous water formed during the combustion is not accounted for), [9].

f. Proximately Analysis

Proximately analysis was calculated following to Ref. TP6/1, [8],

- *Ash Content (AC)*

Ash content of briquette is the non-combustible residue, the soft grey or black powder, left after the briquette is burnt. The ash content of solid fuels affects both the emission of pollutants and the technical design and construction of the combustion plant.

$$\%\text{Ash content} = \frac{(M_{Ash} - M_{crucible})}{(M_{fuel\ after\ dry} - M_{crucible})} \times 100 \quad (5)$$

M_{Ash} : mass ash after burning at temperature 710°C
$M_{crucible}$: mass crucible after dry at temperature 105°C

- *Volatile Matter (VM)*

Volatile components are gaseous compounds which escape under specified conditions when fuel is heated [9].

$$\%\text{Volatile matter} = \frac{(M_{fuel\ after\ dry} - M_{volatile})}{(M_{fuel\ after\ dry} - M_{crucible\ with\ lids})} \times 100 \quad (6)$$

$M_{volatile}$: mass volatile after burning at temperature 900°C

- *Fixed Carbon (FC)*

The fixed carbon found in the material which is left after volatile materials is driven off.

$$\%\text{Fix carbon} = 100 - (\%\text{Ash} + \%\text{Volatile}) \quad (7)$$

3. RESULTS AND DISCUSSION

Five samples of the composite biomass materials (1kg:1kg:0.1,0.2,0.3,0.4,0.5 kg) were carried out twice. The experimental results described in Table 1, average MC, HV and density were 5.19%, 19.04MJ/kg, 1178.8 kg/m^3, respectively. The calorific value was highly dependent on moisture content.

Due to the results of volatile matter and ash content were quite consistent; the results of fixed carbon content were the same, ranged from 17 – 19%. The results of proximate analysis show that the value of volatile matter, ash content, and fixed carbon were quite consistent because the ratio of rice husk and sawdust were the same. Due to the ratio of composition input, except fish oil, does not be changed, then the value of proximate analysis varies within few percent only.

The maximum heating value was about 19.28 MJ/kg at MC of 3.7% belonging to FR300. The minimum heating value of F500 was 18.89MJ/kg at MC of 5.93%. The average heating value, 19.05 MJ/kg, was higher than the average raw material (15.45 MJ/kg). Furthermore, these briquettes were found that they were passed for WRI and the maximum was found at FR400 while lower and higher FR level were slightly decrease. However, one of five samples at FR100 failed in WRI. Regarding the observation of the sample, the surface of briquettes was not densified even the density was increasing almost 10 times. That might cause by too less binder and a cracked section on the outer surface of the briquette. From the obtained density of the briquettes, they were mostly successful for the impact resistance test. The WRI test and density had the same tendency of different FO ratio; F100 and F500 have lower density than F200-400.

Table 1 Result of experiment

No.	Sample	ρ	IRI	WRI	MC	HV	AC	VM	FC
Unit	**Name**	**kg/m^3**	**> 50%**	**>93%**	**%**	**MJ/kg**	**%**	**%**	**%**
1	FR100	1161.89	381%	86%	4.80	19.05	9.76	71.68	18.56
2	FR200	1181.26	615%	97%	5.82	19.09	9.86	70.77	19.37
3	FR300	1187.94	680%	98%	3.72	19.28	10.55	71.30	18.15
4	FR400	1197.42	617%	100%	5.93	18.89	9.35	71.13	19.72
5	FR500	1165.56	523%	97%	5.69	18.92	9.91	72.28	17.81
Average		**1178.814**	**563.2%**	**95.6%**	**5.192**	**19.046**	**9.886**	**71.432**	**18.722**

4. CONCLUSIONS

The experimentally obtained results on investigation of application of fish oil as a binder based on the property values of the briquette, it clearly showed that the fish oil can be a binding material because heating value, WRI and IRI test are qualified and the MC of the briquettes is in good range. According the 5 levels of FO, increasing the percent of FO does not affect on the components (volatile matter, ash content, and fixed carbon) of proximate analysis. Due to this reason, the heating value of all those samples are similar. The advantage is energy density of the biomass briquette is higher than the biomass raw material.

Fish oil mixing ratio of 100g, 200g, 300g, 400g, and 500g were qualified the impact resistant test and water resistant test, however, 100g of FO failed the water resistant test. According to current results, 200g of FO is the most preferable of binder mixing ratio for RH 1kg and SD 1kg. While 100g of FO is not suitable for long term storage either it is not ensure the transporation.

ACKNOWLEDGMENT

We would like acknowledge ARES CUD Project for financial support, Mr. Bun Y for his first idea on applying FR as a binder, Mr. Keo Sokhim and Ms. Pheng Chanlin for their first study, information and screw press machine and Dr. Moly and his assistance for supporting on measurement devices.

REFERENCES

[1] Maninder, R. S. Kathuria and S. Grover, "Using Agricultural Residues as a Biomass Briquetting: An Alternative Source of Energy," *Journal of Electrical and Electronics Engineering,* vol. 1, no. 5, pp. 11-15, 2012.

[2] FAOSTAT, "Cambodia: Rice, paddy, production quantity (tons)," 2017. [Online]. Available: www.factfish.com/statistic/rice, paddy, production quantity. [Accessed 2019].

[3] "Energy Potential of Rice Husk," 14 September 2019. [Online]. Available: https://www.bioenergyconsult.com/tag/rice-husk.

[4] P. Lehtikangas, "Quality properties of pelletised sawdust, logging residues and bark," *Biomass and Bioenergy,* vol. 5, no. 20, pp. 351-360, 2001.

[5] S. Richards, "Physical Testing of Fuel Briquettes," *Fuel processing technology,* no. 25, pp. 89-100, 1990.

[6] K. G. Mansaray and A. E. Ghalay, "Physical and Thermochemical Properties of Rice Husk," *Energy Sources,* vol. 19, no. 9, pp. 989-1004, 1997.

[7] P. Jittabut, "Physical and Thermal Properties of Briquette Fuels from Rice Straw and Sugarcane Leaves by Mixing Molasses," *Energy Procedia,* no. 79, pp. 2-9, 2015.

[8] Geres Cambodia, "Development of a sustainable bamboo production center".

[9] S. Döring, Power from pellets, New York: Technology and Applications, 2013, pp. 31-50.

Investigation on Physical Properties and Measurement of Bulk Modulus of Waste Plastic Diesel

Zin Thu Aung[1] ,Chinda Charoenphonphanich [1*], Hidenori Kosaka[2], Pop-Paul Ewphun[2], Prathan Srichai[3]

[1)] Department of Mechanical Engineering, King Mongkut's Institute of Technology Ladkrabang, 1Soi Chalongkrung 1, Ladkrabang, Bangkok 10520 Thailand
[2)] Department of System and Control Engineering, Tokyo Institute of Technology, Ishikawadai 6th building, Room 323,2-12-1 Ookayama,Meguro-ku,Tokyo,152-8552, Japan
[3)] Department of Mechanical Engineering, Princess of Naradhiwas University, Naradhiwas 96000 Thailand

*Corresponding e-mail: kmitl.chinda@gmail.com

ABSTRACT – Plastics have become an indispensable part in today's world. However, wastes of plastics materials are accumulated without effective decomposition and recycling routes in the landfills. Therefore, conversion of waste to energy is one of the recent trends in minimizing not only the waste disposal but also could be used as an alternate fuel for internal combustion engines The primary focus of this research is measurement of bulk modulus of waste plastic diesel (WPD) that carried out at 4.5 to 10.5 MPa back pressure with increment 2 MPa under Zuech's method and compare with commercial diesel (CD) as well as physical fuel properties. The bulk modulus of commercial diesel is 3.5and 4% higher than that of waste plastic diesel at 6.5 and 10.5 MPa. The measurement results are useful that can determine the proper behaviors of injection characteristics, to provide the best balance of performance, emissions and fuel economy.

Keywords: Bulk modulus of elasticity; Zuech's method; Waste plastic diesel, Commercial diesel

1. INTRODUCTION

Plastics have become an indispensable part in today's world, due to their lightweight, durability, energy efficiency, and design flexibility [1]. At the same time, waste plastics have created a very serious environmental challenge because of their huge quantities and their disposal problems. As the disposal of plastic will take more than 500 years in natural way [2]. Therefore, conversion of waste to energy is one of the recent trends in minimizing not only the waste disposal but also could be used as an alternate fuel for internal combustion engines.

By using fast pyrolysis, the waste plastic diesel (WPD) can be produced. Fast pyrolysis is the most popular process for converting cellulose to high yield of bio oil with relatively low cost [3]. There are several researches about WPD on internal combustion engine, Rajan Kumar et al [4] reported that the engine can operate with neat waste plastic fuel (WPF) and their blends can be used as an alternative fuel for diesel engine without modification and the performance of WPF10D90 is almost similar as that of diesel. Sai Gu et al [5] investigated that the engine failed after 36 hours because a blend of 75% plastic pyrolysis oil and 25% diesel was utilized in the engine for longevity test. Verma et al [6] showed that yield of waste plastic oil was approximately 70% and waste plastic oil can be used to save the 40% diesel without loss of power at constant engine speed.

Although there were many researches about waste plastic oil production and properties of alternative fuels on engine performance, there are no studies available about the bulk modulus measurement of waste plastic diesel and its effect on fuel injection system.

Therefore, the purpose of this research is measurement of bulk modulus and to analyze the effect of bulk modulus and sound velocity of waste plastic diesel on injection system and compare with commercial diesel as well as other physical properties that can determine the proper behaviors of injection characteristics, to provide the best balance of performance, emissions and fuel economy without or minor modification [7].

2. MATERIALS AND METHODS

2.1 Test fuel properties

In this paper CD and WPD were used as test fuel. In Thailand, B7 (Conventional diesel + 7% Palm bio diesel) was used as commercial diesel. As visual inspection, the color of WPD is yellow and clear as shown in figure 1 and it was produced by catalytic fast pyrolysis. The WPD has properties similar to diesel fuel as shown in. Table 1. The fuel properties were tested by using the ASTM standard.

Figure 1 Comparison of CD (left) and WPD (right)

It can be seen that density, viscosity, flash point, and sulfur content of WPD are less than 2.31, 10.49, 34.75 and 16.67% that of commercial diesel. But cetane index and lower heating value are greater than 12.41 and 0.94% that of CD. And the distillation temperature T10 has less than 12.18% that of CD, but T50 and T90 have 0.97% and 9.4%. These differences will take effect significantly on engine performance.

Table 1 Physical properties of CD and WPD

Parameters	**Test Methods**	**CD**	**WPD**
Kinematic viscosity @40·C (cSt)	ASTM D445	3.24	2.9
Density@15·C (kg/m3)	ASTM D4052	824	805
Total Acid Number (mgKOH/g)	ASTM D974	-	0.06
Heating value (MJ/kg)	ASTM D240	45.86	46.29
Initial Boiling Point	ASTM D86	-	127.4
Distillation @ T5 (·C)			162.9
Distillation @ T10 (·C)		207.7	182.4
Distillation @ T50 (·C)		287.9	290.7
Distillation @ T90 (·C)		352.3	385.4
Cetane index	ASTM D976	60.43	67.93
Flash point (·C)	ASTM D93	61.3	40
Copper strip corrosion	ASTM D130	-	1a
Sulfur content (%wt)	ASTM D5453	0.018	0.015

2.2 Experimental set up

Bulk modulus of elasticity is a measure of the compressibility of a fluid. The bulk modulus of CD and WPD were measured by using Zuech method at 6.5 to 10.5 MPa back pressure with increment 2 MPa. All experiments were conducted at ambient temperature 300K±1K. Table 2 displayed the experimental testing conditions.

In Zuech's method, a 4 cm3 chamber was used. A hydraulic hand pump was used to generate pressure inside the chamber (back pressure) which indicated by a static pressure sensor (MURPHY Model PXT 2000). The fast response dynamic piezoelectric sensor (Kistler 6032C2) was installed in the chamber and measured the pressure rise during compression[8].Signals from dynamic pressure sensor were recorded and then transferred to oscilloscope as data acquisition with sampling rate 25000 samples/sec.

Table 2 Experimental testing conditions

Parameters	Conditions
Test fuels	CD,WPD
Back pressure	6.5,8.5,10.5 MPa
Plunger diameter	7.0 mm
Plunger displacement	2.5 mm
Repeat	10 Times / Condition

Fuel bulk modulus was measured by filling the chamber with test fuel using a hand pump until reaching the back pressure setting, and then supplying air to the pneumatic cylinder to push the plunger as shown in figure 1. The movement of the plunger caused chamber volume reduction (ΔV) which led to a pressure rise (Δp) [9]. After that, the bulk modulus can be calculated by equation (1). Each experiment was repeated 10 times with 95 % confidence level.

$$K = V\Delta P / \Delta V \quad (1)$$

$$K = C^2 \times \rho \quad (2)$$

Where,

K = Bulk Modulus of Elasticity (MPa)

ΔP = Pressure Rise (MPa)

ΔV/V = Change of Volume (no unit)

C = Speed of Sound (m/s)

ρ = Density of fuel (kg/m^3)

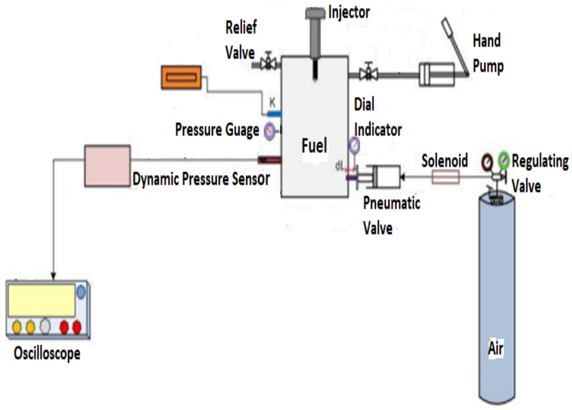

Figure 1 Schematic diagram of Zuech's method

3. RESULTS AND DISCUSSION

3.1 Investigation of WPD Fuel Properties

Density is an important fuel properties. Lower density will impact the mass of fuel injected from injection system and power output.

Viscosity is internal resistance of fuel to flow. A shorter injection delay and faster injection rate may be occurred with less viscous fuel. It will be required less energy to pump the fuel at injection pump. And a lower viscosity fuel causes promote atomization due to increasing turbulence energy at nozzle orifice. This will be influenced combustion characteristics. Both density and viscosity will effect on injection characteristic.

Low flash point, low distillation temperature (T10) and high cetane number of WPD indicate the presence of highly volatile materials in the fuel. These properties will not be affected on fuel injection process. However, it will be strongly effect on spray and combustion.

Flash point is a temperature which the fuel can vaporize to ignite. According to WHMIS, flammable liquids have a flash point below 37.8 ·C (100 ·F) and combustible at or above 37.8·C (100 ·F) and below 93.3·C (200·F) [10]. WPD is a combustible liquid but it is too close to margin. By removing lighter components (such as naphtha/gasoline) the flash point of WPD will be increased.

Distillation temperature is an evaporating ability of fuel. T10, T50 and T90 are temperature of 10%, 50% and 90% distilled volume. The distillation temperature, T10 of WPD has less than 12.18% that of CD, but T50 and T90 have 0.97% and 9.4% as shown in figure 2. Lower T10 will be better to start the engine.

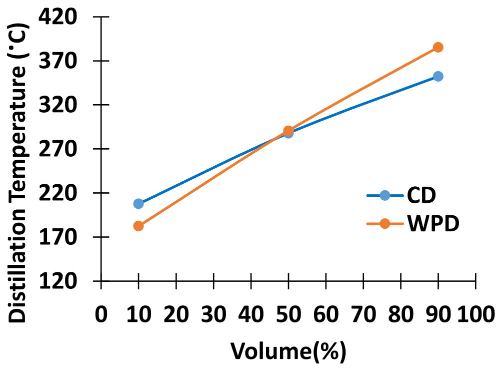

Figure 2 Distillation temperature of CD and WPD

Cetane index was calculated from fuel's density and distillation temperatures. Higher cetane index of WPD is due to lower density and higher T50. It will be affected on combustion, ignition delay, engine performance, exhaust emissions and specific fuel consumption.

Total sulfur content of WPD is lower than CD. It can be called as low sulfur fuel and will be passed Euro III standard. Total acid number also lower than that of CD limits. These two fuel properties must be related with lubricity. This is very important property of fuel injection system. Sulfur is not lubricant but it can combine with the nickel from metal alloys to form eutectic that can increase lubricity. Carboxyl acids content of fuel determines its lubricity, which easy undergoes chemisorption on the clean metal surface [11]. Copper strip corrosion of WPD is 1a. It is best result.

3.2 Measurement of Bulk Modulus and Its Effect

In this study buck modulus was investigated by Zuech's method. The bulk modus was calculated from pressure rise after compression by using equation (1).

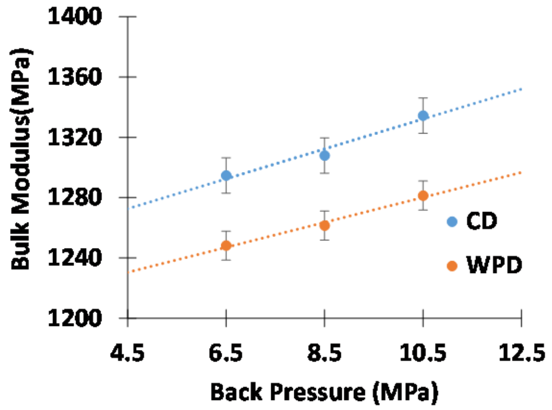

Figure 3 Bulk modulus of CD and WP

Figure 3 shows the results of bulk modulus measurement for CD and WPD. It can be seen that the bulk modulus of WPD is lower than 3.6% and 4% that of CD at low back pressure (6.5 MPa) and high back pressure (10.5 MPa) due to low density of WPD. According to equation (2), bulk modulus is directly proportional to density and sound speed square of fuel and the compressibility of the fuel is the reciprocal of modulus of elasticity or bulk modulus. Therefore, the fuel is compressible there is a time lag between the beginning of delivery by the pump and the beginning of discharge from the nozzle. When lower bulk modulus fuel (WPD) is compressed, the pump produces a slower and lower pressure rise.

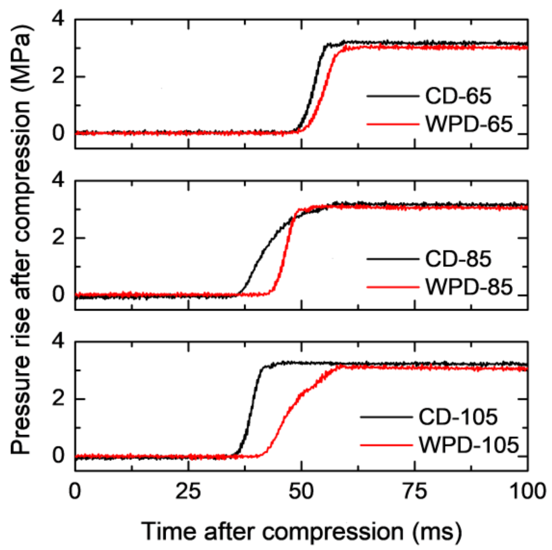

Figure 4 Pressure rise and time at various back pressure

Figure 4 shows the comparison of CD and WPD under difference back pressure on real time pressure rise. In fact that pressure wave initiated by plunger movement is propagated through the discharge tubing at the speed of sound in the fuel. The velocity and amplitude of pressure wave are the sound velocity and pressure rise. The pressure rise is directly proportional to sound velocity.

Because of a lower sound speed, this pressure rise propagates slower and lower from the pump to the injectors.

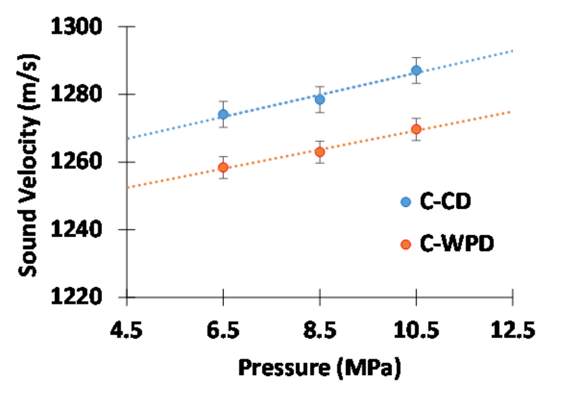

Figure 5 Variation of sound velocity with pressure

Figure 5 displays the relationship of sound speed and back pressure. Sound speed was calculated from equation (2).And a specific gravity and bulk modulus correlation was used for density estimation [12].The sound velocity of WPD 1.23 and 1.35% less than that of CD at 6.5 and 10.5 MPa. The bulk modulus will significantly affect the injection system, injection timing and NOx emission. The higher bulk modulus fuel leads to advanced injection timing and vice versa. Therefore, retarding injection timing and decrease in NOx emissions will be observed operating with WPD fuel due to a later needle valve opening. The trend indicated in figure 3 and 5 follow linear relationship, with a correlation coefficient of R2 0.987 and 0.988.

4. CONCLUSIONS

In this research, measurement of bulk modulus and its effects of waste plastic diesel have been investigated using Zuech's method as a main work and physical properties. Conclusions can be summarized from obtained results:

The bulk modulus of commercial diesel is 3.5 and 4% higher than that of waste plastic diesel at 6.5 and 10.5 MPa. The sound velocity of WPD 1.23 and 1.35% less than that of CD at 6.5 and 10.5 MPa. The lower bulk modulus and sound velocity the pump produces a slower and lower pressure rise in fuel injection system.

The main fuel properties of waste plastic diesel are similar to commercial diesel and some properties are better than diesel. But flash point of WPD is 40°C.It is 34.75% less than that of CD and nearly value of flammable region. Waste plastic diesel have the potential to manage waste plastic and partially replace the commercial diesel in future or being used in blends with commercial diesel to compensate fuel properties. However, further studies are necessary to utilize this fuel as transportation fuel.

ACKNOWLEDGEMENT

This work was supported by ASEAN University Network/Southeast Asia Engineering Education Development Network (AUN/SEED-Net). The authors would like to thank Asso Prf: Dr Kanit Wattanavichien, Center of Fuel and Energy from Biomass (Chulalongkorn University) for his contribution in this work.

REFERENCES

[1] S.B. Desai,C.K. Galage "Production and analysis of pyrolysis oil from waste plastic in kolhapur city" International Journal of Engineering Research and General Science Volume 3, Issue 1, January-February,2015 ISSN 2091-2730

[2] M.Z.H.Khan, M.Sultana, " Pyrolytic waste plastic oil and its diesel blend: fuel characterization" Journal of Environmental and Public Health Volume 2016, Article ID 7869080, 6 pages

[3] Soo-Young No,"Application of bio-oils from lignocellulosic biomass to transporation, heat and power generation- A review"Renewable and Sustainable Energy Reviews 40(2014)1108-1125

[4] Rajan Kumar, M.K Mishra,S.K.Singh,Arbind Kumar "Experimental evaluation of waste plastic oil and its blends on a single cylinder diesel engine" Journal of Mechanical Science and Technology 30(10)(2016)4781~4789

[5] Sai Gu,Guohong Tian, Ioannis Kalargaris," Investigation on the Long-Term Effects of Plastic Pyrolysis Oil Usage in a Diesel Engine"9th International Conference on Applied Energy, ICAE2017, 21-24 August 2017, Cardiff, UK

[6] Ankit Verma,Jeewan V.Tirkey,M.A Quraish," Engine fuel production from waste plastic pyrolysis and performance evaluationin a CI engine with diesel blend"J.Mater.Environ.Sci.,2018,volume 9,Issue 6,page 1712.1721

[7] Balasubramanian, Shambhavi, "Fuel Type Estimation Using Fuel System Parameters" (2016). Open Access Theses. 745.

[8] P Srichai, P Ewphun, C Charoenphonphanich, "Injection characteristics of palm methyl ester blended with diesel using zuech's chamber" International Journal of Automotive Technology, Vol. 19, No. 3, pp. 535−545 (2018)

[9] Pop-Paul Ewphun,"Effect of Hydrogenated Vegetable Oil (HVO) Diesel Blend on Diesel Spray Flame under Low Oxygen Concentration and High Density Surrounding Gas",Master of Engineering in Automotive Engineering,KMITL,2016

[10] Workplace Hazardous Material Information System(WHMIS) Handbook,2008

[11] Leszek Gil, DanielPieniak, Mariusz Walczak,"Impact acid number of fuels on the wear process apparatus for fuel injection in diesel engines" Advances in Science and Technology Research Journal, Volume 8,No.21,March 2014,pp 54-57

[12] D Morris, A L.Boehman,J Szybist " The impact of the bulk modulus of diesel fuels on fuel injection timing" Energy and Fuel 2004,18,1877-1882

Design Optimization of Combined Expansion Tube-Axial Splitting as Impact Energy Absorber

Yuwono Budi Pratiknyo[1,2], I Wayan Suweca[1], Rachman Setiawan[1]

1) Faculty of Mechanical and Aerospace Engineering, Institut Teknologi Bandung,
Jln Ganesa No 10, Bandung, Indonesia
2) Faculty of Engineering, Universitas Surabaya,
Jln Kalirungkut, Surabaya, Indonesia

*Corresponding e-mail: rachmans@edc.ms.itb.ac.id

ABSTRACT – In This paper, a single objective optimization based on response surface methode is adopted in order to calculate the optimalexpansion tube-axial splitting model parameter. Expansion tube-axial splitting as impact energy absorber applied to overcome collision accidents on passenger trains. Impact energy absorber will absorb the energy that occurs during an accident, so passengers are safe. The dimensions of the expansion tube axial splitting module are influenced by several parameters including tube tickness (t), Inner diameter of tube (D_1) and outer diameter of Dies (D_2). That are influential with the total energy absorbed by the impact absorbing module. Formulations that have been obtained in previous studies are optimized to get the best dimensions.

This study resulted in the selection and optimization method of the design of the impact absorbent module that fits the parameters of the impact absorbent module from various module geometry alternatives taking into account the availability of space.

Keywords: Design optimization, crashworthiness, expansion tube, axial splitting, impact energy absorber

1. INTRODUCTION

The combined expansion tube-axial splitting of deformable rigid tube developed as new mechanism as impact energy absorber. The impact absorbing structure consists of two circular tube forming dies, each dies allowing the tube to expand and to split. The latter is used to meant move away radially the debris after expansion and splitting, so that the absorption process can continue without being obstructed by the debris itself [1]. This combination expansion tube-axial splitting module produces absorption impact characteristics wherein the absorption of the second force of the impact absorbing module is more stable. Enhancement on pipe thickness will cause force enhancement that is able to be absorbed by module [2].

The minimization of the impact of accidents is one of the ways to reduction the effect of accident due to collisions on mass transportation (railways). The impact energy absorber (IEA) module is one of the most important components in the application of crashworthiness technology to improve the safety of transportation facilities. The effective mechanism for absorbing impact energy is through the modular deformation of the module structure. The effect of impact energy absorber, the impact energy and impact force which passed to the main structure of the vehicle will be limited during a collision, so the impact of collision on passengers or cargo can be minimized [3]. In its application, the IEA requires a very important component, which is an impact energy absorbing module. The impact energy absorbing module is one of the most important components in applying crashworthiness technology to improve the safety of transportation facilities. The ideal impact absorbing module is an impact absorbent module that is able to regulate the maximum impact strength permitted throughout a stroke in addition to the effect of elastic loading [4]. In previous studies Ezra and Fay have classified specific energy (Se) and stroke efficiencies (Stc) in several impact absorbent modules [5]. Alghamdi has reviewed several forms of impact energy absorbing. modules and produced several forms of deformation [6]. IEA in plastic deformation can be categorized by structure and material. Based on the structure can be divided into drum [7], circular tube [8] [9], tubular ring [10], square tubes [11] [12] [13] [14] [15] [16], corrugated tubes [17], multi corner columns [18], frusta [19], struts [20], honeycomb cells [21], sand-wich plates [22], circular thin-walled tubes [23], top-hat thin-walled sections [24].

The combined expansion tube-axial splitting of deformable rigid tube developed as new mechanism as shown in Figure-1

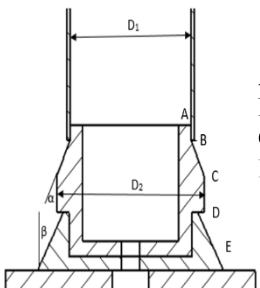

A-B = Pre-compacting process.
B-C = Expansion process.
C-D = Extended expansion process.
D-E = Axial splitting process

Figure-1. Segmented process combined expansion tube-axial splitting

The calculation of combined expansion tube-axial splitting can be explained as follows.

1. Pre-compacting (Zone A-B), at this stage the tube is given a load so that the tube enters the dies and the material is still in the elastic zone.

2. Expansion Process (Zona B-C), at this stage that a new formula has been found to calculate the mean load. The formula mean load (Pm) is as follow:

$$Pm = (\pi t)(D_1 + t)(\sigma_o)\frac{-\frac{K}{t}+ln[D_2-D_1]}{\frac{1}{D_1}+\frac{K}{t}} \quad (1)$$

$$K = \left(\frac{\mu+\tan\alpha}{2\tan\alpha(1-\mu\tan\alpha)}\right) \quad (2)$$

3. Extendex Expansion Process (Zona C-D), at this stage, Tube has the same emphasis as the previous process, so that at this stage it has the same formula as the previous stage
4. Axial Splitting Process (Zona D-E), at this stage that a new formula has been found to calculate the prediction of maximum expanded diameter, that tube will be collapse.

$$\frac{LnD_X}{(D_x)} - \frac{K/_t+LnD_1}{D_x} \le \frac{\varepsilon\pi D_x tE(t+K)}{(\pi t)(D_1+t)(\sigma_o)D_1 t} \quad (3)$$

$$K = \left(\frac{\mu+\tan\alpha}{2\tan\alpha(1-\mu\tan\alpha)}\right) \quad (4)$$

The purpose of this paper is to arrange the methodology for selecting and optimizing the design of impact absorbers modules that meet the parameters of impact absorbers from various alternative geometry modules taking into account the availability of space

2. METHODOLOGY

Design Of Experiments (DOE)

Design of experiments (DOE) is a systematic method to determine the relationship between factors affecting a process and the output of that process. In other words, it is used to find cause-and-effect relationships. This information is needed to manage process inputs in order to optimize the output. An understanding of DOE first requires knowledge of some statistical tools and experimentation concepts. Although a DOE can be analyzed in many software programs, it is important for practitioners to understand basic DOE concepts for proper application.

The most commonly used terms in the DOE methodology include: controllable and uncontrollable input factors, responses, hypothesis testing, blocking, replication and interaction.

- *Controllable input factors*, or *x* factors, are those input parameters that can be modified in an experiment or process. For example, in cooking rice, these factors include the quantity and quality of the rice and the quantity of water used for boiling.
- *Uncontrollable input factors* are those parameters that cannot be changed. In the rice-cooking example, this may be the temperature in the kitchen. These factors need to be recognized to understand how they may affect the response.
- *Responses*, or output measures, are the elements of the process outcome that gage the desired effect. In the cooking example, the taste and texture of the rice are the responses

Response Surface Methodology (RSM)

Response surface methodology (RSM) is a collection of mathematical and statistical techniques for empirical model building. By careful design of *experiments*, the objective is to optimize a *response* (output variable) which is influenced by several *independent variables* (input variables). An experiment is a series of tests, called *runs*, in which changes are made in the input variables in order to identify the reasons for changes in the output response. RSM was developed to model experimental responses (Box and Draper, 1987), and then migrated into the modelling of numerical experiments. The difference is in the type of error generated by the response. In physical experiments, inaccuracy can be due, for example, to measurement errors while, in computer experiments, numerical noise is a result of incomplete convergence of iterative processes, round-off errors or the discrete representation of continuous physical phenomena (Giunta et al., 1996; van Campen et al., 1990, Toropov et al., 1996).

The application of RSM to design optimization is aimed at reducing the cost of expensive analysis methods (e.g. finite element method or CFD analysis) and their associated numerical noise. The problem can be approximated with smooth functions that improve the convergence of the optimization process because they reduce the effects of noise and they allow for the use of derivative-based algorithms. Venter et al. (1996) have discussed the advantages of using RSM for design optimization applications.

3. RESULTS AND DISCUSSION

Optimization Process

The problem optimization can be explain as follow:

Design Variable :

- tube tickness (t),
- inner diameter of tube (D_1). and
- outer diameter of Dies (D_2)

Objective function :

Maximize the specific energy (Se)

Se = EA/m (5)

Maximize stroke effeciency (Le)

Le = L/Lo (6)

Maximize crushing force effeciency (CFE)

CFE = Pm/Ppeak (7)

Equality constrain function:

- $0 \le L/Lo \le 1$ (8)
- $0 \le P_m/P_{peak} \le 1$ (9)
- $0 \le m \le m_{ijin}$ (10)
- $0 \le L_o \le L_{ijin}$ (11)
- $D_2 \le D_x$ (12)

$$\frac{LnD_X}{(D_x)} - \frac{K/_t+LnD_1}{D_x} \le \frac{\varepsilon\pi D_x tE(t+K)}{(\pi t)(D_1+t)(\sigma_o)D_1 t} \quad (13)$$

Where :

EA	= total energy absorbed (J)
m	= module mass (kg)
L	= length after collision (mm)
Lo	= length before collision (mm)
Pm	= mean crushing force (N)
Ppeak	= Peak crushing force (N)

The steps using response surface can be explain as follow:

1. Determine factors, number and range of levels for each factor.
2. Determine the response and learn how to measure it.
3. Compile a first order experimental design.
4. Conduct an experiment according to the design of the first order.
5. Processing the results of the first order experiment. Draft a second order experiment.
6. Conduct experiments according to the design of order II.
7. Processing the results of the second order experiment
8. Determine the optimization model.
9. Determine optimum conditions

First Orde Calculation

Table-1 shows the first order calculation at iteration # 1

Table-1. The first order calculation at iteration # 1

No	t	D1	D2	Pm
1	0,1	10	11	-1099,66
2	0,1	10	81	-251,2976
3	0,1	80	11	#NUM!
4	0,1	80	81	-8858,93
5	2	10	11	-19533,23
6	2	10	81	281856,26
7	2	80	11	#NUM!
8	2	80	81	-173922,35

Range t → $0,1 \le t \le 2$
Range D_1 → $10 \le D_1 \le 80$
Range D_2 → $11 \le D_2 \le 81$
Range Level Not Fulfilled

Table-2 shows the first order calculation at iteration # 2

Table-2. The first order calculation at iteration # 2

No	t	D1	D2	Pm
1	0,5	20	25	4961,31
2	0,5	20	90	30920,76
3	0,5	80	25	Not devined
4	0,5	80	90	47808,41
5	2	20	25	199294,69
6	2	20	90	593805,28
7	2	80	25	Not devined
8	2	80	90	1275658,11

Range t → $0,5 \le t \le 2$
Range D_1 → $20 \le D_1 \le 80$
Range D_2 → $25 \le D_2 \le 90$
Range Level Not Fulfilled

Table-3 shows the first order calculation at iteration # 3

Table-3. The first order calculation at iteration # 3

No	t	D_1	D_2	Pm
1	0,5	20	81	29567,03
2	0,5	20	90	30920,76
3	0,5	80	81	-44117,51
4	0,5	80	90	47808,40
5	2	20	81	573232,37
6	2	20	90	593805,28
7	2	80	81	-173922,34
8	2	80	90	1275658,10

Range t → $0,5 \le t \le 2$
Range D_1 → $20 \le D_1 \le 80$
Range D_2 → $81 \le D_2 \le 90$
Range Level Not Fulfilled

Table-4 shows the first order calculation at iteration # 4

Table-4. The first order calculation at iteration # 4

No	t	D_1	D_2	Pm
1	0,5	20	83,02	29887,40
2	0,5	20	90	30920,76
3	0,5	80	83,02	0,00
4	0,5	80	90	47808,40
5	2	20	83,02	578101,12
6	2	20	90	593805,29
7	2	80	83,02	521767,09
8	2	80	90	1275658,11

Range t → $0,5 \le t \le 2$
Range D_1 → $20 \le D_1 \le 80$
Range D_2 → $83,2 \le D_2 \le 90$
Range Level Fulfilled

Second Orde Calculation

The seconde orde calculation used 3^k factorial (*Three Level Factorial Design*)

Table-5 shows the second order calculation

Table-5. The second order calculation

No	t	D_1	D_2	Pm
1	0,5	20	83	29884,37
2	0,5	20	86,5	30416,21
3	0,5	20	90	30920,76
4	0,5	50	83	59493,91
5	0,5	50	86,5	62001,71
6	0,5	50	90	64279,71
7	0,5	80	83	-257,70
8	0,5	80	86,5	30610,29
9	0,5	80	90	47808,40
10	1,25	20	83	221483,77

11	1,25	20	86,5	224719,29
12	1,25	20	90	227788,81
13	1,25	50	83	469465,91
14	1,25	50	86,5	484959,34
15	1,25	50	90	499032,98
16	1,25	80	83	162627,90
17	1,25	80	86,5	354137,27
18	1,25	80	90	460836,75
19	2	20	83	578055,03
20	2	20	86,5	586137,49
21	2	20	90	593805,29
22	2	50	83	1253050,98
23	2	50	86,5	1292275,82
24	2	50	90	1327906,19
25	2	80	83	517703,30
26	2	80	86,5	1004460,96
27	2	80	90	1275658,11

Validation

Theoritical Calculation

Table-6 shows the theoritical calculation with t = 1 and 1,5, D_1 = 54 mm and D_2 = 60,48 mm

Table-6. Theoritical calculation with t = 1 and 1,5, D_1 = 54 mm and D_2 = 60,48 mm

No	t	D_1	D_2	Pm
1	1	54	60,48	281037,67
2	1,5	54	60,48	357883,20

Experimental Result.

Table-7 shows the experimental result with t = 1 and 1,5, D_1 = 54 mm and D_2 = 60,48 mm

Table-6. Theoritical calculation with t = 1 and 1,5, D_1 = 54 mm and D_2 = 60,48 mm

	T	D_1 (mm)	D_2 (mm)	Pm (N)
1	1	54	60,48	218600
2	1	54	60,48	262610
3	1	54	60,48	254450
4	1	54	60,48	262240
5	1	54	60,48	228800
6	1	54	60,48	225300
7	1	54	60,48	222800
8	1	54	60,48	230900
9	1	54	60,48	338170
10	1,5	54	60,48	349340
11	1,5	54	60,48	357000
12	1,5	54	60,48	372160

Numerical Result

Software: LSDYNA Prepost V4.5 dengan solver R9.10

Model : Lagrangian

Element : Quadrangular element with t = 1.5 mm, D_1 = 54 mm and D_2 = 60,48 mm

Loading : Impactor 107 kg, impact speed 6 m/s

Material : API 5L Grade B for tube, rigid material for dies mild steel properties.

The numerical calculation of combined expansion tube-axial splitting as shown in Figure-2 and Figure -3

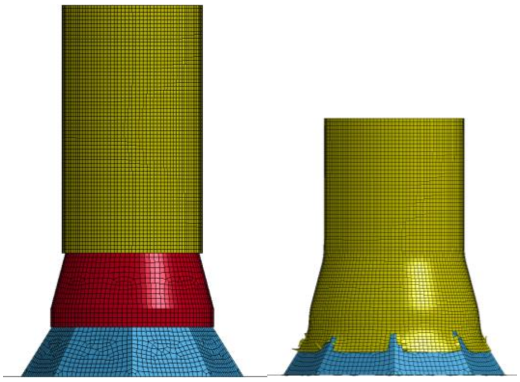

Figure-2. Segmented process combined expansion tube-axial splitting

Figure-3. Comparison numerical and experimental result of combined expansion tube-axial splitting

4. CONCLUSIONS

The application of RSM to design optimization have been reducing the cost of expensive analysis methods (e.g. finite element method or experimental) and their associated numerical noise. The problem can be approximated with smooth functions that improve the convergence of the optimization process.

Multi objective optimization has been applied to combined expansion tube-axial splitting, where optimal decisions need to be taken in the presence of trade-offs between two or more objectives

ACKNOWLEDGEMENT

You may place your acknowledgments here. Write only essential acknowledgments.

REFERENCES

[1] Pratiknyo, Setiawan and Suweca. 2019. Experimental and Theoritical Investigation of Combined Expansion Tube – Axial Splitting as Impact Energy Absorber.

[2] Setiawan, Pratiknyo. 2017. Prelimanary Investigation on Combined Expansion Tube-Axial Splitting Type Impact Energy Absorber. SIGER 2017.

[3] Pratiknyo, Setiawan. 2017. The Overview of Impact Energy Absorber Module on Plastic Deformation Mechanisms. SNTTM XVI.

[4] N. Jones, dalam *Structure Impact*, Melbourne, Camridge University Press, 1997, p. 410

[5] N. Jones dan T. Wierzbicki, Structural Crashworthiness, Butterwoth, 1983

[6] W. J. Stronge, Impact Mechanics, Cambridge: Cambridge University Press, 2000.

[7] E. A. A dan R. J. Fay, "An Assessment of energy absorbing devices for prospective use in aircraft impact situation," *Dynamic response of structure,* vol. 225, p. 46, 1975

[8] A. Alghamdi, "Collapsible impact energy absorber: an overview," *Thin Walled Structures,* vol. 39, pp. 189-213, 2001

[9] C. JF dan P. S, "Energy Dissipation in Braced Cylindrical shell," *International Jurnal Mech Sci,* vol. 30, pp. 203-16, 1988

[10] A. JM, "An Approximate analysis of the collapse of thin cylindrical shell under axial loading," *Quart J Mech Appl Math,* vol. 13, pp. 10-5, 1960

[11] M. Langseth, O. Hopperstad dan A. Hanssen, "Crash behaviour of thin-walled alumunium," *Thin-Walled Structure,* vol. 32, pp. 127-150, 1998

[12] S. Reid, C. Austin dan R. Smith, "Tubular Ring as impact energy absorber," dalam *Structural impact and crashworthiness*, New York, Elsevier, 1984, p. 555.

[13] M. Langseth dan O. Hopperstand, "Static and Dynamic axial crushing of square thin-walled allumunium extrusions," *International Journal Impact Engineering,* vol. 18, pp. 949-68, 1996.

[14] M. Langseth, O. Hopperstand dan T. Berstad, "Crashworthiness of alumunium extrussions; validation of numerical simulation, effect of mass ratio and impact velocity," *International Journal Impact Engineering,* vol. 22, pp. 829-54, 1999.

[15] P. Nannucci, N. Mashall dan G. Nurick, "A Computational investigation of the progressive buckling of square tubes with geometric imperfection," dalam *3rd Asia-Pacific Conference on shock and impact Loads on Structure*, Singapore, 1999.

[16] E. Markiewicz, P. Ducrocq dan P. Drazetic, "An inverse approach to determine the constitutive model parameters from axial crushing of thin walled square tubes," *Int, J. Impact Eng.,* vol. 21, pp. 433-449, 1998.

[17] M. Langseth, O. Hopperstad dan T. Berstad, "Crashworthiness of Alumunium Extrusion: validation of numerical simulation, effect of mass ratio and impact velocity," *International Journal of Impact Engineering,* vol. 22, pp. 829-854, 1999.

[18] H. Huh, K.-P. Kim dan H. S. Kim, "Collapse simulation of tubular structures using a finite element limit analysis approach and shell elements," *International Journal of Mechanical Sciences,* vol. 43, pp. 2171-2187, 2001.

[19] A. Singace dan H. El-Sobky, "Behaviour of axially crushed corrugated tubes," *International Journal Mech Sci,* vol. 39 (3), pp. 249-68, 1997.

[20] T. Weirzbicki dan W. Abramowich, "On the crushing mechanics of thin-walled structure," *J Appl Mech,* vol. 50(4), pp. 727-34, 1983.

[21] W. Mamalis dan W. Johnson, "The Quasi-static crumpling of thin-walled circularcylinders and frusta under axial cmpression," *Int J Mech Sci,* vol. 25(9/10), pp. 713-32, 1983.

[22] J. Harris dan R. Adams, "An assesment of the impact performance of bonded joints for use ini high energy absorbing structures," dalam *Proceeding of the Institute of Mechanical Engineers*, 1985

[23] T. Weirzbicki, "Crashing analysis of metal honeycoms," *International Journal Impact Engineering,* vol. 1(2), pp. 157-74, 1983.

[24] G. Corbett dan S. Reid, "Local Loading of simply-supported steel-grout sandwich plates," *International Journal Impact Engineering,* vol. 13(3), pp. 433-61, 1993

Study the properties of Cambodian natural rubber latex foam by varying sulfur

Bunsreyneang KIM[1], Phanny YOS[2*]

[1)] Department of Chemical Engineering and Food Technology, Institute of Technology of Cambodia, Russian Federation Blvd, P.O. BOX 86, Phnom Penh, Cambodia
[2)] Materials Science and Structure Research Unit, Research and Innovation Center, Institute of Technology of Cambodia, Russian Federation Blvd, P.O. BOX 86, Phnom Penh, Cambodia

*Corresponding e-mail: phannyyos@itc.edu.kh

ABSTRACT – In this study, Cambodian fresh natural rubber latex (latex obtained from rubber tree) is centrifuged in the lab to get the concentration of about 60% total solid content and was frothed to produce natural rubber latex foam. The purpose of this study is to make a basic compound of Cambodian natural rubber latex foam and to introduce the one of the main technologies for manufacturing value-added products using local natural rubber in Cambodia. The foam is characterized in both physical and mechanical properties such as swelling, hardness, ageing, compression set, porosity, density, tensile strength and elongation at break. The samples were prepared with four different compounds with variation of sulfur content, s=1pphr, s=2pphr, s=3pphr and s=4pphr. Dunlop method was used to make natural rubber latex foam. The result showed tensile strength decreased with increasing sulfur contents. Moreover, the increase of sulfur content does not much affect the density of the compound and the compression set of the natural rubber latex foam. Lastly, ageing gives the negative effect to the properties of samples.
Keywords: Natural rubber latex; Curing System; Crosslink density, Latex foam, sulfur

1. INTRODUCTION

Natural rubber (NR) is milky trap from rubber tress (Hevea brasiliensis), which likely to grow in tropic climate [1]. For production of NR, Asia is dominated more than 90% of total world rubber supplier [2]. Cambodia was the 16th country which produced NR in 2010 compare to the world [3]. According to General Directorate of Rubber report (2018), the NR produced was grew by 14% and 15% for produced and exported, respectively.

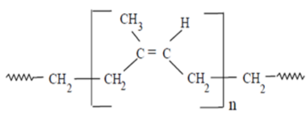

poly-cis-1.4-isoprene

Fig. 1 Chemical structure of rubber

The main chemical compound in NR is poly cis 1.4 isoprene (Fig. 1) [4] which have the concentration of rubber after trapping from the rubber tress is approximately 30 to 40% (**Table 1**) [5].

Table 1. The composition in Natural Rubber latex [5]

Component	Percentage (%)
Rubber	30-40
Water	55-60
Resins	1.5-3.0
Proteins	1.0-1.5
Minerals	0.7-0.9
Carbohydrates	0.1-0.8

To produce foaming latex, the mixture must go through the vulcanizing system, which is a process treat NR latex to give the useful properties such as elasticity, strength, and stability. The mechanism of vulcanization and its acceleration depend on three conditions: the type of rubber, the concentration of each ingredient and the thermodynamic of each step of reaction [6]. The vulcanization makes the increasing of tensile strength, modulus, hardness, abrasion resistance and rebound. In the contrary, it decreases the elongation, aging compression set and solubility [7]. During the vulcanizing, the crosslink between crosslink and rubber partial is created. Sulfur is universal and commonly used for vulcanization process because of low cost and known as low toxicity. Otherwise the understanding mechanism of sulfur is complicated due to each manufactory has developed by their method to produce material based to require of the customer [8].

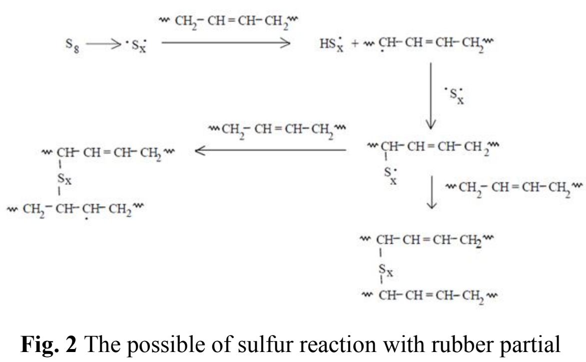

Fig. 2 The possible of sulfur reaction with rubber partial

At room temperature, the sulfur is in rhombic form, which has cyclic eight atoms and then break their own bond to have two free radical atoms. One free radical of sulfur removes hydrogen atoms from polymer chain (C-H) and attaches H to create HS˙. Then other the free radical atoms of sulfur goes to substitute to create new bonds (C-S) and the one side of that free radical atom attach with rubber or continue with other sulfur atoms to create polysulfide crosslinking [5].

The objective of this study aims to compounding natural rubber latex foam by Dunlop method and characterization of physical and mechanical properties such as: swelling test, compression set, porosity, density, ageing, tensile strength elongation at break, and hardness.

2. METHODOLOGY

The formulation and concentration of the reagents used to make NR latex foam are shown in **Table 2**. Firstly, centrifuged NR Latex (TSC 60%) was mixed with sulfur, antioxidant and potassium oleate by stirring at 200rpm for 30min using a stirrer (IKA® EUROSTAR 20). After that, ZMBT and ZDEC were added into the mixture for 30min and were continued stirring at the same speed at room temperature. Then, the NR latex compound was beaten using a hand mixer (STARLUX, SL-135) to make smooth foam until the mixture was increased up to 3 times of initial volume. Then, ZnO and DPG were added into the compound and the mixture was mixed for 90 seconds. SSF was added and was mixed for another 90 seconds. The foam was poured mold, then cured in an oven (ADVANTEC, DRM620DB) at 105 ^{0}C for 2h.

After curing, the foam was washed with water. The NR latex foam was dried in oven for 2 hours at temperature 105 ^{0}C. The final foam got in white off color.

Table 2. The formulation of ingredient in NR latex

Ingredients	pphr*	pphr*	pphr*	pphr*
60% NR latex	100	100	100	100
20% P. O	2	2	2	2
35% Sulphur	**1**	**2**	**3**	**4**
22% Antioxidant	1	1	1	1
35% ZMBT	1	1	1	1
35% ZDEC	1	1	1	1
50% ZnO	3	3	3	3
40% DPG	0.3	0.3	0.3	0.3
25% SSF	1	1	1	1

*pphr= part per hundred rubber

Samples were for physical and mechanical properties such as swelling, hardness, compression set, tensile strength and so on.

3. RESULTS AND DISCUSSION

Fig. 3 shows the initial mass of rubber and final mass of rubber after swell in toluene for 24h in all compounding. The test was conducted with three specimens. The swelling ratio is in percentage.

We see that the swelling ratio decreases compared to increase sulfur content. For sample that has sulfur 1pphr, the ratio was nearly 4 times of initial mass. The proportion is reduced to only 2 times for sample sulfur of 2pphr and continues to slightly decrease for sample sulfur of 3pphr. Additionally, sample sulfur of 4pphr, the rubber swells only 1.5 times compare to initial mass.

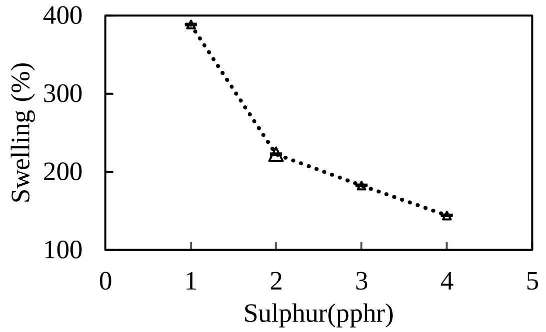

Fig. 3 Swelling ratio of Latex Foam

Hardness data was tested by durometer Shore A0 is shown in **Fig. 4**. The hardness after ageing of NR latex foam sample 1, 2 and 3 increase around two times of hardness before aging. Additionally, the hardness of sample 1 and sample 4 are completely different from 6.88 and 17.68 before aging to 14.04 and 19.2 after aging, respectively.

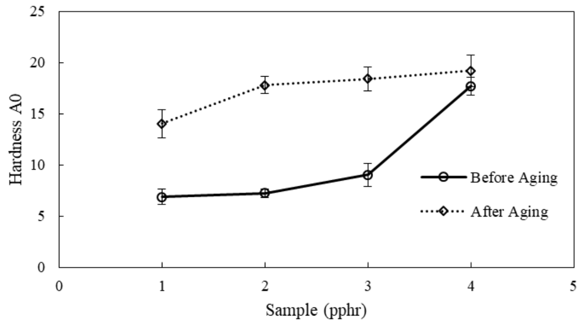

Fig. 4 Hardness results

Figure 5. shows the overall trend of both tensile strengths, before and after ageing test, are declined when increasing sulfur in the compound. Moreover, the tensile strength after ageing are lower than the original one.

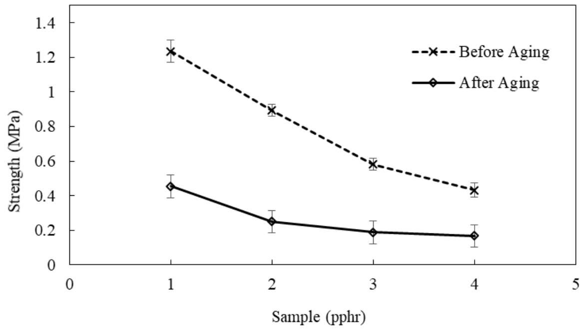

Fig. 5 Tensile strength of Latex Foam

4. CONCLUSIONS

To conclude, the Cambodian natural rubber latex could be produced to become latex foam. As it is basic compounding, the properties are not same as the expectation. With the increase in sulfur content, we noted that the swelling ratio, elongation at break and tensile strength decreases respectively. Additionally, the hardness of rubber is increased with the increase in sulfur content respectively. However, the increase of sulfur does not affect much to the density, and the compression set of the NRLF. Ageing gives the negative effect to all properties of rubber.

ACKNOWLEDGEMENT

I would like to thanks to Royal Government of Cambodia for supporting fund and Cambodia Rubber Research Institute (CRRI) for providing sample and tensile test.

REFERENCES

[1] Jame, C, M. R., and Erman, B., 2013. Ruber elasticity: Basic concepts and behavior. *The Science and Technology of rubber*, 4th Editio, 1–25.

[2] Joseph, R., 2011. An introduction to natural rubber latex. *Practical Guide to Latex Technology*, 1–9.

[3] Freudenberg, M., 2012. World rubber market. Cambodia's rubber production. *Rubber sector profile*, 2012, 3–18.

[4] Verheye, W., 2010. Growth and production of rubber. *life support system*.

[5] Dinsmore, R. P., 2005. Rubber Chemistry. *Industrial & Engineering Chemistry*, 43, 795–803.

[6] Kunststoffe, E. U. N. D., 2005. Conventional and Efficient Crosslinking of Natural Rubber. *Elastomers and Plastics*, 638–643.

[7] Ciullo, P. a. and Hewitt, N., 1999. The Rubber Formulary, in: 1999. , 764.

[8] Lamlong, C., Taweepreda, W., Nu-Mard, R., and Songsiriritthigul, P., 2015. Investigation of Sulfur Crosslinking Interfacial of Natural Rubber (NR) Blending with Carboxyalted Styrene Butadiene Rubber (XSBR) Using X-Ray Absorption Spectroscopy. *Advanced Materials Research*, 1087, 131–136.

Experimental determination of tensile properties of ABS 3D printed material with varying infill percentages

PO Leangpor[1], Yi Liv[1]

1) Department of Industrial and Mechanical Engineering, Institute of Technology of Cambodia, Russian Federation Blvd, P.O. BOX 86, Phnom Penh, Cambodia

*Corresponding e-mail: leangporpo9@gmail.com

ABSTRACT –This work presents experimental results of tensile properties of a 3D printed material with varying infill percentages between 13% and 99%. UP Plus 2 is the printer used in this study. The material used is Acrylonitrile Butadiene Styrene (ABS). ASTM D638 standard was followed for determining the specimen dimensions and testing parameters. The tensile tests were performed with a Shimadzu universal testing machine. The tensile properties reported in this study are ultimate strength, yield strength and Young's modulus. The results show that 99% infill percentage yields the maximum values for the ultimate strength and Young's modulus, but not for the yield strength.

Keywords: 3D printer; ABS (Acrylonitrile Butadiene Styrene); Infill Percentage, Tensile property.

1. INTRODUCTION

The last decade has witnessed the increasing application of 3D printing for prototyping and developing products. A recent survey of 900 companies found that thirty-six percent of companies are already applying or intend to apply 3D printing in their business [1]. The increasing popularity of 3D printing is thanks to the fact that the technology provides freedom of design, mass customization, minimum material waste, and the ability to achieve complex shapes [2].

At an NGO, Golden West Humanitarian Organization, located in Phnom Penh, 3D printing has been used for developing various products for many years. However, the mechanical properties are not known to the product designers. One might opt to use datasheet of their purchased 3D printing filaments for the mechanical properties. Unfortunately, the datasheet from filament manufacturers usually provides the properties obtained from the injection molded specimens but not the 3D printed ones. Therefore, using such values may lead to erroneous unreliable design, especially when it is involved in mechanical load bearing parts.

The objective of this paper is to experimentally determine the tensile properties of 3D printed specimens from filaments and a low-end 3D printer. Infill percentage was varied between 13 and 99%. The information is of interest for designers at the aforementioned organization to select appropriate infill ratios for their applications.

2. METHODOLOGY

In this study, the geometry of the specimens was drawn in the 3D CAD software program SolidWorks, and converted to STL file for 3D printing. Standard test method of ASTM D368 was followed [3]. The specimen type IV was selected as the geometry of the tensile specimen (thickness of 4 mm).

3D printer model "UP Plus 2" was used to print the specimens. Printing parameters were set through the software program "UP Studio". The printer allows thickness to vary between 0.15 mm and 0.40 mm, and a constant printing speed of 10 cm^3/h. The dimensions of the printing bed are 245x260x350 mm. The extrusion temperature was set at 260˚C, and heating temperature of printing bed was at 90˚C.

Octave ABS filament model with the diameter of 1.75 mm and red color was considered in this study.

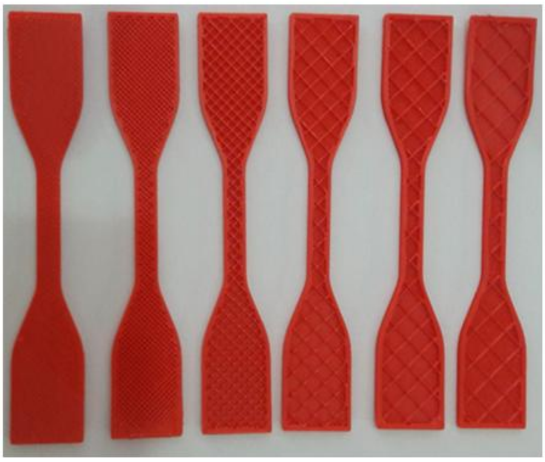

Figure 1: Photographs showing the cross-section cut of specimens with varying infill percentages

Table 1: Test matrix of varying infill percentages and other parameters fixed for the study

Test Case	Layer Thickness (mm)	Orientation	Infill Percentage (%)
1	0.2	0	13
2	0.2	0	15
3	0.2	0	20
4	0.2	0	80
5	0.2	0	99

Universal testing machine of Shimadzu AG-XPLUS series was used, see Figure 2. Five specimens per infill percentage were tested. The loading speed was 5 mm/min for all tests.

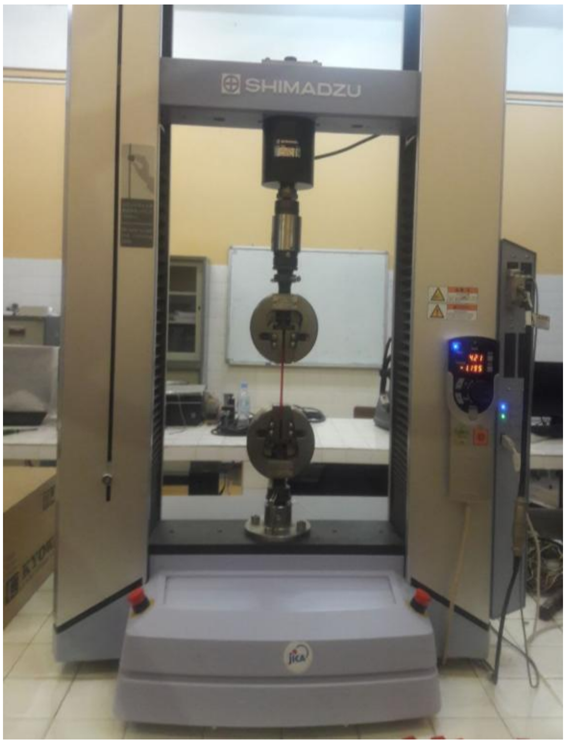

Figure 2: Experimental setup of a tensile test

3. RESULTS AND DISCUSSION

Table 2 shows the mean values of the tensile properties obtained from the tests of specimens with infill percentages being varied between 13-99%.

The ultimate strength does not show a tendency of increase while the infill percentages are no more than 65%. This behavior was not expected because increased infill percentages should give the specimens with higher infill percentage more loading bearing capacity. However, the increasing trend of the strength can be observed when the infill percentage varies from 20-99%, with an increase rate of about 50% in strength.

The yield strength (0.2% offset) appears to be insensitive to the increase in infill percentage. The difference between the minimum and maximum values of the modulus is around 10%. This phenomena is not straightforward, thus requires further study into the mechanism underlying the yield behavior of the printed parts.

The Young's modulus tends to increase with increasing infill percentages. The reason behind this observation may be attributed to the fact that the increased infill percentages result in more amount of material within the same given volume, thus provide more stiffness to the specimen.

Table 2: Test results of tensile properties

Infill percentage (%)	No. of specimens	Ultimate strength (MPa)	Yield strength (MPa)	Young's modulus (MPa)
13	5	21.7	21.2	463
15	5	23.3	22.7	527
20	5	22.2	21.4	496
65	5	23.1	22.2	559
80	5	25.7	20.5	589
99	5	33.0	22.1	777

4. CONCLUSIONS

In this study, tensile properties of ABS specimens printed with UP Plus 2 3D printer were experimentally determined. Infill percentages were varied between 13-99% to observe their influences on the material properties. The results show that the parts obtained from the selected 3D printer and printing filament yield the ultimate strength of at least 21-33 MPa, yield strength of slightly above 20 MPa and Young's modulus within the range of 463-777 MPa. For parts requiring tensile load bearing capacity of near 20 MPa, 13% infill percentage could help to minimize material usage.

ACKNOWLEDGEMENT

We would like to acknowledge Mr. John Wright at Golden West Humanitarian Foundation (NGO) for providing us with the 3D print filaments and access to the printer used in this study.

REFERENCES

[1] Frank Thewihsen, 2016, "If 3D printing has changed the industries of tomorrow, how can your organization get ready today?", Retrieved from https://www.ey.com

[2] Ngo, T.D., Kashani, A., Imbalzano, G., Nguyen, K.T.Q., Hui, D., 2018. Additive manufacturing (3D printing): a review of materials, methods, applications and challenges. Compos. B Eng. 143, 172-196. https://doi.org/10.1016/ j.compositesb.2018.02.012

[3] ASTM D638-10, Standard Test Method for Tensile Properties of Plastics, ASTM International, West Conshohocken, PA, 2010, www.astm.org

Sponsor

AUN/SEED-Net JICA

Co-sponsor

www.tem-trading.com

INSTITUTE OF TECHNOLOGY OF CAMBODIA

Russian Federation Boulevard
P.O. BOX 86 Phnom Penh, Cambodia
www.itc.edu.kh

Telephone : (855)23 880 370
Fax : (855)23 880 369
Email : info@itc.edu.kh